



Quantum optics with single-wall carbon nanotubes

Christophe Galland

► To cite this version:

Christophe Galland. Quantum optics with single-wall carbon nanotubes. Physics [physics]. Eidgenössische Technische Hochschule Zürich (ETHZ), 2010. English. NNT: . tel-00616058

HAL Id: tel-00616058

<https://theses.hal.science/tel-00616058>

Submitted on 19 Aug 2011

HAL is a multi-disciplinary open access archive for the deposit and dissemination of scientific research documents, whether they are published or not. The documents may come from teaching and research institutions in France or abroad, or from public or private research centers.

L'archive ouverte pluridisciplinaire **HAL**, est destinée au dépôt et à la diffusion de documents scientifiques de niveau recherche, publiés ou non, émanant des établissements d'enseignement et de recherche français ou étrangers, des laboratoires publics ou privés.

DISS. ETH NO. 19013

Quantum Optics

with

Single-Wall Carbon Nanotubes

A dissertation submitted to the
SWISS FEDERAL INSTITUTE OF TECHNOLOGY ZURICH

for the degree of
Doctor of Sciences

presented by
CHRISTOPHE GALLAND

Ingénieur Diplômé
de l'Ecole Polytechnique Paris

born 28th of January 1983

citizen of France

Accepted on the recommendation of :

Prof. Ataç Imamoğlu, examiner
Prof. Vahid Sandoghdar, co-examiner

2010

“In June, 1991, I found an extremely thin needle-like material when examining carbon materials under an electron microscope. Soon thereafter the material was proved to have a graphite structure basically, and its details were disclosed. I named these materials “carbon nanotubes” since they have a tubular structure of carbon atom sheets, with a thickness scaled in less than a few nanometers. The name has been widely accepted now. Carbon nanotubes have attracted a lot of researchers in a wide range of fields from academia to industry, not only because of their uniqueness when compared with conventional materials, but also because they are very promising materials in nanotechnology in future technology. ”

Iijama Sumio, Japanese scientist who discovered Carbon Nanotubes

Summary

In this dissertation, we report on experimental and theoretical investigations of the optical properties of semiconducting single-wall carbon nanotubes (SWNTs). We focus on aspects and phenomena involving typically quantum effects, whose descriptions require going beyond the realm of classical physics and Maxwell equations.

Our most significant experimental result is the observation of photon antibunching in the photoluminescence (PL) emitted by SWNTs. Considering the particularities of our sample, in which surfactant-embedded SWNTs are deposited on a functionalized substrate, we show that the suppression of multi-photon emission events is due to localization of the excitons in nanometer-scale traps along the nanotubes. Fast and efficient exciton-exciton annihilation, a consequence of the reduced dimensionality of carbon nanotubes, is playing a determinant role in forbidding photon-pair emission.

The successful reproduction of the broad and asymmetric PL lineshapes by a physical model relying on strong exciton confinement supports this picture. We calculate the PL spectrum of a quantum dot (QD) embedded in a SWNT and demonstrate that exciton coupling to the low-energy acoustic phonons of the nanotube leads to ultrafast, non-markovian pure dephasing of the optically excited state. In the spectral domain, the oscillator strength is transferred from the zero-phonon line into phonon wings bearing a strong asymmetry at cryogenic temperatures.

We prove hereby that our PL data are direct evidences of the experimental realization of the spin-boson model in the (sub-)ohmic regime. This is a consequence of the one-dimensionality of the phonon bath reflected in the spectral density governing the dissipation. We emphasize the qualitative differences compared to traditional QDs embedded in a three-dimensional matrix, and briefly discuss the consequences for the use of SWNT-QDs in quantum information processing.

An exciting possibility opened by strong exciton-phonon coupling in carbon nanotubes is their use as mechanical resonators for laser-assisted cooling. We propose a device based on a suspended SWNT where exciton confinement is controlled by sharp tips acting as gates. The potential applied on the tips can additionally be used to induce exciton coupling to the flexural mode of the SWNT and tune its strength. Inelastic scattering of a weak red-detuned laser then permits to reduce the occupation number of the fundamental flexural mode down to the quantum ground state.

In an attempt to give a unified picture for all our experimental observations, we also suggest a physical origin for the unintentional formation of SWNT-QDs in our sample. We consider the presence of a charged impurity in the surrounding of the nanotube and demonstrate that the resulting electric field effectively traps the SWNT excitons. The peculiar characteristics of the confining potential would explain most of the experimental features.

Finally, we show how non-vanishing spin-orbit coupling recently measured in transport experiments allows for all-optical spin manipulation in carbon nanotubes.

We perform numerical simulations based on Bloch-equations to demonstrate that high-fidelity spin-state preparation is achievable. Coherent optical spin manipulation and possible schemes for the use of SWNT spins in quantum information processing are also discussed.

Combining surprising novel experimental results with diverse theoretical and numerical studies, this work emphasizes on the fascinating potential of carbon nanotubes in the study of quantum physics in materials of reduced dimensionality.

Zusammenfassung

In dieser Dissertation berichten wir über experimentelle und theoretische Untersuchungen der optischen Eigenschaften von halbleitenden einwandigen Kohlenstoff-Nanoröhrchen (SWNTs). Wir konzentrieren uns auf Aspekte und Phänomene, die typischerweise Quanteneffekten sind, deren Beschreibungen erfordern, jenseits der klassischen Physik und der Maxwell-Gleichungen zu gehen.

Unser wichtigstes experimentelles Ergebnis ist die Beobachtung von Photon Anti-bunching in der aus SWNTs emittierten Photolumineszenz (PL). In Anbetracht der Besonderheiten unserer Probe, die aus Tensid-eingebetteten, auf einem funktionalisierten Substrat liegenden SWNTs besteht, zeigen wir, dass die Unterdrückung von Multi-Photonen Emission auf die Lokalisierung der Exzitonen in Nanometerskala Fallen entlang der Nanoröhrchen zurückzuführen ist. Schnelle und effiziente Exziton-Exziton Vernichtung, eine Folge der reduzierten Dimensionalität der Kohlenstoff-Nanoröhrchen, spielt eine entscheidende Rolle, um Photon-Paar Emission zu verhindern.

Die erfolgreiche Wiedergabe der breiten und asymmetrischen PL Linienformen durch ein physikalisches Modell, das auf starke Exziton Entbindung beruht, unterstützt dieses Bild. Wir berechnen das PL-Spektrum einer in einem SWNT eingebetteten Quantenpunkt (QD) und zeigen, dass Exziton Ankopplung zu den niedrig-Energie akustischen Phononen der Nanoröhrchen zu ultraschneller, Nicht-Markovscher reiner Dephasierung des optisch-angeregten Zustands führt. Im spektralen Bereich wird die Oszillator-Kraft aus der Null-Phonon Linie in Phononen-Flügel verlegt, die eine starke Asymmetrie bei kryogenen Temperaturen aufweisen.

Wir beweisen, dass unsere PL Daten direkte Beweise für die experimentelle Realisierung des Spin-Boson Modells in der ohmsche Regime sind. Dies ist eine Folge der Eindimensionalität des Phonon-Bades, die sich in der spektralen Verlustleistungsdichte widerspiegelt. Wir betonen die qualitativen Unterschiede zu herkömmlichen, in einer dreidimensionalen Matrix eingebetteten QDs, und diskutieren kurz die Folgen für die Nutzung von SWNT-QDs in Quanten-Informationsverarbeitung.

Eine spannende Möglichkeit, die sich aufgrund der starken Exziton-Phonon Kopplung in Kohlenstoff-Nanoröhrchen öffnet, ist ihre Verwendung als mechanische Resonatoren für laserunterstützte Abkühlung. Wir entwerfen ein Gerät, das auf ein abgehängtes SWNT basiert, in dem die Exziton Entbindung mit scharfen Spitzen kontrolliert wird, die als Gatter gesteuert werden. Das an den Spitzen angelegte Potenzial kann zusätzlich verwendet werden, um eine Kopplung des Exzitons an die Biegeschwingung des SWNTs zu erzeugen und ihre Stärke einzustellen. Inelastische Streuung von einem schwachen, rot-verschobenen Laser erlaubt dann, die Besetzungszahl der ersten Harmonische der Biegeschwingung bis zum Quantengrundzustand herabzudrücken.

In einem Versuch, ein einheitliches Bild für alle unsere experimentellen Beobachtungen zu bieten, schlagen wir auch eine physische Ursache für die Entstehung von

SWNT-QDs in unserer Probe vor. Wir betrachten die Anwesenheit einer geladenen Verunreinigung in der Umgebung des Nanoröhrchens, und zeigen, dass das resultierende elektrische Feld eine Falle für die SWNT Exzitonen bewirkt. Die besonderen Merkmale des entbindenden Potenzials könnte die meisten experimentellen Features erklären.

Schliesslich zeigen wir, wie die nicht verschwindende Spin-Bahn-Kopplung, die vor kurzem in Transport Experimenten gemessen wurde, rein optische Spin-Manipulation in Kohlenstoff-Nanoröhrchen ermöglicht. Wir führen numerische, auf Bloch-Gleichungen basierende Simulationen auf, um zu beweisen, dass hochgenaue Spin-Zustand Vorbereitung erreichbar ist. Kohärente optische Spin-Manipulation und mögliche Entwürfe für die Nutzung von SWNT-Spins in Quanten-Informationsverarbeitung werden ebenfalls diskutiert.

Indem überraschende neuartige experimentelle Ergebnisse mit unterschiedlichen theoretischen und numerischen Untersuchungen kombiniert werden, betont diese Arbeit die faszinierende Anwendungspotenziale von Kohlenstoff-Nanoröhrchen in der Untersuchung der Quantenphysik in Materialien reduzierter Dimensionalität.

Résumé

Dans cette dissertation nous présentons une étude expérimentale et théorique sur les propriétés optiques de nanotubes de carbone mono-parois (SWNTs) semi-conducteurs. Nous nous concentrons sur les aspects et phénomènes typiquement quantiques dont la description nécessite de sortir du cadre de la physique classique et des équations de Maxwell.

Notre résultat expérimental le plus important est l'observation du dégroupement des photons dans la photoluminescence (PL) émise par les SWNTs. Tenant compte des particularités de notre échantillon qui consiste de SWNTs enrobés dans un surfactant et déposés sur un substrat fonctionnalisé, nous montrons que l'absence d'émission simultanée de plusieurs photons est due à la localisation des excitons dans des pièges de quelques nanomètres de long sur nanotube. L'annihilation exciton-exciton rapide et efficace résultant de la dimension réduite des nanotubes de carbone joue un rôle déterminant pour éviter l'émission de paires de photons.

La fidèle reproduction des larges lignes asymétriques en PL par un modèle physique reposant sur le confinement des excitons supporte cette vision. Nous calculons le spectre d'une boîte quantique (QD) formée sur un SWNT et démontrons que le couplage de l'exciton avec les phonons acoustiques de faible énergie du nanotube cause un déphasage ultra-rapide et non-markovien de l'état optiquement excité. Dans le domaine spectral, la force d'oscillateur est transférée de la transition sans phonon (ZPL) vers des ailes associées aux phonons et présentant une forte asymétrie aux températures cryogéniques.

Nous prouvons que nos données sont des preuves directes de la réalisation expérimentale du modèle spin-boson dans le régime (sous-)ohmique. Ceci est une conséquence de l'uni-dimensionnalité du bain de phonons se réfléchissant dans la densité spectrale gouvernant les dissipations. Nous soulignons les différences qualitatives par rapport aux boîtes quantiques traditionnels dans une matrice à trois dimensions, et discutons brièvement les conséquences pour l'utilisation des SWNT-QDs dans le traitement d'information quantique.

Une possibilité passionnante ouverte par le fort couplage exciton-phonon dans les nanotubes de carbone est leur utilisation comme résonateurs mécaniques pour le refroidissement assisté par laser. Nous proposons un dispositif basé sur un SWNT suspendu où le confinement de l'exciton est contrôlé par de fines pointes servant de grilles. Le potentiel appliqué aux pointes peut en outre être utilisé pour induire le couplage de l'exciton au mode de flexion du SWNT et pour régler sa force. La diffusion inélastique d'un faible laser désaccordé vers le rouge permet alors de réduire le nombre d'occupation du mode fondamental de flexion jusqu'à l'état fondamental quantique.

Dans une tentative de donner une image unifiée pour l'ensemble de nos observations expérimentales, nous proposons aussi une origine physique à la formation de SWNT-QDs dans notre échantillon. Nous considérons la présence d'une impureté

chargée dans les environs du nanotube et démontrons que le champ électrique qui en résulte piège les excitons du SWNT. Les caractéristiques particulières de ce potentiel confinant pourraient expliquer la plupart des caractéristiques expérimentales.

Enfin, nous montrons comment le couplage spin-orbite non-nul récemment mesuré dans des expériences de transport permet la manipulation purement optique du spin dans des nanotubes de carbone. Nous effectuons des simulations numériques basées sur les équations de Bloch pour démontrer que la préparation du spin avec haute fidélité est réalisable. La manipulation optique cohérente du spin et de possibles utilisations du spin des nanotubes de carbone dans le traitement quantique de l'information sont également discutées.

Alliant de nouveaux résultats expérimentaux surprenants et de diverses études théoriques et numériques, ce travail met l'accent sur le potentiel fascinant des nanotubes de carbone dans l'étude de la physique quantique des matériaux de dimension réduite.

Contents

Titel	a
Summary	c
Zusammenfassung	e
Résumé	g
Contents	i
1 Introduction: Carbon Nanotubes Spectroscopy	1
1.1 Band Structure and Excitons	2
1.1.1 Single particle band structure	2
1.1.2 Excitonic binding energy	7
1.1.3 Symmetries, selection rules, Dark and Bright excitons	10
1.2 Photoluminescence	12
1.2.1 Different types of samples	12
1.2.2 Chirality assignment: Kataura Plot	16
1.2.3 Phonon-assisted excitation	16
1.2.4 Photoluminescence bleaching, blinking and spectral diffusion	17
2 Photon Correlation Measurements on Individual Nanotubes	23
2.1 Experimental Details	23
2.1.1 Sample Preparation and Characterization	23
2.1.2 Confocal Microscope Setup	25
2.1.3 Time-resolved spectroscopy	27
2.2 Auto-correlation measurements and Photon antibunching	30
2.2.1 Photon correlation: theory and setup	30
2.2.2 Photon antibunching from carbon nanotubes	33
2.3 The origin of antibunching: discussion	34
2.3.1 Exciton-exciton annihilation	34
2.3.2 Exciton localization in SWNT-Quantum Dots	37
2.3.3 Evidence for ultra-fast Auger recombination	38
2.3.4 Resonant excitation of a SWNT-QD	39
3 Exciton Dephasing Induced by Acoustic Phonons	43
3.1 The Physical Model	43
3.1.1 Carbon Nanotube Quantum Dot	43
3.1.2 Exciton-Phonon Coupling	45
3.1.3 Spin-Boson Hamiltonian	47

3.2	Numerical Calculations and Fits	48
3.2.1	Analytical expression of the spectrum	48
3.2.2	Spin-Boson model in the Ohmic regime	50
3.2.3	Fits and Parameters	53
3.2.4	Radial Breathing Mode replica	56
3.3	Discussion and implications: Non-Markovian decoherence	57
4	Quantum-dots in Carbon nanotubes	63
4.1	Controlled formation and device design	63
4.1.1	Wave-functions and implementation of a SWNT-QD	63
4.1.2	Controlling the exciton-phonon coupling	66
4.1.3	Device proposal and simulations	68
4.2	Unintentional confinement induced by a charged impurity	71
4.2.1	Introduction and physical model	71
4.2.2	Calculation of the confinement potential	74
4.2.3	Comparison with the experimental observations	77
4.3	Exciton coupling to the bending mode: sub-ohmic lineshapes	83
4.3.1	The effective exciton-phonon coupling	83
4.3.2	A new eye on the experimental data: ohmic vs. sub-ohmic fits	86
4.3.3	Statistical analysis and conclusions	89
5	All optical manipulation of a SWNT-QD spin	95
5.1	Spin-Orbit coupling in carbon nanotubes	95
5.1.1	Physical origin of Spin-orbit coupling	95
5.1.2	Spin-orbit interaction in SWNTs: theoretical predictions	97
5.1.3	Experimental observation	103
5.2	Optical Spin Pumping	107
5.2.1	Presentation of the scheme and the model	107
5.2.2	Numerical simulations	112
5.2.3	Discussion of possible complications	117
5.2.4	Extensions	121
6	Conclusion & Outlook	123
	Appendix	125
1	Opto-mechanical cooling of a SWNT resonator	125
1.1	Preliminary remarks	125
1.2	Summary of the calculations	128
1.3	Numerical results: ground-state cooling	131
	Bibliography	I
	List of Publications	IX
	Acknowledgement	XI
	Curriculum Vitae	XIII
	List of Figures	XV

1 Introduction: Carbon Nanotubes Spectroscopy

The simplest carbon nanotube is composed of a single sheet of graphene (a honeycomb network of carbon atoms), rolled up seamlessly into a tubular form. The first experimental observation of carbon nanotubes was reported by Sumio Iijima in 1991 (Fig. 1.1 a)). These were composed of many tubes nesting in a concentric fashion (multi-wall nanotubes, MWNTs) [1]. Two years later he discovered a single-wall carbon nanotube (SWNT) [2] (Fig. 1.1 b)). Tubular carbon structures may be categorized in the fourth allotrope of carbon, following diamond, graphite and fullerenes.

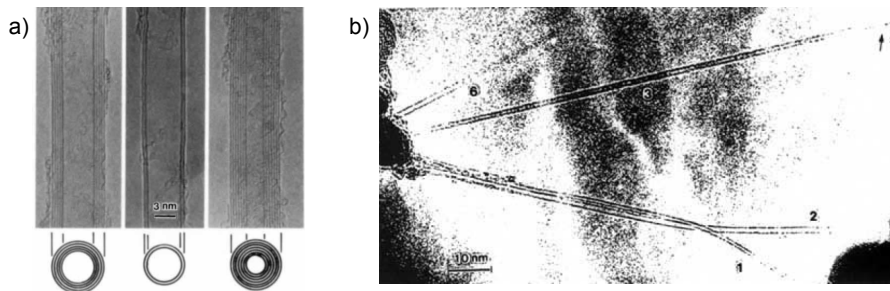


Figure 1.1: First observation of carbon nanotubes by S. Iijima. a) Electron micrographs of *multi-wall* carbon nanotubes, published in [1]. b) Electron micrographs showing *single-wall* carbon nanotubes, published two years later in [2].

Another more general difference of carbon nanotubes with respect to conventional crystalline materials is their sizes: their diameters are on the order of a few nanometers or less while their lengths are typically a few micrometers, and can extend up to millimeters [3]! Because of this small size and large aspect-ratio, carbon nanotubes exhibit unique physical and chemical properties. Single-wall nanotubes, in particular, show more dominant properties originating from this one-dimensionality, which become more pronounced as their diameters become smaller.

An important factor controlling SWNTs properties comes from a variation of tubule structures related to how the honeycomb sheet of carbon atoms is rolled up. There are many possible ways to do this, depending upon the direction of rolling, which is given by the chiral vector. This could result in many chiral arrangements (spiral arrangement of carbon atoms) of the nanotube structure as well as a variety of diameters.

In this dissertation, we will treat exclusively *single-wall* carbon nanotubes, which have the richest and most interesting optical properties. As we shall see, statistically one third of nanotubes are metallic. In a MWNT, electronic and optical properties

are dictated by the smallest band-gap nanotube, and it is found experimentally that MWNTs always show metallic (or small band-gap) characteristics. Although both metallic and semiconducting nanotubes allow for Raman scattering investigations, the observation of visible to near infrared photoluminescence (PL) is limited to semiconducting SWNTs with large enough band-gaps. Another difficulty in optical studies is the very efficient quenching of electronic excitations via inter-tube relaxation and interaction with the substrate. For all these reasons, it took almost one decade after their discovery before PL from SWNTs was first observed by M. J. O'Connell and coworkers in 2002 [4].

This first chapter gives an introduction to the optical properties of SWNTs with a focus on PL. Raman scattering will not be treated here since it is not directly relevant for our work and is already covered by a vast literature. Similarly, optical absorption, being a particularly useful tool for the characterization of ensembles, will not be exposed in detail. We start with a basic theoretical understanding of the electronic states in SWNTs. Their unique properties originate from their reduced dimensionality on the one hand, and from the underlying symmetry of graphene (the presence of two sublattices of carbon atoms), on the other hand. Then we give an overview of PL spectroscopy of SWNTs. We present the possible types of samples and materials that can be used and the different measurement methods. We finally review some important features like phonon-assisted excitation and propensity to PL fluctuations and PL quenching.

1.1 Band Structure and Excitons

The purpose of this section is to provide a detailed but mostly qualitative understanding of the electronic states and band structure of SWNTs, especially of semiconducting type, a more rigorous description being derived in chapter 4.1. We first explain how an approximate single-particle band structure (neglecting curvature effects) is easily obtained from graphene tight-binding calculations by the so-called zone-folding scheme. However, strong confinement of electrons and holes in these one-dimensional systems lead to enhanced many-particle effects. Therefore optical excitations form strongly bound excitons. To account faithfully for these states, we need not only consider their large binding energies, but also their different symmetries (involving spin and valley degrees of freedom) which determine whether an exciton is optically active (bright) or not (dark).

1.1.1 Single particle band structure

Discarding in a first time many-body interactions, we can derive the general electronic structure of SWNTs from the single-particle spectrum of a graphene sheet by imposing suitable boundary conditions on the wave functions. This is the zone-folding method, which we outline here.

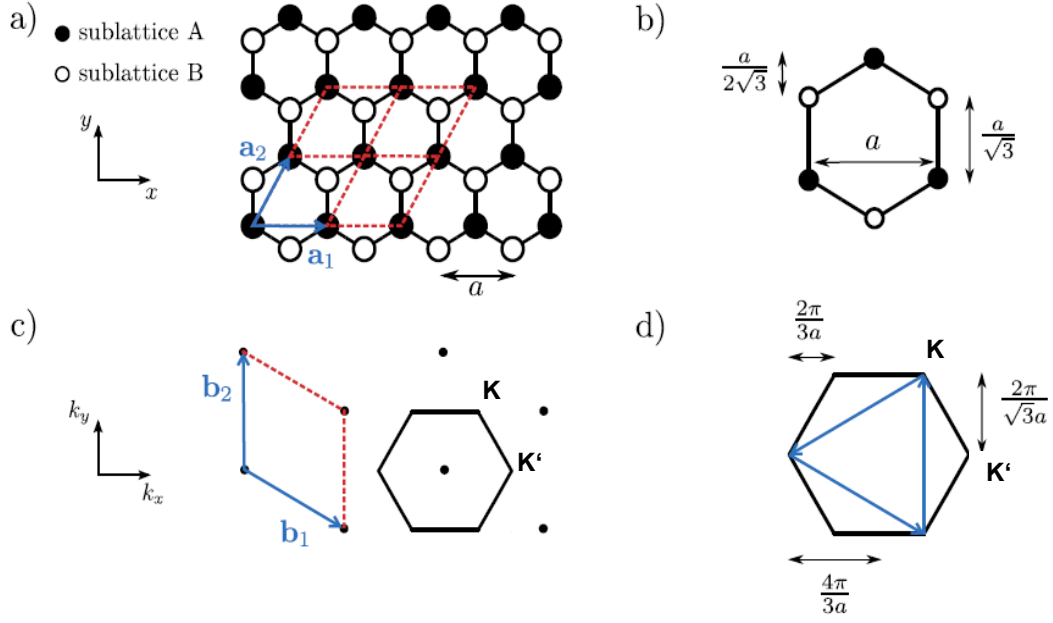


Figure 1.2: a) Graphene real-space lattice with the two sub-lattices A and B. Each red parallelogram represents a unit cell containing one A and one B carbon atom. Some dimensions are given in b), with $a = 0.246$ nm. c) and d) The reciprocal space is also hexagonal with two inequivalent sites K and K' . Figure adapted from [5].

Graphene Tight Binding model

Graphene is a two-dimensional realization of carbon, where the carbon atoms are arranged in a honeycomb network. The honeycomb network itself is not a Bravais lattice, but can be described as a triangular (or hexagonal) lattice with a basis of two atoms. The triangular lattice is generated by the primitive basis vectors as shown in Fig. 1.2. The primitive unit-cell spanned by these vectors is a rhombus with side length $a = 0.246$ nm. In the case of the honeycomb network, there are two basis atoms per unit cell at the positions [5]:

$$\mathbf{a}_1 = \begin{pmatrix} a \\ 0 \end{pmatrix} \quad \text{and} \quad \mathbf{a}_2 = \begin{pmatrix} \frac{1}{2}a \\ \frac{\sqrt{3}}{2}a \end{pmatrix}$$

We usually denote these basis atoms as atom A and B respectively. The basis atoms form two triangular lattices (also named sublattices A and B), that are shifted with respect to each other to obtain the honeycomb network. In this network, each atom has three nearest neighbors of the opposite kind. The distance between neighboring carbon atoms is given as $a_{CC} = a/\sqrt{3} = 0.142$ nm. In the case of a triangular lattice, the reciprocal lattice is again triangular, rotated by 90° with respect to the original one (see Fig. 1.2). The reciprocal lattice is spanned by the primitive basis vectors:

$$\mathbf{b}_1 = \begin{pmatrix} \frac{2\pi}{a} \\ \frac{2\pi}{\sqrt{3}a} \end{pmatrix} \quad \text{and} \quad \mathbf{b}_2 = \begin{pmatrix} 0 \\ \frac{4\pi}{\sqrt{3}a} \end{pmatrix}$$

The first Brillouin zone is constructed as the Wigner-Seitz cell of the reciprocal lattice and has the shape of a hexagon. However, a wave vector in a Bravais lattice

is only defined up to some reciprocal lattice vector. Thus, only two of the six corners in the Brillouin zone are non-equivalent, as always three corners can be connected with a reciprocal lattice vector. These two inequivalent corners are called K -points and are labeled K and K' respectively. Following T. Ando [6], we choose the wave vectors:

$$\mathbf{K} = \frac{2\pi}{a} \begin{pmatrix} \frac{1}{3} \\ \frac{1}{\sqrt{3}} \end{pmatrix} \quad \text{and} \quad \mathbf{K}' = \frac{2\pi}{a} \begin{pmatrix} \frac{2}{3} \\ 0 \end{pmatrix}$$

In a graphene sheet, and when curvature is small also in nanotubes, the s -orbitals and in-plane $p_{x,y}$ -orbitals of the carbon atoms hybridize to form a strongly bound σ system (sp^2 hybridization). Low-energy (i.e. up to few electron-volts) properties are thus governed by the remaining carbon valence electrons in their p_z shells, perpendicular to the graphene plane. We note $\Phi_z(\mathbf{r})$ the wave function of the p_z orbital of a carbon atom located at the origin. In a tight-binding model, we write the electronic wave functions of graphene:

$$\Psi(\mathbf{r}) = \sum_{\mathbf{R}_A} \Psi_A(\mathbf{R}_A) \Phi_z(\mathbf{r} - \mathbf{R}_A) + \sum_{\mathbf{R}_B} \Psi_B(\mathbf{R}_B) \Phi_z(\mathbf{r} - \mathbf{R}_B) \quad (1.1)$$

We further limit ourself to the nearest-neighbor approximation and denote the corresponding transfer integral $-\gamma_0$. The vectors τ_l , $l = 1, 2, 3$ connect the nearest neighbor carbon atoms (see Fig. 1.4):

$$\tau_1 = a \begin{pmatrix} 0 \\ \frac{1}{\sqrt{3}} \end{pmatrix}, \quad \tau_2 = a \begin{pmatrix} -\frac{1}{2} \\ -\frac{1}{2\sqrt{3}} \end{pmatrix}, \quad \tau_3 = a \begin{pmatrix} \frac{1}{2} \\ -\frac{1}{2\sqrt{3}} \end{pmatrix}$$

Neglecting the overlap integral between A and B atoms orbital wave-functions we get the linear system for the eigenstates:

$$\begin{aligned} \varepsilon \Psi_A(\mathbf{R}_A) &= -\gamma_0 \sum_{l=1}^3 \Psi_B(\mathbf{R}_A - \tau_l) \\ \varepsilon \Psi_B(\mathbf{R}_B) &= -\gamma_0 \sum_{l=1}^3 \Psi_A(\mathbf{R}_B + \tau_l) \end{aligned} \quad (1.2)$$

Using Bloch theorem we decompose the coefficients in a product of a slowly varying envelope and a plane-wave component of wave vector \mathbf{k} : $\Psi_{A,B}(\mathbf{R}_{A,B}) = f_{A,B}(\mathbf{k}) \exp(i\mathbf{k} \cdot \mathbf{R}_{A,B})$. After insertion in eq. 1.2 and straightforward simplifications we obtain the matrix equation:

$$\begin{pmatrix} 0 & h_{AB}(\mathbf{k}) \\ h_{AB}(\mathbf{k})^* & 0 \end{pmatrix} \begin{pmatrix} f_A(\mathbf{k}) \\ f_B(\mathbf{k}) \end{pmatrix} = \varepsilon \begin{pmatrix} f_A(\mathbf{k}) \\ f_B(\mathbf{k}) \end{pmatrix} \quad (1.3)$$

with $h_{AB}(\mathbf{k}) = -\gamma_0 \sum_{l=1}^3 \exp(-i\mathbf{k} \cdot \tau_l)$. Solving this eigenvalue equation finally gives the valence and conduction bands of graphene:

$$\varepsilon_{\pm}(\mathbf{k}) = \pm \gamma_0 \sqrt{1 + 4 \cos \frac{ak_x}{2} \cos \frac{\sqrt{3}ak_y}{2} + 4 \cos^2 \frac{ak_x}{2}} \quad (1.4)$$

Using the coordinates of K and K' we see that: $\varepsilon_{\pm}(\mathbf{K}) = \varepsilon_{\pm}(\mathbf{K}') = 0$, and a development of the cosines near K and K' gives for $|\mathbf{k}|a \ll 1$:

$$\varepsilon_{\pm}(\mathbf{k} + \mathbf{K}) = \varepsilon_{\pm}(\mathbf{k} + \mathbf{K}') = \pm\gamma\sqrt{k_x^2 + k_y^2}$$

with $\gamma = \frac{\sqrt{3}}{2}a\gamma_0$. This dispersion is very peculiar since it is quasi-linear around K and K' . Electrons in these states thus behave like mass-less particles, i.e. Dirac fermions.

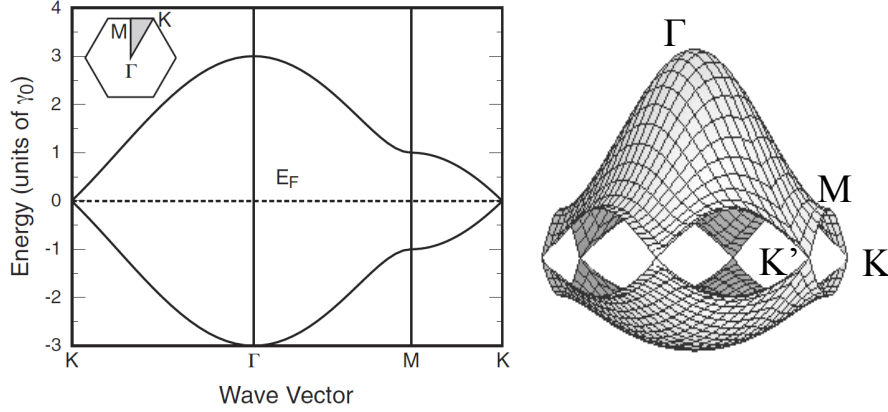


Figure 1.3: A 2-dimensional representation (right) and 1-dimensional cut along the main directions (left) of the graphene energy dispersion as determined by equation 1.4. Note the crossing of the conduction and valence bands at K and K' and the electron-hole symmetry close to these points. Left figure adapted from [6].

From Graphene to Nanotubes: Zone Folding

In order to form a SWNT from a graphene sheet, we only need to choose the chiral vector $\mathbf{C}_h = n_1\mathbf{a}_1 + n_2\mathbf{a}_2$, defining which carbon atoms shall coincide in the rolled (n_1, n_2) nanotube (Fig. 1.4). The energy bands of the nanotube are obtained by imposing the periodic boundary condition on the original graphene wave-function: $\Psi(\mathbf{r} + \mathbf{C}_h) = \Psi(\mathbf{r})$, which is satisfied if and only if: $\exp(i\mathbf{k} \cdot \mathbf{C}_h) = 1$. This means that the wave-vector component along the circumferential direction is now discrete, with allowed values:

$$k_{\perp} = n \frac{2\pi}{C_h}, \quad n \in \mathbb{N} \quad (1.5)$$

($C_h = |\mathbf{C}_h|$ is the circumference of the nanotube). In the limit of an infinitely long nanotube the component k_{\parallel} along the axis remains continuous. In the reciprocal space of graphene this defines 1D cutting lines corresponding to the 1D energy bands of the nanotube (Fig. 1.5 b)). If one of the cutting lines is going through the Dirac points of graphene (K and K') then the nanotube is metallic (in this approximation). This happens when $n_1 - n_2 = 0 \pmod{3}$ (see Fig. 1.5 a)). One third of SWNTs is thus expected to be metallic, and we will concentrate on the properties of the remaining two thirds of semiconducting single-wall carbon nanotubes interesting for PL studies.

In this simplified single-particle picture, the band-gap is given by the lowest energy band-to-band transition. It occurs between the bottoms of the valence and

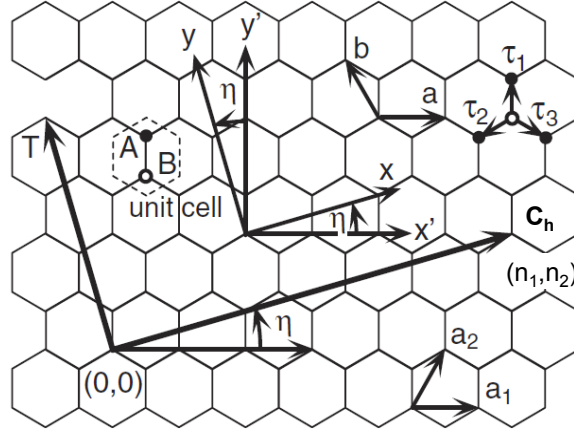


Figure 1.4: Important vectors and parameters defining a particular species of nanotube from the graphene lattice when the sheet is rolled along the chiral vector $\mathbf{C}_h = n_1\mathbf{a}_1 + n_2\mathbf{a}_2$. η is the chiral angle, (n_1, n_2) are the chiral indices. Also shown are the vectors τ_1, τ_2, τ_3 connecting the nearest neighbor atoms in graphene. Adapted from [6].

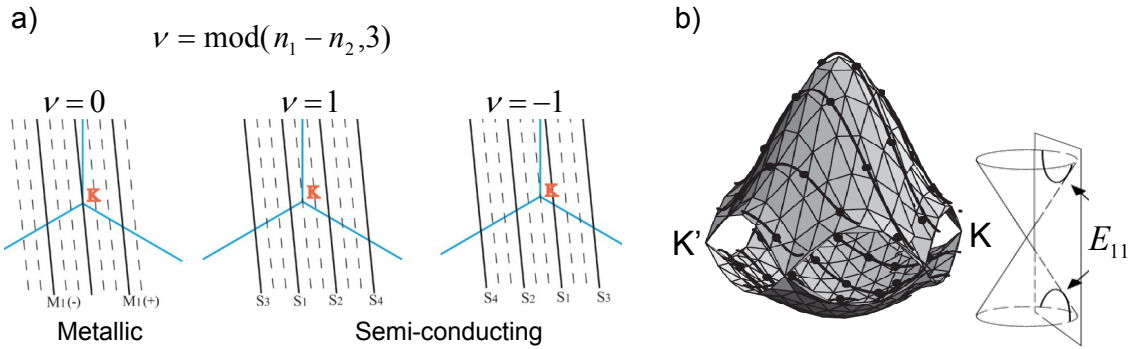


Figure 1.5: a) Depending on the chiral indices, 3 types of SWNTs are possible. Nanotubes with $\nu = 0$ are semi-metal, although a small band-gap may open because of effects neglected in the tight-binding model, like the curvature in narrow diameter tubes. The other two types are semiconducting, with the first band-to-band transition occurring on different sides of the K point. b) The one-dimensional subbands of SWNTs are obtained by plotting the cutting lines defined by eq. 1.5 on the two-dimensional graphene dispersion.

conduction bands that are the closest to the K point. Note that an identical transition exists close to K' ; it is therefore doubly degenerate (in the absence of defect and magnetic flux threading the nanotube). Shifting the origin of the phase of the wave functions, we can attribute to these lowest bands a circumferential wave-vector $k_{\perp} = 0$, that is $n = 0$ in units of $\frac{2\pi}{C_h}$. The neighboring subbands will have $n = \pm 1, \pm 2$, etc. When light is polarized along the nanotube axis, momentum conservation allows transitions with $\Delta n = 0$ only, whereas light perpendicularly polarized leads to transitions with $\Delta n = \pm 1$ (Fig. 1.6).

Although we will see below that the single-particle model is inaccurate to describe SWNTs, it remains an important tool and serves as a starting point for more evolved calculations. It also provides valuable understanding of basic optical properties of carbon nanotubes, like the scaling of the band-gap with $1/d$ (d is the diameter). Moreover, the zone-folding scheme is a very intuitive way to explain and understand a host of physical effects on the electronic structure by referring to the associated displacements of the cutting-lines on the graphene reciprocal space.

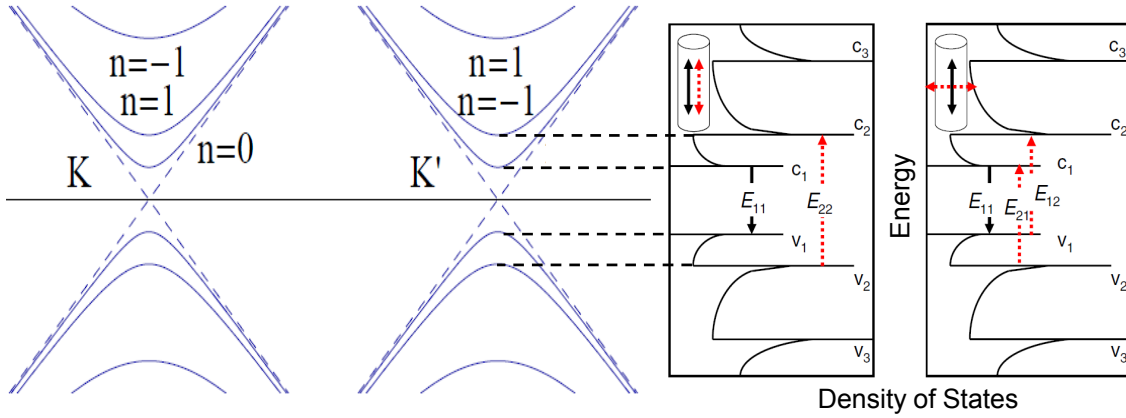


Figure 1.6: The lowest energy optical inter-subband transitions in the single particle picture occur between Van-Hove singularities in the density of states. Typical PL experiments involve E_{22} excitation and E_{11} detection, both polarized along the nanotube axis. It is also possible to use cross-polarized excitation of the E_{12} and E_{21} transitions.

1.1.2 Excitonic binding energy

We have so far neglected many-body interactions in our derivation. These have at least two important consequences on the electronic structure: electron-electron repulsion tends to blue-shift the energies and re-normalize the band-gap; electron-hole attraction leads to the formation of bound excitons instead of free electron-hole pairs (Fig. 1.8). The failure of the single particle description for carbon nanotubes was first evidenced by the "ratio problem". From the linear conic dispersion and electron-hole symmetry around the K point of graphene, the zone-folding scheme leads to the expectation of an energy ratio between the second and first optical transitions being exactly: $E_{22}/E_{11} = 2$. This is in contradiction with experimental

data showing ratios widely spread around ~ 1.7 (see Fig. 1.7), which motivated extensive theoretical investigations.

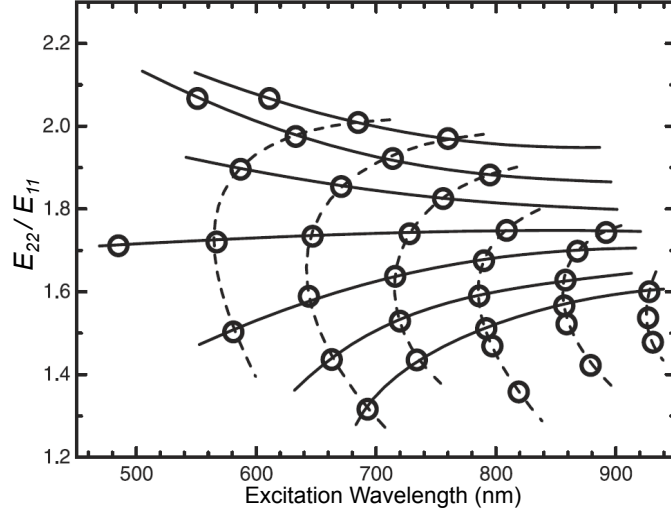


Figure 1.7: The ratio of the second to first transition energies for a large number of nanotube species measured for the first time by Bachilo *et al.* in 2002 [7]. Circles are the experimental data.

The reasons for large many particle effects are two-folds: low screening of electrostatic interactions and strong confinement of carriers in one dimension, both translating into enhanced Coulomb interactions. Whereas the electron-electron repulsion results in an effective renormalization of the energies and is therefore impossible to quantify directly in an experiment, the binding energy of the excitons is a very significant quantity for the photo-physics of nanotubes. For example, the optical spectrum for bound excitons is dramatically different from what is expected based on the Van-Hove singularities in the density of states of the single-particle picture. The oscillator strength is almost completely transferred to the lowest exciton (Fig. 1.8).

The estimation of the binding energy is equivalent to the problem of the hydrogen atom (the hole playing the role of the positively charged nucleus). However, in a truly one-dimensional space, it has been shown by Loudon in 1959 [10] that the binding energy of the lowest state diverges to infinity. This can be overcome by modifying the form of the Coulomb interaction to account for the finite extent of the system in the circumferential direction [10]. With a suitable choice for the effective potential and the effective permittivities of the nanotube and its surrounding, it is possible to use this simple model to estimate the binding energies without any knowledge nor assumption on the detailed electronic structure [8]. Such an approach is also easily extended to otherwise complicated calculations like the binding of positively and negatively charged trions [11].

These simplified approaches agree well in general with finer estimations including ab-initio [12, 13] or density matrix [9] calculations. They all predict exciton binding energies in excess of few hundreds of milli-electronvolts for tubes with diameters

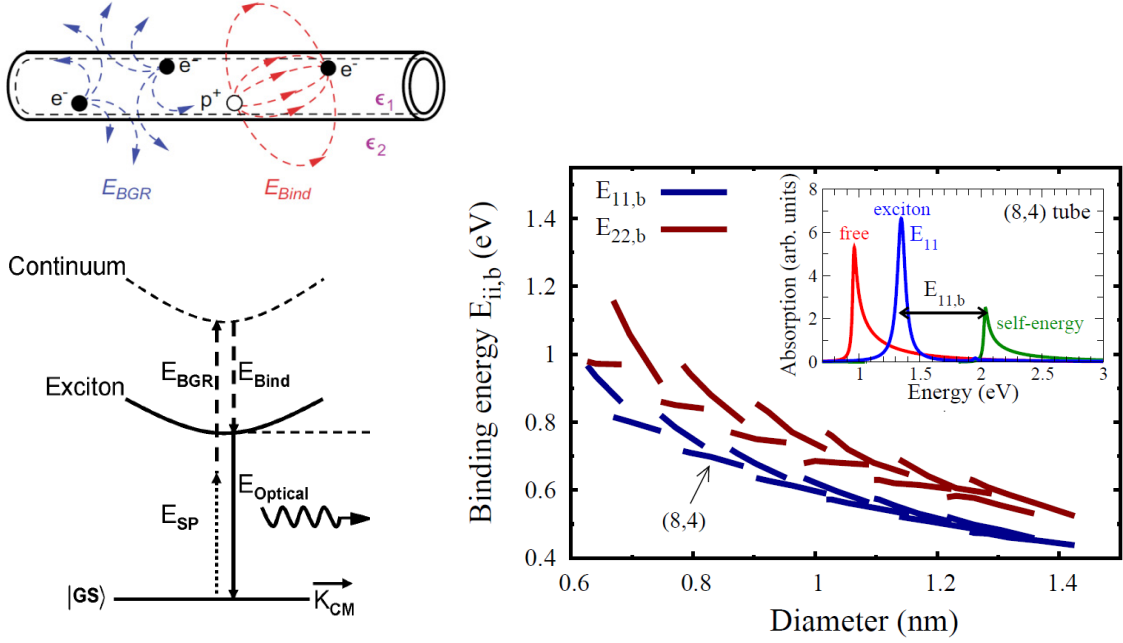


Figure 1.8: Top: Schematic of the two main effects arising from two-body interaction. E_{BGR} stands for Band-Gap Renormalization, due to electron-electron Coulomb repulsion. E_{bind} is the excitonic binding energy caused by electron-hole attraction. Left: Energy dispersion in the excitonic picture showing qualitatively the consequences of these two corrections to the single-particle band-gap E_{SP} . The observed optical transition in PL or absorption has the energy $E_{Optical}$. Figures adapted from [8]. Right: The exciton binding energies for the first two optical transitions and a variety of tube chiralities as calculated by E. Malic *et al.* [9] using a density matrix theory based on Bloch equations. Like the single particle band-gap, the binding energies scale approximately like $1/diameter$. The inset shows the absorption spectra calculated for a (8,4) nanotube, detailing the two effects mentioned above.

$d < 1$ nm, and a scaling following the same trend as the band-gap, i.e. increasing for narrower tubes like $\sim 1/d$ (Fig. 1.8).

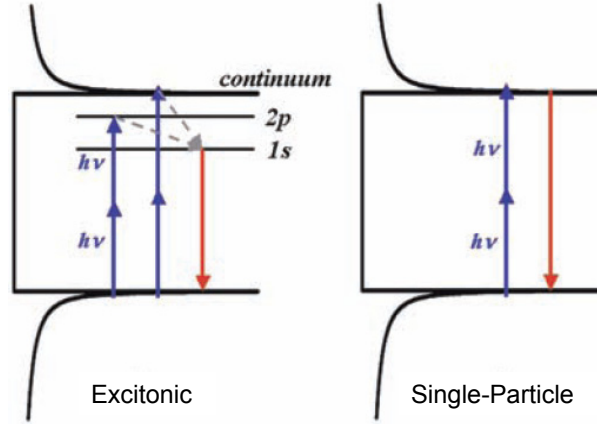


Figure 1.9: Figure from [14] showing the two-photon excitation mechanism.

The first experimental confirmation came in 2005 from Tony Heinz’s group in Columbia [14]. They used two-photon excitation of the PL to access a higher state of the excitonic hydrogenic series, namely the $2p$ -like state. Since this is a bound state lying above the lowest bright $1s$ -like exciton, the energy difference $E_{2p} - E_{1s}$ gives a lower bound to the binding energy. They found values around 300 meV for nanotubes with diameters ~ 0.8 nm, in good agreement with theoretical predictions. This value would be exactly zero in a single-particle picture; their result is thus a proof of the excitonic nature of optical transitions in carbon nanotubes.

1.1.3 Symmetries, selection rules, Dark and Bright excitons

The large excitonic effects in carbon nanotubes do not only affect the transition energies, they also have significant implications on the selection rules for optical processes. We have already seen (Fig. 1.6) that conservation of circumferential momentum restricts allowed band-to-band transitions for a given light polarization axis. Whereas this rule can be understood in a single-particle picture, we just saw above that the observed features from two-photon excitation require an excitonic picture to be correctly described. This is because such selection rules are dictated by the symmetries of the wave-function, the latest differing qualitatively between an exciton and a free electron-hole pair. There are two main approaches to describe symmetry-related properties of carbon nanotubes. So-called symmetry-based calculation of the band structure [13], or the *ad-hoc* inclusion of excitonic effects after single-particle calculations.

The symmetry groups of SWNTs include various operations and depend on the particular chirality of the tube. Very good reviews can be found in [15] and [16]. As far as optical properties are concerned, however, the relevant symmetry operation dictating the selection rules is the $\pi/2$ rotation around an axis perpendicular to the nanotube, labeled C'_2 in Fig. 1.10. Indeed, the dipole operator for light polarized along the nanotube axis transforms like a vector and is odd over C'_2 . Therefore, only

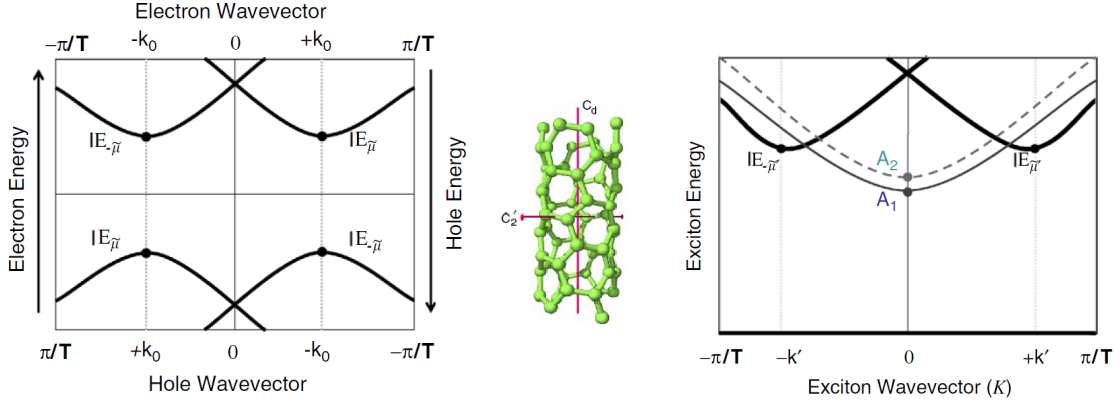


Figure 1.10: Left: Schematic electron and hole dispersion labeled by the symmetry group of the wave functions, as obtained from the zone-folding method. The lowest energy subbands are represented. $\pm k_0$ are the value of the axial component k_{\parallel} of the wave vector at the closest to the graphene K (resp. K') point. Right: The symmetry groups of the resulting exciton is given by the product group of the electron and hole symmetry groups, which decomposes into a sum of 4 groups. Two excitons have non-zero momenta (optically forbidden). A_2 is odd over the $\pi/2$ rotation around C_2' and thus optically allowed for light polarized along the nanotube axis. The lowest lying exciton has even parity and is dark. Figure adapted from [15].

odd excitonic states are nominally bright. Even states are dark excitons (absent perturbation breaking the symmetry).

The particular significance of the formation of excitons is directly linked to the presence of the two inequivalent sites K and K' in graphene. The two degenerate transitions around these two points are mixed by electron-hole Coulomb interactions. As shown in Fig. 1.10, the resulting symmetry of the excitonic wave-function is thus obtained by a decomposition of the product group of electron and hole states. Among the two states having zero center of mass momentum along the nanotube axis, only one of them is bright (i.e. odd), corresponding to the bonding combination of $K \rightarrow K$ and $K' \rightarrow K'$ transitions. It has slightly higher energy than the dark anti-bonding state. However the direct observation of the dark state and its true energy has remained an experimental challenge for years.

The situation described above changes when a magnetic field is applied along the nanotube axis. The Aharonov-Bohm flux threading the tube corresponds to an additional phase in the circumferential part of the wave-function. This changes the boundary condition (1.5) and leads to a lateral displacement of the allowed cutting-lines in the zone-folding picture. Consequently, the energies of the $K \rightarrow K$ and $K' \rightarrow K'$ transitions shift oppositely and the degeneracy is lifted (which is another way of expressing that time reversal symmetry is broken by the magnetic field flux). For large fields, one expects two optically-allowed transitions split by an amount proportional to the Aharonov-Bohm flux, as depicted in Fig. 1.11. Thermal equilibrium between the two states lead to the observation of strong PL from the

lower dark state, as demonstrated by Ajit Sivrastava and coworkers in [17] (see Fig. 1.11).

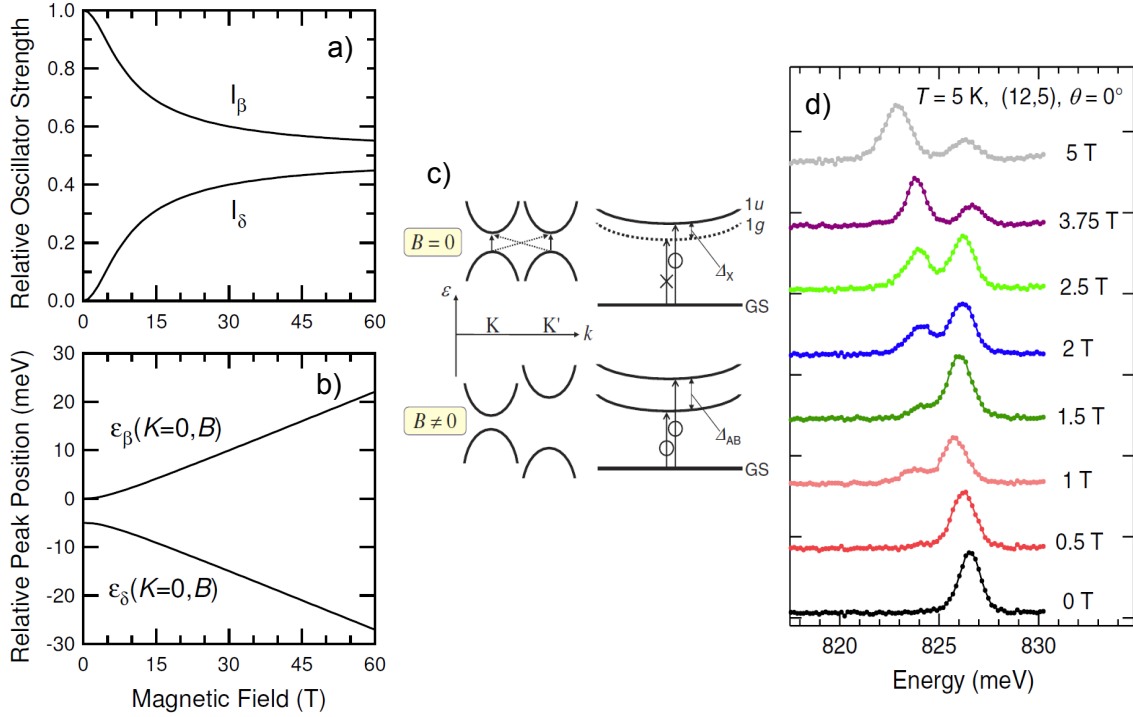


Figure 1.11: (a) Calculated oscillator strengths and (b) energies of the bright and dark excitons when a magnetic field is applied along the nanotube axis (Figure from [18]). (c) The magnetic field creates an Aharonov-Bohm flux lifting the degeneracy between K and K' , both transitions being now optically allowed (Figure from [19]). (d) Experimental demonstration of the brightening of the dark exciton under an axial magnetic field by single nanotube PL spectroscopy at cryogenic temperature (Figure from [17]).

Whereas theoretical predictions for the dark-bright energy splitting range from a few to hundreds of milli-electronvolts, it is now becoming clear from recent experimental works that the lower side of this range is most accurate. For example values between 1 and 7 meV are reported in [17]. As expected there is a trend toward higher values for narrower tubes, but a wide spread of splitting is found inside a same chirality and explained by changes in the local environment.

1.2 Photoluminescence

1.2.1 Different types of samples

Experimental observation of PL from carbon nanotubes requires a careful choice and preparation of the sample. Indeed, SWNTs have very large interface surface areas with their environments (electrons effectively “live” on the sidewalls!). Highly efficient energy transfer thus occurs between neighboring tubes in a bundle or into a nearby substrate, almost completely quenching PL. This conundrum has been

overcome by two different approaches described below: suspending nanotubes over trenches etched in the substrate, or dissolving them in water with the help of a surfactant or DNA (carbon nanotubes may otherwise be directly dissolved in other solvents, like toluene).

Suspended nanotubes

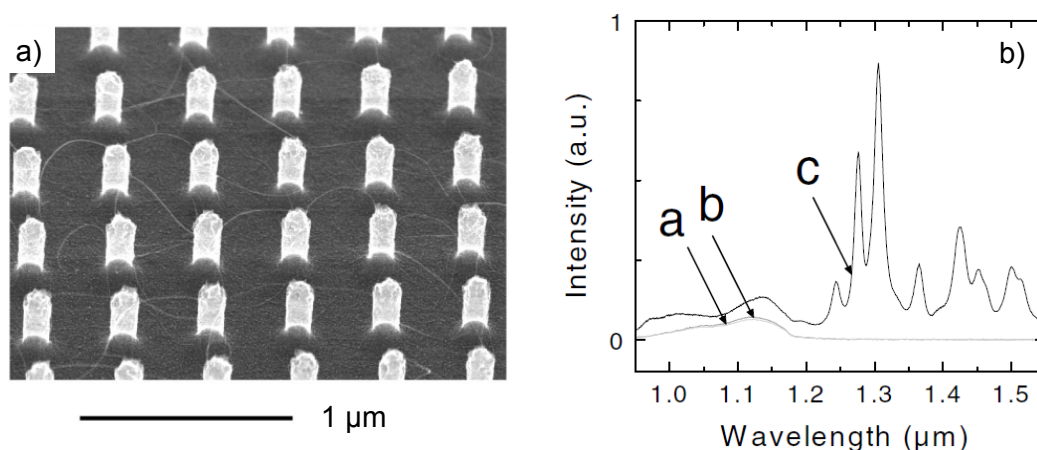


Figure 1.12: a) An SEM picture of SWNTs grown on a substrate pre-patterned with pillars in the group of J. Lefebvre in Montreal. Many nanotubes appear to be air-suspended, crossing between neighboring pillars. b) Photoluminescence spectra from (a) a bare pillar substrate and (b) a flat sample covered with CVD-grown nanotubes, as compared to the spectrum (c) from a pillar area with suspended tubes showing bright PL. Both figures from [20].

The first report of PL from unprocessed carbon nanotubes grown by chemical vapor deposition (CVD) came in 2003 from the group of Jacques Lefebvre [20]. They grew the tubes on a substrate pre-patterned with nano-pillars and observed bright PL emission from areas where nanotubes bridged the gaps between nano-pillars (Fig. 1.12). Similar kind of samples can also be obtained by post-etching or transfer-printing onto a patterned template, but any post-processing reveals detrimental to the sensitive optical properties of SWNTs. Final growth on pre-etched structures is thus the method of choice to obtain clean pristine optically active carbon nanotubes. One hurdle is still the growth of narrow-diameter tubes suited for visible to near-infrared PL emission, a region where higher efficiency detectors are available. A recent review on suspended nanotubes is given in [21].

Surfactant-embedded nanotubes

The most popular way of preparing carbon nanotube samples for absorption and PL experiments remains the one used originally by O'Connell *et al.* in their pioneering work [4], namely the use of a surfactant to enable efficient isolation and solvation of the nanotubes in an aqueous solution. We note here that other similar approaches exist to obtain individual nanotubes in solution:

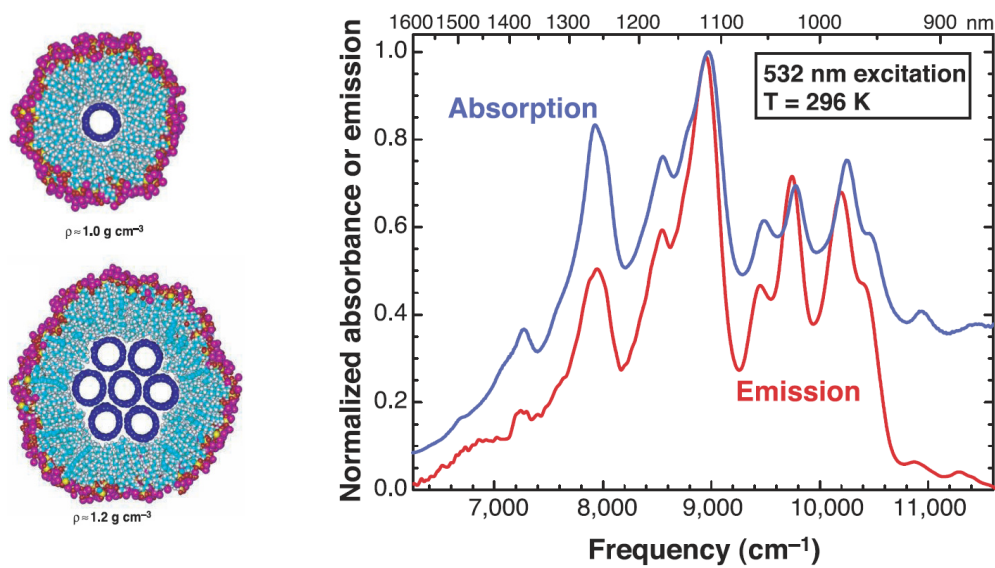


Figure 1.13: Left: The surfactant (here SDS) forms micelles around the nanotubes with the hydrophobic tails pointing toward the nanotube walls. Micelles containing bundles have a higher density and can be removed by ultra-centrifugation. Right: Absorption and emission spectra of a solution containing mostly individual nanotubes embedded in SDS micelles. Both figures from the ground-breaking work of O’Connell and coworkers [4].

- Deoxyribonucleic acid (DNA) can be used to isolate nanotubes. Although it is less efficient than usual surfactants, it is of interest for biological applications (bio-sensors, drug delivery, biological fluorescent markers, etc.).
- Alternatively, covalent functionalization with suitable chemical groups may allow dissolution of nanotubes in water. This method strongly perturbs the pristine electronic structure of SWNTs, which may yet open the way to interesting applications if the changes are understood and controlled.
- Finally, carbon nanotubes can be directly dissolved in solvents other than water, like dichloroethane. Such solutions generally have poorer stability over time.

The starting material can be of any kind, but HipCo and CoMoCat carbon nanotubes are widely used because of their ideal diameter distributions for optical studies. HipCo nanotubes have a relatively wide distribution ($0.7 \text{ nm} < d < 1.2 \text{ nm}$) with emission extending in the infrared (up to 1500 nm), whereas CoMoCat tubes are strongly enriched in narrow diameter semiconducting tubes ($d \sim 0.8 \text{ nm}$) with PL emission peaked around 1000 nm ((6,5) and (7,5) chiralities are dominant).

Raw material comes as a very volatile black powder which is hardly soluble. Moreover strong Van-der-Waals forces between nanotube walls cause the formation of bundles detrimental to PL. The addition of a surfactant to an aqueous solution and subsequent vigorous sonication overcome both problems. Typical surfactants are long polymers with hydrophobic tails wrapping the nanotube and hydrophilic heads pointing outwards (see Fig. 1.13). The resulting structure is called a micelle; it is 1-2 nm thick and isolate very efficiently the nanotube from its environment. Importantly, since no covalent bonds are created, the electronic and mechanical structures of the pristine SWNTs are preserved. The only significant effect on the optical

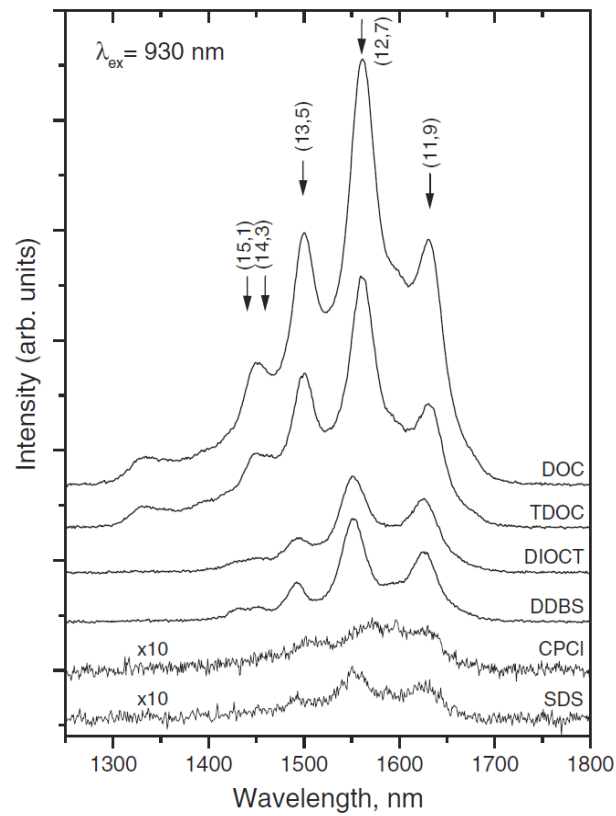


Figure 1.14: Wenseleers *et al.* studied different surfactants for carbon nanotubes solvation [22]. Sharper and stronger PL spectra indicate better dissolution and higher individualization of the nanotubes.

properties is a change of the dielectric constant, the increased screening leading to slightly red-shifted transitions compared to air-suspended nanotubes. We note that different surfactants largely differ in their ability to dilute carbon nanotubes. Recent studies [22] have shown that sodium deoxycholate (DOC), a bile-salt, is one of the best surfactants (Fig. 1.14).

1.2.2 Chirality assignment: Kataura Plot

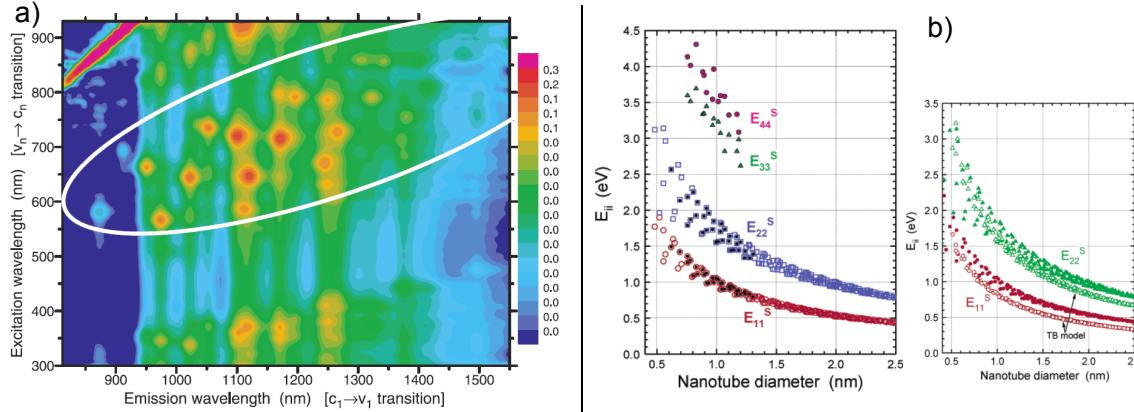


Figure 1.15: a) A two-dimensional PL Excitation color map from an ensemble measurement by Bachilo *et al.* in 2002 [7]. In the white oval region each high intensity point corresponds to a particular chirality excited resonantly at E_{22} and emitting at E_{11} . b) From such PLE maps one can assign the nanotube chiralities and plot the transition energies against the diameter in a so-called Kataura plot. Weisman *et al.* proposed in 2003 the first empirical Kataura plot [23], evidencing family behaviors (branches) and deviation from simple tight-binding calculations.

Micelle-embedded SWNTs solutions are particularly well suited to ensemble PL measurements. Whereas it suffers from inhomogeneous broadening and freezing at low temperature, among others, this method allows the simultaneous observation of a wide range of nanotube chiralities and thus constitutes a valuable characterization tool. Specifically, recording PL spectra upon quasi-continuous tuning of the excitation wavelength yields a two-dimensional PL-excitation (PLE) map (Fig. 1.15 a)). The most prominent features on this map are seen when the excitation is resonant with the second excitonic transition E_{22} of a particular chirality. Since PL emission occurs at the energy E_{11} one has access to the couples (E_{11}, E_{22}) of all observed species, which enables univocal identification of the chirality. The data can eventually be plotted against the nanotube diameters in a Kataura plot (Fig. 1.15 b)). In addition to the $1/d$ scaling of both transition energies, branches are observed in different directions for $\nu = \pm 1$ SWNT types, with the chiral angle increasing along each branch (see Fig. 1.15).

1.2.3 Phonon-assisted excitation

PLE maps also reveal additional resonances in the excitation spectrum related to phonon sidebands. The main sideband is associated to the optical G-mode with an

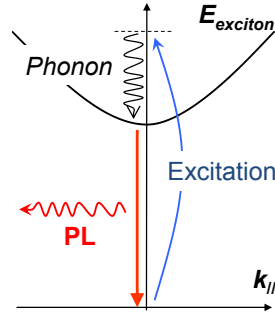


Figure 1.16: Schematic of phonon-assisted PL excitation.

energy of 1600 cm^{-1} or 200 meV . The presence of a large number of chiralities and inhomogeneous broadening makes it difficult to observe and assign weaker sidebands or resonances closer in energy to E_{11} . Here it is desirable to use single-molecule spectroscopy techniques to study the properties of individual nanotubes. Suitable samples are obtained by coating a substrate (quartz, silicon oxide, etc.) with a nanotube solution of the appropriate density. The sample preparation procedure and the experimental apparatus used in the present work will be detailed in Chapter 2, but we already introduce here and in the next section our own experimental data to illustrate significant features of single nanotube PL spectroscopy.

A typical example of data taken at liquid nitrogen temperature (77 K) in our lab is shown in Fig. 1.17. We do observe a phonon sideband in excitation associated with the G-band, but it is much weaker than other resonances closer in energy to the PL emission. We tentatively assign these resonances to phonon-assisted relaxation (Fig. 1.16) from other raman-active phonons which are poorly studied, namely the intermediate frequency modes (see for example [24]). Our assignment is supported by the good match between the observed resonances and the phonon energies.

1.2.4 Photoluminescence bleaching, blinking and spectral diffusion

Although poorly reported and documented in the literature, irreversible photo-induced PL-quenching plagued our beginnings with single-tube spectroscopy and still constitutes a major hurdle to our on-going experiments. Figure 1.18 shows the typical behavior of a CoMoCat SWNT embedded in SDS and deposited on a glass or SiO_2 substrate. At room temperature and under laser excitation, the PL signal bleaches in more or less pronounced steps, most of them irreversible. The bleaching rate increases with the laser power, but even under the weakest intensities we could not measure PL longer than a few minutes. After numerous trials in sample preparation (different substrates, densities, solutions, etc.) we eventually solved the problem by cooling the sample down to 77 K or 4 K , at which we believe condensation of oxygen and other gases account for the improvement.

The first thorough investigation of stepwise PL quenching was published by Laurent Cognet *et al.* in 2007 [25]. From their study of the step numbers and sizes and the control exposure to different chemicals, they conclude that the quenching is caused by the photoinduced chemisorption of initially adsorbed oxygen on the side

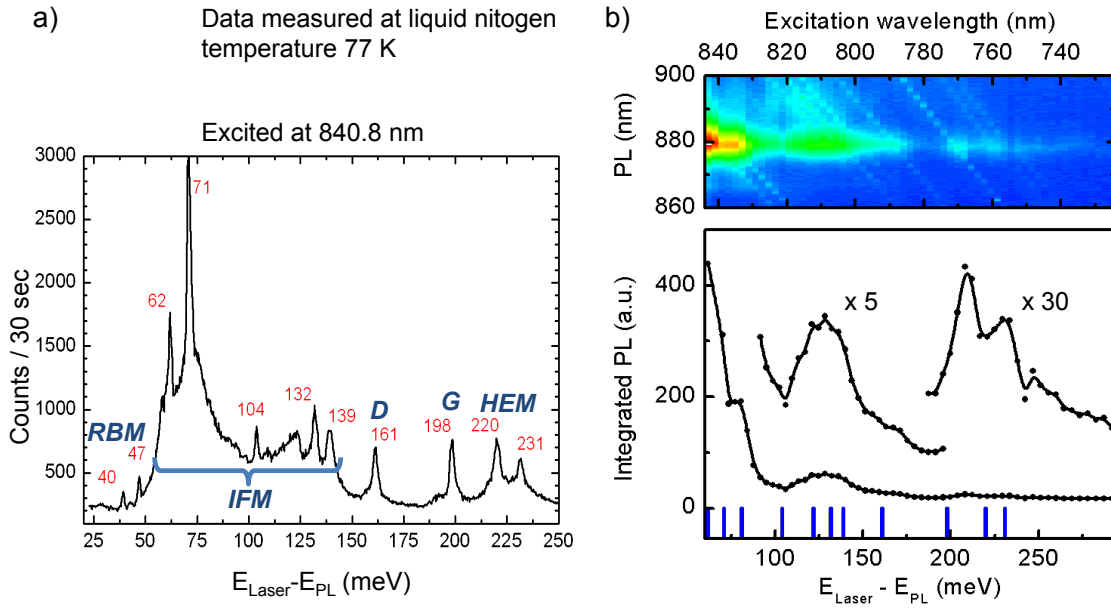


Figure 1.17: a) When a small bundle of nanotubes is excited, strong resonant Raman scattering may be observed. Red numbers indicate the energies of the phonons. In addition to the widely reported radial-breathing modes (RBM), D- and G- modes and high energy modes (HEM), we observe a number of raman-active intermediate frequency modes (IFM) [24]. b) In the PLE map of a single nanotube emitting at 880 nm (top) raman scattering is seen as diagonal lines. When they cross the PL horizontal line phonon-assisted relaxation causes enhanced emission. A cut along the emission line reveals the excitation spectrum of the nanotube (bottom) where we have reported the phonon energies measured in a) (blue bars). The position of the resonances match well the main phonon groups.

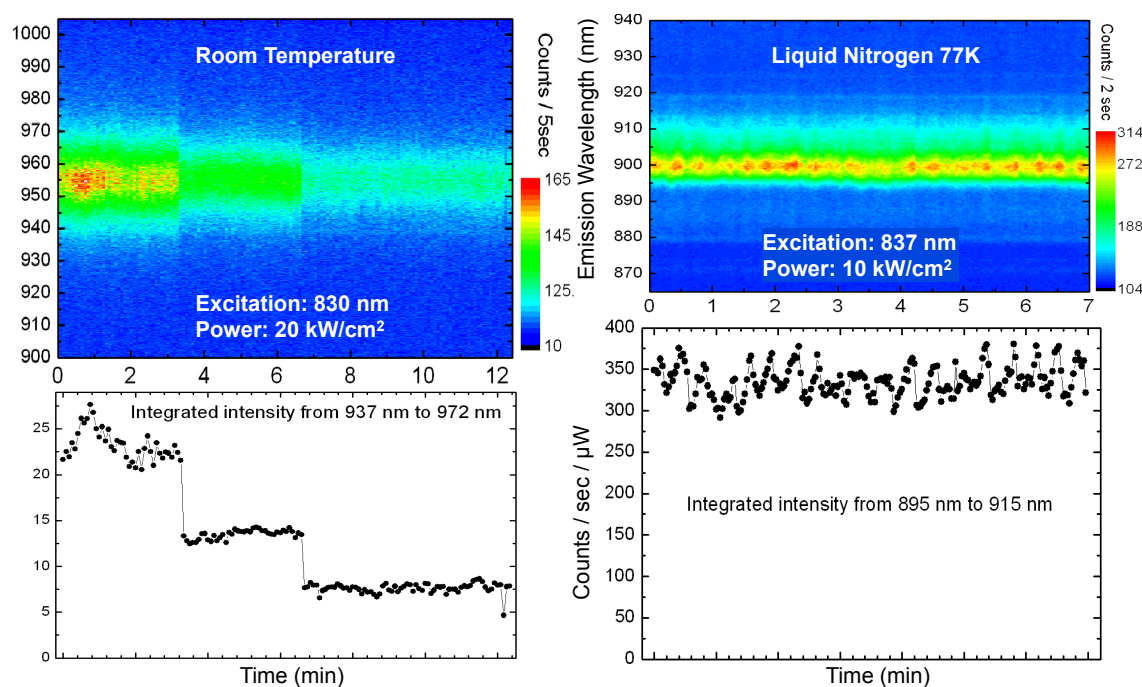


Figure 1.18: Time traces of PL emissions from different individual CoMoCat nanotubes in SDS-micelles at room and liquid nitrogen temperatures, with similar excitation conditions (wavelength and power). In both cases fast intensity fluctuations on seconds (or less) time scales are observed. At room temperature, very clear irreversible stepwise quenching occurs upon laser excitation. This unwanted effect is suppressed at low temperature in low-pressure helium atmosphere, presumably because oxygen and other gases are absent or condensed.

walls of the tubes, as was confirmed in [26]. Resulting sites act as hole dopants, quenching the optical excitation through non-radiative Auger process. The exciton diffusion range derived from these studies is 90 nm [25] to 105 nm [26].

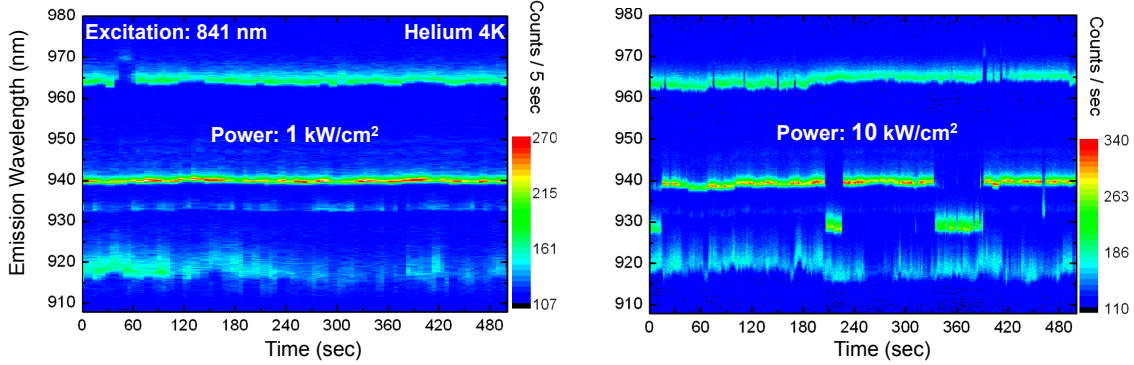


Figure 1.19: PL time traces of a CoMoCat nanotube at 4 K and two different excitation powers.

Another feature which is in contrast rather more prominent at lower temperature is PL blinking, usually accompanied by spectral wandering and/or spectral jumps. Figure 1.19 displays PL time traces of a CoMoCat nanotube taken at the lowest accessible temperature in our helium bath cryostat (4 K). The splitting into multiple lines is a very usual feature of these samples. Remarkably, each line blinks and shifts independently, and the instability is increased under higher excitation intensity. Although the exact cause for blinking and spectral diffusion is not clear, it seems definitely related to the presence of the surfactant micelle. Indeed, Olivier Kiowski *et al.* found in a comparative study [27] that under identical conditions suspended CVD-grown nanotubes showed very stable PL emission intensity and wavelength, in contrast to the SWNTs from a sodium cholate dispersion (see Fig. 1.20). These results highlight the role of the immediate environment of the nanotube in influencing its optical and electronic properties. It is very likely that charges get alternatively trapped in the micelle and released, causing both intensity fluctuations through Auger-induced partial PL quenching, and spectral shifts from the DC stark effect.

I would like here to point out that the occurrence of large spectral jumps, with no correlation between the different PL lines from a same nanotube (as we observe in Fig. 1.19), is a strong indication for localized emitting states. If the different lines corresponded to delocalized excitonic states of the SWNT, they would shift together and rather smoothly as a consequence of charge trapping in the micelle (the stark shift induced by a single charge is expected to be small when averaged over the nanotube or exciton diffusion length).

The observation of very stable emission from suspended CVD-grown nanotubes constitutes a strong motivation for us to use similar samples for future experiments. Unfortunately the growth of very narrow, individual, isolated SWNTs is challenging and we are still optimizing the fabrication process at the time when I am writing.

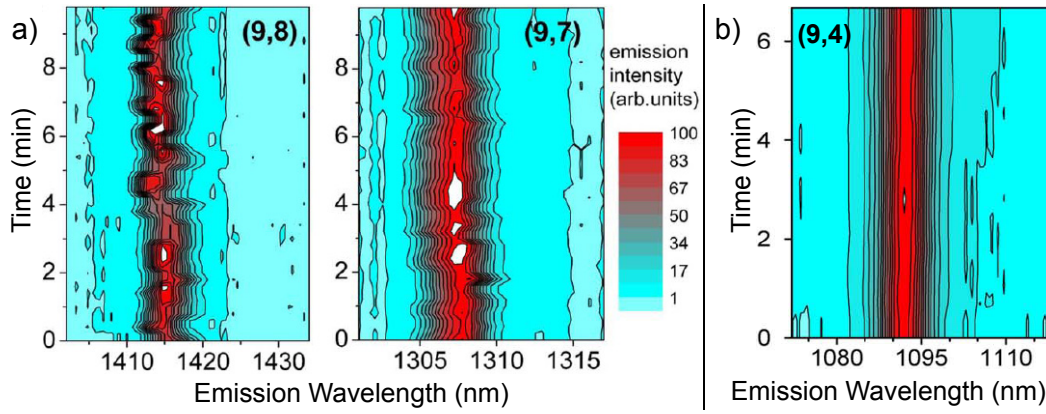


Figure 1.20: In their study, O. Kiowski *et al.* [27] compared PL time traces of individual SWNTs at low temperature (between 6 and 8 K). a) SWNTs from a sodium cholate dispersion show fluctuation in wavelength and intensity, as we also observe. b) On the contrary, PL from suspended CVD-grown SWNTs is very stable in time.

2 Photon Correlation Measurements on Individual Nanotubes

In this chapter and the following, we will report on the main experimental results obtained from the PL spectroscopy of individual CoMoCat SWNTs dispersed in sodium dodecyl benzene sulfonate (SDBS). We first give some details on the samples and the setup we use, then expose the core of the chapter, namely the observation of anti-correlated photon emission from SWNTs, and finally discuss the origin and possible explanations for antibunching.

2.1 Experimental Details

2.1.1 Sample Preparation and Characterization

As mentioned in chapter 1, the easiest and most convenient way to carry out PL experiments on carbon nanotubes is to start from an aqueous dispersion containing a suitable surfactant. Moreover, given the very limited detection range of our equipment (based on silicon technology) in the infrared, we need narrow nanotubes emitting at wavelength below 980 nm (and even below 900 nm for the streak camera). This means diameters on the order of 0.7 nm. This requires the use of HipCo or CoMoCat materials, the only reliable sources of narrow nanotubes. Because of the availability of commercial “ready to use” dispersions of CoMoCat nanotubes and their ideal diameter distribution, we chose this solution to start the new SWNT activity in the group.

The general idea to prepare a sample suitable for single nanotube spectroscopy is to spread homogeneously the nanotube solution on the desired substrate. A key point for us is the final spatial density, which must be compatible with single-molecule spectroscopy (less than one nanotube on average in a spot-size area $\sim 1 \mu\text{m}^2$) and yet high enough to allow for the study of a reasonable number of nanotubes within a reasonable search time. This parameter is controlled mainly by the original density of the dispersion, and weakly depends on the coating procedure (for example the spinning angular velocity) and the substrate’s type.

We also want the nanotubes to adhere well onto the substrate, especially for AFM imaging. Indeed, after coating with the SWNT dispersion, the sample is virtually covered by a layer of surfactant which renders AFM imaging of the nanotubes impossible. We therefore need to rinse it thoroughly (with water, methanol or isopropanol) to get rid of surfactant residues. Of course, if no care is taken, nanotubes may be removed as well in the process. This can be avoided by engineering a strong interaction between SWNTs and the substrate surface. The SDBS micelles surrounding the nanotubes have their hydrophilic heads positively charged. Unfortunately, most

oxides are also characterized by positive surface charges, preventing strong and reliable adhesion of the micelles. The solution is to functionalize the substrate with a self-assembled monolayer of polylysine (PLL) which reverts the polarity of the surface. This additional step permits good fixation and subsequent rinsing without losing the nanotubes.

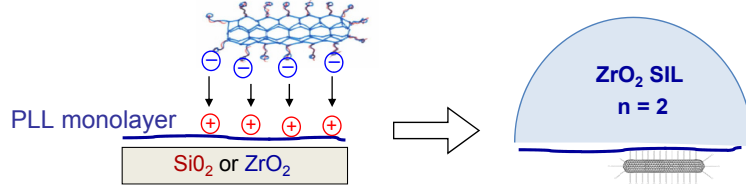


Figure 2.1: Preparation of a sample for single nanotube spectroscopy. The SDBS micelles wrapping the CoMoCat nanotubes in the dispersion have negatively charged outside walls. After functionalization of the substrate with polylysine (PLL), the surface is positively charged, ensuring strong fixation of the SWNTs. The process was carried out on silicon dioxide wafers for AFM characterization, then directly on the flat surface of a hemispherical zirconium solid immersion lens (SIL) for optical measurements.

A simplified description of the sample preparation procedure is shown in Fig. 2.1. The initial step is the cleaning of the substrate in an ultrasonic bath of isopropanol during 10-15 min followed by rinsing with deionized water. The formation of the PLL monolayer is straightforward: covering the substrate with a PLL solution for ~ 1 min and rinsing. A droplet of the nanotube dispersion, previously diluted with DI water and SDBS to get the desired concentration, is then spin-coated (or simply spread and let repose for a few minutes). Finally, if AFM imaging is planned, the sample is rinsed in DI water (or another solvent), possibly under sonication to accelerate the process. $1 \times 1 \text{ cm}^2$ glass or SiO_2 wafers were the most usual substrates because of their convenient handle, their good optical properties (low PL and raman background) and their low roughness for AFM. When all the parameters were optimized, we repeated the process on the flat side of a zirconium solid immersion lens (SIL) for high numerical aperture spectroscopy (see next section).

The optimization of the density and the determination of the physical properties of the CoMoCat nanotubes (in particular their lengths) are most conveniently carried out by AFM imaging. Although it is possible to get an idea of the density by scanning the sample and monitoring PL, this gives only partial information because a small proportion of the nanotubes show detectable PL. Metallic tubes, tubes emitting outside the detection range or those which PL is quenched for some reason are discarded, although they may alter the properties of a neighboring nanotube we wish to investigate. Similarly, our spot-size being at best 500 nm in diameter, the length of shorter emitting objects will not be resolved. Thus we used AFM in non-contact tapping-mode on rinsed samples to characterize the density and length distribution of our nanotubes. Representative images and compiled statistics are shown in Fig. 2.2.

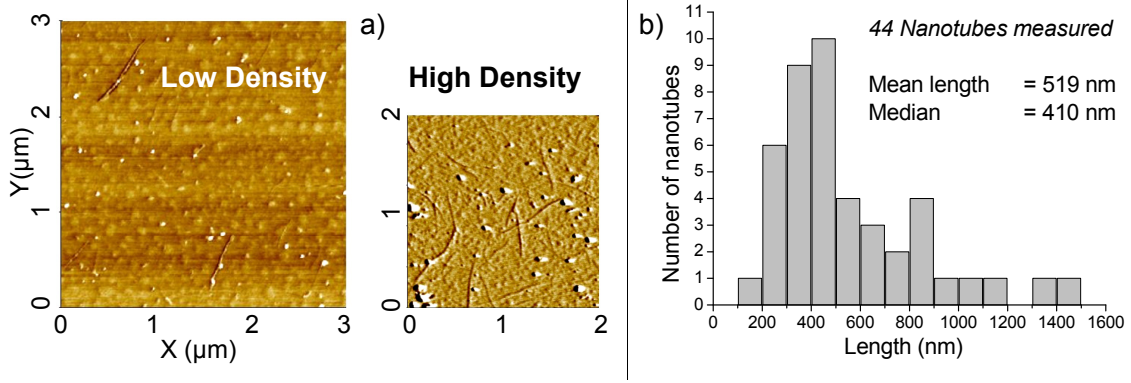


Figure 2.2: a) Example of AFM phase images in non-contact tapping-mode. Samples need to be thoroughly rinsed with water to remove surfactant residues and enable AFM imaging. Many residues are still visible as high-contrast dots. b) From a collection of such images taken at different position on a sample, we built some statistics on the length of the nanotubes. The proportion of very short nanotubes may be under-estimated because they are difficult to distinguish from impurities.

An important feature revealed by this characterization is that the mean length of the SWNTs is on the order of, or smaller than, our spot diameter. This renders difficult any claim about the extent of the emission (localized vs. delocalized) on the sole ground of spatial PL mapping. We note however that a substantial number of nanotubes are longer than $1\ \mu\text{m}$ and should be seen as extended objects in PL if emission were coming from the entire nanotubes.

2.1.2 Confocal Microscope Setup

Although a number of small modifications and improvements have been realized in the course of my thesis, the basic experimental setup remained the same and is schematically represented in Fig. 2.3. The central part is a home-build confocal microscope based on the very versatile Thorlabs cage system and components. Following the path of light from excitation to collection and detection, we briefly describe the main parts:

- The excitation source is a solid state Ti:Sapphire MIRA 900-F laser from the company Coherent, pumped by a 10 Watt output VERDI green laser. The MIRA can be operated in continuous wave (CW) or in pulsed mode with a pulse length of ~ 150 fs and a repetition rate of 76 MHz (time separation between pulsed ~ 13 ns). The wavelength can be tuned reliably from 720 to 980 nm.
- The output light goes through some optics for power control and stabilization (Acousto-optic Modulator with PID feedback from the photodiode). It is then coupled into a single mode optical fiber. Polarization paddles enable to rotate the axis of the linearly polarized excitation light before it enters the confocal microscope.
- The laser light is collimated out of the fiber and goes through a sharp high quality short-pass filter. The filter is needed because the high intensity laser field in the fiber creates a large, broad background of inelastically scattered

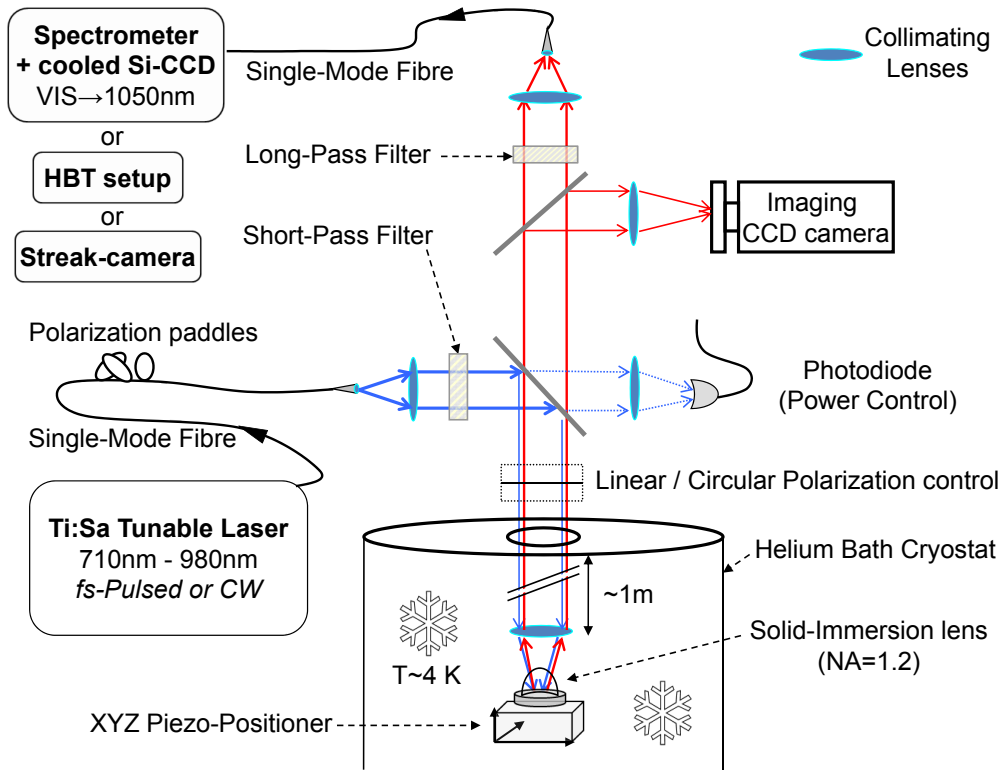


Figure 2.3: A schematic view of the basic setup used for single nanotube confocal microscopy at cryogenic temperatures.

light at longer wavelengths. If unfiltered, this light is reflected on the sample (and other optics on the path) and collected in the spectrometer, covering the signal from the nanotubes.

- How much light is reflected on the 45° glass plate depends strongly on its polarization axis. It is minimal (about one percent) for light polarized along a vertical axis lying in the plane of the figure, whereas it is maximal ($\sim 10\%$) for the orthogonal direction (perpendicular to the plane of figure 2.3). Using the preceding paddles to maximize the intensity reaching the sample thus determines a well-defined linear polarization axis before passing through the polarizing optics.
- To control excitation polarization we plug-in one of the two following optical components: either a quarter-wave plate, transforming linear polarization into circular polarization; or a half-wave plate, which rotates the linear polarization axis by twice the angle between the original direction and the fast axis.
- A hermetically glued window with anti-reflecting coating gives access to the inside of the stainless steel microscope tube. It is initially evacuated and filled with low pressure helium (~ 10 mbar) serving as exchange gas to thermalize the sample at the helium bath cryostat temperature (4 K). The collimated beam is focused on the nanotubes through the combination of a high NA aspherical lens and a zirconium solid immersion lens.
- On the close vicinity of the SIL we mount a thermo-resistor for local heating and temperature control (with resistive read-out). This allows us to tune the local temperature from the 4 K base temperature up to ~ 30 K.

- Reflected, scattered and re-emitted light fields all follow the same path upwards. Some is reflected and lost on the first glass plate. A second glass plate reflects a small portion of the light for real space imaging on a CCD camera. Unfortunately PL emission from the nanotubes is much too weak to be directly detected in this way, but reflection of laser light provides a highly valuable help in aligning the microscope and focusing, as well as for orientation.
- The long-pass filter is critically needed to remove the reflected laser light which is orders of magnitude more intense than the PL signal and would saturate the spectrometer. The respective cut-off wavelengths of the short- and long-pass filters have to be carefully chosen. Their transmission ranges should not overlap, and their particular values also determine which nanotube chiralities we are able to detect and at what energies we can excite them. After the filter, light is coupled in a single-mode fiber and sent to the desired detection and analysis equipment: spectrograph, HBT-setup or streak-camera.
- The spectrograph is a 500 mm focal-length SpectraPro-2500i from the Acton Research Corporation. It features an astigmatism-corrected optical system, triple indexable gratings and triple grating turret. Only two gratings are installed in our system: a 300 g/mm grating giving a spectral resolution of ~ 0.3 meV (at 900 nm) and a 1200 g/mm grating with which we can reach a resolution close to 0.1 meV. If not mentioned otherwise, all the spectra shown in this thesis were taken with the 300 g/mm grating.

To illustrate the main characteristics of our setup we show in Fig. 2.4 a spatial map of PL at liquid nitrogen temperature. We designed a Labview routine controlling simultaneously the Attocube piezo-electric positioners and the spectrometer (through TTL pulses). Such a map is obtained by scanning step by step, line by line a given area of the sample. After each step a spectrum is integrated over a few seconds before the next move. Finally a script written in Origin performs the integration of the signal intensity in each spectrum over the chosen range, providing the data for the matrix coding the color map. As we can see in Fig. 2.4, a single nanotube is emitting around 880-890 nm in the mapped area, and it is strongly selective to the polarization axis of the excitation, as expected from the antenna effect.

2.1.3 Time-resolved spectroscopy

To measure the PL lifetime of the SWNTs, we use a Hamamatsu streak camera with maximal time resolution of 7 ps and detection range extending to 900 nm in the near infrared. This limits its operation to the measurement of the narrowest tubes in our sample. We give here a short description of the functioning principle of this instrument (see Fig. 2.5).

A streak camera transforms the temporal profile of a light pulse into a spatial profile on a detector, by causing a time-varying deflection across the width of the detector. The light pulse enters the instrument through a narrow slit and hits a photocathode, where photoelectrons are ejected via the photoelectric effect. The electrons are accelerated in a cathode ray tube and then deflected through an electric field produced by a pair of parallel plates. During each repetition cycle, electrons emitted first hit the detector at a different position compared to electrons produced

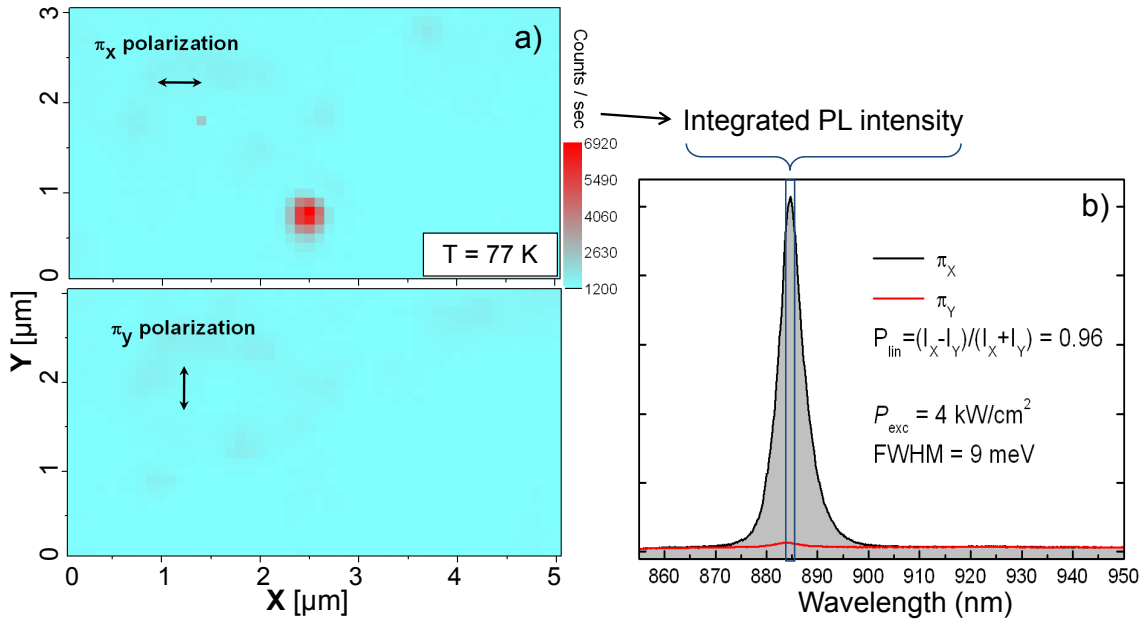


Figure 2.4: a) Automatized PL mapping of the same $5 \times 3 \mu\text{m}^2$ area under two orthogonal linear polarizations of the excitation light. Each pixel of the color map is obtained by integrating the corresponding PL spectrum over the wavelengths between 884 nm and 885.5 nm. It is clear that no other tube emitting in this range lies in the vicinity, a necessary condition for single nanotube spectroscopy. Note also that the emission region is significantly smaller than our spot size since the expected elongated shape in the X-direction is not recognizable. b) The two cross-polarized spectra from the red spot in a), showing the strong suppression of PL emission when the nanotube is excited with cross-polarized light.

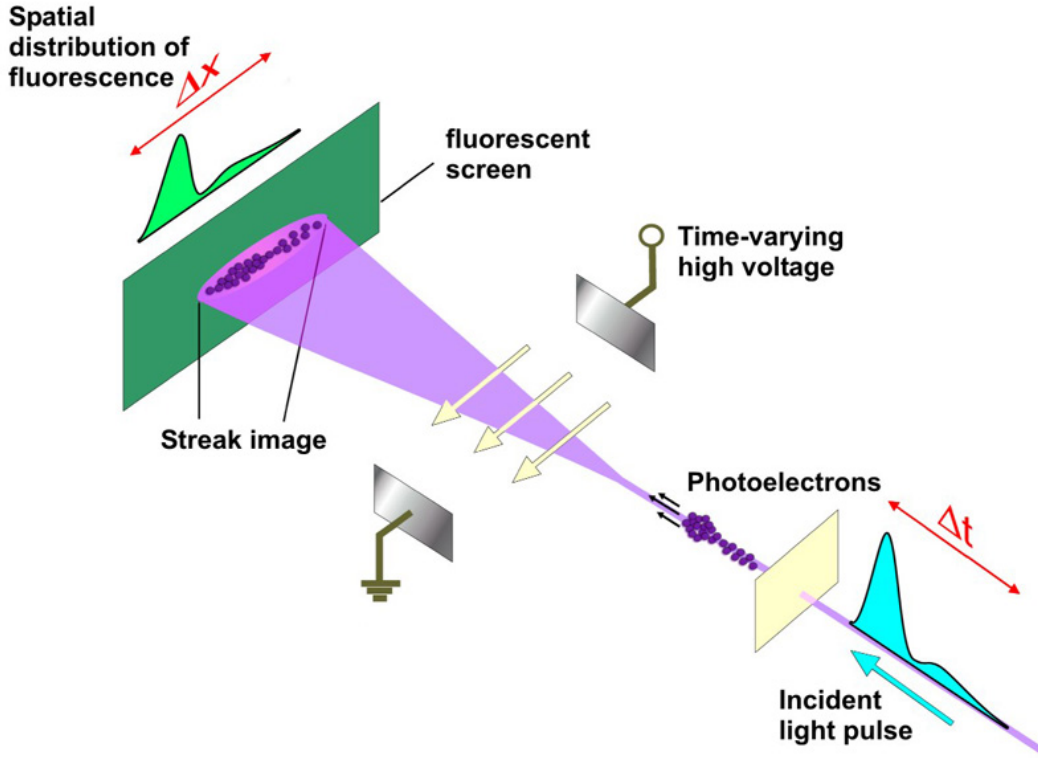


Figure 2.5: Functioning principle of an optoelectronic streak camera.

by photons that arrived later. This cycle is synchronized with the MIRA femtosecond pulses and repeated at a rate of 76 MHz. The accumulating frames form a “streak” of light reproducing the temporal profile of the incoming signal, from which properties like the PL decay time can be inferred.

We performed time-resolved PL (TRPL) measurements on a dozen of CoMoCat nanotubes at temperatures ranging from 4 K to 30 K and under different excitation powers. First let us clarify what dynamics is revealed by TRPL data. It is important to stress that TRPL measures the PL lifetime which is in general different from the radiative lifetime of the exciton. Actually, the discrepancy is significant for carbon nanotubes which are thought to have radiative lifetimes in the nanosecond range, whereas PL lifetimes are tens to hundreds of picoseconds. This means that excitons decay mainly through non-radiative channels, which also accounts for the low quantum efficiency of light emission (a few percents or less).

Figure 2.6 shows a typical TRPL measurement on a CoMoCat nanotube at 4 K, under moderate excitation intensity. The rise-time of the time trace is mainly determined by the streak camera resolution of 7 ps, since the MIRA pulses are much shorter. The majority of the SWNTs studied display a bi-exponential decay, with a short time-constant of 15 to 40 ps and a longer one of 200 to 400 ps. The weight of the short component was always larger, with some nanotubes even showing mono-exponential decay (vanishing longer component). In Fig .2.6, we give the form of the fitting function and the fitting parameters used. For this particular nanotube, an increase in temperature up to ~ 15 K lead to a slight increase in τ_1 , but in general changing the temperature had no detectable or reproducible effect on the measured

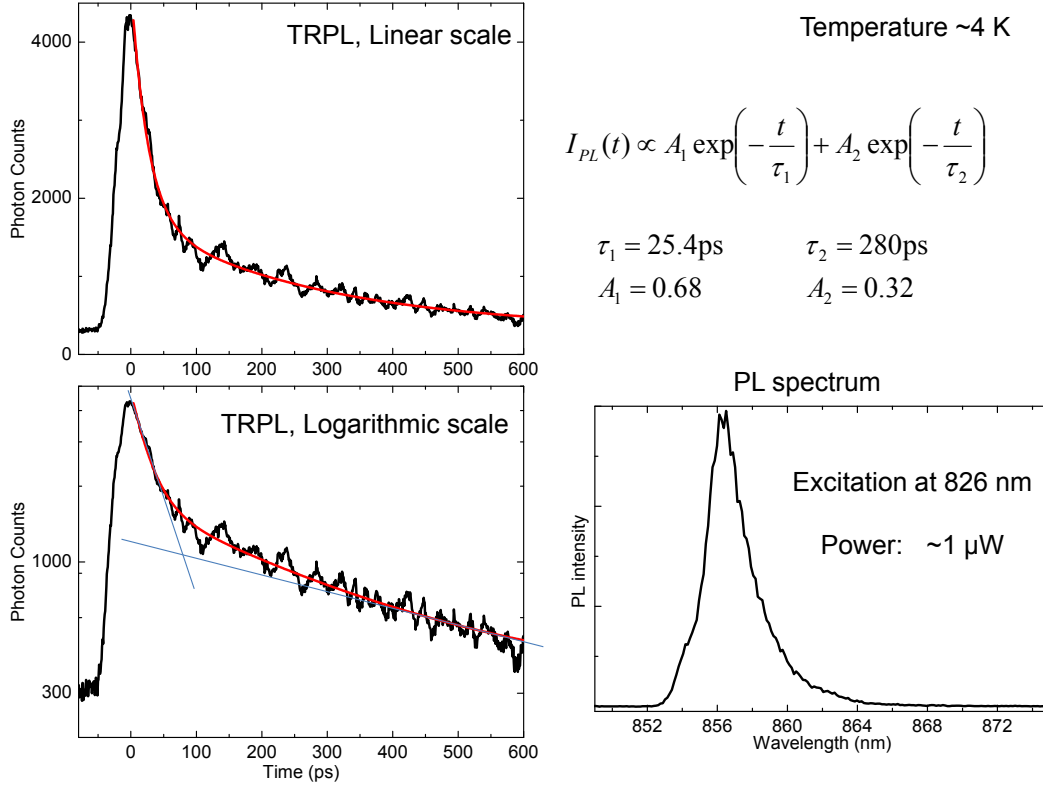


Figure 2.6: Example of time-resolved PL (TRPL) measurement at 4 K using the streak camera.

time dynamics.

The main fast component very likely corresponds to the non-radiative decay of the optically active exciton, although the particular mechanism is still unknown. We attribute the longer component to the re-population of the bright state from a longer-lived dark or quasi dark state, which can be the nominally dark exciton (see chapter 1) or trap state at some particular site on the nanotube.

2.2 Auto-correlation measurements and Photon antibunching

2.2.1 Photon correlation: theory and setup

The definition of the normalized first-order correlation function depending on the time difference τ reads:

$$g^{(1)}(\tau) = \frac{\langle E^*(t)E(t+\tau) \rangle}{\langle E^*(t)E(t) \rangle} \quad (2.1)$$

where $E(t)$ is the total complex amplitude of the electromagnetic field of the beam of light. A measurement of $g^{(1)}$ evaluates the first-order coherence which is equal to the statistical average (denoted by angle brackets) of the correlation between electromagnetic fields. For a stationary source, the statistical average is equal to the

time average, which is what we effectively measure in single nanotube spectroscopy when we integrate the signal over time.

The temporal coherence of light is directly related to the spectral density of the source by a Fourier transformation, according to the Wiener-Khintchine theorem:

$$F(\omega) = \frac{1}{\pi} \Re \left(\int_0^\infty g^{(1)}(\tau) \exp(i\omega\tau) d\tau \right) \quad (2.2)$$

where ω is the angular frequency and \Re denotes the real part of a complex number. All the information retrieved from spectral analysis is thus derived from the first-order correlation properties of the source. To access more interesting properties of the emitter and investigate some of its quantum features, we need to know the second-order correlation function defined as:

$$g^{(2)}(\tau) = \frac{\langle E^*(t)E^*(t+\tau)E(t+\tau)E(t) \rangle}{\langle E^*(t)E(t) \rangle^2} \quad (2.3)$$

An important oft-overlooked point in the above equation is that, generally, the complex electromagnetic fields E do not commute. Therefore, in the general case, the order of the terms cannot be rearranged. In the case of chaotic light, for example, the cancelation of cross-terms between random relative phases allows this reorganization, and we can write:

$$g^{(2)}(\tau) = \frac{\langle E^*(t)E(t)E^*(t+\tau)E(t+\tau) \rangle}{\langle E^*(t)E(t) \rangle^2} = \frac{\langle I(t)I(t+\tau) \rangle}{I^2} \quad (2.4)$$

Since, as we shall see, we have access experimentally only to the zero-delay value $g^{(2)}(\tau = 0)$, the commutation assumption is in our case always satisfied, whatever the coherence properties of the source.

From eq. 2.4 it is clear that we may measure $g^{(2)}(\tau)$ if we are able to correlate the PL intensity from the nanotube with itself at different times. In other word we need to measure the amount of correlation between photons emitted (and arriving on the detectors) at different times. This can be done using a Hanbury-Brown-Twiss setup [28] as depicted in Fig. 2.7.

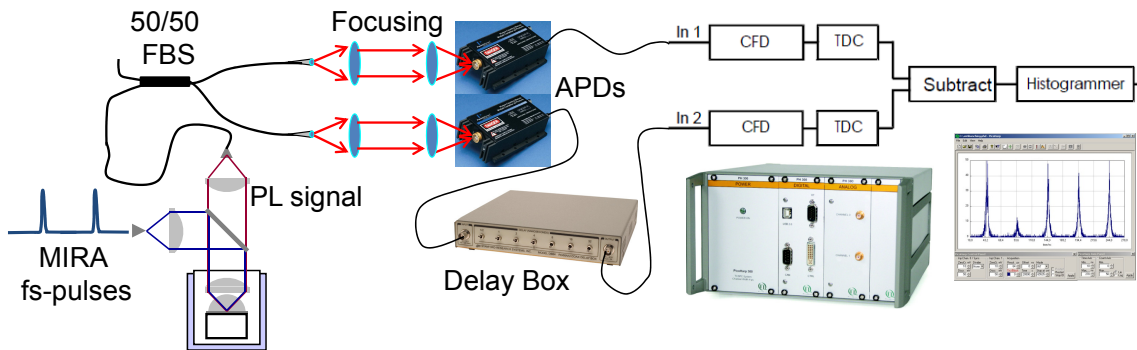


Figure 2.7: A schematic representation of our HBT setup used for correlation measurements. FBS: Fiber-based Beam Splitter; APD: Avalanche Photodiode; CFD: Constant Fraction Discriminator; TDC: Time-to-Digital Converter.

The PL signal coming from our sample is split equally into a pair of beams by a 50/50 fiber beam splitter (FBS), each of them being focused on the chip of a silicon avalanche photodiode (ADP) single photon detector (with quantum efficiency approaching 10% at 900 nm). A photon detection event triggers the emission of an electric pulse. One of the pulse is delayed by a few tens of nanoseconds before entering the correlation electronic. Therein, for each input, a constant fraction discriminator (CFD) distinguishes between noise and real voltage pulses, before a time-to-digital converter (TDC) translates the time delay between pulses in a digital output. The outputs from the two arms are finally correlated to form a histogram of the coincidences.

If two-photon emission never occurs within the duration of a single pulse, we expect no coincidence for zero time delay. On the contrary the detection of a coincidence between two different pulses (whose time separation is large compared to the “memory” of our nanotube) is always possible and completely random (reflecting the fact that $g^{(2)}(\tau) \xrightarrow{\tau \rightarrow \infty} 1$, as explained below). For an antibunched emitter we thus expect the formation of equally high and equally spaced peaks, except from a missing central peak at $\tau = 0$.

We now turn to the particular form of the function $g^{(2)}$ for different kinds of light sources, and its relation to the time statistics of the emitted photons. We show in Fig. 2.8 schematic patterns representing the photons emitted over time by three types of sources. In thermal light, photons tend to be emitted in packets (or bunches) so that $g^{(2)}(0) > 1$ (characteristic of a *quantum* random process). For a poissonian statistic like the one of a laser (or more generally describing a *classical* random process), photons are perfectly uncorrelated for any delay; in particular $g^{(2)}(0) = 1$.

Finally, a single quantum emitter (e.g. a two-level system) cannot emit two photons simultaneously. Some delay is needed before the excited state becomes repopulated and a next photon can be emitted. The resulting light is antibunched, with $g^{(2)}(0) < 1$, ideally $g^{(2)}(0) = 0$. This result cannot be obtained within the realm of classical electrodynamics and reflects therefore a typically quantum property of the source. We note that in the long-delay limit the emitter has no memory of its state long ago: events separated by large delays are always uncorrelated, meaning that $g^{(2)}(\tau) \xrightarrow{\tau \rightarrow \infty} 1$. This is a useful remark for the normalization of the experimental data (collected as raw count numbers).

The forms of the $g^{(2)}$ function for the three cases above are represented in Fig. 2.9.a). If we disposed on extremely fast detectors and electronics (much faster than the PL lifetime of the nanotubes) we could theoretically directly measure these curves, using the HBT setup of Fig. 2.7 with the excitation laser operated in continuous wave. Unfortunately, our APDs have a time jitter of ~ 300 ps which is significantly larger than the typical nanotube PL lifetime of 30 ps or less. The narrow dip expected around $\tau = 0$ would therefore be lost after convolution with the instrument response function.

Nevertheless, even with this “slow” detectors, we can measure the value of $g^{(2)}(0)$ by exciting with very short pulses. The MIRA delivers femto-second pulses, much shorter than the PL lifetime. In a pulsed experiment, provided that the delay

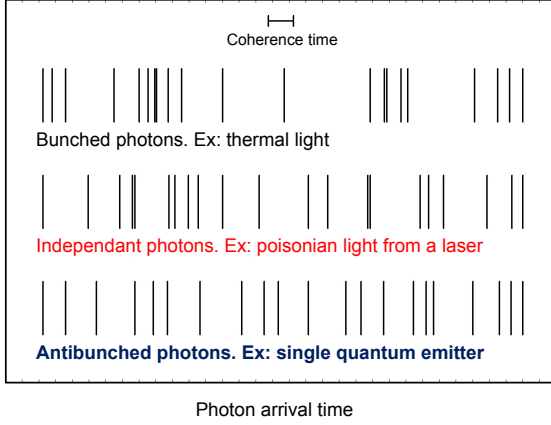


Figure 2.8: Photon statistics of typical emitters.

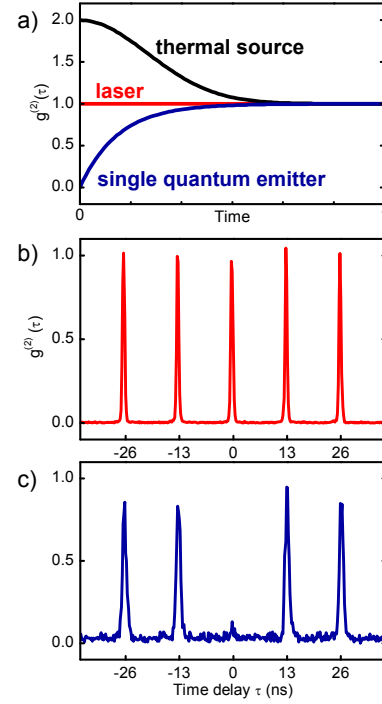


Figure 2.9: Graphs of $g^{(2)}$ for typical sources and data from pulsed measurement.

between pulses is larger than the detector jitter, the time resolution is effectively determined by the pulse duration. We are indeed limited to the measurement of $g^{(2)}(\tau = 0)$, but as we just saw, it contains the most relevant information to distinguish between different types of emitters. Experimental results from a measurement on the attenuated pulsed laser light and on an antibunched SWNT are shown in Fig. 2.9, b) and c), respectively.

2.2.2 Photon antibunching from carbon nanotubes

We used the HBT setup described above to perform photon correlation measurements on about a dozen of CoMoCat SWNTs and found for all of them normalized values of $g^{(2)}(\tau = 0)$ less than 0.5. This result cannot be explained by a classical description of the light emission by the nanotubes and reveals the unique quantum nature of the emitters. Figure 2.10 shows the data from a particularly strongly antibunched SWNTs at different temperatures. The PL spectrum is relatively broad, and very asymmetric at the lowest temperatures, with an obvious persistent red tail. Both features are very representative of the large majority of SWNTs in our sample. Simultaneous two-photon emission occurs with a probability lower than 3 % below 10 K. Since we did not performed background correction this figure constitutes an upper bound. Even at 25 K it remains as low as 15 %.

These results are unexpected for ideal one-dimensional emitters. Antibunching is a well-known characteristic of the light emitted by atoms or systems confined in all directions like quantum dots and nanocrystals (see for example [29]). In all these cases the emitter can be described as a two-level system and phase-space filling

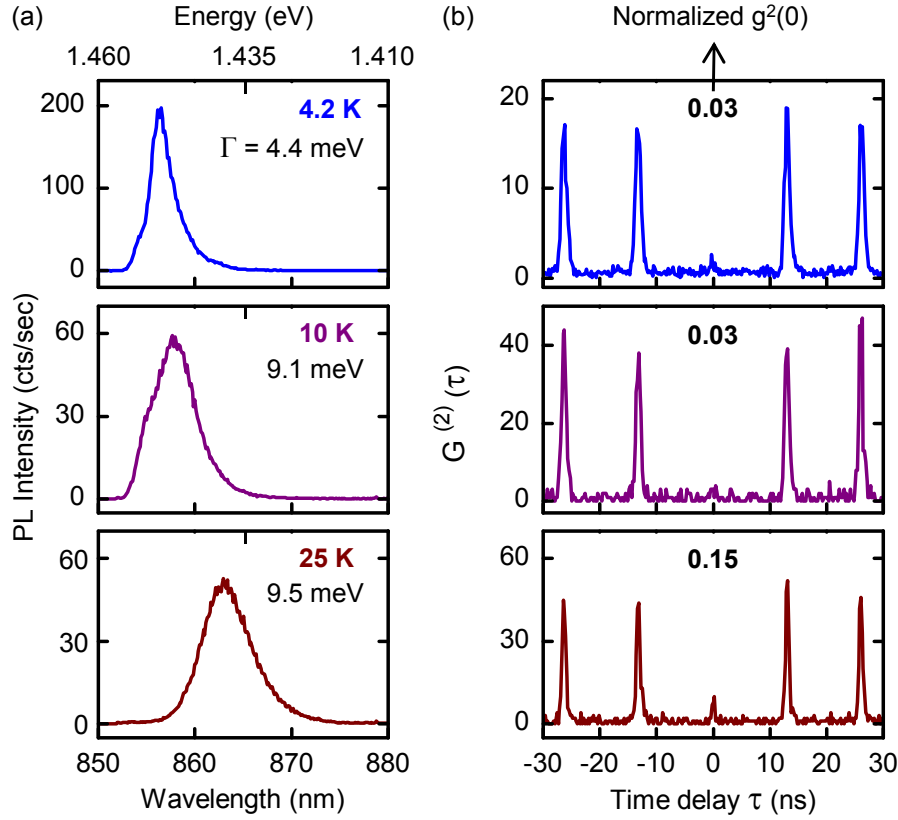


Figure 2.10: Photon antibunching from a SWNT at different temperatures.

ensures the optical anharmonicity causing antibunching. In contrast, carbon nanotubes are extended in one spatial direction and should allow for the simultaneous existence of several optical excitations along their lengths. This in turn should permit multi-photon emission events after each laser pulse, in contradiction with what we observe. The next section is dedicated to the search and discussion of possible mechanisms responsible for antibunching.

2.3 The origin of antibunching: discussion

2.3.1 Exciton-exciton annihilation

In a pulsed excitation experiment, several excitons are usually created along the nanotube length, or within the spot size if the latter is smaller than the SWNT length. The size of an exciton, its Bohr radius, is expected to be less than 2 nm (see for example [30] for an experimental determination). The Bohr radius is a measure of the typical electron-hole separation along the nanotube axis. The lifetime of a single exciton is the inverse of the total unimolecular decay rate $\gamma_r + \gamma_{nr}$. This is the sum of the radiative rate γ_r , calculated to be nanoseconds or tens of nanoseconds, and the dominating non-radiative decay rate γ_{nr} . Since $\gamma_r \ll \gamma_{nr}$, what we actually probe in our PL lifetime measurement is $\gamma_{nr} \approx 2\pi/(30 \text{ ps})$.

During this lifetime, excitons can diffuse along the nanotube. For micelle-encapsulated carbon nanotubes like the ones we are using, the diffusion length L_D

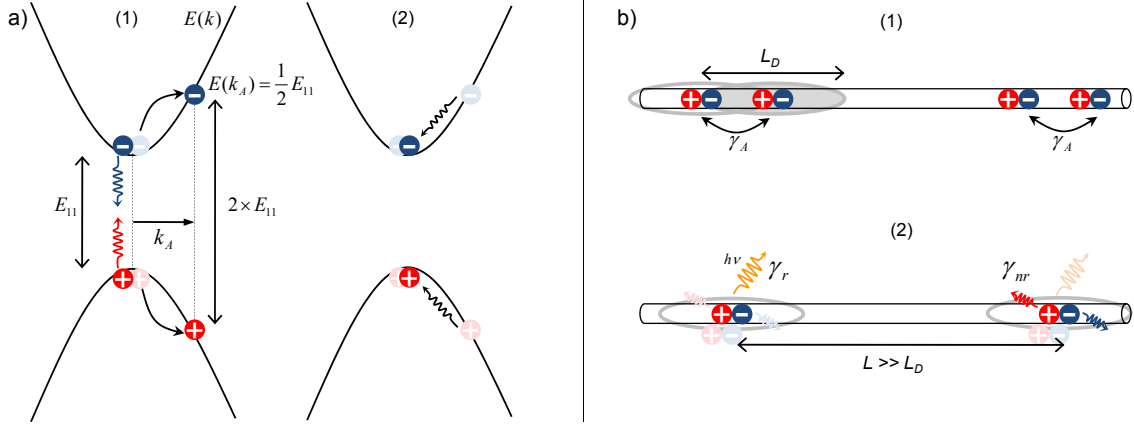


Figure 2.11: Auger recombination: physical process in (a) energy-momentum space and (b) real space. In the first stage (1), two nearby excitons interact through the Coulomb force, one of them recombining non-radiatively. Energy and momentum conservation are satisfied by the excitation of the remaining electron and hole to higher states. (2) The excited electron-hole pair subsequently relaxes in tens or hundreds of femtoseconds to reform a ground state exciton. Finally the remaining excitons are physically separated by distances too large to interact, and each one may emit a photon.

of excitons, that is to say the mean distance they probe along the nanotube before recombining, was found to be 90-100 nm at room temperature (see [25, 31]). When two excitons are created within a segment of length $L < L_D$, because many-particle interactions are enhanced due to the reduced dimensionality of the nanotube, they are extremely likely to undergo exciton-exciton annihilation (EEA), also known as Auger recombination (or bimolecular recombination), as shown in Fig. 2.11.

During this process, one of the exciton recombines non-radiatively while its energy is transferred through Coulomb interaction to the second exciton by promoting the electron and hole to higher energy states. Since there always exists a wave-vector k_A so that $E_c(k_A) - E_v(k_A) = 2E_{11}$ (see Fig. 2.11 a)), no restriction is imposed by energy and momentum conservation, making the process very efficient. The excited electron-hole pair can subsequently relax on very short time scales to the ground excitonic state E_{11} .¹

Recently, the validity of this model has been experimentally confirmed by Murakimi and Kono [32]. They study the saturation of the PL emission intensity from CoMo-Cat nanotubes in an aqueous solution of sodium cholate under pulsed excitation. They observe an upper limit to the exciton density that is very well described by diffusion-limited exciton-exciton annihilation as presented above (with a somewhat shorter diffusion length ~ 45 nm).

This observation has highly relevant implications in our discussion on the origin of antibunching. Both our spot size and the average length of our nanotubes are ~ 500 nm, therefore several times larger than L_D (which is in addition very likely

1. Alternative models of Auger recombination assume that both excitons are lost during the process, but to fix the ideas we will focus on the former scenario.

to become much shorter at cryogenic temperatures). It is then to be expected that each excitation pulse populates the nanotube with excitons separated by distances larger than their diffusion length (see Fig. 2.11 b)). These excitons will never meet each other neither come close enough to interact, thereby finally recombining by one of the possible unimolecular channels γ_r or γ_{nr} . This situation is identical to the presence of N independent quantum emitters, with $N \sim L_{NT}/L_D$ (L_{NT} is the nanotube length and may be replaced by the spot diameter). The calculated zero-delay second-order photon correlation function in this case is $g^{(2)}(0) = 1 - 1/N$. We note that $g^{(2)}(0) \geq 0.5$ as soon as $N \geq 2$, which is expected for SWNTs from the previous discussion. This is in strong contrast with the high level of antibunching we observe in our experiment.

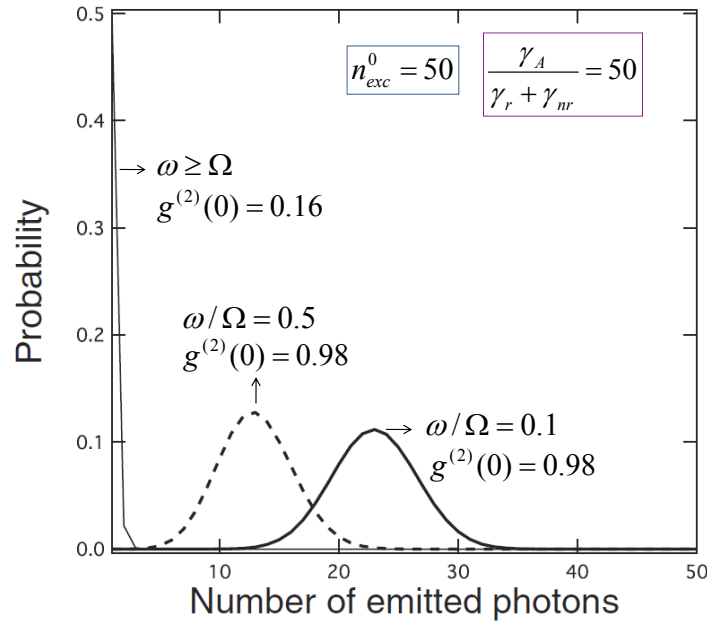


Figure 2.12: Calculated emitted photon number statistics for an extended system after an ultrashort pulsed excitation, adapted from [33]. The Auger rate is fixed to $\gamma_A = 50(\gamma_{nr} + \gamma_r)$ and the initial number of excitons created after each laser pulse in the system is $n_{exc}^0 = 50$. As soon as the effective domain probed by excitons is smaller than the system size $\omega < \Omega$, antibunching is not observed anymore.

Interestingly, K. Seki and M. Tachiya recently calculated the photon emission statistic for a system where unimolecular decay competes with bimolecular Auger annihilation (rate γ_A) [33]. Moreover, they consider the possibility of an extended system of volume Ω in which excitons interact only when they are both contained within a smaller domain ω . This describes very well the situation expected from diffusion-limited exciton-exciton annihilation in carbon nanotubes.

The results obtained by K. Seki and M. Tachiya are reproduced in Fig. 2.12. When all excitons are susceptible to interact ($\omega \geq \Omega$), a moderately fast Auger rate $\gamma_A = 50(\gamma_{nr} + \gamma_r)$ ensures low level of photon pairs emission even at high excitation level ($n_{exc}^0 = 50$). However, as soon as the system is effectively separated in two

domains or more, no significant level of antibunching is found and multi-photon emission occurs with high probability.

2.3.2 Exciton localization in SWNT-Quantum Dots

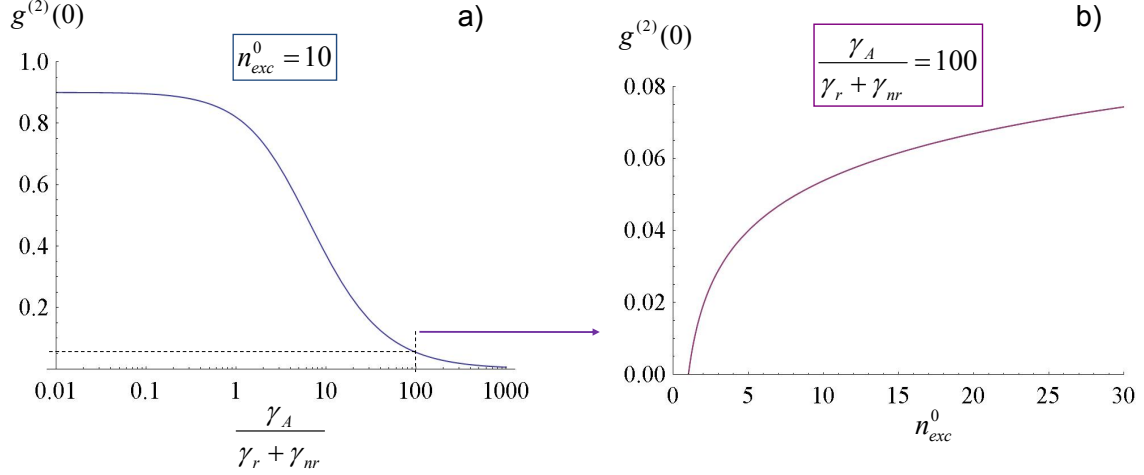


Figure 2.13: a) Second-order photon correlation function at zero-delay, calculated using the formula from [33, 34], as a function of the Auger rate γ_A normalized to the total unimolecular decay rate $\gamma_{nr} + \gamma_r$. Note the independence of $g^{(2)}(0)$ on the ratio γ_r/γ_{nr} . The initial number of excitons created after each laser pulse in the system is fixed to $n_{exc}^0 = 10$. b) For a given Auger rate $\gamma_A = 100(\gamma_{nr} + \gamma_r)$, an increase in pump power translates into an increase in n_{exc}^0 , but antibunching remains significant ($g^{(2)}(0) < 0.1$).

Although Auger rate in carbon nanotubes is known to be extremely fast ($\gamma_A > 100(\gamma_{nr} + \gamma_r)$), the limited diffusion range of excitons should not enable us to observe detectable level of antibunching. We are thus forced to assume that PL emission originates mainly from a single site on the nanotube, whose size σ is smaller than L_D . In other word, we must be detecting PL from SWNT-quantum dots (SWNT-QDs). We use the formula derived in [33, 34] by K. Seki and M. Tachiya to calculate the expected photon pair correlation when Auger annihilation alone prevents multi-photon emission in a hypothetical SWNT-QD. Our results are summarized in Fig. 2.13.

Indeed, the significant levels of antibunching we observe experimentally are in good agreement with the calculated values under the reasonable assumption that $\gamma_A \geq 100(\gamma_{nr} + \gamma_r)$ (i.e. sub-picosecond exciton-exciton annihilation). In these conditions, we expect robust antibunching, slightly degrading under increasing pump power (corresponding to an increasing initial number of excitons n_{exc}^0).

Alternatively, the observation of antibunching from a SWNT-QD could be explained by the existence of a stable and strongly bound bi-exciton. This is indeed expected to be the case, with calculations predicting binding energies for the bi-exciton of 100 to 200 meV. Both explanations are thus likely to participate in reality, but we now present experimental evidences emphasizing on the role played by Auger recombination.

2.3.3 Evidence for ultra-fast Auger recombination

Figure 2.14 displays the PL emission characteristics of a single SWNT under increasing pulsed excitation power. First of all, we do not remark any change in the line shape nor in the emission energy. In particular, no red-detuned bi-exciton peak is observed (up to the highest pump power) within our detection range, extending 185 meV below the single exciton peak. The bi-exciton emission peak should show up at high excitation intensity and its strength should follow a typical quadratic pump power dependence. Most importantly, we clearly see that the PL intensity rapidly saturates, as is expected when Auger annihilation prohibits the existence of several excitons in the quantum dot. Note the irreversible decrease at the highest pump power which is a widely observed feature in our experiment. This cannot directly be explained by the exciton dynamics and is more likely due to modifications in the local environment of the nanotube.

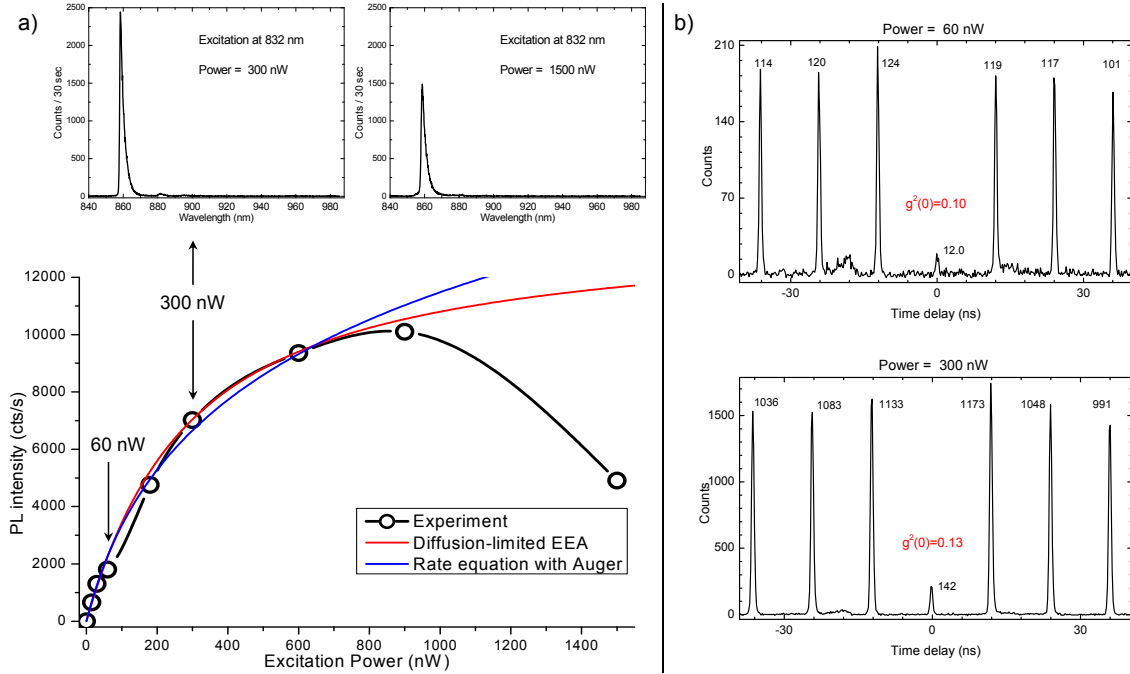


Figure 2.14: a) PL intensity saturation under pulsed excitation. Two PL spectra are shown on top; the shape and energy do not change when the power is increased. The weak red-detuned peak visible at 300 nW is attributed to a RBM phonon replica (see chapter 3) and its intensity follows the same saturation behavior. The blue and red solid curves are tentative fits using the functions derived in [32]. None of them can reproduce the strong intensity drop at high power, which is certainly due to irreversible modification in the nanotube environment. b) Results of pulsed HBT measurements at two different powers (indicated by arrows in (a)). The slight increase in $g^{(2)}(0)$ is indicative from Auger induced antibunching and compares well with the qualitative behavior expected from the calculation in Fig. 2.13.

At low pump fluence, this particular nanotube shows antibunching level of $g^{(2)}(0) = 0.1$. When the power is raised close to the saturation regime, antibunching degrades somewhat but remains significant with $g^{(2)}(0) = 0.13$ at 300 nW pump

power. This behavior closely matches what is expected from the model discussed above and follows well the calculation presented in Fig. 2.13.

All the arguments presented so far bring us to the conclusion that there must exist a single confined emitting site on the nanotube responsible for the broad PL lines showing strong antibunching. The Auger rate being known to be very fast in pristine carbon nanotubes would be even faster between excitons trapped in a same quantum dot along the tube, thus explaining very well the origin of antibunching and in good agreement with experimental observations such as PL saturation.

However, we did not present so far independent evidences for the existence of axially confined and optically active excitons in our SWNTs. Before developing in chapter 3 a model relying on strongly confined excitons to reproduce the broad and asymmetric PL line shapes, we first show in the next section that the PL excitation spectra display remarkable features supporting the picture of SWNT-QDs.

2.3.4 Resonant excitation of a SWNT-QD

We already argued in chapter 1 that phonon-assisted excitation of the ground-state exciton is the mechanism responsible for the resonances observed in the PLE spectra of carbon nanotubes at room and liquid nitrogen temperatures (see Fig. 1.17). At liquid helium temperature, we are confronted to the fact that a single trapping site on the nanotube must be dominating the PL emission in order to account for all experimental features. Yet it would be expected that many different traps should exist along the nanotube, each being a potential source for PL emission.²

However the majority of PL spectra were featuring one or a few lines only, so that there must be a physical mechanism enabling the excitation of a single QD on the nanotube. One possibility could rely on the usual phonon-assisted excitation process, but only if the energy detuning between the different dots is large enough to selectively excite one of them through a phonon sideband. This would be evidenced by the consecutive increases in intensity of different PL lines as the laser is tuned. Although we happen to see this in particular cases, no such behavior is systematically observed.

We report in Fig. 2.15 the PLE map of the nanotube showing strong antibunching already presented in Fig. 2.10. The data were taken just after the HBT measurements were performed overnight. We can see that the spectrum has split in two overlapping lines in the meanwhile. Since no narrow spectral filtering was used during the HBT experiment, it means that these two lines very likely originate from the same quantum dot. We will return to this point in chapter 4.

But the most remarkable feature is the huge and sharp PLE resonance around 45 meV which cannot be assigned to a phonon sideband. Its sheer magnitude is not comparable to the other phonon-related resonances, suggesting that a different and more effective mechanism is involved. Figure 2.15 is presented as a single example for the typical pattern we observe in all the PLE spectra of the broad and asymmetric

2. We must point out here that we indeed measured a variety of spectra but usually discarded the few ones showing too complex features and too many lines. The main reason for this is the difficulty to distinguish between the PL from a collection of quantum dots on the same SWNT, and the emission from a bundle of nanotubes.

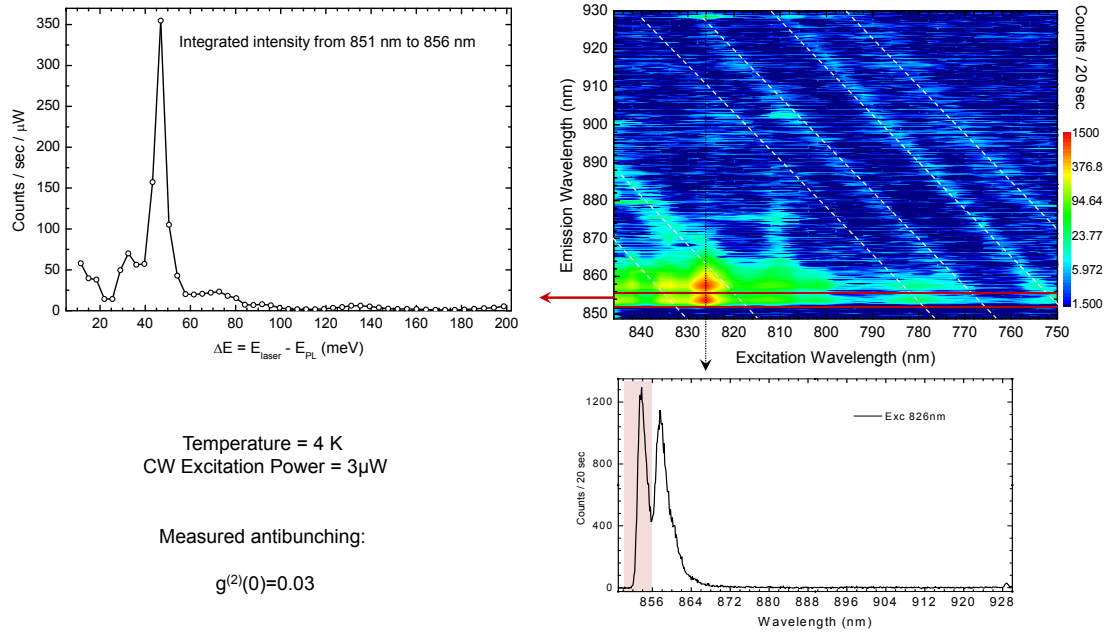


Figure 2.15: Two-dimensional PL excitation color map of the nanotube presented in Fig. 2.10 ($g^{(2)}(0) = 0.03$), taken at 4 K after the HBT measurements. The line-cut on the upper-left is obtained by integrating the PL intensity of the higher energy line. The detuning is calculated between the laser energy and the energy of this PL-peak's maximum. On the lower-right we show a PL spectrum under resonant excitation. The wavelength integration range used for the line-cut is shaded in light red.

lines at 4 Kelvin. We usually note strong resonances occurring at energies between 20 meV and 100 meV away from the emission line. Their sharpness, magnitude, and the randomness in their precise positions strongly contradict the picture of simple phonon sidebands.

It is much more likely that such PLE peaks are due to the resonant pumping of an excited state of the SWNT-QD, in analogy to p -shell excitation in traditional bulk semiconducting quantum dots [35, 36]. We will develop this idea further in chapter 4, where a simple model for the confinement is discussed.

3 Exciton Dephasing Induced by Acoustic Phonons

We already presented in chapters 1 and 2 the typical PL line-shapes of CoMoCat SWNTs at low temperatures. First, they are much broader than the lifetime-limited line-widths expected from the measured PL lifetimes, by a factor of hundred or more. Then they display pronounced asymmetries at 4 Kelvin with steep high-energy shoulders and persistent low-energy tails. Finally, these asymmetric shapes evolves toward non-Lorentzian but more symmetric lines when temperature is increased to 20-30 K.

Although very similar observations were reported by other groups (see in particular [37]), no satisfactory explanation had been given. H. Htoon *et al.* invoked a Fermi-edge singularity origin (without precise model nor calculations), but this would require the nanotubes to be significantly p- or n-doped, which has been shown to quench PL because of Auger recombination of excitons with free carriers. This unresolved issue pushed me to investigate into the possible physical origin of the width and asymmetry. I turned my inquiry toward the role of low-energy phonons. Assuming that PL is coming from confined excitons (SWNT-QDs) I could compute the theoretical spectra and compare them with our experimental data. The very acute agreement is strongly supportive of the validity of the model.

In this chapter we start by presenting the physical model we use, then we report on the analytical solution and numerical calculations performed to fit the experimental data, before extending our discussion to interesting physical implications of our results.

3.1 The Physical Model

3.1.1 Carbon Nanotube Quantum Dot

In the two previous chapters we gave very strong evidences for the formation of SWNT-QDs, meaning that excitons are unintentionally confined along the nanotube axis. The precise mechanism causing tight localization is unknown, but is likely caused either by intrinsic defects, by local strain, by charged impurities trapped in the micelle (see chapter 4), or by varying interactions with the substrate (as recently proved by Shin *et al.* [38]). Photon antibunching strongly supports the assumption that PL is coming from QD-like emitters within the nanotube which can be well described by two-level systems.

In order to develop a physical model of our system allowing quantitative calculation of the spectral features, we need a tractable and simplified description of an optically active SWNT-QD (a more accurate model will be developed in chapter

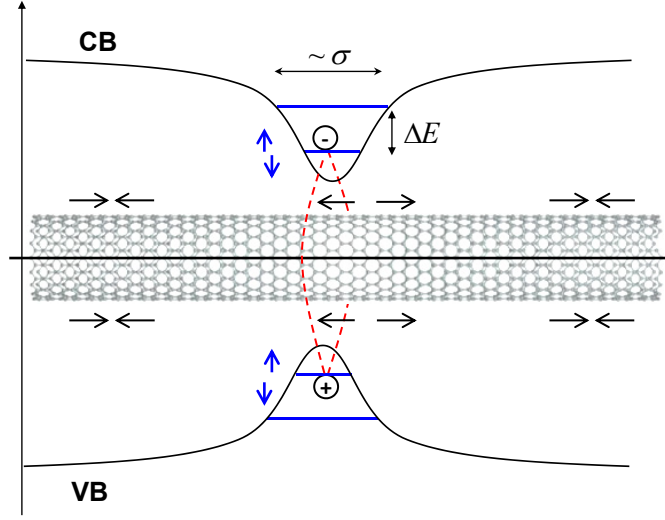


Figure 3.1: Schematic view of a strongly confined SWNT-QD interacting with acoustic phonons. The small confinement length σ oblige the bound exciton to occupy only discrete energy levels spaced by ΔE . Because of the deformation potential electron-phonon coupling the lattice distortion (black arrows) associated with an acoustic phonon mode (eg. here the stretching mode) results in a shift of the QD energies (symbolized by blue arrows).

4.1). As pictured in Fig. 3.1 we assume that the exciton is localized along the nanotube axis (coordinate z) by some confining potential. The precise shape of this potential is *a priori* unknown, and we choose a quite general parabolic form. Beside always being a valid approximation of an analytical function close to a local minimum, it allows an easy expression of the resulting wave-function envelope. For confinement length scales larger then the Bohr radius of the exciton (namely 1 to 2 nm, see for example [39, 40]), we can use an envelope wave-function approximation and express the SWNT-QD states as a superposition of free E_{11} excitons with non-zero wave-vectors along z . More precisely, the ground state in a harmonic potential has a Gaussian envelope:

$$\Psi^{exc}(z) = \frac{1}{\pi^{1/4}\sigma^{1/2}} \exp\left(-\frac{z^2}{2\sigma^2}\right) \quad (3.1)$$

Here σ is the confinement length, and the envelope is normalized so that $\int_{-\infty}^{+\infty} |\Psi^{exc}(z)|^2 dz = 1$. In this harmonic potential, the eigenstates are split by the energy

$$\Delta E = \frac{\hbar^2}{m_{exc}^* \sigma^2}$$

where m_{exc}^* is the effective mass of the exciton. We take $m_{exc}^* \simeq 0.2 \cdot m_e$ (see for example [41]) with $m_e = 9.11 \cdot 10^{-31}$ Kg the mass of the electron. When this energy splitting is large enough compared to the thermal energy (i.e. $\Delta E \gg k_B T$, where $k_B = 1.38 \cdot 10^{-23}$ J/K is the Boltzmann constant) the higher states have negligible thermal population and the SWNT-QD can be very well approximated by a simple two-level system. The ground state $|g\rangle$ is the empty dot whereas the excited state $|e\rangle$ corresponds to one exciton occupying the ground state of the quantum dot.

3.1.2 Exciton-Phonon Coupling

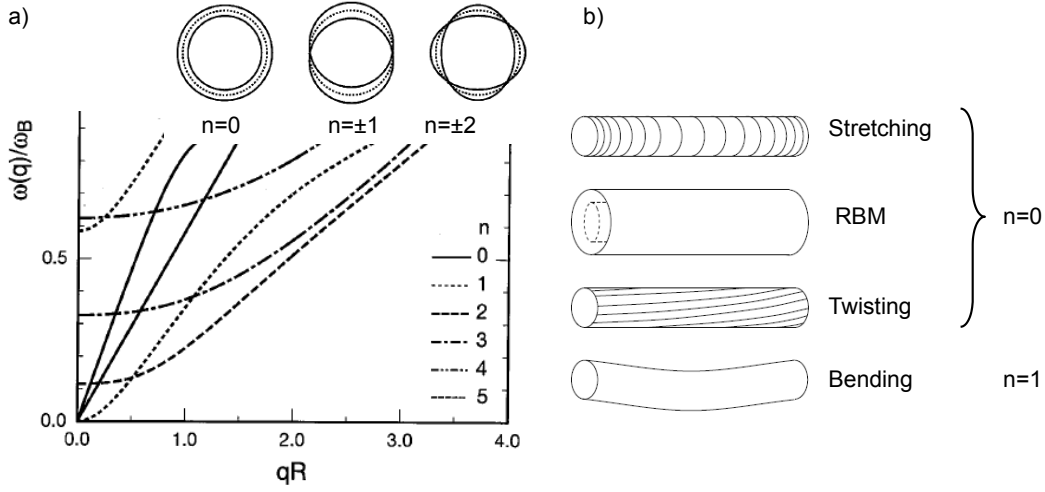


Figure 3.2: a) Dispersion of the low-energy acoustic phonons of SWNTs as calculated by Suzuura *et al.* [42] from a continuum elastic model. n refers to the quantized circumferential wave-vector of the mode, and the horizontal axis corresponds to the quasi continuous component q_z along the nanotube axis. The two modes with vanishing energies in the long wavelength limit and linear dispersions for small q_z are the stretching and twisting modes (see b)) both having $n = 0$. Note the particular quadratic dispersion of the bending mode.

The emission lineshape from isolated the two-level system we just described is a Lorentzian whose FWHM (full width at half maximum) is given by the inverse lifetime of the excited state. As mentioned above, this is in stark contradiction with our observations, since the measured lifetimes would yield PL linewidths on the order of 0.1 meV instead of the observed several meV. We therefore need to account for another broadening mechanism: pure dephasing of the excited state caused by interactions with low-energy acoustic phonons of the nanotube.

We assume that the phonon dispersion of the bare SWNT remains unaltered by the confining potential. Since no atomic bonds are formed with the embedding surfactant, we also assume that coupling to phonons of the surrounding material is negligible. Long-wavelength acoustic phonons in nanotubes are well described by a continuum elastic model, as demonstrated in [42] and [43]. Figure 3.2 (adapted from [42]) shows the calculated dispersion for an armchair (10,10) nanotube. Importantly, the modes can be classified according to their quantized circumferential component of the wave-vector (labeled n), in exactly the same way as we encountered in chapter 1 for electronic states in the zone-folding scheme. For phonon modes the meaning of this circumferential momentum can be easily visualized, as displayed in Fig. 3.2.a). Among the three $n = 0$ modes, the stretching and twisting modes have linear dispersion for long wavelengths, whereas the radial breathing mode (RBM) is a Raman active mode. It has an optical-like dispersion, with an energy ω_{RBM} at $q_z \approx 0$ linked to the nanotube diameter d by the relation:

$$\omega_{RBM}[\text{cm}^{-1}] \approx \frac{227}{d[\text{nm}]} + 7.3 \quad (3.2)$$

Acoustic phonons couple to electrons and holes through deformation potentials [42–44]. This interaction conserves momentum, both its (discrete) circumferential and (continuous) axial components, which has two important consequences. First, since our quantum dot state is formed out of E_{11} exciton states, it has $n = 0$ circumferential momentum. As long as the circumferential symmetry is not broken, it will only couple to phonon modes having also $n = 0$, namely the stretching, twisting and radial breathing modes. Second, conservation of longitudinal momentum q_z would lead to vanishing coupling to the linearly dispersive modes in the limit of free delocalized optical excitations which have $q_z \approx 0$. However, confinement in the quantum dot breaks the translation symmetry along the nanotube and results in a superposition of states with non-zero momenta of the exciton center-of-mass, as we saw in the previous section. The Gaussian envelope we wrote in real space has a Gaussian expression in reciprocal (i.e. momentum) space given by its Fourier-transform:

$$\mathcal{F}^{exc}(q) = \int dz |\Psi^{exc}(z)|^2 e^{iq \cdot z} = \exp -\frac{q^2 \sigma^2}{4} \quad (3.3)$$

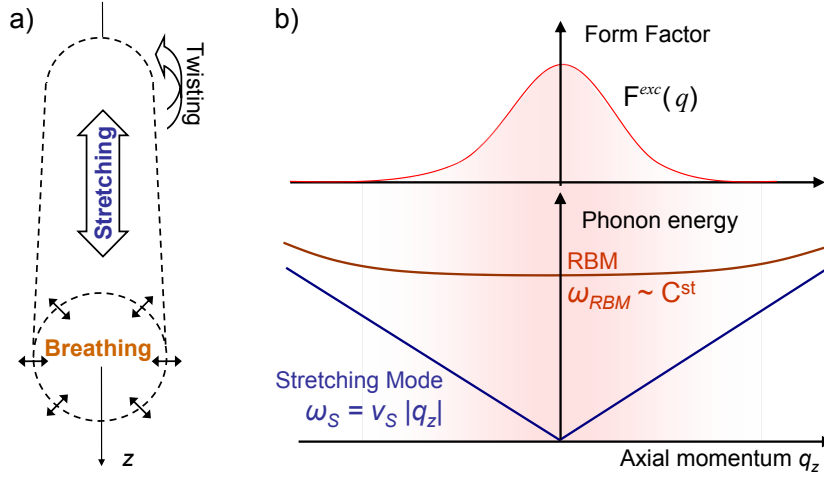


Figure 3.3: a) A pictorial view of the displacements associated with the three acoustic phonon modes having zero circumferential momentum. b) Bottom: The energy dispersions of the two phonon modes coupling to the SWNT-QD exciton, and (Top) the form-factor obtained by Fourier-transform of the confined exciton envelope. The coupling is the strongest for the smallest wave-vectors k_z .

We call $\mathcal{F}^{exc}(q)$ the form factor, and q will design from now on the axial wave-vector component q_z . We want to stress here an important point. A tighter confinement, i.e. a smaller quantum dot, translates into a broader form factor in momentum space. This consequently enables the SWNT-QD to couple to phonons of shorter wavelengths, having higher energies (see Fig. 3.3).¹ We will see that this is directly mirrored into broader PL linewidths for smaller confinement lengths.

1. A physical picture for this is the following: the effects of phonons whose wavelengths are shorter than the quantum dot size cancel out after integration over the length of the quantum dot.

Among the two modes with linear dispersion, the deformation potential of the twisting mode is calculated to be an order of magnitude smaller than the one of the stretching mode. We therefore neglect its effects in our analysis. The deformation potential couplings to the stretching and radial breathing modes can be written, respectively:

$$\mathcal{G}_S(q) = \frac{D_s \cdot q}{\sqrt{2\rho L \hbar \omega_s(q)}}$$

and

$$\mathcal{G}_{RBM}(q) = \frac{D_{RBM}}{\sqrt{2\rho L \hbar \omega_{RBM}}}$$
(3.4)

where L the length of the nanotube and ρ its linear mass density. Including the above-mentioned form factor accounting for momentum conservation, we finally get the QD-phonon coupling matrix elements:

$$g_j(q) = \mathcal{G}_j(q) \cdot \mathcal{F}^{exc}(q)$$
(3.5)

where j stands for S (stretching mode) or RBM (radial breathing mode).

3.1.3 Spin-Boson Hamiltonian

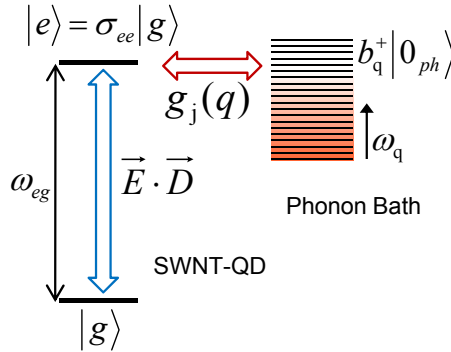


Figure 3.4: QD-phonons coupling: schematic view and notations used in the text.

We have all the ingredients we need to write the Hamiltonian of our complete system (see Fig. 3.4), which we write as a sum of four terms. Using the short notation $\sigma_{\alpha\beta} \equiv |\alpha\rangle\langle\beta|$ for the matrix elements of the two-level system, the bare SWNT-QD is represented by the term:

$$\hat{H}_0 = \hbar \omega_{eg} \sigma_{ee}$$
(3.6)

ω_{eg} is the energy of the bare SWNT-QD ground state, including all other effects than phonon interactions (DC stark shift, strain, etc.).

Then we describe the phonon bath by the term:

$$\hat{H}_{\text{bath}} = \hbar \sum_q \omega_j(q) b_{j,q}^\dagger b_{j,q}$$
(3.7)

$b_{j,q}^\dagger$ and $b_{j,q}$ are the Boson operators for creation and destruction of a phonon in the phonon branch $j = S$ or RBM with wave vector q and energy $\omega_j(q)$.

The exciton-phonon coupling derived in the previous section leads to the QD-bath interaction:

$$\hat{H}_{\text{e-ph}} = \hbar \sigma_{ee} \sum_q g_j(q) (b_{j,q}^\dagger + b_{j,q}) \quad (3.8)$$

If we restrict ourself to this system we get the Hamiltonian $\hat{H}_{\text{IB}} = \hat{H}_0 + \hat{H}_{\text{bath}} + \hat{H}_{\text{e-ph}}$. This is the Hamiltonian of the *Independent Boson Model* extensively studied for its universality in describing numerous physical situations where an effective two-level system (atom, QD, double-well potential...) interacts with a dissipative environment consisting of a bosonic bath. An extensive study of its properties was presented by Leggett *et al.* in 1987 [45]. We will come back in the last section of this chapter to interesting links of our results with respect to the different regimes characterizing the dissipations in this model.

Finally, we use the dipole approximation to write the interaction of the SWNT-QD with electromagnetic field \vec{E} :

$$\hat{H}_{\text{dip}} = \vec{D} \cdot \vec{E} (\sigma_{eg} + \sigma_{ge}) \quad (3.9)$$

Our complete Hamiltonian $\hat{H}_{\text{SB}} = \hat{H}_{\text{IB}} + \hat{H}_{\text{dip}}$ is called the Spin-Boson Hamiltonian [46].

3.2 Numerical Calculations and Fits

3.2.1 Analytical expression of the spectrum

The dephasing dynamic of the optical polarization of a semiconductor quantum dot induced by the coupling to acoustic and optical phonons was calculated by B. Krummheuer *et al.* using the same form of Hamiltonian [46] (a detailed derivation was given by A. Vagov *et al.* in [47]). They obtain an analytical expression for the line shape of the absorption spectrum by computing the linear polarization induced by a δ -like laser pulse, up to linear order in the laser field. We use their results and deduce the PL emission line shape by taking the mirror image of the absorption spectrum.

We note that the exciton-phonon interaction does not lead to a change in the occupation of SWNT-QD levels, because the interaction Hamiltonian $\hat{H}_{\text{e-ph}}$ in Eq. (3.8) commutes with the operator σ_{ee} . Therefore, this model alone does not provide for an energy relaxation mechanism. Nevertheless, the phonon coupling still contributes to the dephasing of the polarization which is called pure dephasing and can be the governing mechanism determining the spectral line shape.

The linear susceptibility $\chi(t)$ ($t \geq 0$) of the SWNT-QD in response to a δ -shaped laser pulse at $t = 0$ can be decomposed into a temperature-independent and a temperature-dependent contribution:

$$\chi(t) = -ie^{-i\tilde{\omega}t} \chi_0(t) \cdot \chi_T(t) \quad (3.10)$$

with

$$\chi_0(t) \propto i \exp \sum_q |\gamma_S(q)|^2 [e^{-i\omega_S(q)t} - 1] \quad (3.11)$$

$$\chi_T(t) \propto i \exp \sum_q |\gamma_S(q)|^2 [-n_S(q) |e^{-i\omega_S(q)t} - 1|^2] \quad (3.12)$$

We have defined $\gamma_j(q) = g_j(q)/\omega_j(q)$; and $n_j(q) = (e^{\hbar\omega_j(q)/k_B T} - 1)^{-1}$ are the phonon thermal occupation numbers (following a Bose-Einstein distribution). The bare transition energy is renormalized by a temperature independent polaron-shift into:

$$\tilde{\omega} = \omega_{eg} - \sum_{j,q} |\gamma_j(q)|^2 \omega_j(q) \quad (3.13)$$

We also include the relaxation of the excited state population with rate γ_{PL} corresponding to the measured PL lifetime:

$$\chi(t) \rightarrow \chi(t) e^{-\gamma_{PL} t} \quad (3.14)$$

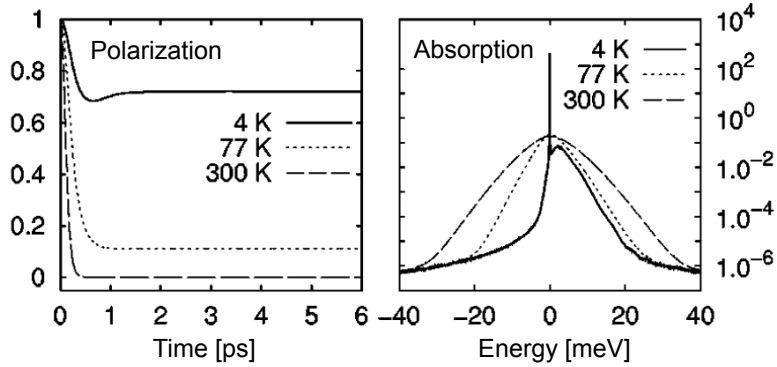


Figure 3.5: Polarization and absorption of a 3-nm quantum dot in a bulk semiconductor calculated by Krummheuer *et al.* [46]. Note the vertical logarithmic scale: the height of the sharp zero-phonon line is about 1000 times higher than the sideband.

Performing the Fourier transform of $\chi(t)e^{-\gamma_{PL} t}$ and taking its imaginary part gives the absorption spectrum of the SWNT-QD. Following the arguments of Mahan [48], the PL emission line shape that we measure is very well approximated by the mirror image of the absorption profile with respect to the zero-phonon line (ZPL).

Figure 3.5 reproduces the results of the calculation by Krummheuer *et al.* [46] for a 3-nm quantum dot interacting through deformation potential coupling with acoustic phonons of the bulk 3-dimensional matrix. There is an obvious asymmetry at low temperature, but a significant difference with our data on SWNT-QDs must be highlighted: In their results, the weight of the lifetime-broadened zero-phonon line remains overwhelming, the phonon sideband having thousands times less intensity. As we will see, the reduced one-dimensionality of the phonon bath in carbon nanotubes is the key reason explaining why we observe the complete disappearance of the ZPL.

3.2.2 Spin-Boson model in the Ohmic regime

As illustrated in Fig. 3.5 the dephasing due to acoustic phonons and the resulting sidebands also occur in more common systems where quantum dots are embedded in a bulk three-dimensional (3D) material. Such line shapes have actually been experimentally observed, for example in [49], [50] and [51]. There is however a striking difference between these line shapes and our data. In bulk semiconductor QDs, the zero-phonon line constitutes by far the dominant feature in PL at low temperature, with a linewidth close to the limit imposed by the Heisenberg uncertainty relation (i.e. lifetime-broadened). On the contrary, we will show that in the PL spectra from SWNT-QDs the oscillator strength completely goes into the sidebands, resulting in very broad and asymmetric line shapes at low temperature. Figure 3.6 presents a comparison of the line shapes obtained for 3D v.s. 1D embedding materials. In the following we formalize these observations using the framework of the independent boson model.

Restricting now the model to one acoustic mode (the stretching mode), we recall the form of the coupling term in the Hamiltonian (see Eq. (3.8)):

$$\hat{H}_{e-ph} = \hbar \sigma_{ee} \sum_q g(q)(b_q^\dagger + b_q) \quad (3.15)$$

To analyze the different dissipation regimes in the independent boson model, it is convenient to define the *spectral function* (see [45]):

$$J(\omega) = \sum_q g(q)^2 \delta(\omega - \omega(q)) \quad (3.16)$$

We define the infrared cut-off ω_I as the lowest energy bath mode effectively coupled to the two-level system. In the case of SWNT-QD it is given by the fundamental stretching mode, whose energy is inversely proportional to the nanotube length. The ultra-violet cut-off ω_U is the high energy boundary, which is for us determined by the width of the form factor. It corresponds to the shortest phonon wavelength contributing to the dissipation. Between these two boundaries, the spectral function can usually be written as a power-law:

$$J(\omega) \approx \alpha \cdot \omega^s \quad (3.17)$$

The coefficient α depends in particular on the strength of the coupling. The exponent s determines the general qualitative behavior of the dissipative system. We distinguish between three different regimes, commonly referred to as: ohmic regime, for $s = 1$, sub-ohmic when $s < 1$ and super-ohmic when $s > 1$. As can be seen from Eq. (3.16), the value of s depends on:

- The particular form of the coupling $g(q)$
- The form of the phonon dispersion $\omega(q)$
- The phonon density of states (DOS) through the weight-factor $\delta(\omega - \omega(q))$

If we consider a QD interacting through deformation potential coupling with acoustic phonons, the two first items are fully determined. The distinction between 3D and 1D systems then arises from the corresponding DOS. In 1D, the linear dispersion results in a constant non-zero DOS for long wavelength acoustic phonons,

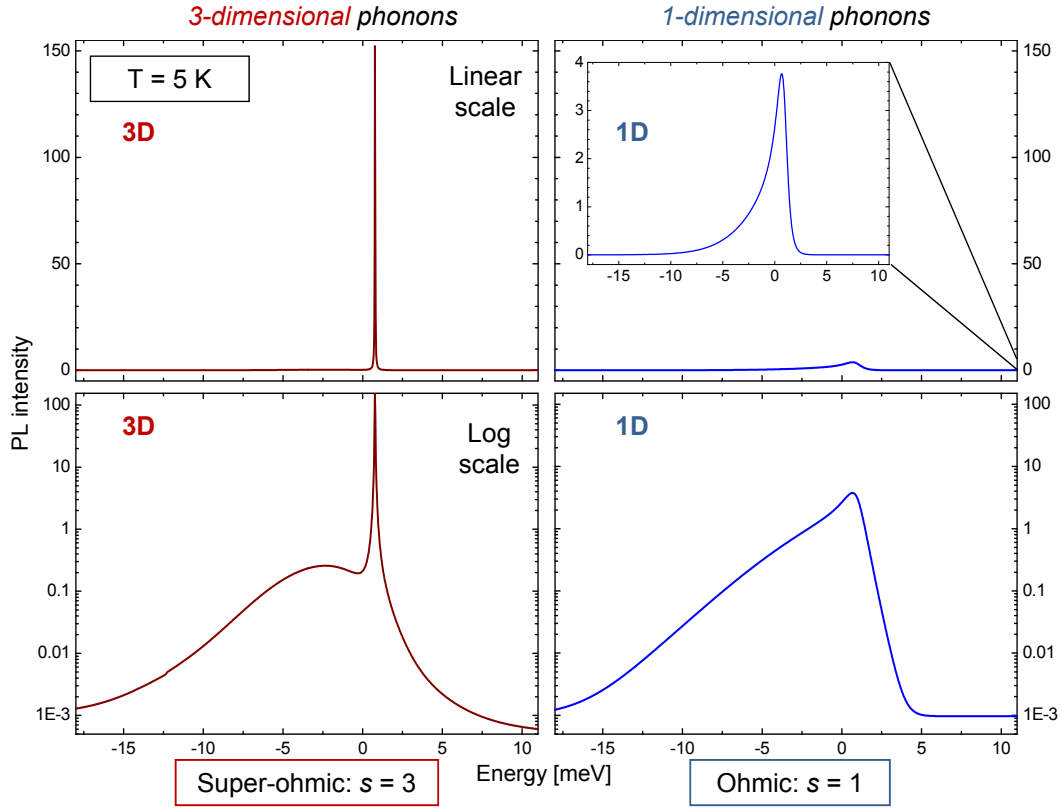


Figure 3.6: Effect of the phonon bath dimensionality on the PL line shapes. We use the same model with identical parameters to calculate the emission spectra of a quantum dot embedded in three- and one-dimensional systems. In the first case we assume a cubic QD and isotropic deformation potential coupling to bulk acoustic phonons with the same sound velocity as the stretching mode ($v_S = 19.9$ km/s). Other parameters are: $D_S = 14$ eV, $\sigma = 3$ nm, $\gamma_{PL}^{-1} = 36$ ps, $T = 5$ K. The upper plots are on a linear scale, where the 3D-phonon sideband is hardly visible. It is better seen on a logarithmic scale (bottom). In one-dimensional systems there is a dramatic suppression of the lifetime-broadened zero-phonon line; all the oscillator strength is transferred into the phonon wings.

whereas it yields a parabolic DOS in 3D. This difference directly translates into distinct exponents in the spectral function.

The common case of a QD embedded in a bulk 3D matrix corresponds to $s = 3$, i.e. the super-ohmic regime. This happens to be the most usual regime occurring in experimental realizations of the independent boson model, and also the most boring one. Indeed, when $s > 1$ the spectral function has a vanishing slope close to $\omega = 0$, meaning that the coupling to low energy modes is strongly suppressed. Therefore the sharp ZPL of the unperturbed two-level system remains unaffected by the dissipation (see Fig. 3.6, left).

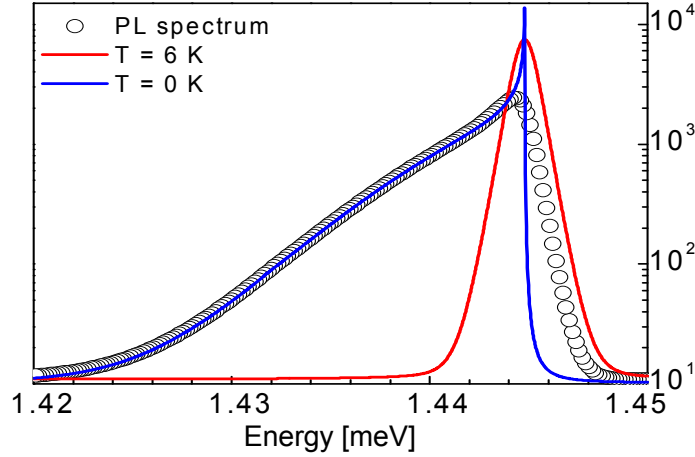


Figure 3.7: The calculated PL spectrum obtained for the fit in Fig. 3.10 (open dots) is de-convoluted to show the distinct temperature-*independent* and temperature-*dependent* contributions defined in Eq. (3.11) and (3.12). We plot in blue the spectrum derived from $\chi_0(t)$ (Eq. 3.11) and in red the one derived from $\chi_T(t)$ (Eq. 3.12). All curves are scaled to span the same integrated area. The red tail seen in the experiment is a signature of the zero-temperature pure-dephasing of the SWNT-QD optical transition. The power-law singularity of the ZPL, however, cannot be resolved in our experiment due to the thermally-induced dephasing. It may be observed at much lower temperatures.

Much more interesting is the case of 1D phonons, as in carbon nanotubes. Here $s = 1$ (ohmic regime) meaning that we have a non-vanishing coupling to low energy phonons. Even at very low temperature, dissipation occurs because of these modes and pure-dephasing of the optical transition remains extremely fast. This is directly seen in Fig. 3.7 where the persistence of the red-tail in the PL spectrum at 4 K is a signature of fast pure-dephasing in the zero-temperature limit.

Moreover, it can be shown that the Dirac function associated with the ZPL becomes under ohmic dissipation a power law singularity in the zero-temperature limit (see Fig. 3.7). What actually determines if it is possible to recover the lifetime-broadened ZPL is the infrared cut-off ω_I . Concretely, as we will develop in chapter 4.1, if we make the nanotube short enough, the fundamental phonon mode can have a non-negligible energy $\hbar\omega_I$ which can be made larger than the natural linewidth of the ZPL. In this case the effect of exciton-phonon coupling becomes similar to

what we saw for the radial breathing mode: we expect the appearance of satellite PL lines shifted from the ZPL by the phonons' energies.

Our results are of extreme significance in the study and the potential applications of quantum dots embedded in quasi one-dimensional structures. Moreover we now demonstrate that our work constitutes the first experimental observation and confirmation of the ultra-fast dephasing predicted by the independent boson model in a 1D system. It evidences the value of carbon nanotubes, the present material approaching the closest to the one-dimensional limit by its aspect-ratio, in investigating the new physics of confined systems.

3.2.3 Fits and Parameters

We use this simple model to compute the PL spectra and fit our experimental data. In this section we restrict ourself to the effects of stretching mode phonons, which are responsible for the broadening of the PL lines and their asymmetric shapes at low temperature. The effects of the RBM phonons are qualitatively different and will be treated in the next section.

Let us first expose the parameters we used for all the calculations we performed, independently of the particular nanotube spectrum being fitted. Since all the nanotubes we studied have comparable diameter $d \sim 0.8$ nm, we take the same linear mass density $\rho = 1.67 \cdot 10^{-15}$ kg/m for all of them. The sound velocity of the stretching mode phonons is $v_s = 19.9$ Km/s [42] and the exciton mass $m_{exc}^* = 0.2 \cdot m_e$ [41]. The electron-phonon deformation potential for the stretching mode is expected from calculations to lie between 9 and 30 eV [42, 43]. The only experimental value $D_S = 14$ eV has been extracted from data on low-field mobilities in semiconducting SWNTs [44]. Moreover, it should depend on the chirality of the SWNT. We therefore consider D_S as well as the confinement length σ as two nanotube-dependent fitting parameters.

Since our model is not designed to predict the band structure and excitonic energies, we naturally have to arbitrarily choose the bare SWNT-QD transition energy. We note that the large and apparently random energy shifts of the PL lines of different nanotubes under varying temperatures is not reproduced by our model. The bare transition energy has thus to be adapted for the fits at different temperatures on a same SWNT. As we mentioned previously these shifts are certainly due to local changes in the environment (see also chapter 4 for possible explanations).

We fitted the PL line shapes of about 30 different nanotubes with very successful results, as demonstrated in Fig. 3.8). The deformation potentials we found varied from 9 to 14.7 eV, consistent with the existing literature. The confinement lengths σ are between 3 and 5 nm, corresponding to a FWHM of the center-of-mass envelope function of the SWNT-QDs around 10 nm. This justifies *a-posteriori* the validity of the effective-mass approximation and the wave function envelope approach. Also, the resulting level splittings in the quantum dots range from 20 to 45 meV, in agreement with our assumption that $\Delta E \gg k_B T \approx 2.8$ meV (at 35 K).

The general fitting procedure is the following: we start by finding the best values of D_S and σ fitting the spectrum at 4 K, adjusting also the temperature T_{fit} used in the model to account for local laser heating. Even for excitation powers below

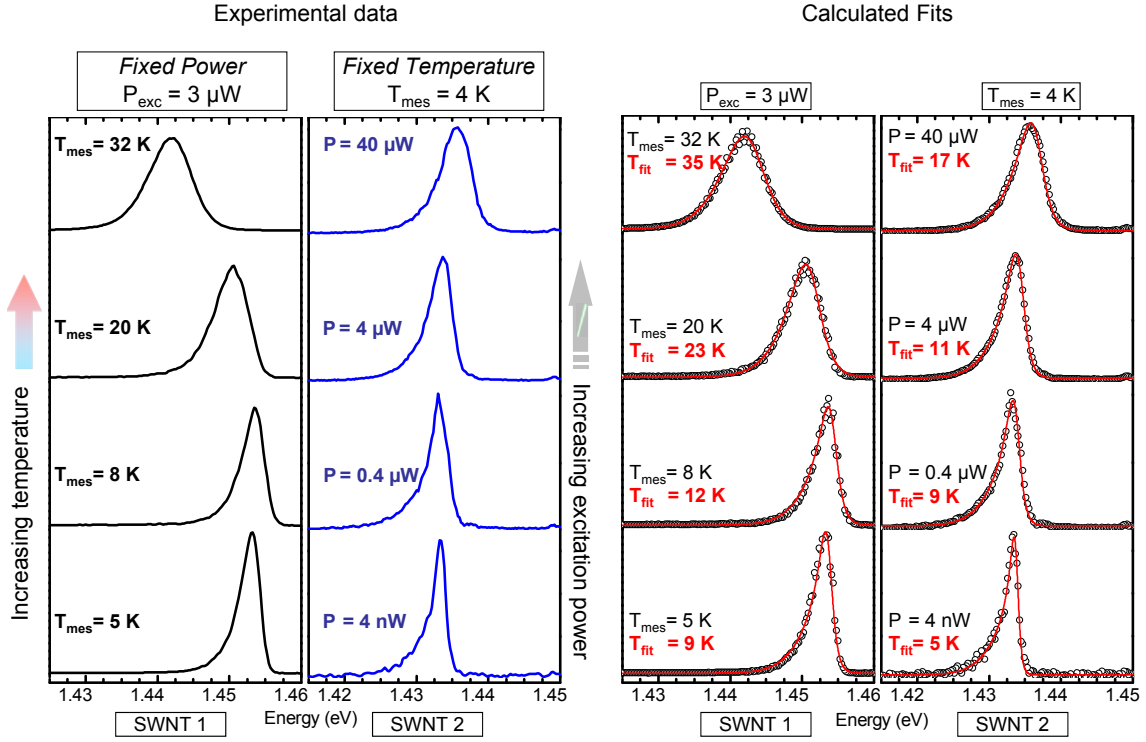


Figure 3.8: Left: experimental PL spectra for two different SWNTs. For SWNT 1, laser power is kept constant while the local temperature is increased thanks to the thermo-resistor. Inversely, the temperature is unchanged for SWNT 2 but we ramp up the laser power. Right: calculated fits to the experimental data. For each nanotube, the temperature used in the calculation T_{fit} and the bare transition energy are the only variables changed from a spectrum to another. The evolution induced by increasing the laser intensity (SWNT 2) are very well reproduced by increasing T_{fit} , suggesting local heating due to the laser. Other parameters are given in the text, apart from the deformation potentials and confinement lengths slightly adapted for each nanotube: for SWNT 1, we use $D_S = 12.7$ eV and $\sigma = 4.2$ nm; for SWNT 2 $D_S = 13$ eV and $\sigma = 4.4$ nm. Note that these values of σ correspond to a FWHM of the center-of-mass envelope function in the SWNT-QD of ~ 10 nm.

1 kW/cm² we usually find the best fit for $T_{\text{fit}} \geq 6$ K. Then we check how the evolution of the experimental PL line shape with increasing temperature is reproduced by the model, only adjusting the bare transition energy ω_{eg} . Typical series of fits for two different nanotubes are presented in Fig. 3.8. The fidelity of the fits is remarkable and very supportive of the validity of our model.

In order to better understand the role of exciton-phonon coupling in the broadening and asymmetry of the PL lines, we give in Fig. 3.9 an intuitive picture for the underlying physical process. Exciton-phonon interaction conserves energy and momentum. The latter constraint has already been considered when we noted the importance of strong longitudinal confinement to allow effective coupling to phonons with non-zero wavevectors. Provided we have a small SWNT-QD, the form factor will have a large width in reciprocal space, and momentum-conserving phonon emission (or absorption) are rendered possible through deformation potential coupling. Since energy is also conserved, the photon simultaneously emitted is detuned from the ZPL.

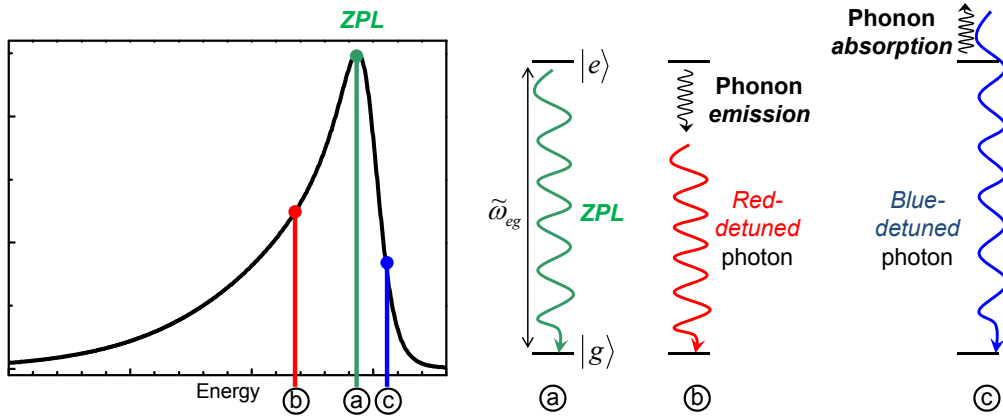


Figure 3.9: An intuitive picture of phonon-induced broadening. The shape of a typical PL spectrum at 4 K shown on the left can be explained by the contributions of phonon-assisted transitions. The red tail originates from simultaneous phonon *emission* (b) and is possible at arbitrarily low temperatures. Phonon *absorption* (c) relies on the presence of thermal phonons in the bath and is therefore unlikely at low temperature, explaining the steep high-energy shoulder in PL.

Phonon absorption results in the emission of a blue-detuned photon, and its probability scales like the phonon thermal occupation number $n_S(q)$. At the lowest temperatures, this process becomes very unlikely and we observe a steep high-energy shoulder in the PL lines. On the contrary, phonon emission probability goes as $n_S(q) + 1$ (like stimulated emission in a laser) and remains possible in the zero-temperature limit. It is responsible for the persistent red tail at low temperature. Although we restricted the discussion to first-order processes for clarity, higher-order multi-phonon emission / absorption should naturally be considered in a perturbative calculation, but the qualitative picture remains valid.

3.2.4 Radial Breathing Mode replica

We now turn to the consequences of the coupling to the Raman-active RBM phonons on the PL line shape. Following the qualitative picture just developed, we expect the photons being emitted during this interaction to be detuned from the ZPL by a fix large energy ω_{RBM} , resulting in a well separated phonon sideband. Moreover, from Eq. (3.2), $\hbar\omega_{RBM}$ is tens of meV for our nanotubes and thermal occupation is vanishingly small, so that we only expect a red-detuned sideband, even at high temperature. This large energy also makes the process quite unlikely and the intensity of the sideband is orders of magnitude smaller than the main PL line, making the experimental observation challenging.

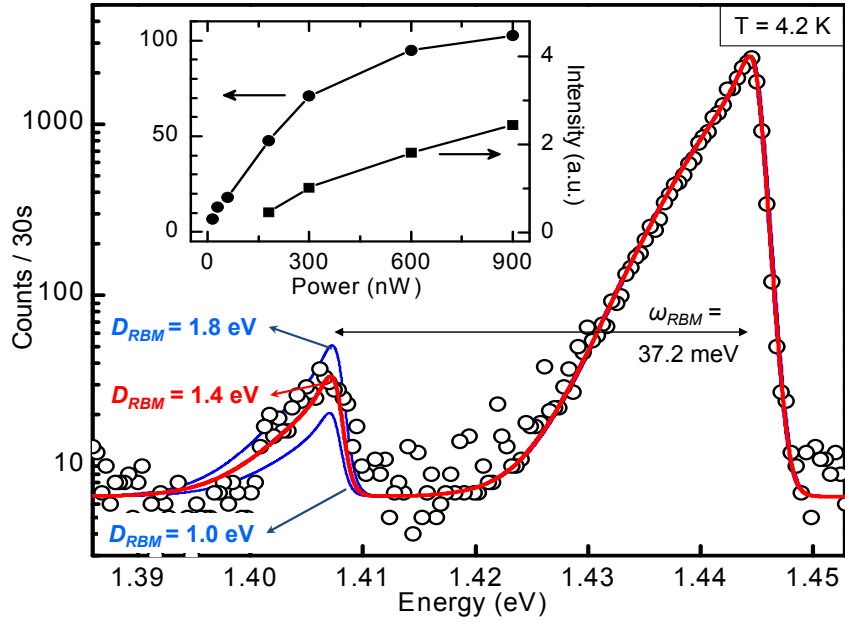


Figure 3.10: Experimental PL spectrum (open dot) and calculated PL line shape (solid red line) for a particularly bright nanotube, plotted on a vertical logarithmic scale. For the fit we used the parameters $D_S = 14$ eV, $D_{RBM} = 1.4$ eV/Å, $\hbar\omega_{RBM} = 37.2$ meV, $\sigma = 3$ nm and $T_{\text{fit}} = 6.3$ K. The blue lines show the calculations for different strengths of the QD-RBM coupling, resulting in poorer fits. The inset presents the evolution of the PL intensity from the main peak and from the replica as a function of the excitation power. Both peaks show a saturation behavior and a sub-linear increase, excluding a biexcitonic origin of the sideband (which would have a quadratic power dependence).

We were however able to find an unusually bright nanotube for which a small red-detuned satellite was detectable in PL at 4 K. Figure 3.10 displays the experimental PL data and the fit obtained from our model by including the coupling to the radial breathing mode. The two additional parameters needed are the coupling constant D_{RBM} and the RBM energy $\hbar\omega_{RBM}$. We find the best fit for $D_{RBM} = 1.4$ eV/Å, in agreement with the literature (see for example [52]). The energy detuning between the main peak and the satellite directly reflects the RBM energy and we find $\hbar\omega_{RBM} = 37.2$ meV. Using Eq. (3.2), this corresponds to a

nanotube diameter of $d \sim 0.78$ nm, exactly in the range expected for CoMoCat nanotubes with chiralities emitting at our detection wavelengths.

The blue curves in Fig. 3.10 demonstrate that the quality of the fit is very sensitive to the input value for D_{RBM} , thus allowing us to effectively measure the strength of the exciton-phonon coupling through the relative intensity of the phonon replica.

Beside the remarkable accuracy of the fit, the power dependence of the peak intensities further supports our picture of RBM replica. Emission from a bound biexcitonic state would show a quadratic increase of its intensity with excitation power, in stark contrast with what we observe (see the inset in Fig. 3.10).

3.3 Discussion and implications: Non-Markovian decoherence

The results and fits presented in the previous section and the agreement of the fitting parameters with values expected from other theoretical and experimental studies constitute strong evidences for the validity of our model. Although our work is not universal to carbon nanotubes since it applies only to confined excitons, i.e. SWNT-QDs, it does apply to any localized emitter embedded in a quasi one-dimensional structure. It has therefore far-reaching implications, ranging from quite academic issues to potential applications of nanotubes and 1-D systems in optoelectronic devices or for quantum information processing. In this section we concentrate on the effects of true acoustic modes, namely the stretching mode in nanotubes.

Quantum error correction Quantum dots, whether in bulk (3D) or one-dimensional substrates, are intensively studied for their potential applications in quantum information processing (QIP). The general idea is to use the state of the QD as a qubit, on which operations are to be carried out. Because of dephasing, the coherence of the qubit rapidly decays and successful quantum computation requires quantum error correction (QEC) schemes in order to keep error levels below a certain value ϵ , typically of order 10^{-3} . A determining quantity for the feasibility of quantum computation is thus the rate ω_{QEC} at which error correction must be carried-out in order to keep the error level below ϵ . Systems having longer coherence times demand lower correction rates and are thus better suited for QIP.

The coherence of a two-level system is given by the value of the off-diagonal elements in the density matrix, in our notation σ_{eg} . Since the dipole operator is also proportional to σ_{eg} , the decay of the polarization reflects the loss of coherence. A direct measurement of this decay is challenging, typically based on four-wave mixing experiments like in [53]. In our case, although we measure the spectral characteristics of the SWNT-QDs, we have nonetheless indirect access to the underlying dynamic of the coherence. Assuming the model we use to fit the data is correctly describing the system, we can retrieve the time evolution of the polarization as obtained from the calculations. The corresponding curves are presented in Fig. 3.11.

Of particular significance for QEC is not only the rate of the initial decoherence, but also the nature of the decay. Most error correction schemes are indeed designed assuming the Markov approximation to be valid. In this approximation, the bath

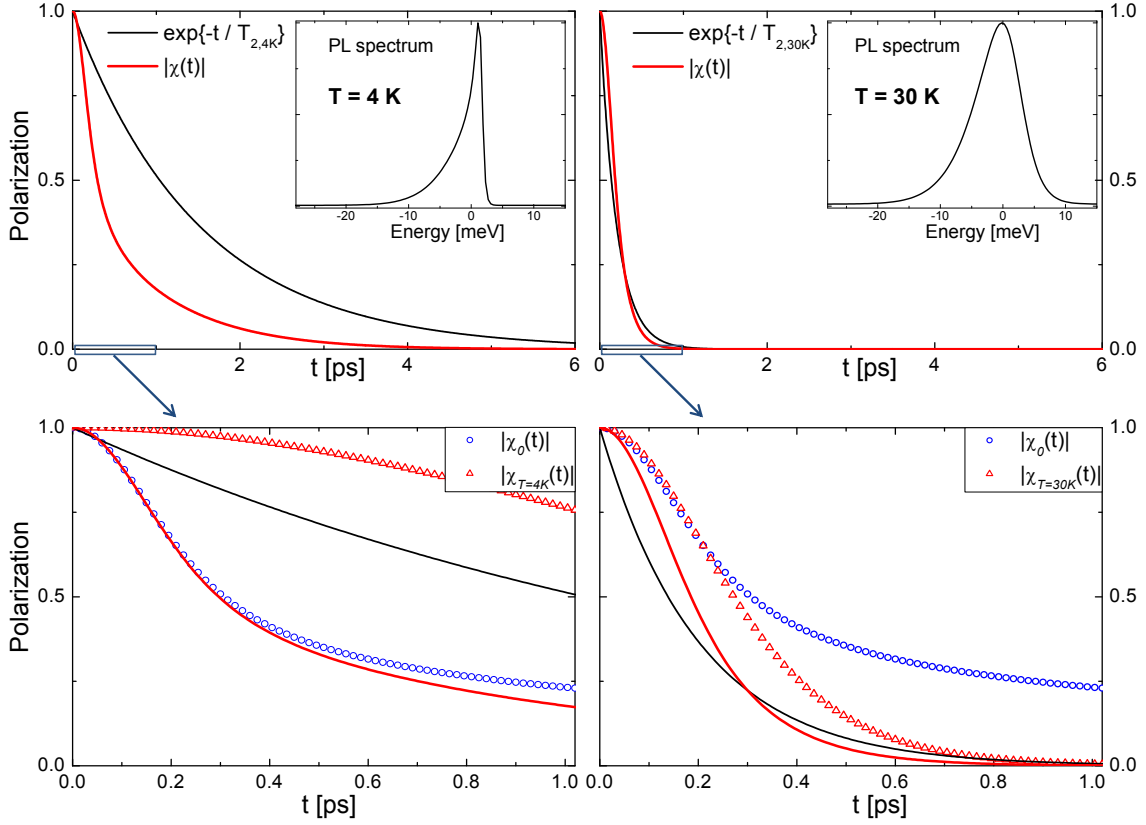


Figure 3.11: Non-Markovian decoherence of the SWNT-QD exciton. Top: the red solid lines are the calculated pure-dephasing of the SWNT-QD polarization (using Eq. 3.10 and assuming no population decay) for typical parameters $D_S = 14$ eV, $\sigma = 3$ nm, at $T = 4$ K (left) and $T = 30$ K (right). The black line is the exponential decay obtained within the Markov approximation, with $T_2(4K) = 1.5$ ps and $T_2(30K) = 0.2$ ps. The insets show the corresponding PL line shapes. Bottom: close view on the short-time decay of the polarization during the first pico-second. In addition we plot separately the temperature-*independent* (i.e. the $T = 0$ K limit) and the temperature-*dependent* contributions, as defined in Eq. (3.11) and (3.12), respectively. At $T = 4$ K, dephasing is governed by the zero-temperature component and is faster than the Markovian decay. At $T = 30$ K, however, coherence is lasting longer than expected in the Markov approximation.

causing decoherence (here the phonons) is assumed to be “memory-less”, meaning that its first-order correlation function is a delta peak $\delta_{\tau=0}$. This widely used assumption yields an exponential decay of the coherence due to pure-dephasing, with time constant T_2 . In the spectral domain, it corresponds to a Lorentzian line shape of width $\sim \hbar/T_2$. Our data from SWNT-QDs clearly show non-Lorentzian line shapes at low temperatures, which is an indication of non-Markovian decay taking place. This is indeed confirmed by the analysis of the polarization dynamic (see Fig. 3.11).

For a more quantitative estimation of the decoherence in our system and to enable a comparison with quantum dots in bulk substrates in the perspective of QIP, we follow the approach and the results recently published by R. Doll *et al.* [54]. Inspired in particular by our work, they analyzed the decoherence dynamic and required correction rates ω_{QEC} for QDs in bulk and 1D substrates, using the independent boson model. As already known, they find and confirm non-Markovian decay in 1D systems.

To go further, it is very instructive to compare the analytically computed dynamic with the one obtained in the Markov approximation. In the latest framework, master equations would give an exponential decay for short times, with a temperature-dependent dephasing time [54]:

$$T_2(T) = \frac{\hbar}{4\pi\alpha k_B T} \quad (3.18)$$

with $\alpha \sim 0.1$ defined in Eq. (3.17). In Fig. 3.11, we plot for comparison the exponential Markovian decay expected at $T = 4$ K and 30 K. First it is obvious that at both temperatures the actual decoherence is strongly non-Markovian. This is a very interesting feature arising from the reduced dimensionality of the phonon bath. But it would be a shortcut to deduce that decoherence is always faster than for Markovian dissipation.

Here the role of the “zero-temperature” pure dephasing is determinant. In the lower panels of Fig. 3.11, we plot explicitly the two contributions χ_0 and χ_T to the polarization decay (see Eqs. 3.11 and 3.12). For $T = 4$ K, the dynamic is clearly governed by $\chi_0(t)$ and the resulting decay occurs on a shorter time-scale than $T_2(4K) = 1.5$ ps. However, at $T = 30$ K, both components have similar and relatively long decay times compared to $T_2(30K)$, yielding to a longer-lasting coherence than in the Markovian case.

These results evidence on the one hand the dramatic effects of the reduced dimensionality of the substrate in the resulting loss of coherence due to QD-bath interactions. On the other hand, we see that non-Markovian decoherence is not obviously synonym for worse situation in view of QIP. In fact, the detailed calculations of R. Doll *et al.* [54] reported in Fig. 3.12 even show that QD in one-dimensional substrates allow slightly slower error correction rates than QD in three-dimensional substrates. This is always true for coupling strength α larger than 0.01. In our SWNT-QD systems we have $\alpha \geq 0.1$ (see chapter 4), which is also a typical value for QDs in bulk. Unfortunately, in both cases the required correction rates ω_{QEC} are on the order of, or larger than, the cutoff frequency $\omega_U \sim 10^{13} \text{ s}^{-1}$, as can be seen in Fig. 3.12. Although such rates may well remain out of experimental reach for

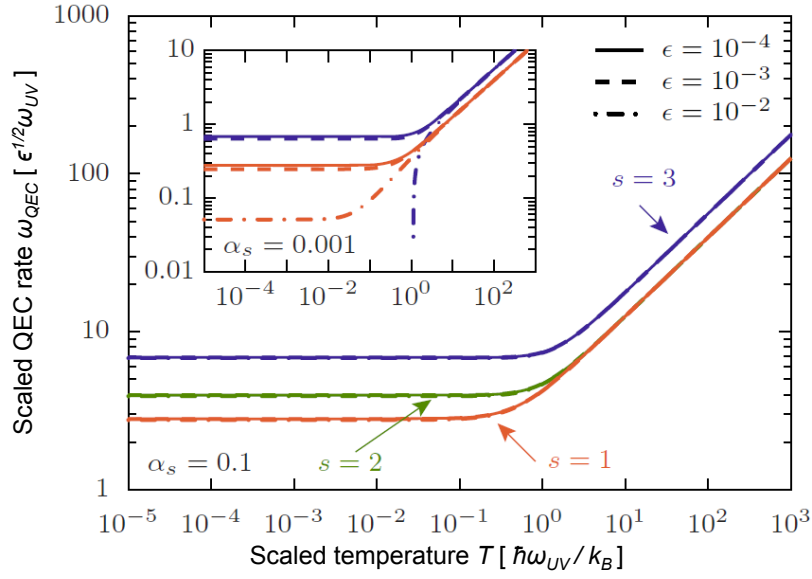


Figure 3.12: Temperature dependence of the quantum error correction rate ω_{QEC} for different spectral densities $J(\omega) = \alpha_s \cdot \omega^s$ with equal couplings α_s , and several threshold values ϵ . For coupling strengths $\alpha \sim 0.1$ actually observed in experiments, one-dimensional substrates ($s = 1$) lead to slower rates than bulk matrices ($s = 3$). Only for very low values of α could bulk systems be advantageous for QIP. As shown in the inset, when $\alpha_3 = 10^{-3}$ the coherence level never decays below 0.99 at temperatures lower than the cutoff, meaning that error correction would then become needless ($\omega_{QEC} \rightarrow 0$). Of course other dephasing processes and the population decay would eventually lead to decoherence, but on much larger time-scales.

long, other approaches, like engineering systems with smaller α or developing new correction algorithms, might enable the effective use of QDs in QIP applications.

4 Quantum-dots in Carbon nanotubes

4.1 Controlled formation and device design

4.1.1 Wave-functions and implementation of a SWNT-QD

Our goal in this first section is two-folds. First we want to give a simplified but rigorous expression of the wave-function of a confined SWNT exciton. Second we propose a practical way of confining the exciton by applying an external DC electric field.

SWNT-QD wave-functions

In order to give a more rigorous description of the wave function of an exciton confined in a small SWNT-QD, we pursue the tight-binding approach of chapter 1 further to derive an effective-mass description of the electronic states of carbon nanotubes. Based on the results and calculations of chapter 1, we can restrict our analysis to the band-edge electronic states corresponding to the two Dirac-points of graphene.

We introduce for this the following notation, $\begin{pmatrix} 1 & 0 & 0 & 0 \end{pmatrix} \cdot \Psi(\mathbf{r})$ (resp. $\begin{pmatrix} 0 & 0 & 1 & 0 \end{pmatrix} \cdot \Psi(\mathbf{r})$) corresponds to a graphene Bloch function with wave-vector \mathbf{K} (resp. \mathbf{K}') constructed from p_z orbitals of carbon atoms from the A sublattice with the phase at the origin being 1 (resp. $e^{i\theta}$). The other two spinors have a similar signification with p_z orbitals of carbon atoms from the B sublattice.

We can now consider the formation of the nanotube by folding around the chiral vector \mathbf{C}_h , imposing the periodic boundary condition on the circumferential wave-vector:

$$\exp(i\mathbf{k} \cdot \mathbf{C}_h) = 1 \Rightarrow k_\varphi = n \frac{2\pi}{C_h}, \quad n \in \mathbb{N} \quad (4.1)$$

The resulting cutting lines (Fig. 1.5) define one dimensional subbands (represented in Fig. 1.6). Conduction bands are labeled by increasing circumferential momentum $n = 0, \pm 1, \pm 2, \dots$ (idem with $n \rightarrow m$ for the valence bands). Semiconducting tubes (i.e. chiralities for which $\nu \equiv \text{mod}(n_1 - n_2) = \pm 1$) have a band gap energy corresponding to the lowest band-to-band transition $n = 0 \rightarrow m = 0$, usually called E_{11} . It can be shown that the boundary condition (4.1) leads to the following wave-functions for the band-edge states of the nanotube at K and K' :

$$|K_{n,\pm}\rangle = \frac{1}{\sqrt{4\pi}} e^{i(n-\nu/3)\varphi} \begin{pmatrix} \text{sgn}(3n - \nu) & \pm 1 & 0 & 0 \end{pmatrix} \cdot \Psi(\mathbf{r}) \quad (4.2)$$

$$|K'_{n,\pm}\rangle = \frac{1}{\sqrt{4\pi}} e^{i(n+\nu/3)\varphi} \begin{pmatrix} 0 & 0 & \text{sgn}(3n+\nu) & \pm 1 \end{pmatrix} \cdot \Psi(\mathbf{r}) \quad (4.3)$$

with \pm for conduction resp. valence states. For example, $|K_{0,+}\rangle$ is the lowest energy state for an electron in the K -valley, whereas $|K'_{1,-}\rangle$ describes a hole in the K' -valley occupying the subband with $m = 1$ ¹. Within this formalism, the complete wave-function of an exciton formed by promoting an electron to the n -band leaving a hole in the m -band can be written in the compact form:

$$|\Psi_{nm,\pm}\rangle = \frac{1}{2} \left(|K_{n,+} K_{m,-}^*\rangle \otimes |F_{nm}\rangle \pm |K'_{-m,+} K_{-n,-}^*\rangle \otimes |F'_{nm}\rangle \right) \otimes (|\uparrow\downarrow\rangle + |\downarrow\uparrow\rangle) \quad (4.4)$$

(The spin-singlet part $(|\uparrow\downarrow\rangle + |\downarrow\uparrow\rangle)$ will be omitted hereafter.) The K - K' degeneracy results in the existence of two possible excitons for each pair of bands labeled by \pm (bonding and anti-bonding combination). In particular it has been explained in chapter 1 that $|\Psi_{00,+}\rangle$ is optically allowed (bright) whereas $|\Psi_{00,-}\rangle$ is a dark exciton, absent any external perturbation or internal defect breaking the K - K' symmetry (such as a magnetic flux through tube).

The real-space envelope functions satisfy: $F_{nm}(z_e, z_h) = F'_{nm}(z_h, z_e)$. They introduce an *ad hoc* localization of the electron and hole along the nanotube axis. We shall use these envelopes to describe the binding of the electron and hole inside the exciton (with typical length scale being the exciton Bohr radius: $a_B \sim 1 - 2$ nm), on the one hand, and the externally induced confinement of the exciton center-of-mass motion, on the other hand. Thus we define the axial coordinates for the relative motion:

$$z_{eh} = z_h - z_e \quad (4.5)$$

and the exciton center-of-mass:

$$z_{CM}^{nm} = \frac{m^{(n)} z_e + m^{(m)} z_h}{m^{(n)} + m^{(m)}} \quad (4.6)$$

with $m^{(n)}$ designating the effective mass of an electron at the bottom of the n -band. Idem for the hole effective mass $m^{(m)}$, with electron-hole symmetry implying $m^{(n)} = m^{(m)}$ if $n = m$. We shall omit the indices n, m and write z_{CM} for the sake of clarity.

Confining potential

We now turn to the actual implementation of a SWNT-QD by confining the exciton along z . The difficulty here is that the exciton is a globally neutral entity which cannot be trapped in a simple potential well, created for example by modulating the Fermi-level with a back-gate. However we demonstrate that an electric field gradient along the nanotube indeed results in a trapping potential for the exciton. We note $U(z)$ the electric potential associated with the external field. If we decompose the electron and hole coordinates in the center-of-mass and relative motion components

1. As can be seen in Fig. 1.6 the next higher energy electron or hole state after $n, m = 0$ may have $n, m = 1$ as well as $n, m = -1$, depending on the valley and the value of $\nu = \pm 1$.

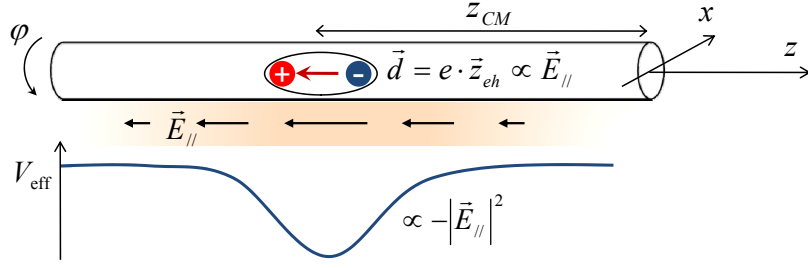


Figure 4.1: Schematic of exciton confinement by a longitudinal electric field gradient. We choose the axis z along the nanotube, x perpendicular to it, and φ is the circumferential coordinate. In an axial electric field \vec{E}_{\parallel} , the exciton becomes polarized and acquires an electric dipole \vec{d} proportional to the field strength. This dipole then interacts with the externally applied electric field, resulting in a confining potential V_{eff} proportional to the square of the longitudinal field.

(given by Eq. 4.5 and 4.6, respectively) and use the fact that $|z_{\text{CM}}| \gg |z_{\text{eh}}| \sim a_B$ for smooth confinement, we can derive the following approximation for the Hamiltonian describing the exciton-field interaction:

$$\begin{aligned}
 \mathcal{H}_{\text{int}}^{\parallel} &= e [U(z_h) - U(z_e)] \\
 &= e \left[U\left(z_{\text{CM}} + \frac{\mu}{m_h} z_{\text{eh}}\right) - U\left(z_{\text{CM}} - \frac{\mu}{m_e} z_{\text{eh}}\right) \right] \\
 &\approx e \hat{z}_{\text{eh}} \frac{\partial U}{\partial z}(z_{\text{CM}})
 \end{aligned} \tag{4.7}$$

where $e = +1.6 \times 10^{-19}$ C is the absolute value of the electron charge, and μ is the reduced mass of the exciton. We now need the form of the envelope function of the relative coordinate z_{eh} . As we mentioned in chapter 1, the exciton binding relates directly to the one-dimensional hydrogen atom problem. Using a regularized Coulomb potential to avoid infinite binding energy, one obtains for the eigenstates the 1D hydrogenic series $|l\rangle$, $l \geq 0$. The explicit form of these wave-functions is not relevant to us, but the important point is the alternating symmetry of the states: even $|l\rangle$ are symmetric upon electron-hole exchange (i.e. $z_{\text{eh}} \rightarrow -z_{\text{eh}}$) whereas states with odd l are anti-symmetric. This means that the ground state of the exciton has no dipole moment along the nanotube axis and does not interact with the field to first order in a perturbative approach. In other word, since $\langle 0 | \hat{z}_{\text{eh}} | 0 \rangle = 0$, we have to first order:

$$\langle \Psi_{nm,\pm} | \mathcal{H}_{\text{int}}^{\parallel} | \Psi_{nm,\pm} \rangle = 0 \tag{4.8}$$

To second order in perturbation theory, we obtain an effective interaction mediated by the excited states of the hydrogenic series, leading to the effective potential for the exciton:

$$\begin{aligned}
V_{\text{eff}} &\approx \sum_{l>0} \frac{|\langle l | \mathcal{H}_{\text{int}}^{\parallel} | 0 \rangle|^2}{E_0 - E_l} \approx -\alpha_X^{nm} \left(\frac{\partial U}{\partial z} \right)^2 (z_{\text{CM}}) \\
&\approx -\alpha_X^{nm} E_{\parallel}^2 (z_{\text{CM}})
\end{aligned} \tag{4.9}$$

where we have defined the quantity:

$$\alpha_X^{nm} = e^2 \sum_{l>0} \frac{|\langle l | \hat{z}_{eh} | 0 \rangle|^2}{E_l - E_0} > 0 \tag{4.10}$$

In a classical picture, the external electric field polarizes the exciton that subsequently experiences a force proportional to the field squared, as displayed in Fig. 4.1. Therefore, if we create a field gradient along the nanotube, the exciton can be trapped around the position where the field is maximal. It is legitimate to assume a parabolic confining potential close to the minimum of V_{eff} . In this harmonic potential, the ground state for the exciton center-of-mass motion is a Gaussian. Moreover, the lowest-energy state of the exciton relative motion (i.e. the ground state $|0\rangle$ of the regularized 1D hydrogenic series) is very well approximated by a Gaussian envelope as well [40]. The envelope function for each of the SWNT-QD ground states $|\psi_{nm,\pm}\rangle$ can thus be explicitly written:

$$F_{nm}(z_e, z_h) = \frac{1}{\sqrt{\pi\sigma_{\text{eh}}^{nm}\sigma_{\text{CM}}^{nm}}} \mathcal{G}(\sigma_{\text{eh}}^{nm}, z_{\text{eh}}) \mathcal{G}(\sigma_{\text{CM}}^{nm}, z_{\text{CM}}) \tag{4.11}$$

where we defined a general Gaussian function:

$$\mathcal{G}(\sigma, z) = \exp -\frac{z^2}{2\sigma^2} \tag{4.12}$$

4.1.2 Controlling the exciton-phonon coupling

As we show in the Appendix 6, carbon nanotube resonators hold promising perspective for opto-mechanical cooling. To achieve this we need an effective coupling between the quantum dot embedded in the nanotube and the relevant phonon mode. For the bending mode, this is a non-trivial issue: in a pristine unperturbed carbon nanotube, the lowest energy SWNT-QD state $|\psi_{00,\pm}\rangle$ has zero net circumferential momentum (corresponding to the E_{11} transition). In other words, electron and hole wave functions (and thus probability distributions) have rotational symmetry around the nanotube axis. The exciton is fully delocalized along the circumferential direction. On the other hand, the flexural phonon mode locally leads to compression and dilation on opposite sides of the tube, as pictorially shown in Fig. 4.2.a). The net deformation potential couplings thus cancel out. Mathematically, this is a result of circumferential momentum conservation, for the bending mode is a $n = 1$ phonon mode (see Fig. 3.2, chapter 3).

Perturbative effect of a perpendicular electric field on the QD ground state

In order to create a non-vanishing coupling between our SWNT-QD and the bending mode, we therefore need to break the rotational symmetry of the exciton, i.e. to

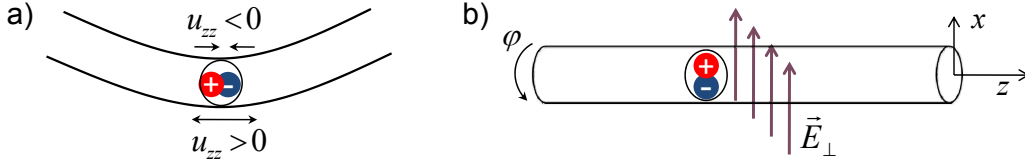


Figure 4.2: a) The bending mode leads to a local compression on one side $\hat{u}_{zz}(\hat{r}) < 0$ and an extension on the opposite side $\hat{u}_{zz}(\hat{r}) > 0$ (meaning it has one unit of circumferential momentum). In the absence of external perpendicular field, the charge distribution of the SWNT-QD states $|\psi_{00\pm}\rangle$ (with zero circumferential momentum) have rotational symmetry. Therefore the net coupling vanishes after integration of the interaction around φ (which is equivalent to say that circumferential momentum is conserved by the interaction). b) When an external electric field is applied with a component \vec{E}_{\perp} perpendicular to the nanotube (i.e. along x) it breaks the rotational symmetry by pulling apart electron and hole. The result is an effective tunable coupling of the exciton to the flexural mode

polarize the exciton in the x direction orthogonal to the nanotube axis. A natural way of doing so is to apply a strong DC electric field perpendicular to the nanotube, as presented in Fig. 4.2.b).

More precisely, we consider the effect of the perpendicular component E_{\perp} of the external electric field on $|\psi_{00\pm}\rangle$ to lowest order in perturbation theory. In principle the linear correction $|\psi_{00\pm}^{(1)}\rangle$ involves contributions from all four excitonic manifolds for which $|n| = 1$, $m = 0$ or $n = 0$, $|m| = 1$, namely E_{12} , E_{21} , E_{13} , E_{31} . Indeed, all these excitons have one unit of circumferential momentum and their interaction with the bending mode satisfies the conservation rules. They have non-vanishing exciton-phonon coupling to the bending mode. We find however that the contributions from E_{12} and E_{21} vanish identically and obtain

$$|\psi_{00\pm}^{(1)}\rangle \approx \xi \sum_l (|\psi_{-\nu 0 \pm, l}^{(0)}\rangle + |\psi_{0 -\nu \pm, l}^{(0)}\rangle) \langle F_{-\nu 0, l} | E_{\perp}(\hat{z}_e) | F_{00} \rangle \quad (4.13)$$

where $\xi = eR/2\epsilon_{\perp}(E_{11} - E_{13})$ ($R = d/2$ is the radius of the nanotube), $E_{\perp}(z) = -\frac{\partial U}{\partial x}(0, z)$, and l labels a complete set of envelope functions for the E_{13} and E_{31} manifolds.² $\epsilon_{\perp} \approx 1.6$ denotes the intrinsic relative permittivity normal to the CNT axis [58] and accounts for the so-called depolarization effect. The small diameter of the nanotube is responsible for a significant screening of the external field in the perpendicular direction.

Perturbative expression of the QD-phonon coupling

As discussed in chapter 3, since the low energy acoustic phonons in carbon nanotubes have relevant phonon wavelengths λ much larger than the SWNT radius R , they are very well described in a continuum shell model ("thin rod elasticity", TRE) [42, 59]. To the lowest orders in R/λ , the complete electron-phonon interaction reads in the four-dimensional space introduced in the previous section:

2. To estimate the energy difference $E_{11} - E_{13}$ we use as a guideline the analysis in Refs. [55–57].

$$\mathcal{H}_{\text{e-ph}} = \begin{pmatrix} \hat{H}_{DP}^{(1)} & \hat{H}_{DP}^{(2)} & 0 & 0 \\ \hat{H}_{DP}^{(2)*} & \hat{H}_{DP}^{(1)} & 0 & 0 \\ 0 & 0 & \hat{H}_{DP}^{(1)} & -\hat{H}_{DP}^{(2)*} \\ 0 & 0 & -\hat{H}_{DP}^{(2)} & \hat{H}_{DP}^{(1)} \end{pmatrix} \quad (4.14)$$

The diagonal term is the “true” deformation potential coupling:

$$\hat{H}_{DP}^{(1)} = g_1 [\hat{u}_{\varphi\varphi}(\hat{r}) + \hat{u}_{zz}(\hat{r})] \quad (4.15)$$

It corresponds to a shift of the Fermi energy proportional to the local change in surface area of the nanotube lattice. Because of electron-hole and K - K' symmetry this term alone does not lead to any finite coupling to the exciton. Non-zero coupling only arises from the off-diagonal part of this Hamiltonian:

$$\hat{H}_{DP}^{(2)} = g_2 e^{3i\theta} [\hat{u}_{\varphi\varphi}(\hat{r}) - \hat{u}_{zz}(\hat{r}) + 2i\hat{u}_{\varphi z}(\hat{r})] \quad (4.16)$$

with $\hat{u}_{ij}(\hat{r})$ the corresponding Lagrangian strain. Both compressional and flexural deformations have the structure of a local stretching so that the strain components satisfy $u_{\varphi z} = 0$, $u_{\varphi\varphi} = -\sigma u_{zz}$; with

$$u_{zz} = -R \cos \varphi \frac{\partial^2 \phi_f}{\partial z^2} \quad (4.17)$$

for flexural modes and

$$u_{zz} = \frac{\partial \phi_c}{\partial z} \quad (4.18)$$

for compressional modes where $\phi_{f/c}$ are the 1D fields introduced in [60] and $\sigma \approx 0.2$ is the SWNT Poisson ratio [61, 62]. Then Eq. (4.13), the aforementioned approximation for $|\psi_{00\pm}^{(1)}\rangle$, and the single particle Hamiltonian (4.16) allow us to obtain the lowest order contributions in the electric field to the interaction Hamiltonian $\mathcal{H}_{\text{e-ph}}$ between the exciton states $|\psi_{00\pm}\rangle$ of the SWNT-QD and low frequency phonons

$$\langle \psi_{00\pm} | \mathcal{H}_{\text{e-ph}} | \psi_{00\pm} \rangle = -2\nu g_2 (1+\sigma) \cos 3\theta \times \langle F_{00} | \left[\frac{\partial \hat{\phi}_c}{\partial z}(\hat{z}_e) + \xi R \frac{\partial^2 \hat{\phi}_f}{\partial z^2}(\hat{z}_e) E_{\perp}(\hat{z}_e) \right] | F_{00} \rangle$$

where we have exploited the completeness of $\{|F_{-\nu 0, l}\rangle\}$.

The most important point to note in Eq. (4.19) is the effective coupling we obtain to the flexural mode (through the second derivative $\frac{\partial^2 \hat{\phi}_f}{\partial z^2}(\hat{z}_e)$) which is proportional to the perpendicular component of the external electric field $E_{\perp}(\hat{z}_e)$. We have thus demonstrated that our scheme enables a tunable interaction between the SWNT-QD and the bending mode phonons of the suspended nanotube.

4.1.3 Device proposal and simulations

Let us summarize the results of the two previous sections: we have shown first that the exciton can be confined along z by the application of a longitudinal electric field gradient E_{\parallel} , and that the confining potential is proportional to $-E_{\parallel}^2(z_{\text{CM}})$ (see Eq. 4.9). Then we have proved that a tunable interaction between exciton and flexural phonons can be achieved, with a strength proportional to the perpendicular component of the external field.

Device geometry

The question that arises now is: how to implement the above-mentioned features in a device, allowing independent control over the confinement and over the QD-phonon interaction? The answer we propose is to use a double-tip configuration, as shown in Fig. 4.3. We consider a nanotube suspended over a narrow trench (we will comment on the width later) and two sharp conducting tips approaching the tube from both sides in its central part. Both sides of the trench are grounded whereas the potentials V_1 and V_2 are applied to the top (resp. bottom) tip.

It is then easy to see that the field component E_{\parallel} along the nanotube depends only on the symmetric combination $\frac{1}{2}(V_1 + V_2)$ whereas the perpendicular component is determined by the potential difference between the tips $\frac{1}{2}(V_1 - V_2)$. This versatility in controlling independently the confinement length and the strength of the QD-phonon coupling would constitute a huge experimental advantage, and it gives a realistic support to the following calculations.

We note here that the device is completely symmetric upon reflection about a central plane orthogonal to the nanotube containing the tips' axis. Therefore, the confining potential will have the shape of a double-well, with one QD formed on each side of the middle point of the nanotube. However, since the distance between these two wells (~ 40 nm) is much shorter than the wavelength of the light tuned on the QD transition (typically on the order of $1 \mu\text{m}$), only the bright linear combination of the two QD states is relevant in our study. This remark is yet of importance for the correct estimation of the coupling strength, for example, when a factor of 2 could easily be forgotten.

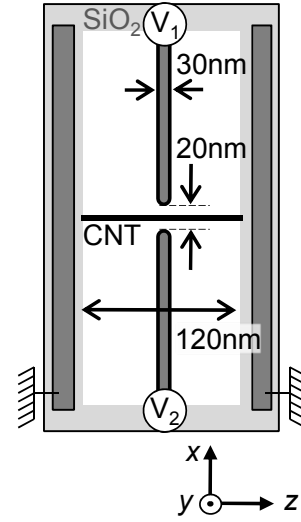


Figure 4.3: Schematic view of the device we envision.

Finite element method

In order to validate this proposal, to determine the optimal dimensions of the device, and to obtain figures for the confinement and the QD-phonon coupling along with the required potentials to be applied to the tips, we performed finite element method (FEM) numerical simulations. We used the electrostatics module available in the commercial FEM software COMSOL (version 3.5a) within the Multiphysics package. A completely faithful simulation of the 3D geometry of the device is very demanding and would require defining boundary conditions at infinity along the y direction (Fig. 4.3). Instead we approximate the real device by a cylinder with revolution symmetry around the tips (the symmetry axis is shown in Fig. 4.4). We also checked that the chosen vertical x dimension of the trench (typically 500 nm) is large enough so that the field distribution around the nanotube does not depend on its particular value.

After having defined the geometry and the boundary conditions corresponding to the device we want to simulate, the next step is to construct an adequate mesh. In addition to automatically refining the mesh around angles and curved surfaces,

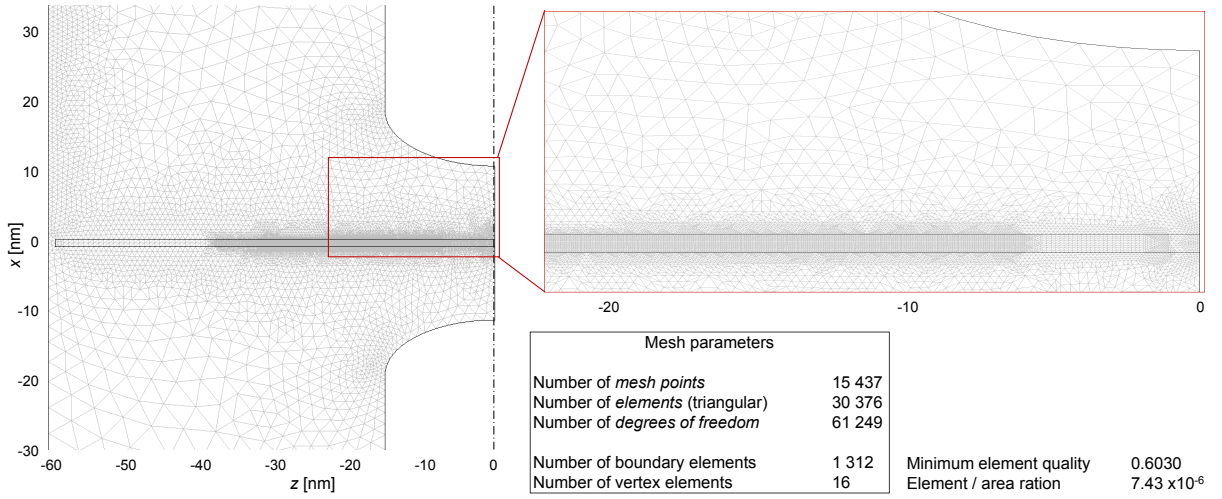


Figure 4.4: View of the mesh used in the FEM simulations. The entire device extends between $x = -500$ nm and $x = +500$ nm to exclude any dependence of the field around the nanotube on this dimension. The view is restricted to the region of interest, with a zoom-in on the refined mesh in the central part. The higher mesh density gives a better resolution when plotting the relevant quantities along a cross-section of the nanotube, as in Fig. 4.5. We also show the mesh parameters as reported by COMSOL. The element quality can take values between 0 and 1.

COMSOL offers the possibility to reduce locally the mesh size. Since we want to obtain detailed knowledge of the field only along the nanotube, we take advantage of this feature to increase the mesh density around the central part of the nanotube and the tip ends, without considerably slowing the calculation of the complete field distribution. Figure 4.4 displays the mesh used in the final simulation along with important parameters.

Finally, the Poisson equation is solved over the entire domain on the constructed mesh. The result of the calculation is the static electric field distribution in the device created by the applied potential to the tips. From this, all quantities of interest, for example V_{eff} along the nanotube axis, can be obtained and plotted.

Device's characteristics optimization

The particular shape of the tips, their diameters and the width of the gap between them all critically affect the field pattern and strength. The most time-consuming work was therefore to optimize these parameters by running a number of simulations. But what is the quantity to optimize in first place? Because of the screening of the perpendicular electric field in the nanotube, and the perturbative origin of the tunable exciton-phonon coupling, reaching the interaction strength between the QD and the flexural phonons for efficient opto-mechanical cooling requires very large perpendicular field E_{\perp} around the SWNT-QD position z_0 (on the order of $200 \text{ V}/\mu\text{m}$). On the other hand, the highest value of the electric field E_{max} will always occur close to the sharp tip ends, and care must be taken that no electric breakdown occurs. This is expected to happen for fields larger than a few V/nm .

Some useful heuristic considerations serve as a guide in the optimization process. In particular, the position of the confining potential minimum along the nanotube should satisfy $|z_0| \sim w$ where w is the gap between the tips. This position does not depend much on the numerical values of the applied potentials. As a result, the ratio $E_{\perp}(z_0)/E_{\max}$ is virtually constant for a given geometry, regardless of the particular values of the potential on the tips. We thus have a methodology for the optimization procedure: we choose a fixed potential configuration (preferably close to the one we expect to be eventually required) and vary the tips' shape, diameter d and gap w in order to maximize the ratio $E_{\perp}(z_0)/E_{\max}$. The best device should allow to apply the maximal perpendicular field on the SWNT-QD without electrical breakdown; therefore maximizing this ratio is our goal.

The results of the final “fine tuning” of the device dimensions is presented in the following table:

Diameter d [nm]	Gap width w [nm]	z_0 [nm]	$E_{\perp}(z_0)/E_{\max}$
30	15	21	0.304
30	18	21	0.315
30	21	21	0.319
30	24	22.5	0.282
30	27	23.25	0.260
30	27	23.25	0.260
33	18	23.25	0.313
33	24	24.75	0.288
36	21	25.5	0.301
27	18	19.5	0.294
27	24	21	0.263
24	21	19.5	0.257

The best ratio is obtained for a tip diameter $d = 30$ nm and a gap of $w = 21$ nm, values that we used for the simulation in Fig. 4.4 and 4.5.

The results of the FEM simulation for this optimized geometry and realistic parameters are summarized in Fig. 4.5.

4.2 Unintentional confinement induced by a charged impurity

4.2.1 Introduction and physical model

As we have demonstrated in chapters 2 and 3, we have several reasons to think that the antibunched PL, featuring broad and asymmetric line shapes, observed at low temperature, originates from strongly confined excitons. We further deduce

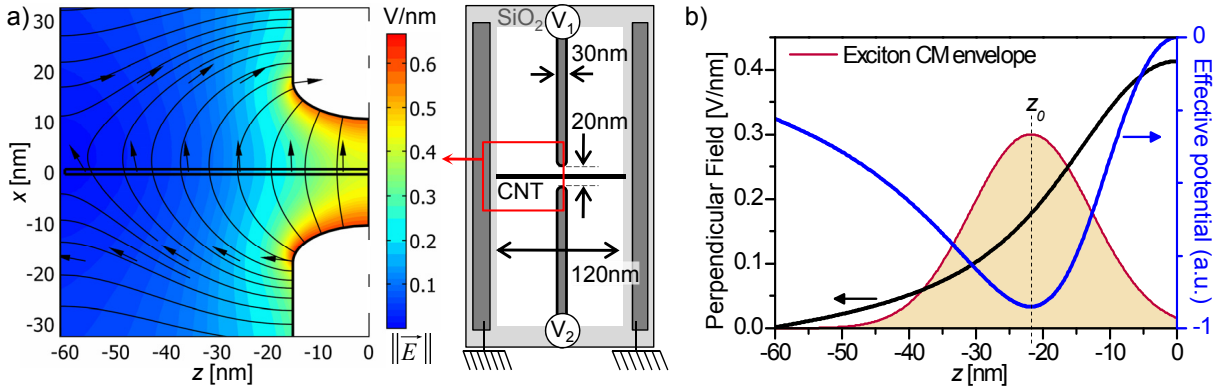


Figure 4.5: Results of the FEM simulations for the optimized tip geometry and the potentials $V_1 = -4.5$ V, $V_2 = +5.5$ V. a) Electric field magnitude (color scale) and field lines (field direction given by the arrows) in the region close to the tips' ends. b) Cross-sectional plot along the nanotube axis of $E_{\perp}(z)$, V_{eff} and the corresponding Gaussian envelope of the exciton center-of-mass motion, obtained after a parabolic approximation of V_{eff} around z_0 .

from the width of the spectra that the confinement length scale should be on the order of a few nanometers only. Finally, spectral diffusion, line splitting, large energy shifts with temperature, etc. all indicate a high sensitivity of the SWNT-QD to its environment.

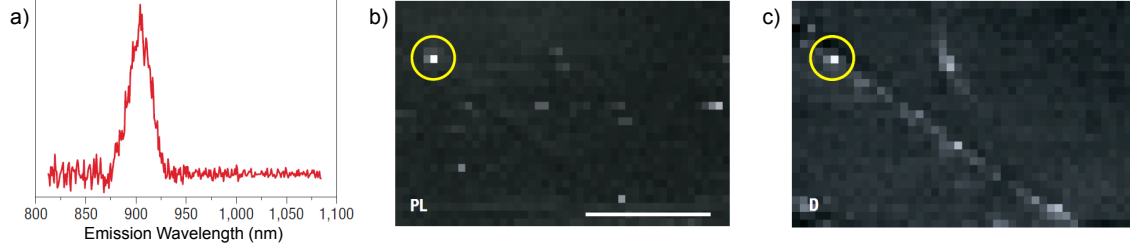


Figure 4.6: Observation of localized PL from a negatively charged defect by Indhira O. Maciel *et al.* [63]. a) Photoluminescence emission from the emissive spot. The nanotube chirality is attributed to be (9,1). Note the slight blue detuning of the PL (central emission at 904 nm) compared to the expected emission wavelength of 912 nm for a (9,1) SWNT. b) Near-field photoluminescence image of the SWNT revealing localized excitonic emission. The scale bar denotes 250 nm. c) Near-field Raman imaging of the same SWNT, where the image contrast is provided by spectrally integrating over the defect-induced D bands. Independent analysis of the high energy G' raman peak reveals that the defect is negatively charged.

The unintentional confinement of carriers in carbon nanotubes has been observed by many other groups, mainly in transport experiments through the observation of Coulomb blockade. A recent example is the finding by Li *et al.* that DNA-wrapped carbon nanotubes naturally split in an array of consecutive quantum dots [64]. Another powerful technique for such investigations is optical near field spectroscopy, mainly lead by the group of Achim Hartschuh in Munich. In a collaboration with other groups, they reported in 2008 in *Nature Materials* [63] that PL emission

from CVD-grown nanotubes was localized on a single negatively-charged defect (see Fig. 4.6). Their spatial resolution put an upper bound on the trap's size to 25 nm. Simultaneous Raman scattering measurements enabled them to reveal the presence of the negatively-charged defect at the very same position.

This last observation is of uppermost interest for us. First of all we may just be in the very same situation and see PL from intrinsic charged defects in the nanotubes. This is nonetheless hard to prove with our data and remains a speculative statement. But this report also emphasizes on the role that a charged impurity in the close vicinity of the nanotube may play in inducing exciton confinement and localized PL. We presented in chapter 2 how we fabricated our sample. The zirconium solid-immersion lens is functionalized by a polyisin monolayer to enable strong binding of the micelles. The interaction occurs between oppositely charged interfaces, so that the presence of trapped charged impurities around the micelles is indeed very likely. Another possibility could be the charging of the substrate itself under laser illumination, as was reported by Freitag *et al.* [65].

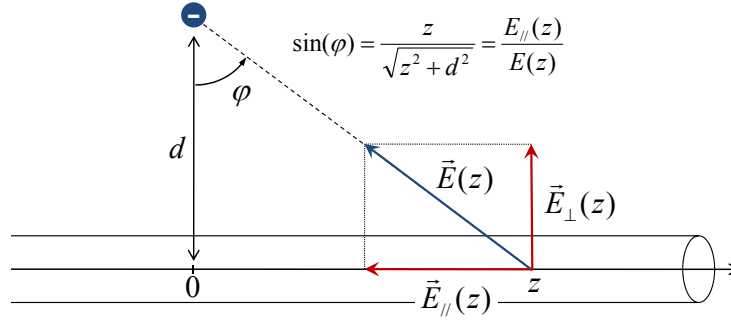


Figure 4.7: Sketch of a charged impurity trapped in the close vicinity of a SWNT at a distance d from its axis. The origin of the z axis (along the nanotube) is set at the impurity position.

On the light of these encouraging remarks, we would like to propose in this chapter a model that could account for all the peculiar experimental features we have reported so far (strong exciton localization, spectral shifts, line splitting, resonant p -shell excitation, etc.). In addition, this will naturally lead us to consider an alternative origin for the lineshape's asymmetry and width by invoking the coupling to the bending mode phonons, which results in a sub-ohmic dissipation regime. We will show in the second part that we can also fit the data very accurately within this assumption.

Figure 4.7 displays a schematic view of the physical situation we consider throughout this chapter. A charged impurity is supposed to be trapped close to the nanotube, at a distance d (typically a few nanometers) from its axis. To fix the ideas we will take the charge to be a single negative one: $q = -e$. We also take into account the screening of the field in the surfactant micelle through the relative permittivity $\varepsilon_S = 2$. The impurity position along the nanotube axis defines the origin $z = 0$.

The electric field caused by the charge at a position z along the carbon nanotube is then:

$$E(z) = \frac{-e}{4\pi\epsilon_S\epsilon_0} \frac{1}{z^2 + d^2} \quad (4.19)$$

where $\epsilon_0 \approx 8.8 \times 10^{-12}$ C/(Vm) denotes the vacuum permittivity. The axial component of the field (i.e. along the nanotube axis) is:

$$E_{\parallel}(z) = \frac{-e}{4\pi\epsilon_S\epsilon_0} \frac{z}{(z^2 + d^2)^{3/2}} \quad (4.20)$$

4.2.2 Calculation of the confinement potential

We showed in section 4.1 that the exciton experiences a force proportional to the square of the electric field axial component. As a result it is trapped at the field maxima. More precisely, we derived an effective potential:

$$V_{\text{eff}}(z) = -\alpha_X E_{\parallel}^2(z) \quad (4.21)$$

where $z = z_{\text{CM}}$ is the center of mass coordinate of the exciton, and:

$$\alpha_X \approx 2 (4\pi\epsilon_{\parallel}\epsilon_0)\sigma_X^3 \quad (4.22)$$

Here $\sigma_X \sim 1.5$ nm is the exciton Bohr radius and $\epsilon_{\parallel} \sim 7$ is the relative longitudinal permittivity along the carbon nanotube. With these numbers we obtain: $\alpha_X \approx 10^{-35}$ C.m²/V.

Panel (a) in Figure 4.8 presents the calculated longitudinal field profiles created by a single negatively charged impurity for two possible values of the distance d . Note the exact analogy of this situation to the one described in section 4.1 where we considered the double-tip device. The main difference resides in the length scales being roughly an order of magnitude smaller. The associated effective trapping potential is shown below in panel (b). We find a double-well potential whose depth V_{eff}^0 strongly depends on the distance d .

To find an analytic expression to the position of the potential minima $\pm z_0$ we solve the equation:

$$\frac{\partial}{\partial z} E_{\parallel}^2(z) = \frac{2z(d^2 - 2z^2)}{(z^2 + d^2)^4} = 0 \quad (4.23)$$

and find $z_0 = \pm d/\sqrt{2}$ ³. These are also mentioned in Fig. 4.8 (b) and depend linearly on d .

For each of these wells we can do, to lowest non-zero order, the parabolic approximation around $z = \pm z_0$:

$$V_{\text{eff}}(z) \approx \frac{1}{2} V'' z^2$$

with $V'' \doteq \frac{\partial^2}{\partial z^2} V_{\text{eff}}(z) |_{z=z_0}$. Within this approximation, the zero-point center of mass motion, in other word the confinement length of the exciton, is given by:

$$\sigma_{\text{CM}} = \frac{\sqrt{\hbar}}{(m_{\text{exc}} V'')^{1/4}}$$

3. The third solution $z = 0$ corresponds to a maximum of the potential.

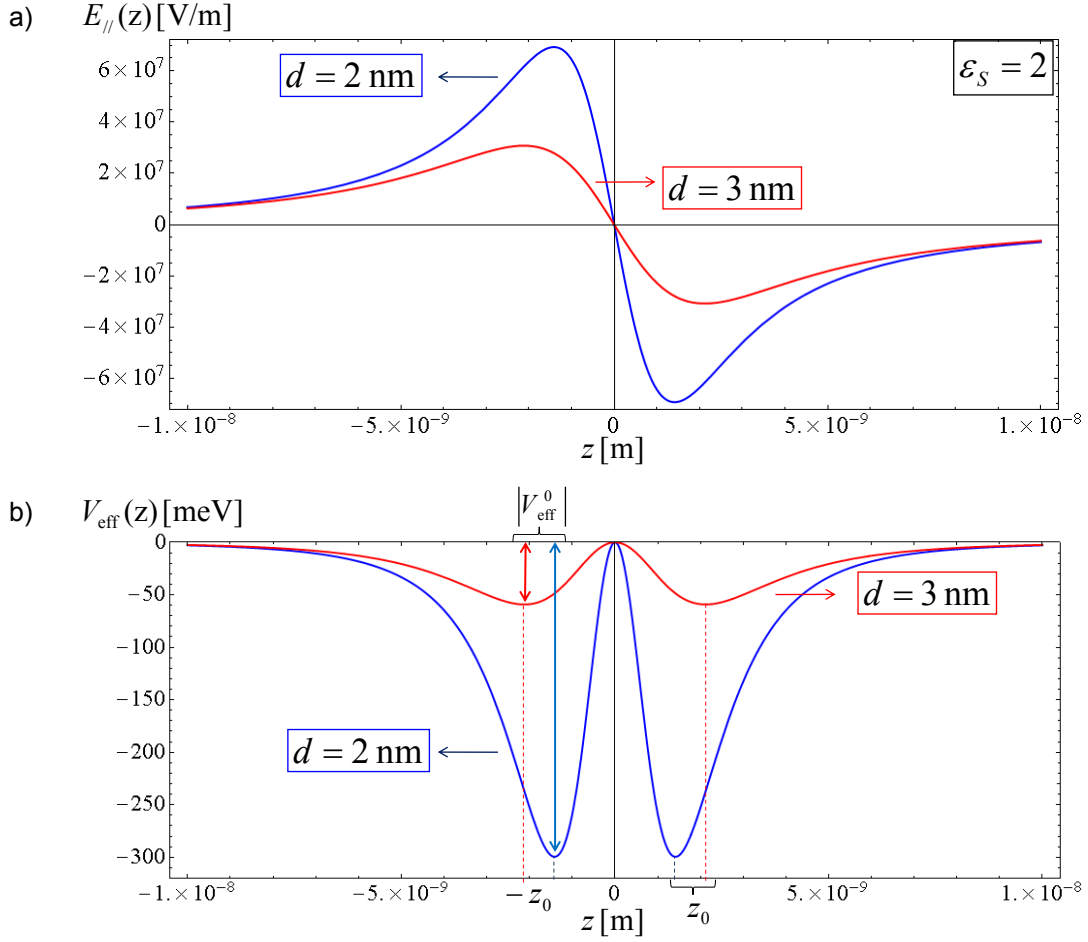


Figure 4.8: (a) Parallel field and (b) effective exciton confinement potential caused by a charged impurity residing at a distance d from the nanotube axis. We fix the relative permittivity of the surfactant micelle to $\epsilon_S = 2$. For the red curves $d = 3$ nm and the potential $V_{\text{eff}}(z)$ has its maximal depth $V_{\text{eff}}^0 \sim -60$ meV at $z_0 = d/\sqrt{2} \sim 2.1$ nm. The blue curves show the calculations for $d = 2$ nm, yielding $V_{\text{eff}}^0 \sim -300$ meV and $z_0 \sim 1.4$ nm.

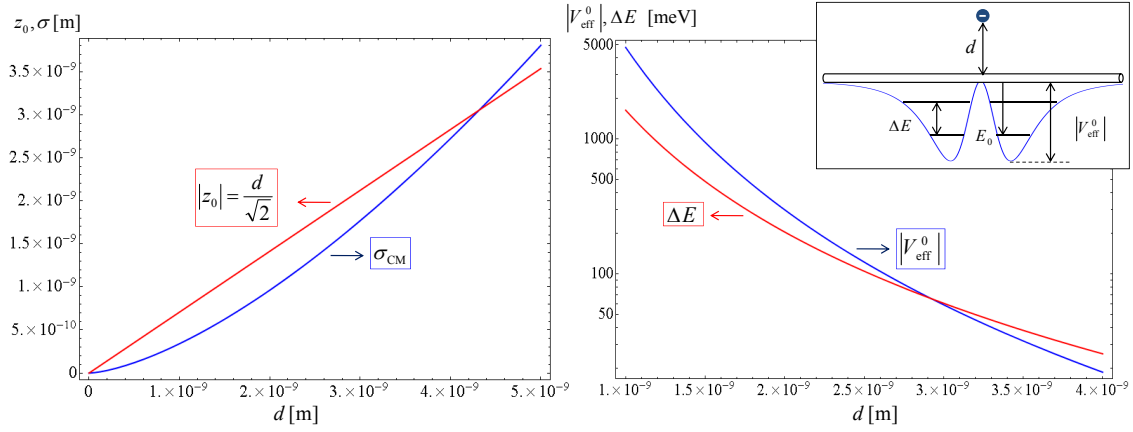


Figure 4.9: Left: Exciton center of mass zero-point motion σ_{CM} and position of the potential minimum z_0 as a function of the nanotube-charge distance d . Both lengths are comparable, justifying the assumption that tunneling between the two wells should lead to strong mixing. Right: Potential depth $|V_{\text{eff}}^0|$ and QD-levels energy splitting ΔE (in meV) as a function of the distance d , on a logarithmic vertical scale.

The effective mass of the exciton is taken to be: $m_{\text{exc}} \sim 0.2 m_e \sim 2 \times 10^{-31}$ Kg. We plot in Figure 4.9 (left panel) the calculated evolution of σ_{CM} with the distance d , along with the trap's center position z_0 . There are two important remarks to make regarding these quantities:

- For a charged impurity trapped somewhere around the micelle, the distance d will be a few nanometers, and so will be the confinement length of the exciton, in agreement with the values derived from the fits of the experimental data in chapter 3.
- For the whole range of distances considered here we have $|z_0| \sim \sigma_{\text{CM}}$. This means that tunneling between the two wells will be quite strong and couple efficiently the two identical quantum dots. As a result we should expect the eigenstates of the system to be bonding and anti-bonding superpositions of single-dot states. For a perfectly symmetric potential only one of those would be optically active and emitting PL. But a breaking of the symmetry would lift the degeneracy and lead to the formation of two non-degenerate partially bright quantum dot states.

On the right part of Fig. 4.9, the calculated potential depth $|V_{\text{eff}}^0|$ and the level splitting $\Delta E = \frac{1}{2m_{\text{exc}}} \left(\frac{\hbar}{\sigma_{\text{CM}}} \right)^2$ are plotted against d . Here again, we would like to point out important characteristics:

- For all distances d contemplated we find that $|V_{\text{eff}}^0| \gg k_B T \sim 0.32$ meV at 4 K. Therefore the potential is always deep enough to trap the exciton at cryogenic temperatures and up to several tens of Kelvin.
- The dependence of $|V_{\text{eff}}^0|$ on d is extremely steep. It is easy to see from the analytical expressions that it is proportional to $1/d^4$.
- The level energy splitting ΔE on the other hand scales like $1/d^3$. We see that the first quantum dot excited state (referred to as the “ p -shell”) is expected to lie some tens to hundreds of meV above the ground state.

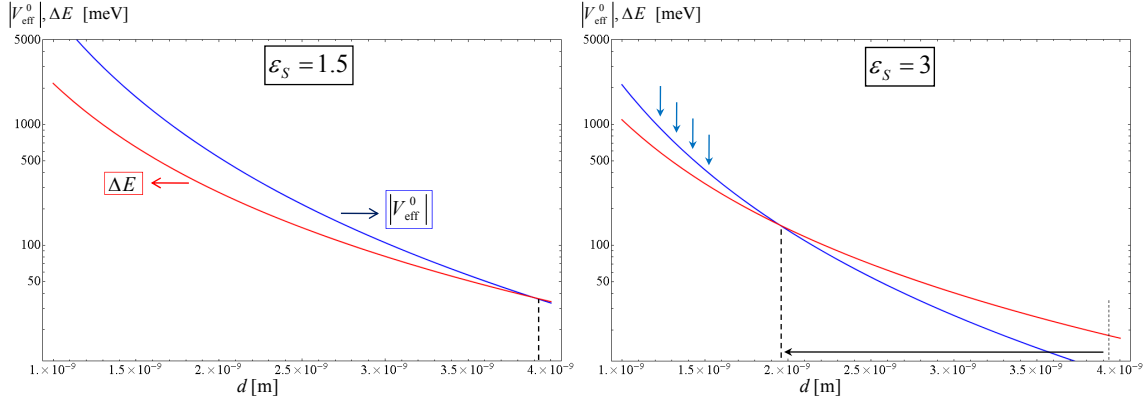


Figure 4.10: Potential depth $|V_{\text{eff}}^0|$ and level splitting ΔE as a function of the distance d , for two slightly different values of the relative permittivity of the surfactant micelle. Increased screening yields much shallower potential (at equal d) whereas the confinement length determining the level splitting is hardly affected.

- Because of the different scaling exponents we observe a cross-over of the two curves for $d \sim 3$ nm. Strictly speaking this means that for $d > 3$ nm the first excited state would already be in the continuum. However, we must remark that the position of this crossing is strongly dependent on the value of the relative permittivity chosen for the surfactant micelle, as illustrated in Fig. 4.10. Indeed, the potential depth is proportional to the square of the field strength, and therefore scales like $1/\varepsilon_S^2$. In contrast the level splitting is a function of the curvature of the potential around $\pm z_0$ (through σ_{CM}) and is much less sensitive to variation in ε_S . Given the simplicity of our model and the approximations we make, we should not however give too much relevance to these features, but rather concentrate on qualitative behaviors and orders of magnitude.

4.2.3 Comparison with the experimental observations

We now wish to discuss in more detail some peculiar experimental features already mentioned in previous chapters that may find natural explanation in the model presented here. In each case we first recall the experimental observations before comparing them to the predictions of the model.

Energy shifts and spectral diffusion

One surprising and quite anomalous behavior is the very large energy shifts of the PL peak emission with temperature. We observe for the majority of nanotubes shifts being as large as several tens of meV upon a temperature increase of less than 30 K. Moreover, these shifts are not always monotonous, although usually going towards lower energies. Large spectral jumps may also happen suddenly at some critical temperature, not always reversibly. Figure 4.11 shows in the left panel a typical temperature evolution of a SWNT PL line.

It is obvious that all these features strongly contrast with the smooth and weak temperature dependence of the E_{11} energy for pristine carbon nanotubes. As predicted by theory [66] and confirmed in experiments [67, 68], the pure temperature

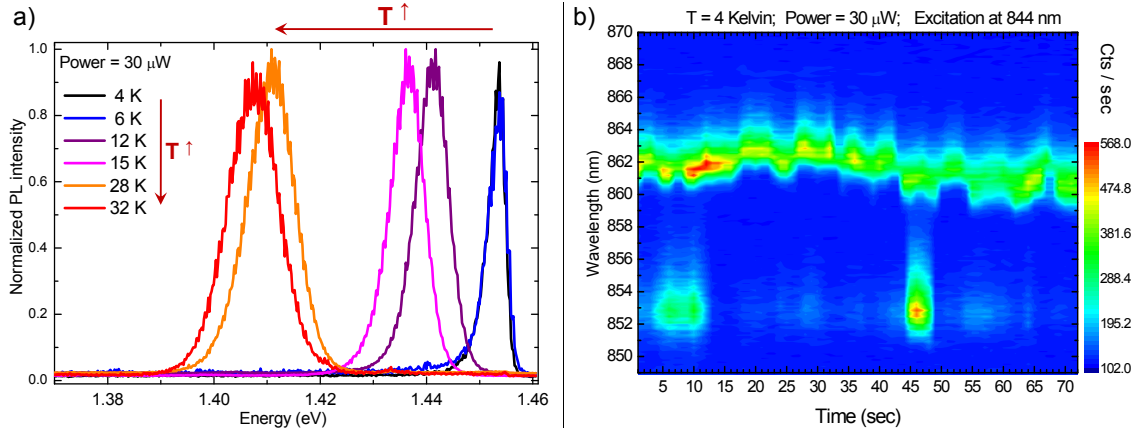


Figure 4.11: (a) Example of the dramatic energy shift in the PL emission occurring when we heat the sample through the thermo-resistor. We also frequently observe sudden jumps of several tens of meV. (b) Data from another nanotube illustrating quite typical spectral diffusion on a seconds time scale. Note the intensity variation as well as the on/off blinking of a blue-detuned peak.

shift (ignoring external strain) cannot exceed 20-30 μ ev/K. This would translate in a shift of less than 1 meV for the accessible temperature range in our experiment, more than one order of magnitude smaller than what we report. It seems very difficult to account for this discrepancy under the assumption of non-localized excitons as the origin of the PL emission.

Another related phenomena presented in the right panel of Fig. 4.11 is spectral diffusion (or spectral wandering). The peak emission energy is seen to fluctuate on timescales ranging from seconds to minutes, and it is likely that fluctuations do occur on even shorter timescales, partly responsible for the linewidth of the peak. Again, shifts of several meV are quite usual, along with intensity fluctuations, blinking and spectral jumps.

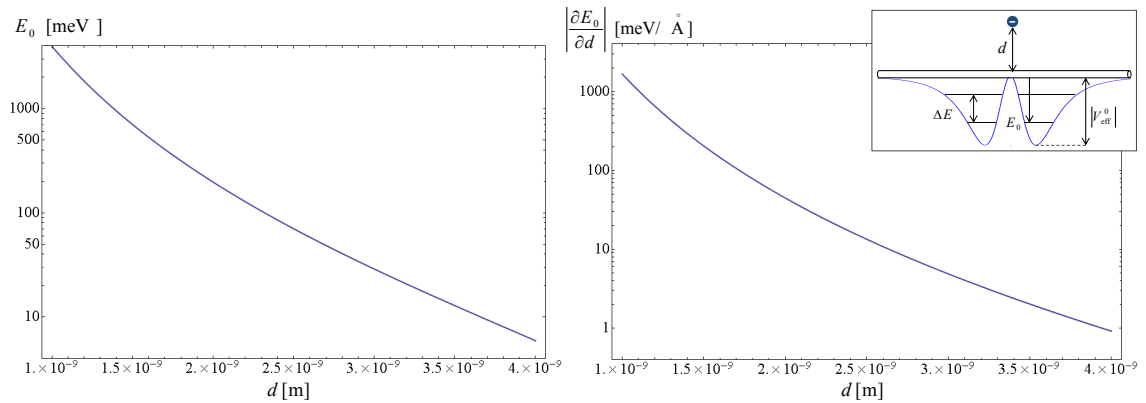


Figure 4.12: Left: Calculated energy of the quantum dot ground state E_0 measured positively from the free exciton energy (see inset on the upper right), as a function of the distance d . Right: Derivative of E_0 with respect to the impurity distance d , in meV/Å. Both graphs are plotted on a logarithmic vertical scale.

Although we are well aware that all these features most certainly have complex and multiple physical origins, we would like to show here that our simplified confinement model allow for a very plausible and unified explanation. As we demonstrated in the previous section, our model consistently predicts the formation of a quantum dot having the characteristics we want (confinement length, potential depth, level splitting) if we assume that it is caused by a charged impurity trapped somewhere around the micelle, presumably at a distance of ~ 2 nm from the nanotube.

The confinement energy of the quantum dot ground state, defined as $E_0 = |V_{\text{eff}}^0| - \frac{1}{2}\Delta E$, is plotted as a function of d in Fig. 4.12. Assuming that the energy of the free E_{11} exciton remains virtually constant, any change in E_0 will be directly observed as a corresponding shift in the PL wavelength of the SWNT-QD. Therefore we calculate the derivative of E_0 with respect to the impurity distance d (Fig. 4.12, right).

It is striking to see how strongly the PL is calculated to shift upon small displacement of the charged impurity, with typical values of 10 to 100 meV/Å for realistic mean distances. Such small movements are quite likely to occur naturally over time under laser illumination, or during the heating of the sample. Small configurational changes in the micelle/impurity complex would also lead to appreciable spectral jumps like the one we observe, in analogy to what happens in polymers [69]. We therefore argue that our model is, if not explaining, at least consistent with the observation of spectral diffusion and large temperature-related energy shifts typical in our sample.

Line splitting and cross-correlation

Another widespread and very singular observation of ours is the splitting of the PL spectra in two distinct lines. It must be stated here that we found at numerous places on the sample even more than two PL peaks from a single spot, but in those cases it is hard to exclude the possibility of small nanotube bundles or spatially separated quantum dots along the same nanotube. This is in particular true when the lineshapes are dissimilar and behave differently with respect to excitation energy, temperature change, etc.

In this section we concentrate on more specific, yet commonly occurring, situations in which the PL emission is split (or splits over time) in two similar peaks (although their respective intensities can vary quite substantially). A typical example is shown in Fig. 4.13: we started our measurement on a single line which split in two distinct peaks during ongoing laser illumination. On the third day of the experiment, the energy splitting between the two peaks was as large as 13 meV.

In order to try and understand the origin of the photons emitted at the two different wavelengths, we performed cross-correlation measurements on the two lines. For this purpose, the HBT setup used for auto-correlation (see chapter 2) is slightly modified by placing two bandpass filters, one in each arm, each transmitting the photons coming from one of the two lines only. Even if each peak separately shows perfect antibunching, we should measure $g_{\text{cross}}^{(2)}(0) \geq 0.5$ in the case of independent emitters.

In contrast, we find that the level of cross-correlation is similar to the auto-correlation value of each separate peak and $g_{\text{cross}}^{(2)}(0) \approx 0.27$, clearly smaller than 0.5.

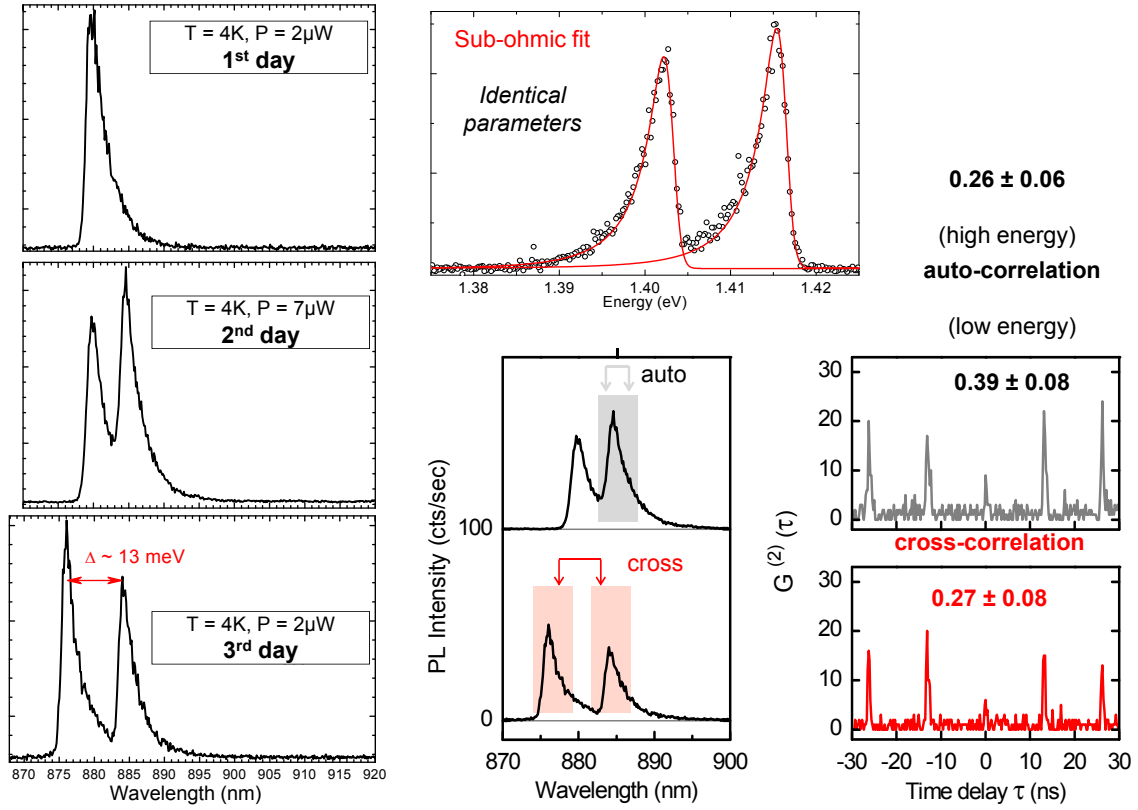


Figure 4.13: Under continuing laser illumination, the PL spectrum from this nanotube splits and the energies of the two lines change further over time. Remarkably, photons emitted at the two different peak wavelengths are strongly correlated ($g^{(2)\text{cross}}(0)$ well below 0.5), ruling out the existence of two spatially separated quantum dots, and supporting the picture of two emitting states from the same quantum dot. Further evidence for this interpretation is shown in the central top panel: calculated spectra in the sub-ohmic coupling regime (see second part of this chapter) with identical parameters (confinement length and coupling strength) fit both lines equally well. Completely similar fits were obtained within the ohmic regime (cf. chapter 3).

This means that the two peaks are strongly quantum correlated, which seems to exclude the possibility of two spatially separated quantum dots. Much more likely is the existence of two optically-allowed states in a single SWNT-QD, decaying into the same final state. An alternative explanation would rely on one QD-like emission site having two temporal states of different energies. In this case, the nonzero central peak in cross-correlation implies that the switching between the two distinct temporal states must occur on a time scale shorter than the characteristic PL decay time of 20-40 ps, which appears quite unlikely.

Further support for any of these two scenarios is given in Fig. 4.13 in the top panel. We used two variants (only one is shown) of the exciton-phonon coupling model presented in chapter 3 (and extended in the next part) to fit the two PL peaks. Remarkably, the same set of parameters can reproduce both lines with equal accuracy, from which we deduce that the confinement length and exciton-phonon coupling strength is the same for the two states involved. This is very suggestive of a single quantum dot with two own emitting states.

How does this interpretation relates to the confinement model we are discussing now? As pointed out previously, a very peculiar feature of the confinement potential created by the charged impurity is its symmetric double-well shape (see Fig. 4.8). If the tunnel coupling between the two wells is non-negligible, the true eigenstates of the system are linear combinations of these single-dot states. In particular, when nothing breaks the symmetry between the two sides, the eigenstates are exact bonding and anti-bonding superpositions, one of which only is optically allowed. These two eigenstates are split by an energy ΔE_{tun} characterizing the strength (or rate) of the tunnel coupling.

It is well known that the tunneling rate depends exponentially on the height and on the width of the barrier, so that it would be misleading to try and derive meaningful precise values within such a simplistic model. It is however instructive to look for an order-of-magnitude estimate of the tunnel coupling we expect. For this we make a crude approximation for the potential and consider a simple rectangular barrier separating the two wells. Under this assumption, a lowest order approximation for the tunnel coupling is:

$$\Delta E_{\text{tun}} \approx \frac{8}{\pi} \sqrt{\frac{E^3}{V_0 - E}} e^{-\kappa w} \quad (4.24)$$

Here E and V_0 are the energy of the single-well ground state and the barrier height, respectively, both measured from the minimum of the potential. In our case we have $E = \frac{1}{2}\Delta E$ (ground state energy) and $V_0 = |V_{\text{eff}}^0|$ (see inset in Fig. 4.14). The width of the barrier is w and we define:

$$\kappa = \frac{1}{\hbar} \sqrt{2m_{\text{exc}}(V_0 - E)}$$

Since our potential barrier is not rectangular, we choose for its width $w = d$, which should be quite a good approximation based on the fact that $z_0 = \pm d/\sqrt{2}$. We thus finally obtain an expression for ΔE_{tun} depending only on the variable d through the three parameters $|V_{\text{eff}}^0|$, $\frac{1}{2}\Delta E$ and w .

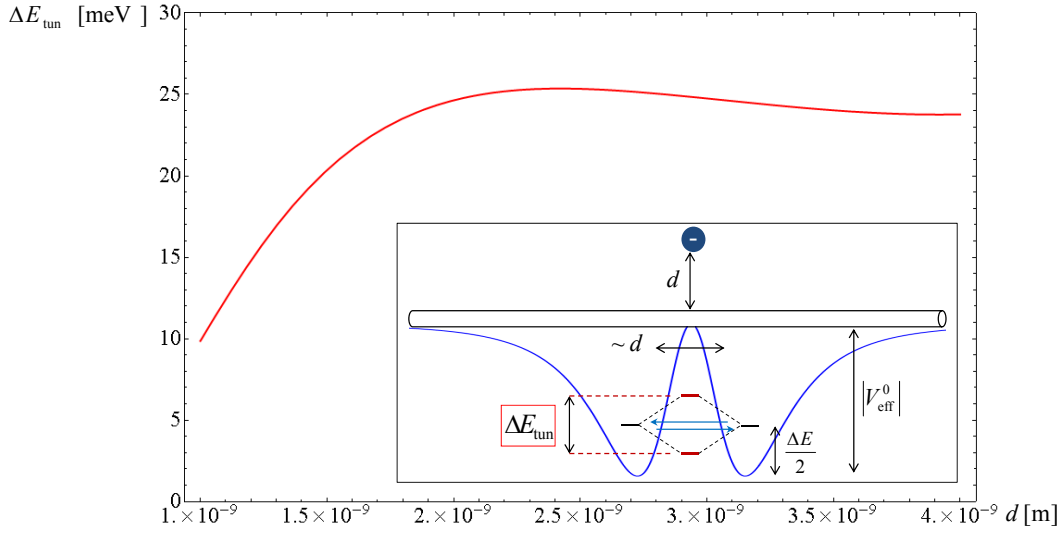


Figure 4.14: Estimated energy splitting due to tunnel coupling ΔE_{tun} (in meV) as a function of the distance d .

We plot the calculated tunneling energy splitting obtained in this way in Fig. 4.14. We repeat that no relevance should be given to the precise value of ΔE_{tun} nor to its exact dependence on d . Yet it is quite remarkable that the size of the splitting predicted here compares very well with the splitting actually measured in the experiment. In addition, we remark that the curve in Fig. 4.14 is surprisingly flat, given the exponential sensitivity to the parameters. This is so because a change in d has two compensating effects. When d is decreased, the potential barrier becomes higher (the wells become deeper) but its width is simultaneously reduced, leading to small net variations in $e^{-\kappa w}$. This weak dependence of the splitting on d is a requirement for the plausibility of the model, and could even be seen as an indication of its validity.

On the light of this finding, we propose the following mechanism to account for the PL line splitting. Due to the complexity of the environment and the extreme sensitivity of the potential to the charge position mentioned just before, one may reasonably expect that the symmetry between the two wells should be easily broken by any kind of perturbation in the surrounding micelle, induced for example by the laser excitation (free carriers, local heating, etc.).

Once the degeneracy is lifted, the two double-dot eigenstates will split further and, most importantly, will become both optically-allowed, resulting in a double PL emission peak. Since these two emitting states are eigenstates of the very same double quantum-dot and decay into the same final “empty-dot” state, it is natural to expect the cross-correlation results reported above, as well as their similar lineshape.

Single quantum-dot resonant excitation

We conclude this section by very briefly coming back to the issue of resonant excitation of the SWNT-QD discussed at the end of chapter 2. The main argument we can bring forward in this context is that our model predicts the right energy

scale for the first (“ p -shell”) excited state, as can be seen from Fig. 4.9. The sharp resonances we observe in the PL excitation spectra between 20 and 100 meV (see Fig. 2.15) could therefore be accounted for by resonant excitation of an excited state of the SWNT-QD. This is a well-known feature in the spectroscopy of II-VI [35] and III-V [36] semiconductor self-assembled quantum-dots. In our case, the quantum-dot excited state would play a role similar to the E_{22} exciton, providing a real state for the optical excitation, greatly enhancing the absorption cross-section.

If this picture is correct, it does not, nevertheless, completely explain why we usually find only a single or a few SWNT-QDs emitting from the same nanotube, even as we tune the excitation energy. But here again, our trapping model could provide a plausible explanation. As soon as a trap is created along the nanotube, the presence of a (say) negatively charged particle would forbid any other negative impurity to form a second stable trapping site in the vicinity, because of the strong Coulomb repulsion. A logical consequence would be the existence of a single SWNT-QD within our spot size in a majority of cases.

4.3 Exciton coupling to the bending mode: sub-ohmic lineshapes

We demonstrated in the previous part that the “charged impurity” picture could possibly account for a wide range of experimental observations. In addition, as we will show in the following sections, it opens up an exciting alternative interpretation of the peculiar broad asymmetric lineshapes typical of our sample. Indeed, the physical model presented in chapter 3 and used to fit the data is not specific to the stretching mode phonons nor to the corresponding ohmic regime. Moreover, we saw in section 4.1 that an effective coupling of the exciton to the bending mode phonons is induced as soon as a perpendicular electric field breaks the circumferential symmetry of the SWNT exciton. Interestingly, a charged impurity close to the nanotube do create a strong perpendicular field at the place where the exciton is confined.

Putting these pieces together leads us to investigate whether the PL lineshapes could be reproduced by the same spin-boson model, but involving the bending mode instead of the stretching mode phonons. As a result of the quadratic energy dispersion of the former, the spectral function is proportional to $\sqrt{\omega}$: the so-called sub-ohmic regime. After introducing the relevant theoretical framework, we show in the second section that equally good fits may be derived under this assumption, opening new possibilities in the interpretation of the data. We discuss the supportive elements for the validity of either regime in the last section.

4.3.1 The effective exciton-phonon coupling

Our approach in this chapter is somewhat different from the one adopted in chapter 3, although the underlying physic is basically the same. In order to compare the spectra and fits derived from the two possible phonon modes involved, we choose a more formal description to deal with the ohmic and sub-ohmic regimes on an equal footing. For this, we write the spectral density (or spectral function), which contains all the information on the exciton-bath interaction:

$$J(\omega) = 2\pi\alpha \omega_U^{(1-s)} \omega^s \theta(\omega - \omega_I) e^{-\omega/\omega_U} \quad (4.25)$$

The exponent s determines the dissipative regime. It depends, through the phonon density of states, on the form of the phonon dispersion and on the bath dimensionality. The cases we need to consider here are: $s = 1$ (ohmic regime) for the stretching mode; and $s = 1/2$ (sub-ohmic regime) for the bending mode. The constant α measures the strength of the exciton-phonon coupling. We will see that it depends in both cases on the chiral angle of the carbon nanotube, and for the bending mode additionally on the perpendicular electric field.

The remaining two parameters are ω_U and ω_I , the ultra-violet (UV) and infrared (IR) cutoff frequencies, respectively. In chapter 3 we gave a quite precise physical meaning to the UV cutoff frequency by relating it to the form-factor (the Fourier transform of the exciton center-of-mass envelope function). Here the exponential form of the cutoff function is more arbitrary but ω_U is still related to the size of the quantum dot.

Conversely, the IR cutoff is determined by the total length of the nanotube and the resulting lowest energy phonon mode. We assume that our nanotubes are few hundreds of nanometers long, which is in practice enough to make the results independent of the precise value of ω_I . Therefore we omit the factor $\theta(\omega - \omega_I)$ in the following expressions, although we did include it in all the numerical calculations.

Stretching mode and ohmic regime

The coupling to the stretching acoustic phonons yields an ohmic spectral density:

$$J(\omega) = 2\pi\alpha \omega e^{-\omega/\omega_U} \quad (\omega \geq \omega_I) \quad (4.26)$$

The UV cutoff is given by $\omega_U \approx v_S/\sigma_{CM}$ where $v_S \approx 2 \times 10^4$ m/s is the sound velocity. The expression for α is:

$$\alpha = \frac{1}{2\pi^2\hbar} \left(g_2^2 (1 + \sigma_P)^2 \sqrt{\frac{\sigma_G}{(E_Y h)^3}} \right) \cos^2(3\theta) \quad (4.27)$$

The parameters appearing in eq. 4.27 and their numerical values are:

- $g_2 \approx 3$ eV; the off-diagonal (“bond-length change”) electron-phonon coupling matrix element.
- $\sigma_P \approx 0.2$; the Poisson ratio of the carbon nanotube.
- $\sigma_G \approx 7.7 \times 10^{-7}$ Kg/m²; the surface mass density of graphene.
- $E_Y \approx 1$ TPa; the Young-modulus of the carbon nanotube.
- $h \approx 0.66$ Å; the effective shell thickness describing carbon nanotubes in the thin-rod elasticity model.
- θ ; the chiral angle of the carbon nanotube.

Bending mode and sub-ohmic regime

In the presence of a perpendicular (to the nanotube axis) component of the electric field E_\perp , we obtain an effective coupling to the bending (flexural) mode and a sub-ohmic spectral density:

$$J(\omega) = 2\pi\alpha \sqrt{\omega_U} \sqrt{\omega} e^{-\omega/\omega_U} \quad (\omega \geq \omega_I) \quad (4.28)$$

As is apparent in eq. 4.28, the true “physical” strength of the exciton-phonon coupling is expressed by the factor $\alpha\sqrt{\omega_U}$, instead of α alone in the ohmic expression. It is therefore more convenient for physical interpretation and for comparison with the ohmic density to write eq. 4.28 in the form:

$$J(\omega) = \sqrt{\pi\omega_*} \sqrt{\omega} e^{-\omega/\omega_U} \quad (\omega \geq \omega_I) \quad (4.29)$$

with the implicit relation: $\sqrt{\pi\omega_*} = 2\pi\alpha\sqrt{\omega_U}$. The coupling strength is now characterized by the square root of the frequency:

$$\omega_* = 2^{5/2}\pi \left(\frac{\xi^2 g_2^2}{2\pi^2 \hbar E_Y h} \right)^2 \frac{(1 + \sigma_P)^4}{R^3} \sqrt{\frac{\sigma_G}{E_Y h}} \cos^4(3\theta) \quad (4.30)$$

The new parameters appearing in eq. 4.30 are the nanotube radius R and the dimensionless parameter $\xi = e\mathcal{E}_\perp R/2\epsilon_\perp(E_{11} - E_{13})$ measuring the perturbation induced by the perpendicular electric field. We have introduced the effective field \mathcal{E}_\perp which can be computed exactly by integrating the bare field E_\perp along the nanotube, weighted by the exciton center-of-mass envelope function. We have no analytical expression for the confined wavefunction, but since the exciton is tightly localized close to the charged impurity we can take to a good approximation: $\mathcal{E}_\perp \approx E_\perp(z=0)$.

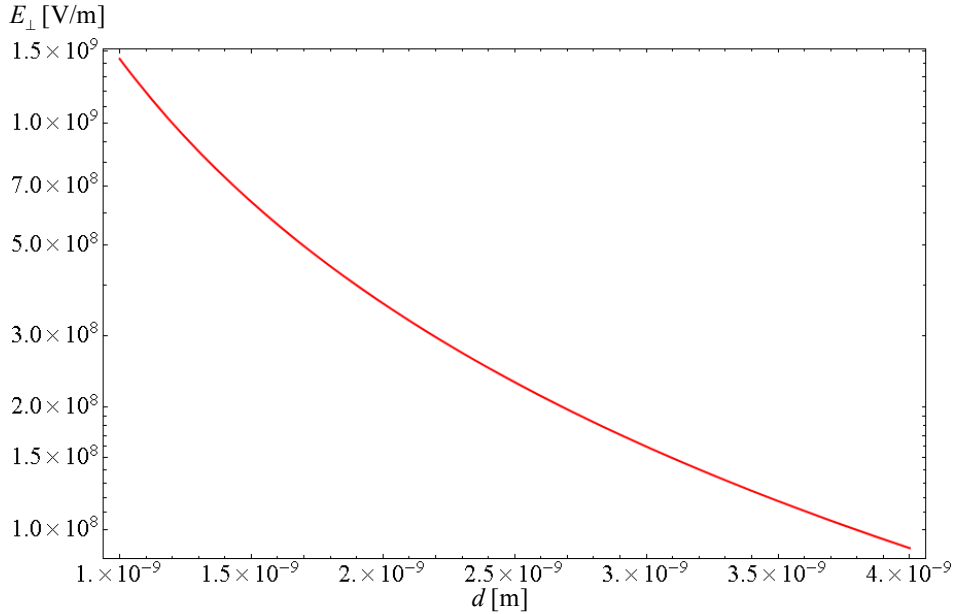


Figure 4.15: Perpendicular electric field created by the charged impurity at the origin $z = 0$.

The UV cutoff in this case is related to the confinement length by $\omega_U \approx c_B/(\sigma_{CM})^2$ where c_B is the coefficient in the bending mode energy dispersion: $\omega(q) = c_B q^2$. The thin-rod elasticity theory predicts $c_B = v_S R/\sqrt{2}$, yielding $c_B \approx 5 \times 10^{-6} \text{ m}^2/\text{s}$ for $R \approx 0.35 \text{ nm}$.

Figure 4.15 shows the computed value of the electric field component perpendicular to the nanotube induced by the charged impurity at the origin $z = 0$. Once more, it is not the exact value but rather the order of magnitude of the field that is relevant to us. We see that we expect the confined exciton in the SWNT-QD to experience a perpendicular field close to 1 V/nm.

4.3.2 A new eye on the experimental data: ohmic vs. sub-ohmic fits

The absorption spectrum as a function of the detuning $\delta\omega$ from the zero phonon line is given by⁴:

$$A(\delta\omega) \propto \Re \int_{-\infty}^{+\infty} d\tau e^{i(\delta\omega)\tau} e^{-\frac{\Gamma}{2}|\tau|} e^{\varphi(\tau)} \quad (4.31)$$

where $\Gamma = \gamma_{PL}$ is the total PL decay rate and we have defined:

$$\varphi(\tau) = -\frac{1}{\pi} \int_0^\infty d\omega \frac{J(\omega)}{\omega^2} \left[(1 - \cos \omega\tau) \coth \frac{\beta\omega}{2} + i \sin \omega\tau \right] \quad (4.32)$$

with the usual notation $\beta = 1/k_B T$. This is equivalent to the formula we use in chapter 3 in the particular case of the stretching mode (see eq. 3.10 and followings), but expressed in the frequency variable ω instead of the wavevector q . The great advantage of eqs. 4.31 and 4.32 is their dependence on the spectral function $J(\omega)$ (and on the temperature T) only. This allows us to compute the ohmic and sub-ohmic spectra within the same Matlab code, simply by choosing the parameter: $s = 1$ or $1/2$.

We follow the fitting procedure presented in chapter 3 for each SWNT-QD, repeating it independently with the ohmic and sub-ohmic spectral densities. We concentrate our efforts on nanotubes for which we have data at several temperatures, but extend our study to a larger set of nanotubes, including some for which the 4 K spectrum only was available. We determine the optimal values of α and ω_U to fit the complete data set by changing only the temperature in the computation. The temperature measured in the experiment unfortunately contains high uncertainty above 15-20 K. In this range, we thus allow for some freedom in the choice of the best fitting temperature. Yet this issue does not have noticeable impact on the uncertainty in α and ω_U because the sensitivity of the lineshape on their values is maximal at the lowest temperatures (below 10 K, see Fig. 4.17), for which T_{exp} is known within 1 K. Nevertheless, note that local heating on the laser spot would not be detected by the thermo-resistor (glued on the side of the sample), explaining why we usually need to assume slightly higher temperatures in the fits.

A typical result is presented in Fig. 4.16. It is quite remarkable how accurately both spectral densities can be used to fit the experimental data. This finding is completely general and valid for the 35 different SWNT-QDs on which we applied the procedure. Consequently, it is impossible from the mere quality of the fit to

4. Source: Ignacio Wilson-Rae, personal communication.

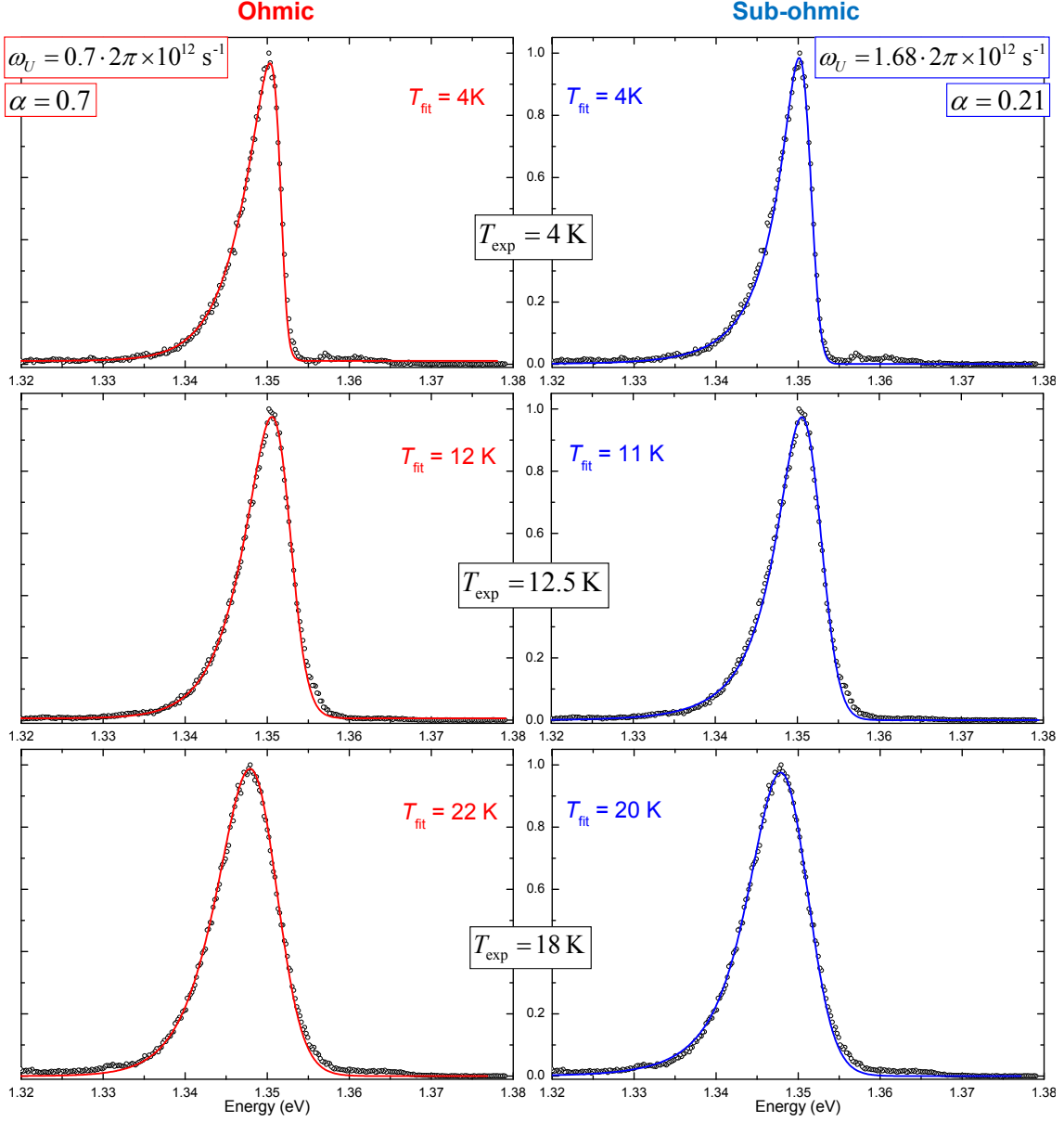


Figure 4.16: Comparison of the fitting spectra obtained for the same SWNT-QD within the ohmic (left) and sub-ohmic (right) coupling regimes. Open dots are the experimental data; solid lines show the computed lineshapes. The temperature deduced from the measured thermo-resistance is indicated by T_{exp} . In each series, the parameters α (coupling strength) and ω_U (ultra-violet cutoff) are kept constant while the temperature T_{fit} is changed. Better fits are usually obtained for temperatures T_{fit} differing slightly between the two models, but within the experimental uncertainty in T_{exp} .

argue which model is more likely to correspond to the physical reality. It could also be that both phonon modes are contributing more or less equally to the dephasing.

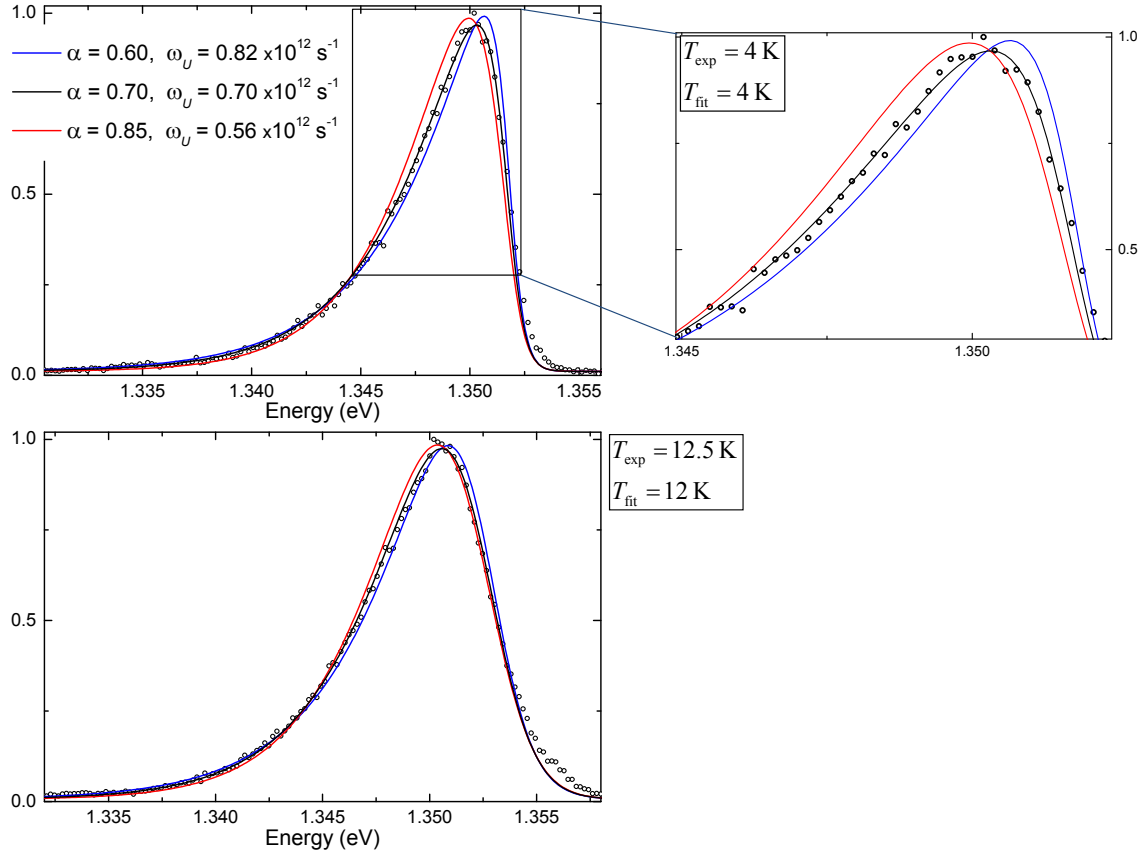


Figure 4.17: Assessing the uncertainty in the fits. Experimental PL spectra (open dots) from the SWNT-QD shown in Fig. 4.16 fitted by ohmic lineshapes computed with three different sets of parameters (α , ω_U) (solid lines). The deviation of the blue ($\alpha = 0.60$) and red ($\alpha = 0.85$) curves from the experimental data is most obvious at low temperature ($T = 4$ K) and cannot be compensated by the independent optimization of ω_U . The best fit is obtained for $\alpha = 0.70$ (black curve). We conclude that our uncertainty in extracting the value of α is typically $\pm 15\%$.

Before arguing further, we have to ask ourselves: with what precision can we determine the value of α and ω_U from the fitting procedure? Of particular concern is whether a change in one of the parameters can be compensated for by modifying the second one. This would allow for a wide range of couples of values to yield acceptable fits, and would therefore seriously question the validity of the whole procedure. Qualitatively, it is our experience that changes in the two parameters have different effects on the resulting lineshape, so that they can be optimized quite independently.

Increasing the coupling strength α tends to uniformly broaden the spectrum and to render the high energy shoulder less steep. Increasing the cutoff frequency ω_U mainly affects the extent and weight of the low-energy tail prominent at lower temperatures.

It is therefore difficult to cancel out the effect of modifying one parameter by simply changing the other.

To address the issue quantitatively we present in Fig. 4.17 the results of different choices for (α, ω_U) values (in the ohmic model) on the quality of the fits. In particular, we are most interested in the value of α , for which we have explicit expressions depending on the nanotube chirality. Starting from the optimal couple found in Fig. 4.16 (black curve), we increase (resp. decrease) the value of α , simultaneously trying to compensate for the change by tuning the cutoff ω_U , until no acceptable fit can be obtained anymore. The most obvious deviations from the experimental data are observed at the lowest temperature $T = 4$ K. The parameter α can thus be determined within $\pm 15\%$ with reasonably high confidence. The sub-ohmic fits (not shown) are even more sensitive to changes in parameters, so that at least the same level of confidence can be attributed to them.

4.3.3 Statistical analysis and conclusions

At this point of our data analysis, we are confronted with the impossibility of adopting or rejecting any one hypothesis on the basis of the fits' accuracies. We try here an alternative statistical approach by comparing the range of values obtained for α (respectively ω_*) with the expectations from eqs. 4.27 and 4.30. After having addressed the self-consistency of the charged impurity picture, we conclude that this new analysis is also unable to definitely discard one of the possible model.

Difficulties

As mentioned previously we applied the comparative fitting procedure to the PL spectra from 35 different nanotubes measured on our sample. Although we tried to consider the largest variety of PL characteristics, there is inevitably some selectivity in the data. Firstly, our detection and excitation ranges are technically limited, so that only a subset of nanotube chiralities can be studied. Secondly, further filtering occurs because a minimum PL intensity is required to enable data acquisition. It is possible that we selected only specific kinds of nanotubes or strongly confined excitons simply due to their stronger PL emissions (e.g. resulting from higher quantum efficiencies or cross sections). Finally many other effects like blinking, bleaching, spectral instabilities, multiple lines, etc. led us to discard many experimental data from thorough analysis.

The next difficulty we encounter is the attribution of a clear-cut chirality to each SWNT. The only information we dispose of is the PL emission energy. Each chirality should have a well-defined E_{11} transition energy. Experimental tables of those are readily available in the literature (see for example the empirical Kataura-plot from Weisman and Bachilo [23]), but are limited to carbon nanotubes in aqueous suspension at room temperature.

The first problem is thus to extrapolate these values to single nanotubes lying on a substrate at cryogenic temperatures. Indeed, band gap and exciton binding energies in carbon nanotubes are extremely sensitive to the surrounding media, to

temperature changes and increasing strain likely associated. Consequently, there may be substantial deviation of the PL emission wavelength in our sample from the values tabulated in the literature.

The second complication arises from the axial confinement of the exciton in SWNT-QDs, which is obviously causing additional energy shifts from the free exciton E_{11} . Although we expect exciton trapping to result in a red-shift, it is quite challenging to estimate its precise magnitude. Moreover, this confinement energy is certainly different from dot to dot. Altogether, the best we can hope to achieve for each SWNT is an educated guess of possible chiralities, based in large part on the limited range of species expected to be dominant in CoMoCat material. Unfortunately, this make a one-to-one comparison of the empirically determined α and ω_* with the theoretical predictions quite pointless.

For all these reasons we adopt here a comprehensive approach and consider statistical results like averages, minimal or maximal values.

Table 4.1: Theoretical predictions

Chirality		E_{11} [eV]	Radius [nm]	Ohmic	Sub-ohmic, $E_{\perp} = 1$ V/nm
n	m			α	$\sqrt{\pi\omega_*} [\times 10^6 \text{ s}^{-1/2}]$
7	2	1.55	0.32	0.53	0.15
6	4	1.42	0.34	0.09	0.07
9	1	1.36	0.37	0.65	0.24
8	3	1.3	0.39	0.33	0.19

First of all, we try to determine what nanotube chiralities are most likely to be observed in our experiment. For this, we consider the expected diameter distribution of CoMoCat SWNTs (centered around $d \sim 0.7 - 0.8$ nm) along with the limitation imposed by our PL detection range ($1.25 \text{ eV} \leq E_{\text{PL}} \leq 1.46 \text{ eV}$). Table 4.1 summarizes the selected nanotube chiralities and their E_{11} energies at room temperature in aqueous solution, taken from [23]. The theoretically predicted values for α and $\sqrt{\pi\omega_*}$ (under the assumption of a perpendicular electric field $E_{\perp} = 1$ V/nm) are also presented.

Consistency of the impurity picture

In order to analyze the data resulting from the previously described fitting procedure applied to about 30 different SWNTs, we proceed as follow. We calculate the average, minimum, maximum and standard deviation of the experimental values of $\sqrt{\pi\omega_*}$ and σ_{CM} deduced from the best fits. Then we want to compute the same statistics on the theoretical values in a manner meaningful for comparison. For this, we tentatively attribute a chirality to each measured SWNT from the ones listed in Table 4.1, based solely on the PL emission energy. This is a very speculative exercise and is only intended to obtain a weighted distribution of chiralities occurring in our data set⁵. This distribution can then be used to simulate the statistical results that

5. Indeed, we note that higher emission energies are slightly over-represented

would be obtained with the theoretical values of Table 4.1. We also scale $\sqrt{\pi\omega_*}$ by a factor corresponding to the presence of a perpendicular electric $E_\perp = 2.8$ V/nm. Since we have no *a priori* knowledge of the real field, this particular value was chosen to bring the average (weighted by the empirically determined chirality distribution) in equation to the experimental average. It can thus be viewed as an empirical deduction of the mean real electric field in the SWNT-QDs, under the assumption that we are actually in the sub-ohmic regime.

Table 4.2: Summary of the results from 30 SWNT-QD sub-ohmic fits.

	$\sqrt{\pi\omega_*} [\times 10^6 \text{ s}^{-1/2}]$		Conf. length σ_{CM} [nm]
	Experiment	Theory, $E_\perp = 2.8$ V/nm	Experiment
Minimum	0.61	0.58	1.3
Maximum	2.78	1.99	2.7
Average	1.29	1.29	1.75
Stand. Dev.	0.42	0.51	0.37

Table 4.2 summarizes the results of this analysis.

- The last column lists the exciton center-of-mass confinement lengths deduced from the UV cutoff frequencies used in the fits. These values are in remarkable agreement with the length-scales predicted by the charged impurity model. Although the calculations of Fig. 4.9 predict $\sigma_{\text{CM}} < 1$ nm, we demonstrated earlier that the exciton is certainly delocalized over the two potential wells due to strong tunnel coupling. The effective confinement length defining the cutoff frequency may thus rather be given by $\sim 2z_0$ instead of σ_{CM} , bringing it in the range of the experimental findings of Table 4.2.
- The statistical distribution of $\sqrt{\pi\omega_*}$ also compares very well to the theoretical expectation. However, the strength of the perpendicular electric field $E_\perp = 2.8$ V/nm required to reproduce the experimental data is somewhat higher than expected from our model (see Fig. 4.15). A possible explanation lies in the fact that none of the numerous parameters appearing in eq. 4.27 is known with good accuracy. Due to the highly sensitive scaling of ω_* on most of these parameters, the uncertainty on the theoretically derived value is hard to evaluate, but certainly very large. Therefore we should concentrate here again on orders of magnitudes.

The instructive conclusion we can draw from the above analysis, comments and discussion is that the charged impurity model provides a self-consistent picture for the experimental observations.

Ohmic or sub-ohmic?

We now apply exactly the same statistical treatment to the data obtained from the ohmic fits on the same set of nanotubes. The results are summarized in Table 4.3.

Here again, the agreement between the experimental and theoretical values of α is pretty good, considering the uncertainty in the parameters entering eq. 4.27. Small

Table 4.3: Summary of the results from 30 SWNT-QD sub-ohmic fits.

	α		Conf. length σ_{CM} [nm]
	Experiment	Theory	Experiment
Minimum	0.30	0.09	19.0
Maximum	0.85	0.65	66.7
Average	0.53	0.41	31.83
Stand. Dev.	0.13	0.22	12.36

adjustments in any of them could easily scale the “theory” column by a suitable factor to bring it closer to the experimental values.

The careful reader may note that the confinement lengths presented here differ quite substantially from the ones we reported in chapter 3. This is first partly due to the fact that we restricted our report in chapter 3 to much fewer different SWNT-QDs, chosen for their particularly obvious broad and asymmetric PL emission. Such spectra are obtained for large UV cutoff frequencies, corresponding in turn to small confinement lengths. The present data set is much more comprehensive and includes SWNT-QDs with lower UV cutoffs, thus larger confinement lengths.

A second cause to the discrepancy is the artificial form of the cutoff function used here. The exponential cutoff in frequency (eq. 4.26) corresponds to the same functional cutoff in wavevector space due to the linear dispersion of the stretching mode. This is certainly a much poorer physical picture than the Gaussian cutoff used in chapter 3, which resulted directly from the choice of a Gaussian envelope function for the exciton center-of-mass motion.

An important issue that we have overlooked until now and that may affect equally the comparison to the ohmic and sub-ohmic models is the contribution of spectral diffusion to the lineshape and linewidth. Indeed, we have reported in previous chapters that most PL lines show spectral fluctuations over seconds and longer timescale. Since we cannot measure the spectra with much better time resolution, it remains open whether significant spectral shifts occur on shorter timescales. If this were the case, this would translate into an additional broadening of the time-averaged PL spectra. In this sense, we should consider the values empirically derived for α and $\sqrt{\pi\omega_*}$ as upper-bounds rather than exact estimates.

We have however a good reason to think that the low-temperature spectra are in most cases only weakly affected by such potential broadening mechanism. Assuming very fast spectral fluctuations do occur, it is natural to model them as a symmetric, typically Gaussian, broadening of the lineshape. This in turn should result in blurring out the steep high energy shoulder characterizing the low-temperature PL spectra. Since we can fit the experimental spectra assuming temperatures close to 4 K in the model, it seems that spectral diffusion is not prominently contributing to the lineshape.

Conclusion

In the light of the previous findings and discussions, we conclude this chapter by evoking a third possibility that may actually best describe the physical origin of our PL data. We saw in the first section that the charged impurity picture is a promising candidate to account for the exciton trapping and agree well with a wealth of experimental observations. In the second section we contemplated an alternative interpretation of the PL lineshapes based on the new possibility of exciton coupling to the bending mode phonons. We could not, nevertheless, decide on a particular phonon mode (stretching or bending) being responsible for the exciton pure dephasing.

Yet, if we assume that the parameters used in the theoretical evaluation of the ohmic and sub-ohmic α are reasonably trustworthy, we could argue that the statistical analysis presented above favors the ohmic regime as yielding better agreement between experiment and theory. Indeed, the perpendicular electric field $E_{\perp} = 2.8$ V/nm required in the sub-ohmic model appears very large and unlikely. The computation would rather predict a field on the order of 0.1 V/nm, and this would lead to undetectable effects on the PL lineshape.

The remaining open possibility consistent with all these considerations is that the confinement is actually due to the presence of a nearby charged impurity, but the induced perpendicular is too weak to make the sub-ohmic dissipation relevant. On the other hand, the coupling to the stretching mode does not rely on any external perturbation and is expected to cause fast pure dephasing irrespective of the origin of exciton confinement. This means that ohmic dissipation is most likely accounting for the asymmetric PL lineshapes and is the dominating source of pure dephasing.

We finally repeat that we cannot give any definite evidence of the validity of the particular trapping mechanism we propose. However we hope to have convinced the reader in this chapter of the consistence of our model. It seems to us quite likely that the kind of mechanism described here, if not exactly this one, is responsible for the formation of SWNT-QDs and the associated experimental features.

5 All optical manipulation of a SWNT-QD spin

5.1 Spin-Orbit coupling in carbon nanotubes

The spin-orbit interaction (SOI, also called spin-orbit effect or spin-orbit coupling) refers to any interaction of a particle's spin with its own motion. The first and best known example of this is that spin-orbit interaction causes shifts in the electron's atomic energy levels (detectable as fine structure splitting of the spectral lines), due to electromagnetic interaction between the electron's spin and the nucleus's electric field, through which it moves. In condensed matter, in particular in the field of spintronics, spin-orbit effects for electrons in semiconductors and other materials can be used to control the spin degree of freedom by optical or electrical means.

The SOI energy increases with the atomic number because stronger fields exist around the nucleus. The intrinsic (i.e. atomic) SOI is therefore very small in carbon, which naturally leads to think that spin-orbit effects should be negligible in carbon nanotubes. Although this seems to be the case in flat graphene sheets, the curvature of the nanotube's wall and the cylindrical topology induces a coupling of the electron and hole spins to their own circumferential momenta. The resulting interaction has recently been shown in transport experiments to cause a zero-magnetic field splitting and to break the electron-hole symmetry [70].

5.1.1 Physical origin of Spin-orbit coupling

We begin with a short derivation of the spin-orbit interaction for an electron in a hydrogenic atom, using semiclassical electrodynamics and non-relativistic quantum mechanics. A more rigorous derivation of the same result would start with the Dirac equation, and achieving more precision would require small corrections from quantum electrodynamics. This is of course out of the scope of this work.

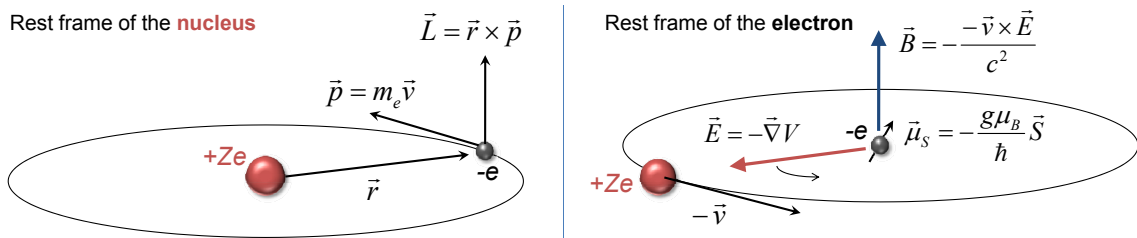


Figure 5.1: Spin-Orbit interaction in a hydrogenic atom.

As presented in Fig. 5.1 we consider an electron (charge $-e$, mass m_e) orbiting with velocity \mathbf{v} at a distance \mathbf{r} from a nucleus with charge $+Ze$ (the atomic number

$Z = 6$ for carbon). In the rest frame of the electron (right in Fig. 5.1), ignoring for now that this frame is not inertial, the nucleus moving with speed $-\mathbf{v}$ around the electron produces a magnetic field:

$$\mathbf{B} = -\frac{(-\mathbf{v}) \times \mathbf{E}}{c^2} = \frac{\mathbf{v} \times \mathbf{E}}{c^2} \quad (5.1)$$

The electric field being radial, we can write it $\mathbf{E} = -(E/r)\mathbf{r}$. Using also $\mathbf{p} = m_e \mathbf{v}$ we obtain:

$$\mathbf{B} = \frac{\mathbf{r} \times \mathbf{p}}{m_e c^2} (E/r) \quad (5.2)$$

Next, we express the electric field as the gradient of the electric potential. Here we make the central field approximation, that is, that the electrostatic potential is spherically symmetric, so is only a function of the radius¹. In this case $|E| = \frac{1}{e} \frac{\partial V}{\partial r}$, where V is the potential energy of the electron in the central field. Remembering from classical mechanics that the angular momentum of a particle reads $\mathbf{L} = \mathbf{r} \times \mathbf{p}$ we get from equation (5.3):

$$\mathbf{B} = \frac{1}{m_e e c^2 r} \frac{\partial V}{\partial r} \mathbf{L} \quad (5.3)$$

The intrinsic angular momentum of the electron is represented by the spin vectorial operator $\mathbf{S} = \frac{\hbar}{2} \boldsymbol{\sigma}$, where $\boldsymbol{\sigma}$ is the vector of Pauli matrices. Associated with it is an intrinsic magnetic dipole moment:

$$\mu_S = -g \mu_b \frac{\mathbf{S}}{\hbar}$$

where $\mu_b \equiv \frac{e\hbar}{2m_e}$ is the fundamental unit of magnetic moment called the Bohr magneton, and $g \simeq 2$ is the spin gyromagnetic ratio of the electron. Finally, the interaction energy $H_{\text{SO}} = -\mu_S \cdot \mathbf{B}$ reads:

$$\tilde{\mathcal{H}}_{\text{SO}} = \frac{2\mu_b}{\hbar m_e c^2 r} \frac{\partial V}{\partial r} (\mathbf{L} \cdot \mathbf{S}) \quad (5.4)$$

However, the electron is not in an inertial frame of reference. In transforming back into the inertial frame, a relativistic effect called Thomas precession results in a factor 1/2 so that:

$$\mathcal{H}_{\text{SO}} = \frac{\mu_b}{\hbar m_e c^2 r} \frac{\partial V}{\partial r} (\mathbf{L} \cdot \mathbf{S}) \quad (5.5)$$

Explicitly, in the hydrogenic atom model considered above, we have $\frac{\partial V}{\partial r} = Ze^2/r^2$, which yields after substituting also $\mu_b = \frac{e\hbar}{2m_e}$ in (5.5):

$$\mathcal{H}_{\text{SO}} = \frac{Ze^2}{2m_e^2 c^2 r^3} (\mathbf{L} \cdot \mathbf{S}) \quad (5.6)$$

Another way of writing Hamiltonian (5.5) which is more general and can be used as a starting point for calculations in solid state systems is:

1. This approximation is exact only for hydrogen-like systems

$$\mathcal{H}_{\text{SO}} = \Delta(\mathbf{L} \cdot \mathbf{S}) \quad (5.7)$$

where Δ , the intra-atomic spin-orbit coupling constant, can be either directly evaluated from first principles (using eq. 5.5) or empirically determined from experimental data.

5.1.2 Spin-orbit interaction in SWNTs: theoretical predictions

The complete spin-orbit Hamiltonian

We keep the notations of chapter 4.1 and use the same coordinate system: z is along the nanotube axis and φ is the circumferential coordinate, whereas x and y are both orthogonal to the nanotube, forming with z an orthonormal direct basis. To simplify the heavy 4×4 matrix notation used in chapter 4.1, we introduce the Pauli matrices $\sigma_{1,2,3}$ (resp. $\tau_{1,2,3}$) acting on the sublattice A/B (resp. valley K/K') space. We chose numerical indices 1, 2, 3 to emphasize on the non-geometrical nature of the spaces in which the operators act, in contrast to the spin Pauli matrices $s_{x,y,z}$, whose eigenbasis $|\uparrow\rangle, |\downarrow\rangle$ corresponds to the possible spin projections along z .

Considering Hamiltonian (5.5) or (5.7) as a perturbation in a tight-binding calculation, T. Ando [71] and Daniel Huertas-Hernando *et al.* [72] were the first to derive an effective spin-orbit hamiltonian for the relevant states of carbon nanotubes close to the Fermi level (i.e. in the vicinity of K and K'). We concentrate here on the final expressions and follow the notation used by D. V. Bulaev *et al.* [73] to discuss the different terms appearing in the total spin-orbit interaction Hamiltonian:

$$\mathcal{H}_{\text{SO}} = \mathcal{H}_{\text{SO}}^{\text{int}} + \mathcal{H}_{\text{SO}}^E + \mathcal{H}_{\text{SO}}^{\text{curv}} \quad (5.8)$$

- The intrinsic SOI: $\mathcal{H}_{\text{SO}}^{\text{int}} = \Delta_{\text{int}}\tau_3\sigma_3s_z$ is the same as in graphene where it opens a tiny gap $\Delta_{\text{int}} \propto \Delta^2$ at the Dirac points. The effect is however extremely small because of the weakness of the intra-atomic spin-orbit coupling of carbon Δ . It is estimated to be $\Delta_{\text{int}} \approx 1 \mu\text{eV}$ [72] and has not been experimentally evidenced so far.
- The Rashba (or Bychkov-Rashba) term: $\mathcal{H}_{\text{SO}}^E = \Delta_E(\tau_3\sigma_1s_z - \sigma_2s_x)$ is an extrinsic effect related to a breaking of the mirror symmetry about the graphene plane. This happens when an electric field is applied orthogonally to the graphene sheet (or the nanotube). More precisely Δ_E corresponds to processes due to the intra-atomic spin-orbit coupling and the intra-atomic Stark effect between different orbitals of the π and σ bands, together with hopping between neighboring atoms. This term vanishes in the absence of electric field, and remains very small for realistic field strengths ($\Delta_E < \Delta_{\text{int}}$ for $E < 0.1 \text{ V/nm}$).
- The dominant term in carbon nanotubes is very clearly the curvature induced SOI: $\mathcal{H}_{\text{SO}}^{\text{curv}} = \Delta_{\text{curv}}^{\parallel}\tau_3\sigma_1s_z - \Delta_{\text{curv}}^{\perp}\sigma_2s_x$. In this case the local curvature of the graphene surface couples the π and σ bands. The strengths of the two different terms are comparable and estimated to be: $\Delta_{\text{curv}}^{\parallel} \approx 0.17 \text{ meV/R[nm]}$ and $\Delta_{\text{curv}}^{\perp} \approx -0.26 \text{ meV/R[nm]}$. From now on we therefore neglect the two first terms (intrinsic and Rashba SOI) and focus on the curvature-induced SOI.

The first term: $\Delta_{\text{curv}}^{\parallel}\tau_3\sigma_1s_z$ is proportional to the spin operator s_z and its sign depends on the valley K or K' through τ_3 . Because it involves σ_1 , it corresponds

to a shift in the allowed wave-vectors k_\perp [71] and leads to a zero-field spin splitting $\Delta_{\text{SO}} = 2\Delta_{\text{curv}}^\parallel$ between states with parallel and anti-parallel spin and orbital magnetic moments.

Let us analyze the second term: $-\Delta_{\text{curv}}^\perp \sigma_2 s_x$. Because it involves the operator s_x , it mixes states with opposite spins s_z . But the coupling only occurs between states differing by one unit of circumferential momentum $\Delta n = \pm 1$. This is again a consequence of angular momentum conservation. In other words, we can write the operator s_x in the nanotube coordinates $s_x = i(-s_+ e^{i\varphi} + s_- e^{-i\varphi})$ where s_\pm are the raising / lowering operators, i.e. correspond to spin-flip events. It is then clear that states between which this term induces non-vanishing coupling must differ by a factor $e^{\pm i\varphi}$, that is to say by one unit of circumferential momentum.

We may use first order perturbation theory to evaluate how the eigenstates of $\mathcal{H}_0 + \Delta_{\text{curv}}^\parallel \tau_3 \sigma_1 s_z$ are modified by $-\Delta_{\text{curv}}^\perp \sigma_2 s_x$. Because the energy differences between the lowest subbands are on the order of several 100 meV in narrow nanotubes, energy denominators of the type $(E_n - E_{n\pm 1})^{-1}$ account for a very weak state mixing². We therefore discard this term in what follows and consider exclusively the spin-orbit interaction reduced to: $\mathcal{H}_{\text{SO}}^\parallel = \Delta_{\text{curv}}^\parallel \tau_3 \sigma_1 s_z$.

Spin-orbit coupling as a topological effect

We already explained in chapter 1 that a magnetic field applied along the longitudinal direction of the nanotube breaks the time-reversal symmetry and therefore lifts the K - K' degeneracy. For a quantitative understanding of this we have to consider the Aharonov-Bohm (AB) effect. The latter is a general result from the requirement that quantum physics be invariant with respect to the gauge choice for the electromagnetic potential, part of which is formed by the magnetic vector potential \mathbf{A} . A particle with charge q traveling along a path P thus acquires a phase shift:

$$\Delta\varphi = \frac{q}{\hbar} \int_P \mathbf{A} \cdot d\mathbf{x} \quad (5.9)$$

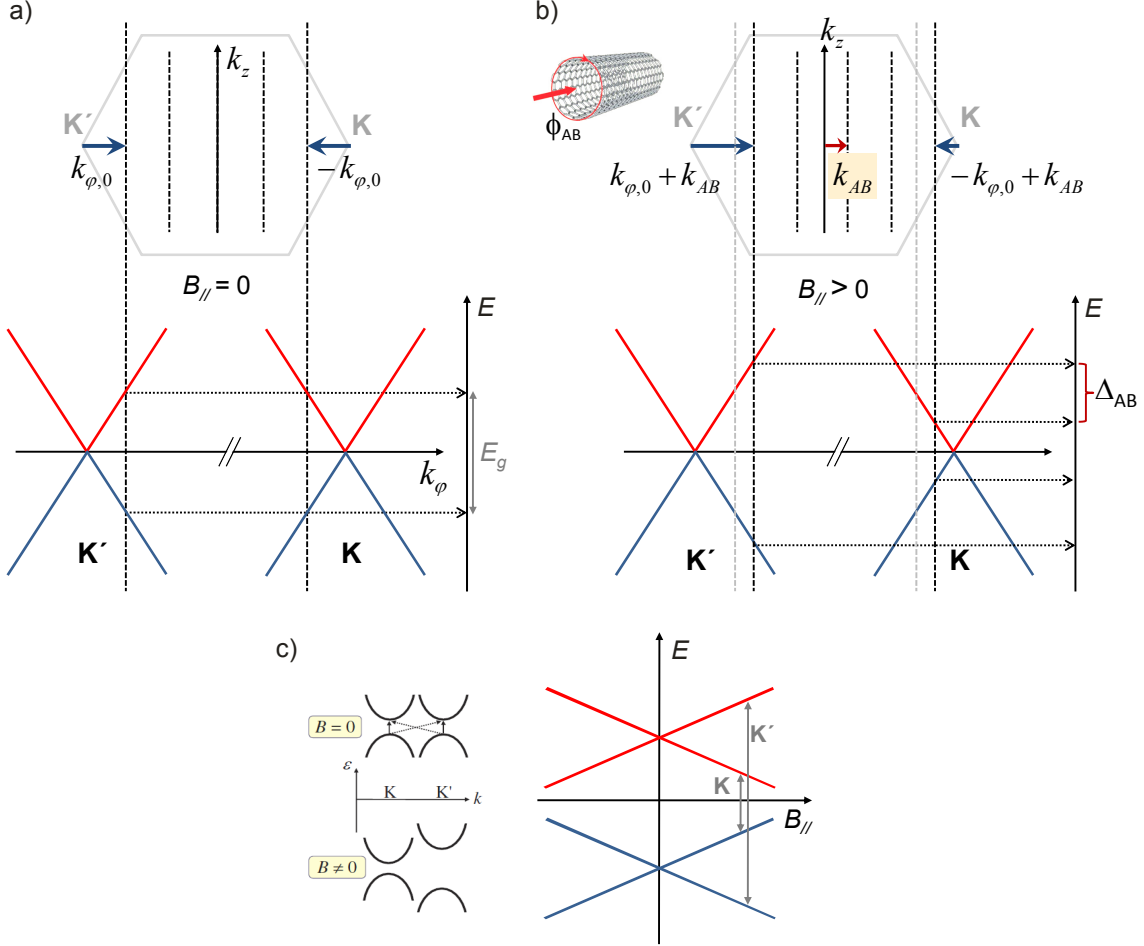
Using Stokes' theorem and $\mathbf{B} \doteq \nabla \times \mathbf{A}$ we can write eq. 5.9:

$$\Delta\varphi = \frac{q\phi_{\text{AB}}}{\hbar} \quad (5.10)$$

where $\phi_{\text{AB}} = \oint_S \mathbf{B} \cdot d\mathbf{n}$ is the Aharonov-Bohm flux. Here S is the surface enclosed by the path P and \mathbf{n} is a unit vector normal to it. For an electron circling around the nanotube in a uniform axial magnetic field B_\parallel it is clear that the AB flux takes the form: $\phi_{\text{AB}} = B_\parallel \pi R^2$ (see Fig. 5.2), with $R = d/2$ the radius of the SWNT. In the absence of AB flux, the circumferential periodic boundary condition (cf. chapter 1): $\Psi(\mathbf{r} + \mathbf{C}_h) = \Psi(\mathbf{r})$ imposes: $\exp(i\mathbf{k} \cdot \mathbf{C}_h) = 1$, leading to the quantization: $(2\pi R)k_\varphi = n(2\pi)$ responsible for the opening of the gap in semiconducting nanotubes (Fig. 5.2 a)). The additional AB phase-shift modifies this condition into:

$$n(2\pi) = (2\pi R)k_\varphi + \Delta\varphi = (2\pi R)k_\varphi - \frac{2\pi e}{\hbar} \phi_{\text{AB}} \quad (5.11)$$

2. Using this term to manipulate the spin would also require using transverse electric fields which couple weakly to the nanotube because of the antenna effect



This translates directly into a shift of the allowed wave-vectors by:

$$k_{AB} = \frac{1}{R} \frac{\phi_{AB}}{\phi_0}$$

where $\phi_0 = h/e$ is the flux quantum. As is evidenced in Fig. 5.2 b), the resulting changes in the lowest subbands' energies have opposite signs at K and K' , lifting the degeneracy. Figure 5.2 c) summarizes the dependence of the lowest conduction and highest valence bands' energies under a magnetic field, neglecting for now the Zeeman splitting associated with the electron's spin.

We now come back to the effect of spin-orbit coupling on the electronic states and energies of SWNTs close to the Dirac points. Figure 5.3 a) gives a pictorial view of the topological flux associated with spin-orbit interaction. Consider an electron with spin s_z pointing along the nanotube axis. The electron occupies the π orbitals of the carbon atoms, which are pointing perpendicular to the nanotube surface. States around K and K' correspond to electrons having a fast circular motion around the nanotube's circumference (related to the momentum $\hbar k_\varphi$). In the rest frame of the electron the underlying π orbital revolves around the spin exactly once every rotation. In the presence of atomic spin-orbit coupling, Δ , a constant phase accumulates during each rotation (independently of the circumference's length), which can be described by a *spin-dependent* topological flux, $\pm\phi_{SO} \propto \Delta$, threading the nanotube cross-section.

This flux has exactly the same effect as the “real” Aharonov-Bohm flux ϕ_{AB} created by an external magnetic field, except that its sign depends on the spin projection along z , and that it is *independent of the nanotube diameter* (thus topological). As shown in Ref. [71], this flux modifies the quantization condition of the wave-function around the circumference according to:

$$k_\varphi = k_{\varphi,0} - \frac{1}{R} s_z \frac{\phi_{SO}}{\phi_0} = k_{\varphi,0} \pm \frac{1}{R} \frac{\phi_{SO}}{\phi_0} \quad (5.12)$$

with $\phi_{SO} \approx 10^{-3}\phi_0$. The resulting effect is presented in Fig 5.3 b). As before, we can attribute a wave-vector shift $k_{SO} = s_z \frac{1}{R} \frac{\phi_{SO}}{\phi_0}$ related to the SO flux. Interestingly, the sign of the energy shift is now depending both on the spin $s_z = \pm$ and the valley K - K' . In other words, spin-orbit interaction in carbon nanotubes couples the spin and orbital degrees of freedom and results in a zero-magnetic field energy splitting:

$$\begin{aligned} \Delta_{SO} &= 2\Delta_{\text{curv}}^{\parallel} = 2\hbar v_F |k_{SO}| \\ &= \frac{2\hbar v_F}{R} \frac{\phi_{SO}}{\phi_0} \end{aligned} \quad (5.13)$$

Here $v_F \approx 10^6$ m/s is the Fermi velocity in graphene [74]. Note the dependence: $\Delta_{SO} \propto \frac{1}{R}$, in contrast to $\Delta_{AB} \propto R$ (Fig. 5.2 b)).

A closer look to Fig 5.3 b) reveals a very important feature of SOI. Let us focus for example on the K valley. It is obvious that for a given spin eigenstate, the energies of the conduction and valence states shift in opposite directions. Therefore, SOI breaks the electron-hole symmetry in carbon nanotube, a point on which we will come back later since it is essential in the scheme we propose for optical spin manipulation.

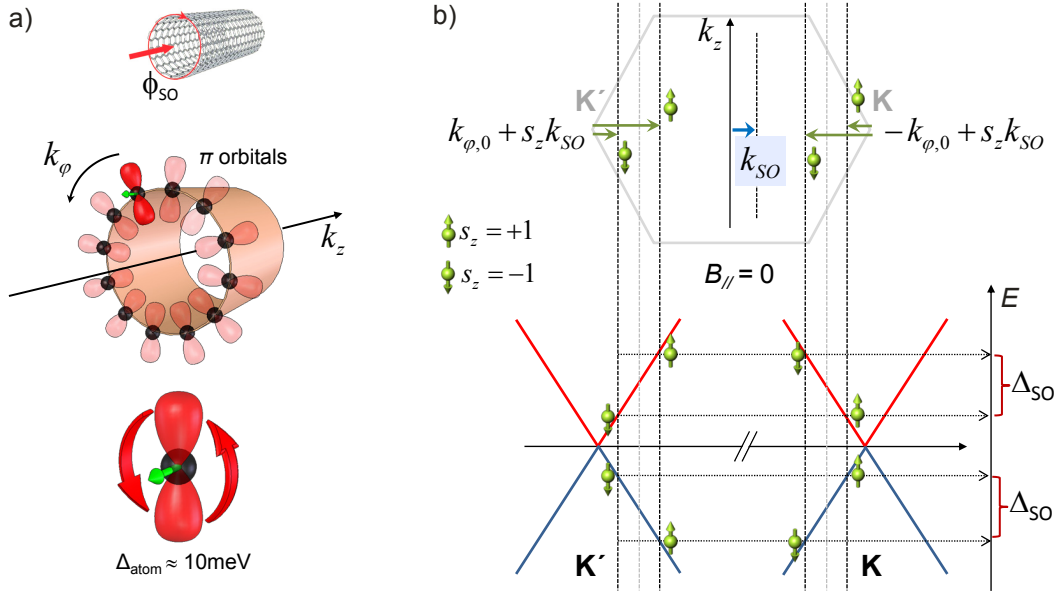


Figure 5.3: Spin-Orbit coupling as a topological flux. a) A heuristic explanation for the SO flux can be given by considering the circumferential motion of an electron occupying a π orbital. In the rest frame of the electron, the orbital performs a complete rotation around the carbon nucleus. Since the π orbital's angular momentum is $l = 1$, the non-vanishing intra-atomic SO coupling Δ leads to a phase accumulating during each revolution. This is equivalent to the presence of a spin-dependent topological flux $\pm\phi_{SO} \approx \pm 10^{-3}\phi_0$. b) In exact similitude with the AB flux, we can associate a spin-dependent wave-vector shift $k_{SO} = s_z \frac{1}{R} \frac{\phi_{SO}}{\phi_0}$, leading to an energy shift dependent on both spin and valley degrees of freedom. The result is a zero-field spin-splitting $\Delta_{SO} = \frac{2\hbar v_F}{R} \frac{\phi_{SO}}{\phi_0}$.

Spin-orbit coupling in a semi-classical picture

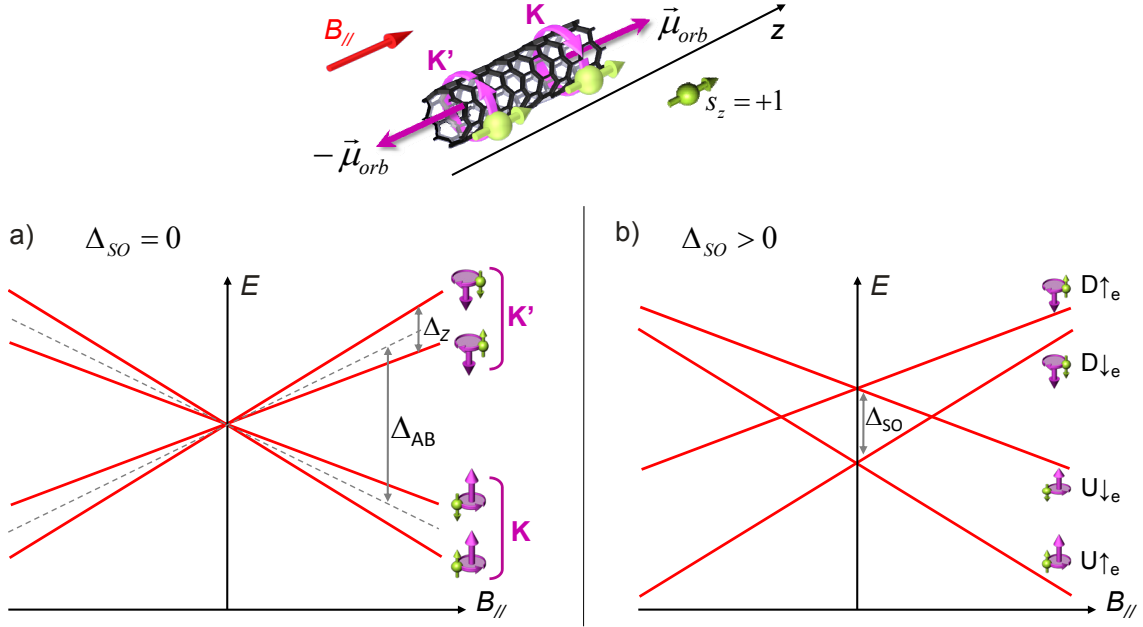


Figure 5.4: a) Orbital and Spin magnetic moments independently couple to the applied magnetic field B_{\parallel} . The first leads to the Aharonov-Bohm splitting Δ_{AB} , the second to the Zeeman splitting Δ_Z . b) When SOI is taking into account, it accounts for an effective coupling between these two otherwise independent degrees of freedom. To stress the analogy between orbital and spin magnetic moments, we label the valley degree of freedom with D (for “Down”) instead of K' , and U (for “Up”) instead of K .

This analogy between magnetic field and SOI can also be expressed in a more classical picture, as shown in Frig. 5.4. The circular motion of the charged electron occupying a state close to K or K' produces an orbital magnetic moment, μ_{orb} , pointing along the nanotube axis. Under an external magnetic field B_{\parallel} , we expect this magnetic moment to interact with the field according to the Hamiltonian:

$$\mathcal{H}_{AB} = -\mu_{orb} \cdot \mathbf{B} \quad (5.14)$$

If we go back to the expression for the energy splitting derived above:

$$\frac{1}{2}|\Delta_{AB}| = \hbar v_F |k_{AB}| = \frac{\hbar}{2\pi} v_F \frac{1}{R} \frac{|B_{\parallel}| \pi R^2}{\hbar/e} = \frac{e v_F R}{2} \cdot |B_{\parallel}| \quad (5.15)$$

we see that the interaction is indeed of the form $\mu_{orb} \cdot B_{\parallel}$ with $\mu_{orb} = \frac{R e v_F}{2} \propto R$. States originating from different valleys have opposite circumferential momenta and thus exhibit orbital magnetic moments pointing in opposite directions. Similarly, the electron’s spin corresponds to an intrinsic magnetic moment along z : $\mu_S = \frac{g \mu_B}{2} s_z$, which couples to the external field through the Hamiltonian:

$$\mathcal{H}_Z = -\mu_S \cdot B_{\parallel} \quad (5.16)$$

This produces the well-known Zeeman splitting: $|\Delta_z| = g\mu_b|B_{\parallel}|$ between opposite spin eigenstates. The resulting energy diagram in a magnetic field is presented in Fig. 5.4 a).

In this picture, the zero-field spin-splitting due to SOI can be seen as a consequence of an effective coupling between orbital and intrinsic (spin) magnetic moments. As shown in Fig. 5.4 b), the zero-field four-fold degeneracy is lifted, with the formation of two doublets of states with parallel (resp. anti-parallel) alignment of orbital and spin magnetic moments.

5.1.3 Experimental observation

It was not until late 2007 that the expected effect of spin-orbit interaction in carbon nanotube could be observed and measured directly in a transport experiment by Ferdinand Kuemmeth *et al.* [70]. Our proposal presented in the next section was significantly motivated by these beautiful results and by exciting discussions with one of the author (Shahal Ilani) during a winter-school in Kirchberg-in-Tirol early 2008. We would like to give here a brief account of the experiment and the results obtained by the P. McEuen group.

For the reason cited above it was widely believed that spin-orbit interaction in carbon nanotubes was too small to have significant effects on the electronic structure. In particular, all experiments were hinting at a four-fold degeneracy at zero magnetic field, as expected for independent spin and orbital degrees of freedom. The reasons why spin-orbit coupling effects were not detected previously are likely related to the poor quality of the nanotubes, with disorder-induced lifting of the K - K' degeneracy hiding the small zero-field spin splitting. Also electron-electron interactions in multi-electron quantum dots may have hindered this observation.

The breakthrough from the McEuen group was the use of ultra-clean carbon nanotubes: the CVD-growth was the last step to be performed, avoiding degradation and defect creation during post-processing. Moreover, their design (see Fig. 5.5) allows the controlled charging of the SWNT-QD with single electrons and holes. Their system is thus perfectly suited to study the evolution of a single-particle state under an externally applied magnetic field, in a close to ideal defect-free nanotube.

The idea of the experiment is to perform low temperature transport spectroscopy on a gate-defined carbon nanotube quantum dot containing a single charge-carrier, under different magnetic fields B_{\parallel} . The measurement of the differential conductance, $G = dI/dV_{sd}$, when varying source-drain (V_{sd}) and back-gate (V_g) voltages allows the observation of the single-particle energy levels. Beyond the well-known Coulomb diamond marking the transition between an empty and singly-charged SWNT-QD, they observe distinct resonances corresponding to excited states of the first electron. Their main results are reproduced in Fig. 5.6.

Without going into the experimental details, we focus here on the conclusions of their work. As can be seen in Fig. 5.6 c), the energy diagram they obtain from their measurements exactly reproduces the one we derived from theoretical considerations in Fig. 5.4 b), when spin-orbit coupling is taken into account. In particular the lifting of the four-fold degeneracy and the splitting in two doublets at zero field is a clear

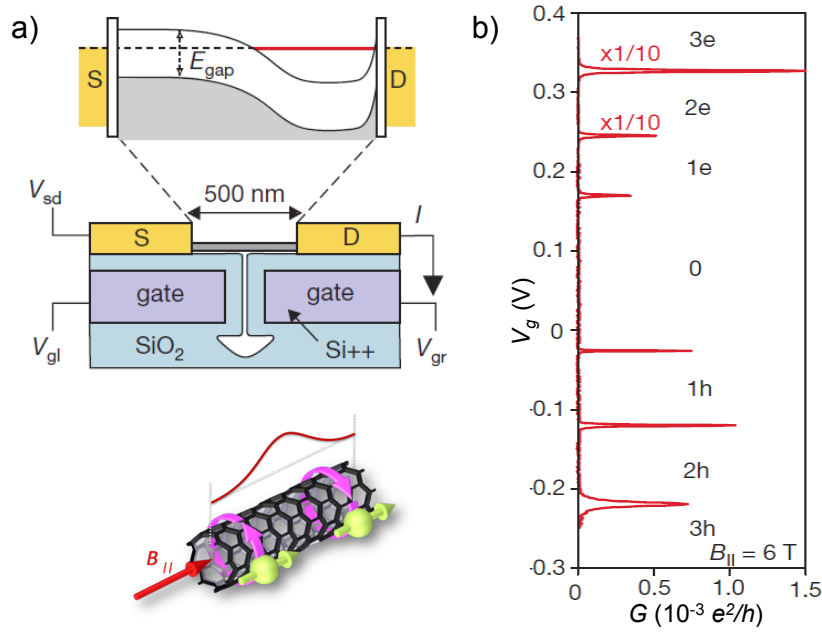


Figure 5.5: Experimental device used by Kuemmeth *et al.* (Adapted from [70]). a) A single nanotube is contacted between source and drain electrodes, separated by 500 nm, and is gated from below by two gate electrodes made of highly p-doped silicon. The two gate voltages (V_{gl} , V_{gr}) are used to create a quantum dot localized either above the right or above the left gate electrode. The energy band diagram is shown for the first case, in which an electron is trapped above the right gate. b) The measured linear conductance, $G = dI/dV_{sd}$, as function of gate voltage, V_g , for a dot localized above the right gate ($B_{||} = 6$ T, temperature $T = 30$ mK). The number of electrons or holes in the dot is indicated. The conductance of the top two peaks is scaled by 1/10.

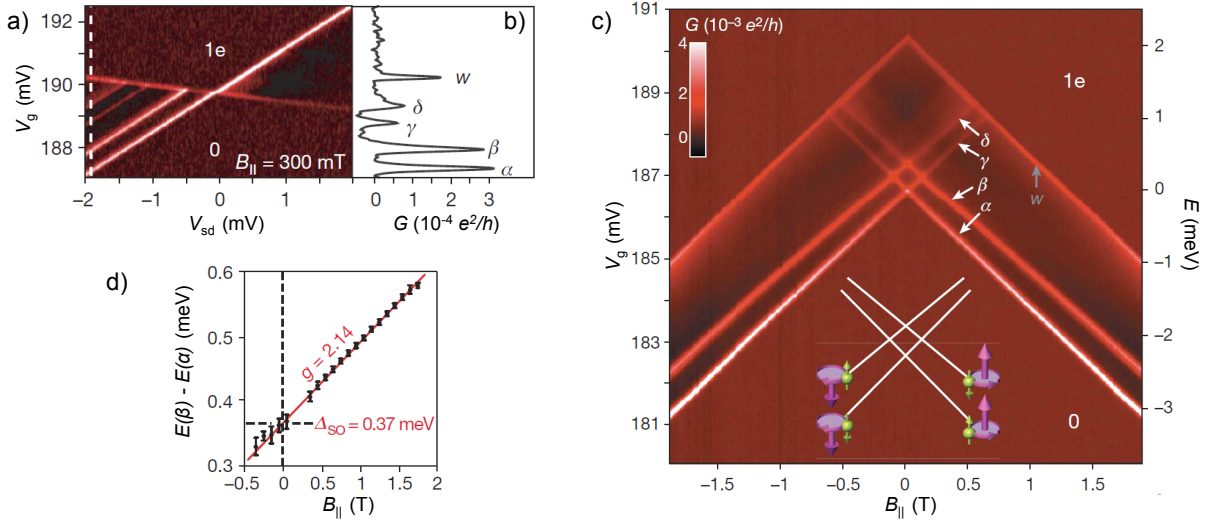


Figure 5.6: Experimental results from Kuemmeth *et al.* (Adapted from [70]): Excited-state spectroscopy of a single electron in a nanotube dot. a) Differential conductance, $G = dI/dV_{sd}$, measured as a function of gate voltage, V_g , and source-drain bias, V_{sd} , at $B_{||} = 300$ mT, displaying transitions from zero to one electron in the dot. b) A line cut at $V_{sd} = -1.9$ mV reveals four energy levels α , β , γ and δ as well as another peak w corresponding to the edge of the one-electron Coulomb diamond. c) $G = dI/dV_{sd}$, as a function of V_g and $B_{||}$ at a constant bias $V_{sd} = -2$ mV. The resonances α , β , γ , δ and w are indicated. They obtain the energy scale on the right by scaling ΔV_g with the conversion factor extracted from the slopes in a). Inset: orbital and spin magnetic moments they assign to the observed states. d) Energy splitting they extract between the states α and β as a function of $B_{||}$ (dots). The linear fit (red line) gives a Zeeman splitting with $g = 2.14 \pm 0.1$, and a zero-field splitting of $\Delta_{SO} = 0.37 \pm 0.02$ meV.

signature of non-vanishing SOI. From the slope of the energy shift with magnetic field they can assign to each state its spin and orbital magnetic moments, and subsequently confirm their parallel and anti-parallel configuration in each doublet.

In addition to this qualitative observations, they obtain a very valuable quantitative estimation of the zero-field splitting $\Delta_{\text{SO}} = 0.37 \pm 0.02$ meV. Since they estimate the diameter of their nanotube to be ~ 5 nm, and since Δ_{SO} scales inversely with the diameter d , we can deduce a value of $\Delta_{\text{SO}}^e \approx 1.9/d$ meV/nm for electrons. The splitting for holes is found to be slightly smaller, $\Delta_{\text{SO}}^h \approx 1.6/d$ meV/nm. Finally they confirm the breaking of the electron-hole symmetry by mapping also the first hole energy levels under a magnetic field.

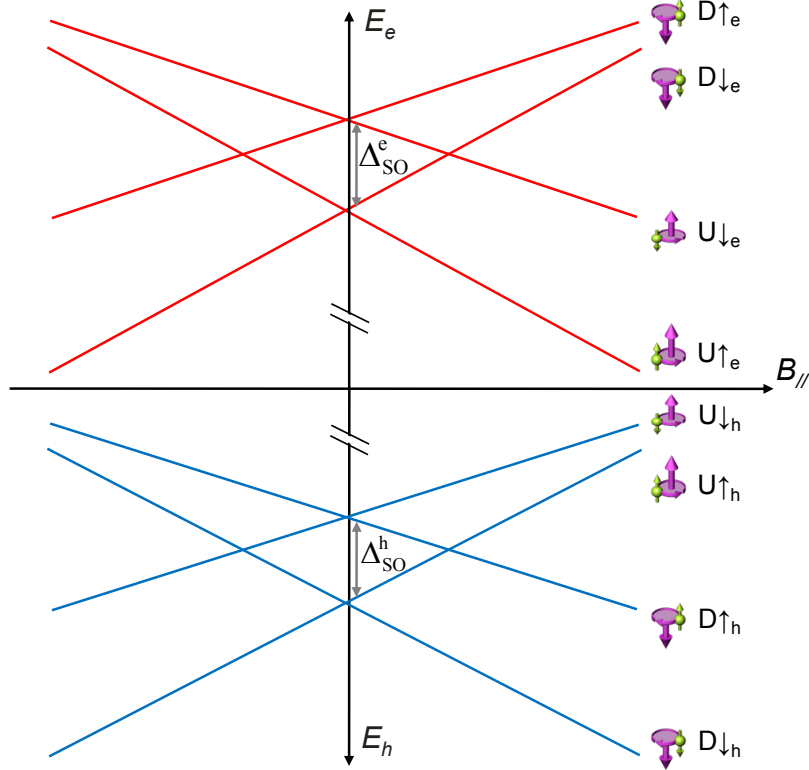


Figure 5.7: First electron and first hole energy levels as a function of the external longitudinal magnetic field B_{\parallel} , as expected from the theory and confirmed by the experiment. We introduce the notation that we will use in the next sections.

We summarize the conclusions of this section in Fig. 5.7 with a plot of the first electron and first hole energy levels as a function of the magnetic field, according to the agreeing theory and experimental data. Electron-hole symmetry would imply that the energy diagram for the first hole should be the mirror image of the electron levels about the horizontal axis. This, however, is not the case, indicating the breaking of the particle-hole symmetry typical of graphene. As a result, whereas the ground state of a single electron in the SWNT-QD at zero magnetic field corresponds to a parallel orientation of its spin and orbital magnetic moments, the lowest hole state favors on the contrary anti-parallel configurations.

5.2 Optical Spin Pumping

Our goal in this section is to show that the non-vanishing spin-orbit interaction and the resulting electron-hole symmetry breaking in carbon nanotubes allow for optical spin pumping of a SWNT-QD electron spin using resonant laser fields. We first present our scheme and build a simplified model of the optically-addressed singly-charged SWNT-QD as a 4-level system. We propose a Hamiltonian including all coherent processes and add the relaxation terms to obtain optical Bloch-equations for the time evolution of the density matrix. Next we perform the numerical calculations of the steady-state populations and the optical polarization for realistic parameters and different magnetic fields, showing that high fidelity spin-state preparation is readily achievable. We finally discuss possible complications to the 4-level system and relaxation pathways assumed here, and conclude by suggesting interesting perspectives for applications in quantum information.

5.2.1 Presentation of the scheme and the model

Introduction

Let us begin by recalling the results of the previous section and introducing our scheme and notations in Fig. 5.8 a). U and D label states from different valleys K' and K according to the direction of their orbital moment, i.e. to the clockwise or anti-clockwise circular motion of the electron around the nanotube circumference. Similarly, the spin projection along z is used for the spin eigenbasis (\uparrow, \downarrow), eigenstates of the operator \hat{s}_z with eigenvalues $(+1, -1)$. The subscripts “e” or “h” denote electron or hole states, respectively.

As we just saw, the first electron and hole states in a (weakly confined) SWNT-QD couple to the axial component of the external magnetic field simultaneously through their orbital magnetic moment μ_{orb} and their spin magnetic moment μ_S . The first coupling is responsible for the Aharonov-Bohm splitting Δ_{AB} between states U and D from different valleys, whereas the second gives rise to the Zeeman splitting Δ_Z between states of opposite spin along z . Because even for small-diameter nanotubes ($d \sim 1$ nm) we have $|\mu_{\text{orb}}| > |\mu_S|$, the slope due to the Aharonov-Bohm effect is steeper than the one due to the Zeeman effect.

In the presence of spin-orbit interaction the four-fold degeneracy expected at zero-field is lifted and a splitting appears between states with parallel ($U\uparrow$ and $D\downarrow$) and anti-parallel ($D\uparrow$ and $U\downarrow$) orbital and spin magnetic moments. This energy splitting is not obligatory the same for electrons and holes, so we assume two possibly different values Δ_{SO}^e and Δ_{SO}^h . Moreover it was shown by Kuemmeth *et al.* [70] that the lowest hole state has the opposite configurations than the lowest electron state (breaking electron-hole symmetry).

The existence of the zero-field splitting leads to new features in the energy diagram of Fig. 5.8 a), namely two level-crossings (for each direction of B_{\parallel}). The first crossing involves states with identical spins originating from different valleys. In an ideal defect-free carbon nanotube, the K - K' symmetry is perfect and the states should just cross without mixing. However, even in “ultra-clean” nanotubes studied by Kuemmeth *et al.*, they observe a small anti-crossing and a corresponding splitting

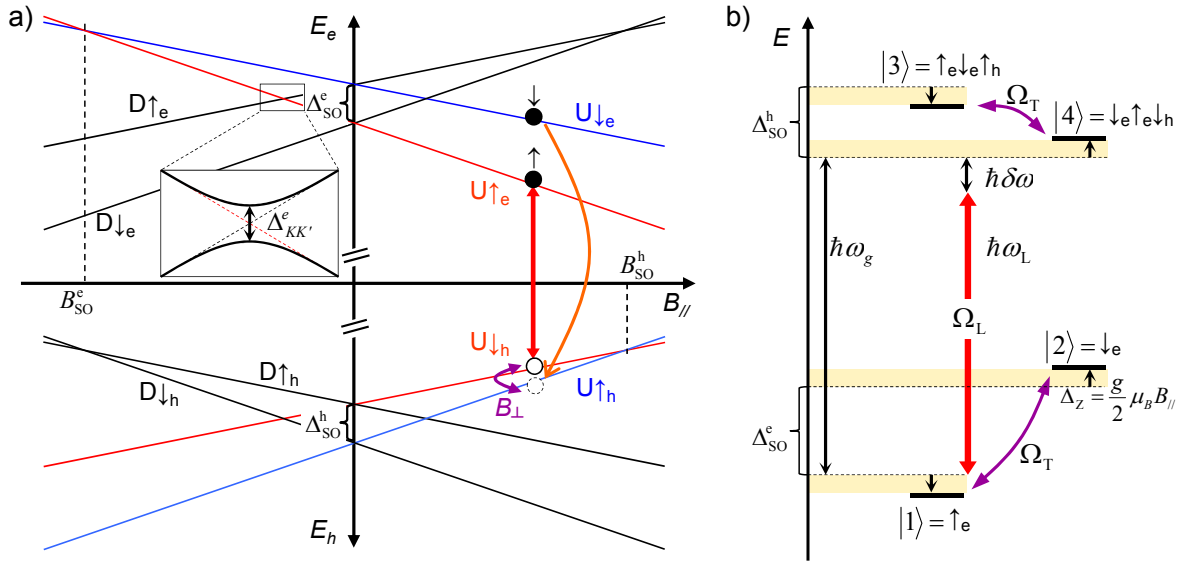


Figure 5.8: a) Energy diagram of the lowest electron and hole states in a nanotube quantum dot as a function of the applied axial magnetic field B_{\parallel} . We assume that a strong enough magnetic field is applied to lift the valley degeneracy and focus on the two lowest electron and hole levels. b) Simplified energy level diagram of a singly charged quantum dot under this assumption, showing only the directly accessible optically excited states (numbered 1 to 4) and the coherent couplings between them (entering the Hamiltonian part of the master equation). Because of the Aharonov-Bohm flux, the effective optical gap is given by: $\hbar\omega_g = E_g - 2\mu_{\text{orb}}B_{\parallel}$, where E_g is the gap at zero field (see also Fig. 5.2).

$\Delta_{KK'}$. This effect will be neglected in a first time, but we shall discuss it in the third subsection.

The second crossing is of higher significance for our purpose. When the Zeeman splitting equals the spin-orbit splitting for holes or electrons, the two spin eigenstates are degenerate and a coherent interaction can efficiently couple them and lead to ultra-fast spin-flip. This situation occurs for the axial magnetic fields:

$$B_{SO}^{e,h} = \Delta_{SO}^{e,h}/(g\mu_b) \quad (5.17)$$

Such a coherent spin-flip interaction can be provided for by a perpendicular component B_\perp of the magnetic field (orthogonal to the nanotube axis). It is represented as a purple double arrow in Fig. 5.8.

Model: the 4-level system and its Hamiltonian

Assuming that a strong enough axial magnetic field is applied, the valley degeneracy can be completely lifted and we may consider only the lowest two electron states ($U\uparrow_e$ and $U\downarrow_e$) and lowest two hole states ($U\downarrow_h$ and $U\uparrow_h$) of the SWNT-QD. An appropriately tuned laser field, polarized along the nanotube axis z , couples electron and hole states from the same valley ($U \rightarrow U$ or $D \rightarrow D$ transitions) and opposite spins, so that optically excited pairs have zero total spin projection along z ($\uparrow_e\downarrow_h$ or $\downarrow_e\uparrow_h$).

Considering now a singly-charged SWNT-QD containing a resident electron, we can restrict our analysis to the four-level system presented in Fig. 5.8 b). the two ground states are the two possible spin states of the electron (we drop here the U index for clarity): $|1\rangle = \uparrow_e$ and $|2\rangle = \downarrow_e$. The optically excited states are the two trions: $|3\rangle = \uparrow_e\downarrow_e\uparrow_h$ and $|4\rangle = \downarrow_e\uparrow_e\downarrow_h$, in which the two electrons form a singlet state, so that the net spin corresponds to the hole's one. With this labeling of the states it is convenient to define the matrices

$$\hat{\sigma}_{ij} = |i\rangle\langle j|, \quad i, j = 1, 2, 3, 4 \quad (5.18)$$

The full Hamiltonian of the system is decomposed as follows:

$$\mathcal{H}_{\text{full}} = (\mathcal{H}_0 + \mathcal{H}_B^\parallel) + (\mathcal{H}_{SO} + \mathcal{H}_Z) + (\mathcal{H}_B^\perp + \mathcal{H}_{\text{Laser}}) \quad (5.19)$$

The first part ($\mathcal{H}_0 + \mathcal{H}_B^\parallel$) defines the effective energy gap $\hbar\omega_g$ shown in Fig. 5.8 b) for a given axial magnetic field B_\parallel :

$$\mathcal{H}_0 + \mathcal{H}_B^\parallel = (E_g - 2\mu_{\text{orb}}B_\parallel)(\hat{\sigma}_{33} + \hat{\sigma}_{44}) = \hbar\omega_g(\hat{\sigma}_{33} + \hat{\sigma}_{44}) \quad (5.20)$$

\mathcal{H}_0 describes the electronic band structure of the nanotube at zero magnetic field and without spin-orbit interaction, and the SWNT-QD confinement, leading altogether to an effective optical gap E_g . Under an axial magnetic field, the Aharonov-Bohm effect represented by \mathcal{H}_B^\parallel modifies this energy gap to $\hbar\omega_g = E_g - 2\mu_{\text{orb}}B_\parallel$. This part of the Hamiltonian will play a minor role since it will be eliminated when we later do the rotating-wave approximation (RWA).

The second part ($\mathcal{H}_{SO} + \mathcal{H}_Z$) also consists of purely diagonal terms leading to further energy detunings between the different levels. The zero-field spin-orbit induced level splitting is described by:

$$\mathcal{H}_{\text{SO}} = \Delta_{\text{SO}}^e \hat{\sigma}_{22} + \Delta_{\text{SO}}^h \hat{\sigma}_{33} \quad (5.21)$$

whereas the Zeeman splitting under a magnetic field is:

$$\mathcal{H}_Z = -\frac{g}{2}\mu_b B_{\parallel} \hat{s}_z = -\frac{g}{2}\mu_b B_{\parallel} (-\hat{\sigma}_{11} + \hat{\sigma}_{22} - \hat{\sigma}_{33} + \hat{\sigma}_{44}) \quad (5.22)$$

where we have translated the spin Pauli matrix \hat{s}_z into our 4-level matrix notation. we note here that these terms are responsible for the above-mentioned crossing when the Zeeman splitting just cancels the electron or hole zero-field splitting.

The third part represents the off-diagonal elements (i.e. the coherent couplings). The perpendicular component of the magnetic field induces a coherent interaction between spin eigenstates:

$$\mathcal{H}_B^{\perp} = g\mu_b B_{\perp} \hat{s}_x = \hbar\Omega_T (\hat{\sigma}_{12} + \hat{\sigma}_{21} + \hat{\sigma}_{34} + \hat{\sigma}_{43}) \quad (5.23)$$

where we have defined the coupling rate $\Omega_T = g\mu_b B_{\perp}/\hbar$. The laser field polarized along the nanotube axis, with optical frequency ω_L and Rabi frequency Ω_L , leads to the term:

$$\mathcal{H}_{\text{Laser}} = \mathcal{H}_{\text{Laser}}(t) = \hbar\Omega_L \cos(\omega_L t) (\hat{\sigma}_{13} + \hat{\sigma}_{31} + \hat{\sigma}_{24} + \hat{\sigma}_{42}) \quad (5.24)$$

We define the detuning $\delta\omega = \omega_g - \omega_L$. Since the energy scale $\hbar\omega_g$ is much larger than all other energy detunings and coupling strengths in the system, it is legitimate to use the rotating-wave approximation (RWA) to eliminate the fast oscillating terms and conserve only the terms with frequency $\delta\omega$. This is achieved by the unitary transformation given by the matrix:

$$\mathcal{U} = \hat{\sigma}_{11} + \hat{\sigma}_{22} + e^{i\omega_g t} (\hat{\sigma}_{33} + \hat{\sigma}_{44}) \quad (5.25)$$

In the new basis the new Hamiltonian is:

$$\mathcal{H}_{\text{RWA}} = \mathcal{U}\mathcal{H}\mathcal{U}^{\dagger} - i\hbar\mathcal{U}\frac{\partial\mathcal{U}^{\dagger}}{\partial t} = \mathcal{U}\mathcal{H}\mathcal{U}^{\dagger} - \hbar\omega_L\mathbb{I}_{4\times 4} \quad (5.26)$$

with $\mathbb{I}_{4\times 4}$ designing the 4×4 identity matrix. Substituting $\cos(\omega_L t) = \frac{1}{2}(e^{i\omega_L t} + e^{-i\omega_L t})$ in (5.26) and eliminating the term oscillating at high frequencies: $\pm(\omega_g + \omega_L)$, we finally obtain our effective *time-independent* Hamiltonian:

$$\mathcal{H} = \mathcal{H}_{\text{SO}} + \mathcal{H}_Z + \mathcal{H}_B^{\perp} + \mathcal{H}_L \quad (5.27)$$

with the new (time-independent) expression for the interaction with the laser field:

$$\mathcal{H}_L = \frac{\hbar\Omega_L}{2} (\hat{\sigma}_{13} + \hat{\sigma}_{31} + \hat{\sigma}_{24} + \hat{\sigma}_{42}) \quad (5.28)$$

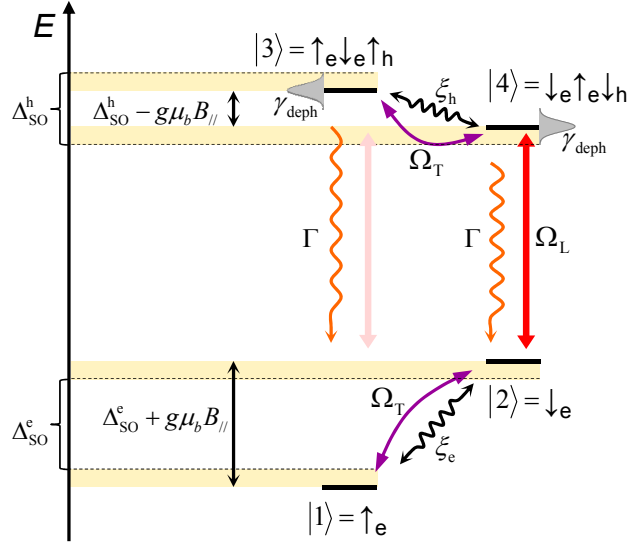


Figure 5.9: Diagram of the four-level system showing all relaxation terms we include in the master equation. γ_{deph} is a pure-dephasing rate responsible for the observed linewidth of the optical transitions.

Relaxation mechanisms and master equation

We now turn to the different relaxation mechanisms present in the system. These terms lead to population decay and decoherence and cannot be included in the hermitian Hamiltonian describing the coherent evolution. They enter the master equation through the non-hermitian Lindblad operators \mathcal{L}_j . The relevant relaxation pathways and rates are represented in Fig. 5.9.

- The lifetimes of the optically-excited states $|3\rangle$ and $|4\rangle$ are assumed to be identical and are described by the decay rate Γ from $|3\rangle$ to $|1\rangle$ and from $|4\rangle$ and $|2\rangle$. It accounts for both radiative and non-radiative decays.
- Incoherent spin-flip events can occur due to co-tunneling (interaction with the electrons in the leads) or more probably through hyperfine interaction with the fluctuating nuclear field from residual carbon 13 nuclei. Such processes are described by the rates ξ_e and ξ_h ; they are expected to be slow compared to other rates in our system.
- Finally, for a realistic account of the experimental PL linewidths, we introduce a Markovian pure-dephasing of the optical transition: $\gamma_{\text{deph}} \gg \Gamma$. We will moreover contemplate two possible situations in the following subsection, depending on whether or not the coherence between the two trions $|3\rangle$ and $|4\rangle$ also undergoes dephasing at the same rate. This may not be the case if the interaction causing pure-dephasing is insensitive to the spin degree of freedom, as is probably true for phonon-induced decoherence.

We can finally write a master equation of the Lindblad form for the time-evolution of the system:

$$\frac{\partial}{\partial t} \hat{\rho}(t) = \frac{i}{\hbar} [\hat{\rho}(t), \mathcal{H}] + \mathcal{L}[\hat{\rho}(t)] \quad (5.29)$$

where $\hat{\rho}_{ij}(t) = \rho_{ij}(t) \hat{\sigma}_{ij}$ is the density matrix of the four-level system and \mathcal{L} is the Lindblad super-operator accounting for all the above-mentioned relaxations.

5.2.2 Numerical simulations

Methodology

From the master equation (5.29) one gets a set of 16 differential equations for the 16 components of the 4×4 density matrix: $\frac{\partial}{\partial t}\rho_{ij}(t) = \dots$. Since the density matrix has to be Hermitian, only 6 of the 12 off-diagonal elements are independent. Moreover the diagonal elements are real positive numbers corresponding to the populations of the states. In a closed system, the sum of the populations (or occupation probabilities) is constant and normalized to one: $\sum_j \rho_{jj}(t) = 1$, at all time. As a result only 3 of the 4 diagonal elements are independent. Finally, we have a system of 9 independent linear differential equations plus a normalization condition.

We are not interested in solving the real-time dynamics of the system, but we just want to calculate the steady-state solution. Therefore we have to solve equation (5.29) for: $\rho_{ij}(t) = \text{constant}$, meaning $\frac{\partial}{\partial t}\rho_{ij}(t) = 0$, $\forall i, j$. After re-ordering the elements ρ_{ij} in a single vector, we obtain a system of linear equations expressed in a matrix form. Solving it requires the diagonalization of the system's matrix, which is easily carried out numerically in Matlab.

The quantities of interest we then extract from the calculated steady-state density matrix are:

- The steady-state populations of the two single-electron ground states: $|1\rangle = \uparrow_e$ and $|2\rangle = \downarrow_e$, given by ρ_{11} and ρ_{22} , respectively.
- The scattering rate of the laser light, which is proportional to: $\Im(\rho_{13} + \rho_{24})$. For meaningful interpretation, this quantity has to be normalized to the scattering rate in the absence of spin pumping (for example by setting $B_\perp = 0$, see next section). This is the quantity measured during a differential-transmission experiment, in which the laser frequency is tuned over the SWNT-QD resonance(s) while monitoring the transmitted light intensity with a photodiode.

Parameters' values

In order for our proposal to fulfill realistic requirements imposed by current optical technologies, we choose to consider a quantum dot defined on a semiconducting carbon nanotube with a diameter: $d \sim 1.2$ nm, therefore having its lowest optical transition in the near-infrared ($\sim 1.5 \mu\text{m}$)³, i.e. in the telecommunication window. In addition to ensuring the existence of suitable equipments at this wavelength (although NIR single photon detectors are not well developed), this would make such a device potentially useful for quantum communication and information processing.

We now briefly present the values we use for the system's parameters in the simulations.

- To determine the orbital and spin magnetic moments and the spin-orbit splittings for electrons and holes, we refer to the latest published experimental data [70, 75] and use the scaling laws predicted by the theory to derive numbers for our particular nanotube's diameter. The transport measurements under magnetic field reported in [75] yield an orbital magnetic moment: $\mu_{\text{orb}} \approx 0.3 \cdot d[\text{nm}] \text{ meV/T}$, which mean for our nanotube: $|\mu_{\text{orb}}| = 0.36 \text{ meV/T}$.

3. Confinement in the quantum dot will of course lead to a small energy shift compared to the bare nanotube transition, but its relative magnitude is small.

In the work presented in section 5.1.3 [70], the authors measure similar g -factors for electrons and holes both close to $g = 2$, which is the value we adopt, yielding: $|\mu_S| = 0.06$ meV/T. From the spin-orbit splittings they report we expect for a diameter $d = 1.2$ nm: $\Delta_{\text{SO}}^e \approx 1.5$ meV for electrons and $\Delta_{\text{SO}}^h \approx 0.9$ meV for holes. From these numbers we deduce the axial magnetic fields at which the electron and trion states with opposite spins cross (see Fig. 5.8 a)):

$$B_{\text{SO}}^e = -\Delta_{\text{SO}}^e/(g\mu_b) = -12.5 \text{ T} \quad \text{and} \quad B_{\text{SO}}^h = \Delta_{\text{SO}}^h/(g\mu_b) = 7.5 \text{ T}$$

- The decay rate Γ of both excited states is given by the PL lifetime; we can therefore use the value measured in our own experiments ($1/\Gamma \approx 40$ ps) and take: $\Gamma/2\pi = 4$ ns⁻¹. The pure dephasing rate γ_{deph} is responsible for the broader linewidths actually observed. Importantly, we consider here a weakly confined SWNT-QD and the results presented in chapter 3 do not apply. This means that the PL linewidth should be close to the one of a free exciton. Recent experiments in our lab on HiPco nanotubes have revealed narrow PL peaks down to 120 μeV FWHM. We therefore assume the value $\hbar\gamma_{\text{deph}} = 0.25$ meV (i.e. $\gamma/2\pi = 15$ $\Gamma = 60$ ns⁻¹), which is supported by reports from other groups.
- The last unknown rates are the electron and hole spin relaxations. One cause of relaxation is hyperfine interaction with carbon 13 nuclear spins, but it is expected to be very slow, and can be made arbitrarily small by growing pure carbon 12 nanotubes. The dominant rate is likely to be spin-orbit-mediated, phonon-assisted spin-flip processes. Estimations in [73] predict rates varying from 1 μs^{-1} to slower than 1 ms⁻¹, and we choose the safe side by assuming $\xi_e = \xi_h = (2\pi) 0.1 \mu\text{s}^{-1}$.

The remaining parameters all correspond to experimental “knobs” that can be tuned and varied: the magnetic field components B_{\parallel} and B_{\perp} , the laser Rabi-frequency Ω_L (proportional to the laser intensity) and the laser detuning $\hbar\delta\omega = \Delta_{\text{SO}}^e$. In all simulations we keep the Rabi-frequency $\Omega_L \sim \Gamma/10$ below saturation, and all the results obtained do not depend significantly on the precise value of Ω_L as long as this condition is fulfilled.

Results

We use the commercial software Matlab to solve numerically the steady-state optical Bloch equations and plot the quantities of interest for different sets of experimental control-variables. The implementation of optical spin-pumping relies on differential-transmission experiments as mentioned in the previous section. Before analyzing complete simulated laser-transmission curves obtained during frequency-scans, we focus on the maximal spin-state preparation fidelity that can be achieved when the laser is tuned on the lower-energy transition $|2\rangle \rightarrow |4\rangle$. For this we set $\hbar\delta\omega = \Delta_{\text{SO}}^e$ (see Fig. 5.8 b)) and calculate the steady-state population difference $\Delta\rho \doteq \rho_{11} - \rho_{22} = \rho_{\uparrow e} - \rho_{\downarrow e}$ under a wide range of axial and perpendicular magnetic fields. Figure 5.10 presents the most important result of our work.

The only difference between panels a) and b) is whether or not the coherence between the two optically-excited states is conserved by the pure-dephasing mechanism described by the rate γ_{deph} . It is an important check for the credibility of our claims that the two scenarios offer qualitatively and quantitatively very similar

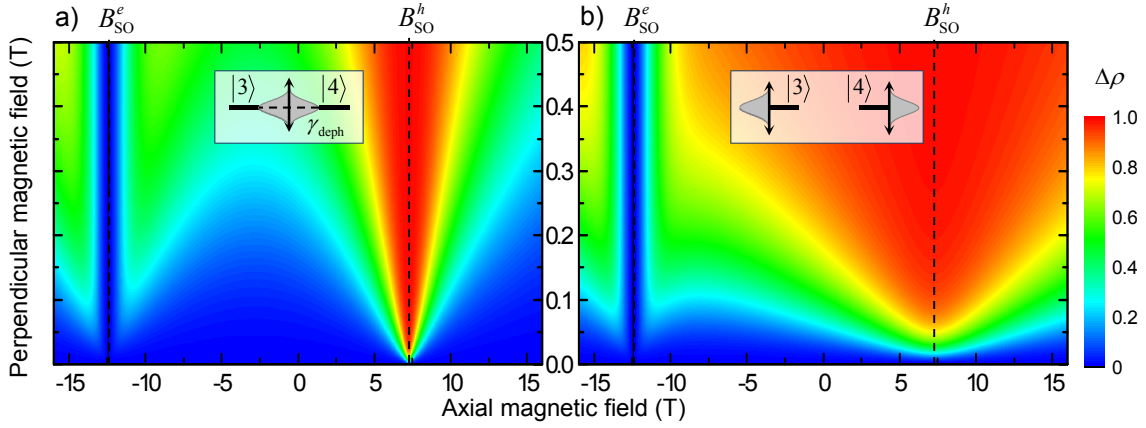


Figure 5.10: Color map of the spin-state preparation fidelity (i.e. the steady-state population difference $\Delta\rho = \rho_{11} - \rho_{22}$ between $|1\rangle = \uparrow_e$ and $|2\rangle = \downarrow_e$) as a function of the external magnetic field components B_{\parallel} (horizontal axis) and B_{\perp} (vertical axis). The laser is resonant with the transition: $|2\rangle \rightarrow |4\rangle$ (the detuning is $\hbar\delta\omega = \Delta_{\text{SO}}^e$). In a) pure-dephasing is assumed to conserve the coherence between the two trion states. In b) this coherence also undergoes fast dephasing at rate γ_{deph} . The axial magnetic field values B_{SO}^e and B_{SO}^h correspond to the level crossings indicated in Fig. 5.8 a).

results. We choose to concentrate from now on on the second case (panel b) in Fig. 5.10), since it is quite likely that the excited trions undergo faster dephasing than the single-electron ground states.

The first obvious feature is the existence of a wide range of magnetic fields for which a population transfer approaching unity is readily achievable, as evidenced by the large red areas in Fig. 5.10. More precisely, the favorable region is centered on a vertical line $B_{\parallel} = B_{\text{SO}}^h = 7.5$ T, when the axial magnetic field value is such that the two trion states are in resonance. Around this line, even a small perpendicular magnetic field component of a few hundreds of mT is enough to induce a sufficient spin-precession rate of the hole in the trion and lead to high fidelity spin-state preparation of the SWNT-QD electron.

On the contrary, we observe a blue band centered on $B_{\parallel} = B_{\text{SO}}^e = -12.5$ T where spin-pumping remains impossible at any perpendicular magnetic field, hinting at a very efficient electron-spin randomization mechanism.

To gain better understanding of these features we present in Fig. 5.11 the level diagrams corresponding to the two particular configurations $B_{\parallel} = B_{\text{SO}}^e$ and $B_{\parallel} = B_{\text{SO}}^h$. When $B_{\parallel} = B_{\text{SO}}^e$, the two electron-spin ground states are in resonance and are efficiently mixed by the perpendicular magnetic field. Spin is therefore randomized in spite of optical pumping, leading to $\rho_{11} = \rho_{22}$ and explaining the blue region in Fig. 5.10.

In contrast, when $B_{\parallel} = B_{\text{SO}}^h$, resonant coupling occurs between the trion states and allows for very efficient spin-flip Raman transition (represented by the curved red arrow in Fig. 5.11). This inelastic scattering process corresponds to the sequence:

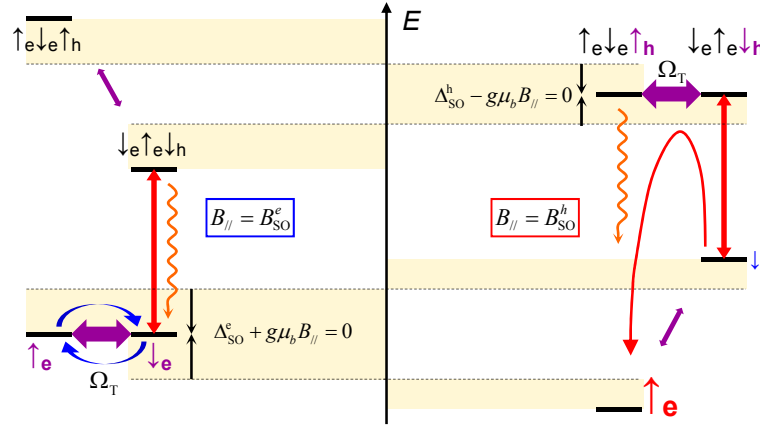


Figure 5.11: Simplified picture of the spin pumping mechanism for the two resonance conditions $B_{\parallel} = B_{\text{SO}}^e = \Delta_{\text{SO}}^e/(g\mu_b)$ (left) and $B_{\parallel} = B_{\text{SO}}^h = \Delta_{\text{SO}}^h/(g\mu_b)$ (right). The laser is tuned on the “red” (lower energy) transition: $\hbar\delta\omega = \Delta_{\text{SO}}^e$.

laser excitation \rightarrow spin precession \rightarrow decay, and results in population transfer from $|2\rangle = \downarrow_e$ to $|1\rangle = \uparrow_e$. Using rate equation we can show that in the absence of any broadening or spin relaxation the effective rate for this process is proportional to:

$$\gamma_{\uparrow\downarrow} \propto \frac{B_{\perp}^2}{(\Delta_{\text{SO}}^h - g\mu_b B_{\parallel})^2} \quad (5.30)$$

We indeed see that this rate diverges for $\Delta_{\text{SO}}^h \sim g\mu_b B_{\parallel}$, i.e. for $B_{\parallel} \sim B_{\text{SO}}^h$, accounting for the very efficient spin-flip mechanism. In addition, the large energy detuning between \uparrow_e and \downarrow_e states ensures weak mixing and slow spin depolarization, resulting in very high fidelity for spin-state preparation.

To conclude this section on spin-state preparation we present some calculations of the directly accessible experimental quantity, namely the rate of laser light scattering by the SWNT-QD. In a differential-transmission experiment, a weak laser is slowly tuned over the QD optical resonance. The transmitted light intensity is monitored by a photodiode placed below the sample, revealing how much light is resonantly scattered by the QD. The acquisition time of the signal during each frequency step is much longer than all physical time scales in the system so that steady-state properties are measured.

The amplitude of the actual signal naturally depends on the optical cross-section of the quantum-dot and on experimental characteristics such as the laser spot size and the collection efficiency. Even with light focused to the diffraction-limit and high numerical apertures, the contrast is usually very low, and amplification techniques such as lock-in modulation have to be used. The resulting data are plotted as transmission curves against the laser energy, like the black solid lines simulated in Fig. 5.12.

Let us first consider the situation at zero perpendicular magnetic field (Fig. 5.12 (a), point A in (c)). Since the spin relaxation rates $\xi_{e,h}$ are very slow, the two optical transitions form two almost isolated 2-level systems. The Rayleigh scattering line-shape of each transition is a Lorentzian of width $\hbar\gamma_{\text{deph}}$ and we do

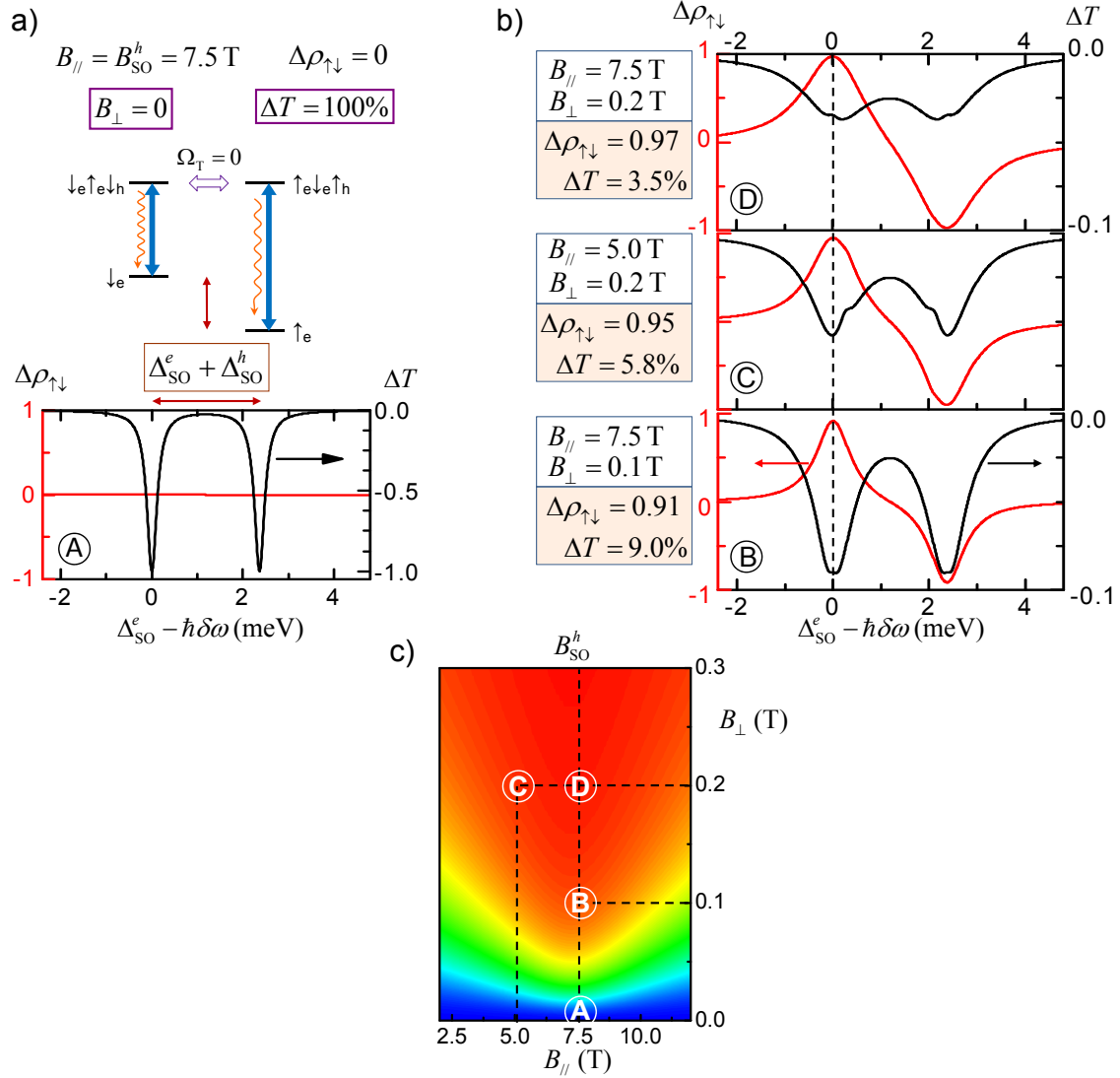


Figure 5.12: Differential transmission and spin preparation during laser scans. a) In the absence of perpendicular magnetic field, no mixing occurs between the spin states and we have actually two independent 2-level systems. A simulated laser scan displays two Lorentzian transmission dips detuned by the energy $\Delta_{SO}^e + \Delta_{SO}^h$. We use the depth of these dips as a reference to normalize the differential transmission ΔT . b) Simulated laser scans for different magnetic field configurations (indicated in c) on the fidelity map extracted from Fig. 5.10 b)) presenting the population difference $\Delta\rho_{\uparrow\downarrow} = \rho_{11} - \rho_{22}$ (red solid lines) and normalized laser transmission ΔT (black solid lines). We report these values at $\Delta_{SO}^e - \hbar\delta\omega = 0$ in each case (when the laser is resonant with the lower energy transition).

obtain two corresponding dips in the calculated transmission. They are detuned by the energy $\Delta_{\text{SO}}^e + \Delta_{\text{SO}}^h$ as expected. Note that this detuning is independent of the magnetic field.

We now switch-on a perpendicular magnetic field mixing the spin states $s_z = \pm 1$ and keep the axial magnetic field close to the trion crossing point B_{SO}^h . As explained in the previous paragraphs, efficient spin-flip Raman transition leads to spin population transfer into state \uparrow_e . In other words, the single electron trapped in the SWNT-QD has with very high probability (that is, most of the time) his spin pointing up (\uparrow_e). Because of Pauli exclusion principle, it is impossible to excite another electron with spin up also occupying the QD ground state. Therefore, the only optically-allowed transition is to the trion $|3\rangle = \uparrow_e \downarrow_e \uparrow_h$, but it is largely detuned (by the energy $\Delta_{\text{SO}}^e + \Delta_{\text{SO}}^h$) and completely off-resonance from the laser light. The reverse spin-flip Raman rate is thus extremely slow. This results in vanishing scattering of the incoming laser field, which is directly measurable as increased differential-transmission: the QD becomes transparent to the laser.

Figure 5.12 b) presents the simulated laser scans for three different magnetic field configurations at which spin-pumping takes place. We also plot on the same graphs the calculated population imbalance $\Delta\rho$. As expected, when the laser detuning is $\hbar\delta\omega = \Delta_{\text{SO}}^e$, the spin population is transferred to state \uparrow_e and laser transmission drops below 10 % of its value in the absence of spin-pumping. The experimental observation of this drop in absorption is the signature of optical spin pumping, and its magnitude is a measure of the spin-state preparation fidelity.

We point out that optical pumping into the other electron spin state (\downarrow_e) with the same level of fidelity is straightforward, by just tuning the laser on the “blue” (higher energy) transition: ($|1\rangle = \uparrow_e \rightarrow |3\rangle = \uparrow_e \downarrow_e \uparrow_h$). This corresponds to the laser detuning $\hbar\delta\omega = -\Delta_{\text{SO}}^h$ (see Fig. 5.8 b)). The associated features are indeed clearly observed in Figure 5.12 b), with $\Delta\rho$ approaching -1 and a corresponding suppression of the laser absorption peak. This is completely expected and in accordance with the perfect symmetry of our system model with respect to the reversal of the spin along z .

We finally stress that the critical requirement for the realization of optical spin pumping is the breaking of the electron-hole symmetry resulting from the spin-orbit interaction. This is quite obvious that our scheme relies on a large enough energy detuning between the two optical transitions $|1\rangle \rightarrow |3\rangle$ and $|2\rangle \rightarrow |4\rangle$. The presence of electron-hole symmetry means in our notations: $\Delta_{\text{SO}}^h = -\Delta_{\text{SO}}^e$. The two transitions would then be degenerate, whatever the magnetic field, and spin-flip Raman scattering would always occur with identical rates in both directions. No net spin population imbalance would be created. The asymmetry induced by spin-orbit coupling in carbon nanotubes is therefore the key to our proposal for optical spin manipulation.

5.2.3 Discussion of possible complications

In this section we address several effects and unsettled issues that have been neglected in the calculations and may alter the possibility or the fidelity of optical

spin pumping.

K - K' mixing

In a pristine carbon nanotube the perfect symmetry between the two sublattices A and B is reflected in reciprocal space by the K - K' degeneracy. Long range disorder and smooth external potentials varying on length scales much longer than the interatomic distance $a_{CC} = 0.142$ nm do not perturb the A - B symmetry. The presence of lattice defects, however, like atomic vacancies or Stone-Wales defects⁴, breaks the A - B symmetry, which results in an effective mixing between the states from the K and K' valleys.

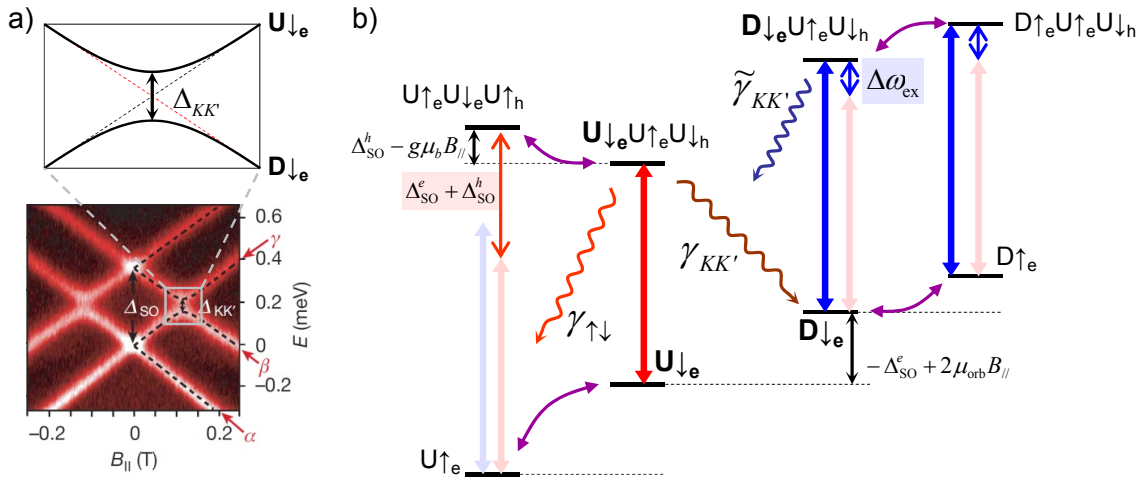


Figure 5.13: Effect of K - K' mixing on the spin-pumping scheme. a) Experimental data from [70] evidencing the avoided crossing between states from different valleys as a signature of K - K' coupling. b) Because of this mixing, the 4-level system we have considered so far has to be extended to account for the possibility of laser-assisted valley-flip $\gamma_{KK'}$.

Although investigating “ultra-clean” carbon nanotubes, F. Kuemmeth and co-workers did observe such an effect in their transport spectroscopy measurements, as reproduced in Fig. 5.13 a) [70]. In a carbon nanotube with unbroken K - K' symmetry, states from different valleys should cross without mixing when an axial magnetic field is applied. Experimental data however clearly reveal an avoided crossing with an energy gap $\Delta_{KK'}$ characterizing the strength of the K - K' coupling. In our spin-pumping scheme this valley-coupling will result in a finite probability for the electron spin to leave the Hilbert space spanned by $U\downarrow_e$ and $U\uparrow_e$.

To quantify this effect, we first define an effective magnetic field $B_{KK'}$ by: $g\mu_b B_{KK'} = \Delta_{KK'}$. We denote as before the effective spin-flip Raman scattering rate from state $U\downarrow_e$ to $U\uparrow_e$ with $\gamma_{\uparrow\downarrow}$. As shown in Fig. 5.13 b) we introduce an additional “valley-flip” Raman transition from $U\downarrow_e$ to $D\downarrow_e$ and note its effective rate:

4. the Stone Wales defect creates a pentagon and heptagon pair by rearrangement of the bonds.

$\gamma_{KK'}$. Using rate equations we obtain:

$$\frac{\gamma_{\uparrow\downarrow}}{\gamma_{KK'}} \approx \frac{B_{\perp}^2 / (\Delta_{SO}^h - g\mu_b B_{\parallel})^2}{B_{KK'}^2 / (\Delta_{SO}^e - 2\mu_{orb} B_{\parallel})^2} \quad (5.31)$$

which is maximum when $B_{\parallel} \rightarrow B_{SO}^h$.

We take for $\Delta_{KK'}$ the value measured in [70]: $\Delta_{KK'} = 65 \mu\text{eV}$ and evaluate expression (5.31) in the magnetic field range around $B_{\parallel} = B_{SO}^h$ where optical spin pumping is the most efficient (see Fig. 5.10). The resulting color plot is shown in Fig. 5.14 on a logarithmic scale. We see that a very broad region exists where the spin-flip rate $\gamma_{\uparrow\downarrow}$ remains more than three orders of magnitude faster than the valley-flip rate $\gamma_{KK'}$.

Even if $\gamma_{KK'} \ll \gamma_{\uparrow\downarrow}$, once the system goes through a valley-flip Raman scattering to state $D\downarrow_e$, the applied laser field will be detuned from the transition to the state $D\downarrow_e U\uparrow_e U\downarrow_h$ by an amount $\Delta\omega_{ex}$ (see Fig. 5.14 b)) due to the exchange terms of Coulomb interaction. The reverse valley-flip process $\tilde{\gamma}_{KK'}$ may therefore be very slow and the electron could be stuck

in the D valley. It may therefore be necessary to use a second re-pumping laser on this transition (blue in Fig. 5.14) to reintroduce the electron in the U valley. Another complication can still arise if $\Delta\omega_{ex} \sim \Delta_{SO}^h + \Delta_{SO}^e$ because this second laser would be close to resonance with the higher-energy transition of our 4-level system, thus inducing spin-pumping in the opposite direction to the first laser. Even in this worst-case scenario, since we have $\gamma_{KK'} \ll \gamma_{\uparrow\downarrow}$ it should be possible to use much weaker intensity for the blue laser. Unfortunately, we are not aware of any calculation nor experimental determination of the exchange coulomb interaction in trion states, so that it is difficult to estimate $\Delta\omega_{ex}$.

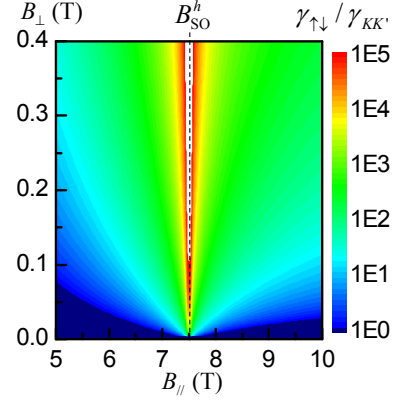


Figure 5.14: Ratio $\gamma_{\uparrow\downarrow}/\gamma_{KK'}$ from eq. (5.31)

Nature of the non-radiative decay

In most experiments it has been observed that the lifetime of excitons is more than an order of magnitude shorter than the predicted radiative lifetime. While radiative broadening can be enforced by embedding CNTs in cavity structures with a large Purcell factor [76], understanding the nature of non-radiative relaxation is crucial for identifying the limits of optical spin manipulation. In particular, if this relaxation is not spin-conserving, then spin pumping becomes efficient for an even larger range of applied magnetic field strengths. Most probable mechanisms for fast non-radiative decay proposed so far are phonon-assisted relaxation and/or multi-particle Auger processes [77]. Since these processes are spin conserving, they will not alter the efficiency of spin-pumping.

Strong confinement and phonon sidebands

A useful device for quantum information processing or quantum communication applications would exploit the spin-state of a single electron (or hole) as a qubit. For

this the implementation of a quantum-dot on a carbon nanotube is necessary, and it is one of our assumption that the confinement of the carriers in the axial dimension of the SWNT does not induce drastic changes in the electronic and optical properties of the pristine nanotube. Yet we demonstrated with experimental data and calculations in chapter 3 that strong confinement of the exciton enhances the interaction with acoustic phonons and results in broad and asymmetric emission/absorption line-shapes.

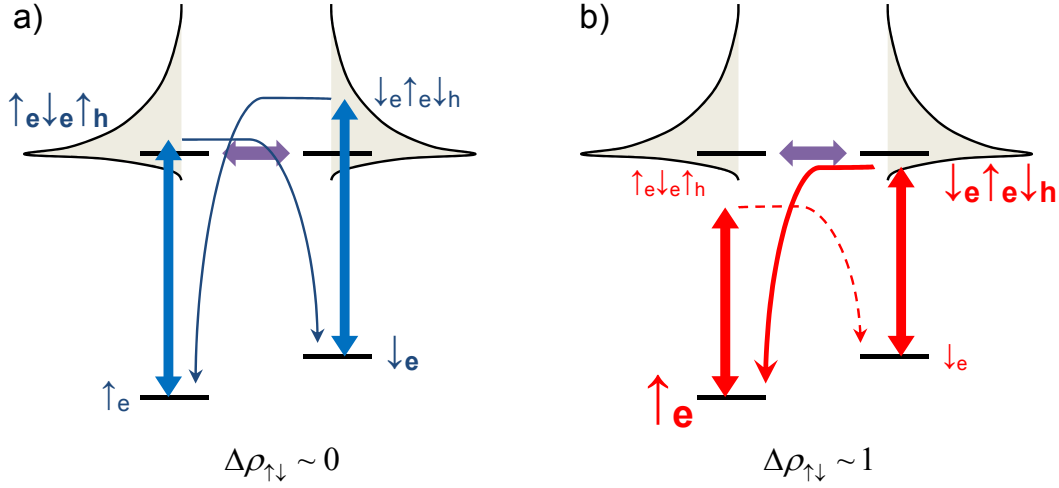


Figure 5.15: Optical spin-pumping in the presence of broad asymmetric absorption lines. a) A laser tuned on the blue transition also excites the red transition because of the phonon sideband in absorption. This results in two-way spin-flip processes and renders spin-pumping inefficient. b) To achieve high fidelity, we need to tune the laser on the red transition. The sharp red edge in absorption at low temperature ensures that the laser remains off-resonance with the blue transition, forbidding the reverse spin-flip Raman scattering.

It is of course legitimate to assume that the confinement potential is indeed smooth and has no effect on the free-exciton spectrum. Nevertheless, we want to show here that even in the case of strong confinement (i.e. on a length scale of ~ 10 nm) optical spin pumping with high fidelity is still possible, albeit restricted to a one-way transfer. This is schematically explained in Fig. 5.15 where we assume asymmetric absorption lines as expected for tightly localized trions. The blue tail in absorption that would persist at low temperature would hinder optical pumping into state \downarrow_e because both transitions would be effectively addressed by the laser (Fig. 5.15.a). On the contrary, tuning the laser on the red transition still enables high fidelity optical spin-state preparation in state \uparrow_e (Fig. 5.15.b). Indeed the absorption red tail is caused by processes where the missing photon energy is provided by the thermal phonon bath. The thermal population can be made vanishingly small at cryogenic temperatures, and the experimental data presented in chapter 3 actually reveal sharp transition edges at 4 K. Therefore the higher-energy optical transition remains unaddressed by the red-detuned laser, and spin-flip Raman scattering occurs unidirectionally.

Quantitatively, we measure linewidths at 4 K of 2-4 meV mainly due to the red tail in PL emission, corresponding to the blue tail in absorption. Since the energy detuning between the two optical transitions of the 4-level system is $\Delta_{\text{SO}}^h + \Delta_{\text{SO}}^e \approx 2.4$ meV, the situation depicted in Fig. 5.15 a) is quite realistic and the present discussion is highly relevant when addressing the limitations of spin pumping fidelity in strongly confined quantum-dots.

5.2.4 Extensions

Coherent spin manipulation

Having demonstrated how to prepare a single spin optically in a SWNT-QD with fidelity approaching unity, we briefly evoke coherent spin rotation and spin measurement. By using two laser fields satisfying two-photon Raman resonance condition under the same external magnetic field configurations that allow for efficient spin pumping, we can implement deterministic spin rotation, as demonstrated in Ref. [78].

To realize all-optical spin measurement, the field B_{\perp} mixing the electron (hole) spin-states must be turned off. In this limit, presence or absence of light scattering (or absorption) upon excitation by a resonant laser conveys information about the spin-state [78]. For spin measurements, minimizing spin-flip non-radiative relaxation and inter-valley scattering is crucial. We accidentally point out here that all of our results would apply for a single-hole charged SWNT-QD as well.

Spin-photon interface

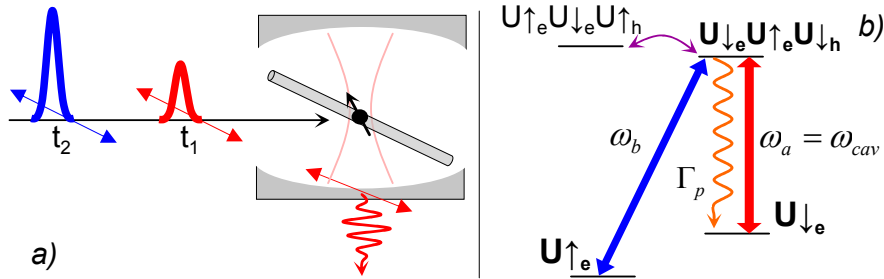


Figure 5.16: a) Sketch of the cavity-QED setup discussed in the text. Both laser pulses are polarized along the nanotube axis. Provided that the pulse separation $t_2 - t_1$ is larger than all the other time scales (inverse Rabi-frequency and cavity enhanced exciton decay rate) quantum information can be efficiently encoded in a photon time-bin qubit. b) Energy diagram of the nanotube quantum dot with the relevant transitions and rates used in the scheme.

Next, we address the possibility of transferring quantum information stored in the SWNT-QD electron spin to a generated photon. Given that the polarization of the photon is fixed by the geometry, the logical choice is to use time-bin entanglement [79]. We assume that our SWNT-QD is coupled to an optical cavity whose energy ω_{cav} is resonant with the transition $U_{\downarrow e} \rightarrow U_{\downarrow e}U_{\uparrow e}U_{\downarrow h}$ (Fig. 5.16). Using

combinations of laser pulses one can prepare an initial state in the coherent spin superposition:

$$|\psi_{in}\rangle = (\alpha|U \uparrow_e\rangle + \beta|U \downarrow_e\rangle) \otimes |0_c\rangle$$

where $|0_c\rangle$ is the empty cavity mode. We now send two well separated π -pulses at time t_1 and t_2 with respective energies ω_a and ω_b as shown in Fig. 5.16. We define the two creation operators a^\dagger (b^\dagger) for cavity-mode photons emitted immediately after pulse 1 (pulse 2). The optical transition at frequency ω_b is allowed because of the mixing induced by B_\perp , and the rates of both transitions can be made identical by adjusting the pulse intensities.

The first pulse excites the trion state if and only if the spin is initially down. In this case Purcell effect ensures very fast spontaneous emission and projection onto the state $|U \downarrow_e\rangle \otimes a^\dagger|0_c\rangle$. If the spin is initially up, the transition is Pauli-blocked and we are left with $|U \uparrow_e\rangle \otimes |0_c\rangle$. The initial state has thus evolved to:

$$|\psi_1\rangle = \alpha|U \uparrow_e\rangle \otimes |0_c\rangle + \beta|U \downarrow_e\rangle \otimes a^\dagger|0_c\rangle$$

We can do the same analysis for the second pulse and find that the final state is:

$$|\psi_f\rangle = |U \downarrow_e\rangle \otimes (\alpha b^\dagger + \beta a^\dagger) \otimes |0_c\rangle$$

where quantum information has been mapped onto a photon time-bin qubit. We emphasize that time-bin qubits are promising candidates for long range quantum communication using optical fibers [80] and that single-wall carbon nanotubes can be chosen to emit in the desired wavelength window.

Nuclear-spin ensembles manipulation

We conclude this section by evoking one of the most interesting perspectives enabled by the considerations of this chapter, namely the study of nuclear spin physics. The possibility of electron spin pumping should allow for the optical manipulation of nuclear spin ensembles, which has been successfully achieved in GaAs based structures (see for example [81]). However, experimental knowledge of the strength and characteristics of hyperfine interaction in carbon nanotubes is still limited. Of particular interest in this context would be dynamic nuclear spin polarization in a SWNT-QD where hundreds or thousands of ^{13}C atoms would form an ideal $I = \frac{1}{2}$ spin bath. Alternatively, using high-purity ^{12}C carbon nanotubes, one may realize QDs interacting with only 1 or 2 nuclear spins [82].

6 Conclusion & Outlook

Optical studies of carbon nanotubes, in particular based on single nanotube spectroscopy, are still a very young field. Many basic properties of excitons in SWNTs are poorly known and much experimental work is required to fully understand them. Examples range from the exact nature of the non-radiative decay channel dominating the PL dynamics, to the origin of PL intensity and spectral fluctuations in surfactant-embedded nanotubes.

The present work contributes to improving our knowledge and understanding of optical properties of SWNTs. In chapter 2, we reported on the first observation of photon antibunching in the photoluminescence of SWNTs. Strong localization of the exciton combined with extremely efficient exciton-exciton annihilation together forbid simultaneous emission of more than one photon. This opens the prospect of using SWNT-QDs as single photon sources.

In chapter 3 we gained further insight in the physics of SWNT-QDs. Using the formal spin-boson hamiltonian to model exciton-phonon coupling, we fitted the experimental PL spectra with remarkable accuracy. This evidences the enhanced effects of electron-phonon interactions in one-dimensional systems and has general and far-reaching implications.

Chapters 2 and 3 clearly demonstrate that we observe PL from optically active SWNT-QDs rather than free excitons. This led us to consider in chapter 4 some possible mechanisms causing exciton localization. We first developed an accurate description of quantum-dot states in a SWNT, and suggested a device architecture enabling intentional and controlled creation of SWNT-QDs. We then gave a tentative explanation for the origin of unintentional confinement occurring in our sample, considering a charged impurity trapped close to the nanotube. We demonstrated that this picture agrees with most of the experimental features, but could not give definitive proof of its validity.

The two previous scenarios rely on the same field-induced confinement mechanism. Moreover, both implicitly allow for exciton-phonon coupling to the bending mode due to the presence of a strong perpendicular electric field. If controlled, this interaction could enable laser-assisted cooling of a nanotube resonator, as shown in the appendix. If naturally present in our sample, it could provide an alternative description of the asymmetric PL lineshapes involving the sub-ohmic dissipation regime.

Beside opto-mechanical resonators, a second implementation of carbon nanotubes in quantum mechanical devices was proposed in chapter 5. Motivated by recent experimental reports, we formally demonstrated that non-vanishing spin-orbit coupling enables all-optical spin manipulation in SWNTs. Our results highlight the promises held by carbon nanostructures as building blocks of future quantum computers.

The experimental part of our work highlights an important characteristic of carbon nanotubes. Because of their high sensitivity on the surrounding environment,

experiments on SWNTs can produce widely divergent results. Some of our conclusions are obviously not universal and apply to a limited type of samples and materials. Consequently, one of the biggest challenge in the field is to achieve suitable control over single SWNTs and their environment. We suggested a way to do this in section 4.1 and we showed in chapter 5 and in the appendix the exciting possibilities this would open.

Outlook This remark naturally brings us to consider which future directions are to be followed. It seems to us that ultra-clean, suspended, CVD-grown carbon nanotubes are the material of choice to gain further physical insight. This has been evidenced by ground-breaking experiments in low-temperature transport spectroscopy, where the use of such material was essential in obtaining high resolution measurements and revealing the intrinsic properties of unperturbed pristine SWNTs.

We have therefore recently oriented our efforts toward the CVD-growth of SWNTs suitable for optical studies. This remains a challenging task to achieve the level of control required for the production of narrow-diameter nanotubes. However, we believe it is worth the effort, because available instrumentation in the near visible wavelength range would allow advanced optical studies, like photon correlation and other time-resolved measurement.

Many fundamental properties are still to be discovered by studying very simple SWNT-based devices. Recent papers already report on very different results obtained in suspended nanotubes compared to their surfactant-embedded counterparts. An example is the much longer exciton diffusion length, reflecting the higher material's quality and the reduced environmental disturbances. Finally, the ultimate goal is to achieve complete control over the system by designing elaborate nano-scale architectures around single SWNTs.

Appendix

1 Opto-mechanical cooling of a SWNT resonator

As we saw in chapter 3, electron-phonon interactions in carbon nanotubes have significant effects on their optical properties, enhanced by the reduced dimensionality of the system. While this may be detrimental for those applications where the phonon bath is mainly a source of decoherence, electron-phonon coupling can also be advantageously used to optically control the mechanical motion of the SWNT. This is the general idea underlying the expanding field of nano-opto-mechanics.

Motivated in addition by the very high mechanical quality factors recently measured [83], we would like to design an experiment allowing the optical cooling of the fundamental flexural mode of a suspended carbon nanotube. We show in this section that using the device proposed in chapter 4 ground state cooling of the nanotube resonator should be within reach, opening exciting perspectives.

1.1 Preliminary remarks

We have extensively studied in chapter 3 the effects of exciton-phonon coupling on the PL line shape (or equivalently on the absorption spectrum) of a SWNT-QD. We had then discarded the bending mode on ground of the selection rules: conservation of circumferential momentum forbids deformation potential coupling of the E_{11} excitons to this $n = 1$ phonon mode. In the previous sections, we just showed how to overcome this restriction and engineer a tunable interaction between the SWNT-QD and the bending mode.

As we already noticed in chapter 3, the coupling to long-wavelength phonons can lead to qualitatively different effects on the optical spectrum (see Fig. 1). In one case, the spectral density of low-energy phonons can be close to a continuum, i.e. the energy spacing between the consecutive harmonics (the free spectral range) can be small compared to the ZPL line-width or the experimental resolution. Then, for an ohmic (stretching mode) or sub-ohmic (bending mode) spectral density, we expect to observe a broadening of the ZPL, as is nicely confirmed in our experiments (Fig. 1.a). In the other case, for a very short nanotube, the free spectral range can be larger than the natural ZPL line-width. We then have a situation similar to the one encountered for the radial breathing mode, i.e. the appearance of well-resolved replicas (phonon sidebands) detuned from the ZPL (Fig. 1.b).

The general idea behind opto-mechanical cooling is pictured in Fig. 2: one uses the sideband corresponding to the fundamental resonance of a phonon mode to decrease its occupancy by inelastically scattering the photons from a laser (near-resonant with this sideband). The significance of having a large splitting between phonon harmonics, and therefore a short nanotube, is thus twofold:

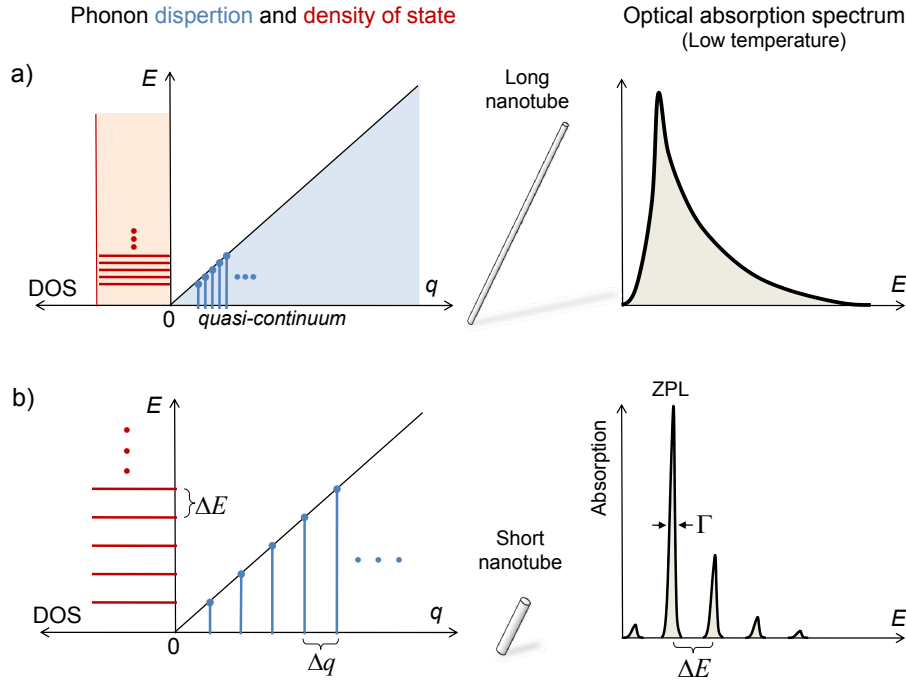


Figure 1: Qualitatively different effects from phonon coupling in (a) long vs. (b) short nanotubes. The boundary conditions at the ends of the nanotube determine the allowed longitudinal phonon wave-vectors: $q = k \frac{2\pi}{L}$ ($k \in \mathbb{Z}^*$) spaced by $\Delta q = \frac{2\pi}{L}$. Depending how the corresponding free spectral range $\Delta E = \hbar v_s \Delta q$ compares with the natural width of the zero-phonon line Γ , two scenarios may occur. a) For long nanotubes, the acoustic phonons form a quasi-continuum and $\Delta E < \Gamma$, resulting in a broadened asymmetric absorption spectrum at low temperature. b) If the nanotube is made short enough, the discrete nature of the allowed phonon wavelengths may become evident. When $\Delta E > \Gamma$ one can resolve distinct phonon absorption replicas detuned from the zero-phonon line by multiples of ΔE .

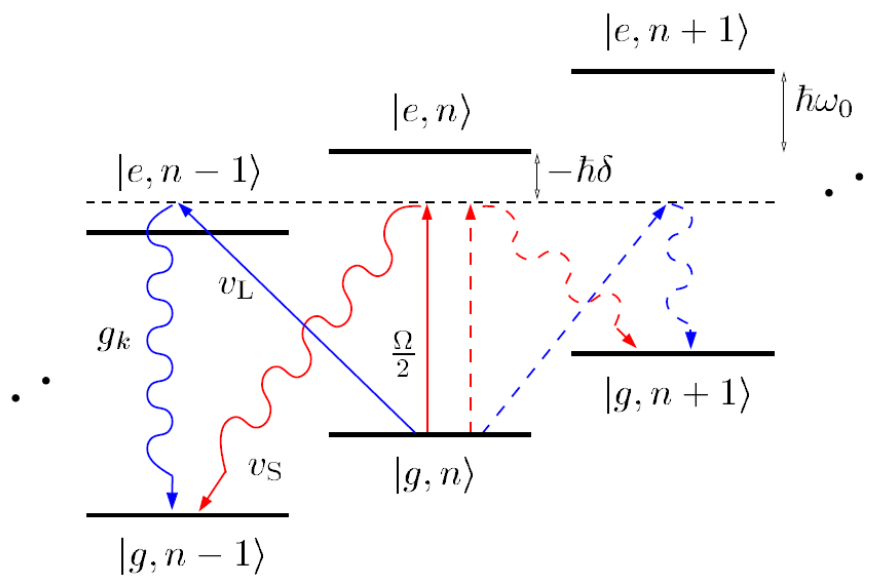


Figure 2: In this level ladder, the states are labeled $|\alpha, \beta\rangle$ where $\alpha = g, e$ denotes the state of the SWNT-QD (empty or with one exciton) and $\beta = n \in \mathbb{N}$ stands for the occupation number of the fundamental flexural mode. When the laser is detuned by an amount $-\hbar\delta \sim \hbar\omega_0$ from the QD bare transition, it is near-resonant with the red-detuned phonon sideband. Cooling occurs through two possible paths: absorption of one phonon simultaneously with photon absorption (path v_L), or phonon emission during the photon re-emission (path v_S). Both lead to a decrease of the phonon occupancy by one unit, and the process can reiterate itself.

- for the bending mode (the fundamental resonance of which we want to cool), we need a high enough frequency to get a well-resolved sideband, and a high quality factor.
- for the stretching mode we want to avoid the resulting broadening of the ZPL which would otherwise prevent us from addressing the flexural sideband.

This is why we consider a device where the nanotube is suspended over a length of only $L = 120$ nm (Fig. 4.3). Interestingly, because of the quadratic dispersion of the bending mode close to $q = 0$, the resulting energy of the fundamental resonance is much smaller than the one of the stretching mode (with linear dispersion). The situation is thus ideal for our purpose, because a short nanotube offers a readily addressable flexural phonon sideband and a sharp ZPL. Quantitatively, for $L = 120$ nm, the fundamental in-plane flexural resonance has a frequency $\omega_0/2\pi = 725$ MHz, whereas the lowest stretching mode occurs at $\omega_{S,0}/2\pi = v_S/L = 167$ GHz. This last frequency corresponds to an energy of 0.7 meV, well above the lifetime-limited width of the SWNT-QD ZPL.

Another important characteristic of our scheme is to use the nominally dark, lower lying exciton $|\psi_{00-}\rangle$. Applying a magnetic flux threading the nanotube renders the dark exciton weakly optically allowed [17]. This enables experimental control over the radiative rate of the SWNT-QD transition, which can thus be made arbitrarily small, in order to reduce lifetime broadening.

1.2 Summary of the calculations

We now give a short account of the calculations describing opto-mechanical cooling of the fundamental flexural resonance, needed for a quantitative estimation of the final occupancy within experimental reach. They were carried out by Ignacio Wilson-Rae on the line of previously published work [60, 84, 85]. Similar calculations were already performed for QD embedded in semiconducting beam structures [84] and our present work relies mainly on new parameters. We do not want to report here on all the technical aspects of this derivation, but we summarize instead the main steps.

1. In a first time, we single-out the fundamental flexural mode from the “bath modes” including all other phonon modes of the nanotube coupled to the substrate through phonon tunneling at the physical junctions. For this we follow the formalism developed in [60] and adopt a resonator-bath representation. The resonator mode has the annihilation operator b_0 , angular frequency ω_0 and quality factor Q . The scattering eigenmodes of the bath are labeled by q with the corresponding operators b_q , angular frequency $\omega(q)$ and lateral displacement components $u_{x,q}(z)$ and $u_{z,q}(z)$. The effective field operators $\hat{\phi}_{f/c}$ introduced in Eq. (4.17) and (4.18) are decomposed accordingly:

$$\begin{aligned} \frac{\partial^2 \hat{\phi}_f}{\partial z^2}(\hat{z}_e) &\rightarrow \frac{\partial^2 \phi_0}{\partial z^2}(\hat{z}_e) \sqrt{\hbar/2\mu_l\omega_0}(b_0 + b_0^\dagger) \\ &+ \sum_q \frac{\partial^2 u_{x,q}}{\partial z^2}(\hat{z}_e) \sqrt{\hbar/2\rho_s\omega(q)}(b_q + b_q^\dagger) \end{aligned} \quad (1)$$

$$\frac{\partial \hat{\phi}_c}{\partial z}(\hat{z}_e) \rightarrow \sum_q \frac{\partial u_{z,q}}{\partial z}(\hat{z}_e) \sqrt{\hbar/2\rho_s\omega(q)}(b_q + b_q^\dagger) \quad (2)$$

Here $\phi_0(z)$ is the normalized resonator 1D eigenmode, μ_l is the linear mass density of the nanotube and ρ_s is the substrate's density.

2. We can now follow Ref. [84] and write the hamiltonian of the complete system, namely the SWNT-QD coupled to the resonator mode, to the phonon bath and to the radiation field (with annihilation operators a_k and couplings g_k), in a polaronic representation (i.e. shifted by the polaron energy):

$$\mathcal{H} = \mathcal{H}_{\text{sys}} + \mathcal{H}_{\text{int}} + \mathcal{H}_B \quad (3)$$

Taking $\hbar = 1$, the three terms read:

$$\mathcal{H}_B = \sum_q \omega_q b_q^\dagger b_q + \sum_k (\omega_k - \omega_L) a_k^\dagger a_k \quad (4)$$

$$\mathcal{H}_{\text{sys}} = -\frac{\delta}{2} \sigma_z + \frac{\Omega}{2} (\sigma_+ B^\dagger + \text{H.c.}) + \omega_0 b_0^\dagger b_0 \quad (5)$$

$$\mathcal{H}_{\text{int}} = \sum_k g_k \sigma_+ B^\dagger a_k + \sum_q \left(\zeta_q b_0^\dagger + \frac{\lambda_q}{2} \sigma_z \right) b_q + \text{H.c.} \quad (6)$$

where δ is the laser detuning from the ZPL and Ω the Rabi frequency. Pauli matrix notation refers to the optical pseudo-spin ($\sigma_z = 1$ corresponds to $|\psi_{00-}\rangle$ and $\sigma_z = -1$ to the empty SWNT-QD). We have applied a shift to the phonon modes q , and adopted a rotating frame at the laser frequency ω_L . We have also defined the translation operator $B \equiv e^{\eta(b_0 - b_0^\dagger)}$. The parameter η , which characterizes the strength of the exciton-resonator coupling ($e^{-\eta^2/2}$ is the Frank-Condon factor) is given by:

$$\eta = -2^{3/4} \nu (1 + \sigma) \frac{g_2 \sigma_G^{1/4} \xi \mathcal{E}_\perp}{R(Eh)^{3/4} (q_0 L)} \sqrt{\frac{L}{\pi \hbar}} \cos 3\theta \quad (7)$$

Here we have introduced the effective field (see Eq. (4.19) for its origin):

$$\mathcal{E}_\perp \equiv (\sqrt{L}/q_0^2) \langle F_{00} | \frac{\partial^2 \phi_0}{\partial z^2}(\hat{z}_e) E_\perp(\hat{z}_e) | F_{00} \rangle \quad (8)$$

where q_0 is the TRE phonon wavevector for the resonator mode, $h = 0.66 \text{ \AA}$ is the effective thickness for the continuum shell model [61, 62], $E = 1 \text{ TPa}$ is the nanotube's Young modulus, and $\sigma_G = 7.7 \times 10^{-7} \text{ Kg m}^{-2}$ is the mass density of graphene. The couplings ζ_q and λ_q to the bath modes lead, respectively, to the resonator mode's phonon tunneling dissipation and to pure dephasing of the SWNT-QD.

3. We find that for all realistic environmental couplings the Born-Markov approximation is valid. After eliminating the bath phonon modes and the radiation field, we obtain a master equation for the SWNT-QD coupled to the resonator with a Hamiltonian contribution given by \mathcal{H}_{sys} and a dissipative contribution of Lindblad form with collapse operators:

$$\sqrt{\Gamma} \sigma_-$$

$$\frac{\sqrt{\gamma_D/2} \sigma_z}{\sqrt{\omega_0 n(\omega_0)/Q} b_0^\dagger}$$

and

$$\sqrt{\omega_0 [n(\omega_0) + 1]/Q} b_0$$

Here Γ is the SWNT-QD exciton decay rate, $n(\omega_0)$ is the thermal equilibrium occupancy at the ambient temperature and γ_D is the phonon-induced dephasing rate. The master equation thus reads:

$$\begin{aligned} \dot{\rho} = & -i [\mathcal{H}_{\text{sys}}, \rho] + \frac{\Gamma}{2} (2\sigma_- B \rho B^\dagger \sigma_+ - \rho \sigma_+ \sigma_- - \sigma_+ \sigma_- \rho) \\ & + \frac{\gamma_D}{2} (\sigma_z \rho \sigma_z - \rho) + \omega_0 \frac{n(\omega_0)}{2Q} (2b_0^\dagger \rho b_0 - b_0 b_0^\dagger \rho - \rho b_0 b_0^\dagger) \\ & + \omega_0 \frac{n(\omega_0)+1}{2Q} (2b_0 \rho b_0^\dagger - b_0^\dagger b_0 \rho - \rho b_0^\dagger b_0) \end{aligned}$$

Other relevant sources of dissipation beyond those considered in Hamiltonian (3) can be incorporated by adopting in Eq. (9) modified values of Q [83]¹ and Γ ². The dephasing rate γ_D is determined by the low frequency behavior of the phonon spectral density $J(\omega) = \pi \sum_q |\lambda_q|^2 \delta(\omega - \omega_q)$ (with $q \in$ compressional branch). For a *bridge geometry* the scattering modes derived in [60] result in $J(\omega) = 2\pi\alpha_{\text{con}}\omega$, for ω much smaller than the fundamental compressional resonance $\omega_{S,0} \gg \omega_0$ (i.e. Ohmic behavior), which leads to $\gamma_D = 2\pi\alpha_{\text{con}}k_B T/\hbar$. In turn, it can be shown that the “confined” dimensionless dissipation parameter satisfies $\alpha_{\text{con}} = \alpha/\pi Q_c$, where Q_c is the clamping-loss limited Q -value of the fundamental compressional resonance [60] and α the dissipation parameter that would result for an infinite length. The latter can be calculated using Eq. (4.19) and reads:

$$\alpha = g_2^2 \sqrt{\sigma_G} (1 + \sigma)^2 \cos^2 3\theta / 2\pi^2 \hbar R (Eh)^{3/2}$$

It markedly depends on the chirality and for small radius zigzag tubes may approach unity. Then the smallness of α_{con} warrants the aforementioned Born-Markov approximation in the treatment of the pure dephasing in the regime $\gamma_D \gtrsim \Gamma/2$ where the latter influences the dynamics.

4. Finally, in complete analogy with the Lamb-Dicke limit, one can expand up to second order the translation operator B and adiabatically eliminate the SWNT-QD to obtain from Eq. (9) a rate equation for the populations of the resonator’s Fock states. This incorporates both the mechanical dissipation and the dissipative effects induced by the scattering of laser light. The latter result in cooling and heating rates A_\mp that read the same as in [84] with the quantum dot Liouvillian \mathcal{L}^{QD} including now the pure dephasing γ_D given by the third term in Eq. (9). We note that as $\gamma_D \rightarrow 0$, the steady state occupancy for $Q \rightarrow \infty$, i.e. the quantum backaction limit $A_+/(A_- - A_+)$, becomes independent of Ω (in stark contrast to atomic laser cooling) and reduces to the same simple expression valid for the cavity-assisted backaction

1. For relevant parameters the phonon tunneling contribution to $1/Q$ is only of order 10^{-7} [60].

2. This has an additional contribution from the non-radiative recombination rate [86] which for an ultra-clean nanotube dark exciton has not been measured so far.

cooling [85, 87] with the cavity decay rate $1/\tau$ replaced by the spontaneous emission rate. For the optimal detuning $\delta = -\omega_0$ this fundamental limit for the occupancy yields $(\Gamma/4\omega_0)^2$.

1.3 Numerical results: ground-state cooling

Within the formalism developed above, we arrive at the following expression for the final steady-state resonator occupancy, starting from the ambient thermal occupation number $n_{eq}(\omega_0)$:

$$n_f(\omega_0) \doteq \langle b_0^\dagger b_0 \rangle_{ss} = \frac{n_{eq}(\omega_0) + \eta^2 Q A_+ / \omega_0}{1 + \eta^2 Q (A_- - A_+) / \omega_0}$$

From the available experimental knowledge on carbon nanotubes, we consider the following parameters: $Q = 2 \times 10^5$, $\eta = 0.17$, $\Gamma = \omega_0/3$, and $\hbar\gamma_D/k_B T = 4.7 \times 10^{-4}$. These values correspond, for example (cf. Fig. 4.5), to a (9,4) nanotube ($\alpha = 0.2$ and $R = 0.45$ nm) of length $L = 120$ nm ($\omega_0/2\pi = 725$ MHz, $Q_c = 908$) with $\mathcal{E}_\perp = 147$ V μm^{-1} (this last value is directly calculated in the ComSol simulation).

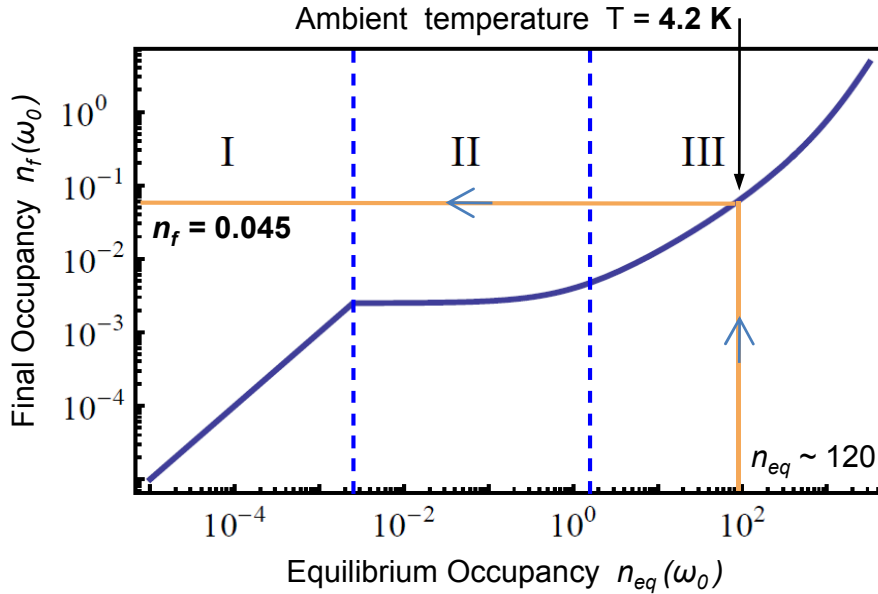


Figure 3: Numerical results: temperature dependence of the optimal steady-state resonator occupancy.

The remaining free parameters are the laser Rabi-frequency Ω and detuning δ . For any given temperature T we therefore minimize the quantity $n_f(\omega_0)$ with respect to δ and Ω to obtain the curve shown in Fig. 3. In particular, for an ambient temperature $T = 4.2$ K (easily accessible in a conventional Helium cryostat), our scheme allows the optical cooling of the fundamental flexural mode from an equilibrium occupancy $n_{eq}(\omega_0) \simeq 120$ down to $n_f(\omega_0) = 0.045$. The corresponding input power for a diffraction-limited spot size being below 1 nW, radiation pressure effects are completely negligible.

This result highlights the promises held by carbon nanotube resonators for achieving the quantum ground-state cooling of a macroscopic mechanical degree of freedom. The impacts would be considerable in numerous fields: high precision metrology, investigation of the quantum-to-classical transition, development of quantum technologies, to mention just a few.

Bibliography

- [1] Sumio Iijima. Helical microtubules of graphitic carbon. *Nature*, 354(6348):56–58, November 1991. [1](#)
- [2] Sumio Iijima and Toshinari Ichihashi. Single-shell carbon nanotubes of 1-nm diameter. *Nature*, 363(6430):603–605, June 1993. [1](#)
- [3] Shaoming Huang, Xinyu Cai, and Jie Liu. Growth of millimeter-long and horizontally aligned single-walled carbon nanotubes on flat substrates. *Journal of the American Chemical Society*, 125(19):5636–5637, May 2003. [1](#)
- [4] Michael J. O’Connell, Sergei M. Bachilo, Chad B. Huffman, Valerie C. Moore, Michael S. Strano, Erik H. Haroz, Kristy L. Rialon, Peter J. Boul, William H. Noon, Carter Kittrell, Jianpeng Ma, Robert H. Hauge, R. Bruce Weisman, and Richard E. Smalley. Band Gap Fluorescence from Individual Single-Walled Carbon Nanotubes. *Science*, 297(5581):593–596, 2002. [2](#), [13](#), [14](#)
- [5] Michael Wimmer. *Quantum transport in nanostructures: From computational concepts to spintronics in graphene and magnetic tunnel junctions*. PhD thesis, 2008. [3](#)
- [6] Tsuneya Ando. Theory of electronic states and transport in carbon nanotubes. *Journal of the Physical Society of Japan*, 74(3):777–817, 2005. [4](#), [5](#), [6](#)
- [7] Sergei M. Bachilo, Michael S. Strano, Carter Kittrell, Robert H. Hauge, Richard E. Smalley, and R. Bruce Weisman. Structure-Assigned Optical Spectra of Single-Walled Carbon Nanotubes. *Science*, 298(5602):2361–2366, 2002. [8](#), [16](#)
- [8] Andrew G. Walsh, A. Nickolas Vamivakas, Yan Yin, Stephen B. Cronin, M. Selim nl, Bennett B. Goldberg, and Anna K. Swan. Scaling of exciton binding energy with external dielectric function in carbon nanotubes. *Physica E: Low-dimensional Systems and Nanostructures*, 40(7):2375 – 2379, 2008. Proceedings of the E-MRS 2007 Symposia L and M: Electron Transport in Low-Dimensional Carbon Structures and Science and Technology of Nanotubes and Nanowires. [8](#), [9](#)
- [9] Ermin Malic, Matthias Hirtschulz, Stephanie Reich, and Andreas Knorr. Excitonic absorption spectra and ultrafast dephasing dynamics in arbitrary carbon nanotubes. *physica status solidi (RRL) - Rapid Research Letters*, 3(6):196–198, 2009. [8](#), [9](#)
- [10] Rodney Loudon. One-dimensional hydrogen atom. *American Journal of Physics*, 27(9):649–655, 1959. [8](#)

-
- [11] M. Semina, R. Sergeev, and R. Suris. The binding energy of excitons and x+ and x- trions in one-dimensional systems. *Semiconductors*, 42(12):1427–1433, December 2008. [8](#)
- [12] Catalin D. Spataru, Sohrab Ismail-Beigi, Lorin X. Benedict, and Steven G. Louie. Excitonic effects and optical spectra of single-walled carbon nanotubes. *Phys. Rev. Lett.*, 92(7):077402, Feb 2004. [8](#)
- [13] Eric Chang, Giovanni Bussi, Alice Ruini, and Elisa Molinari. Excitons in carbon nanotubes: An ab initio symmetry-based approach. *Phys. Rev. Lett.*, 92(19):196401, May 2004. [8](#), [10](#)
- [14] Feng Wang, Gordana Dukovic, Louis E. Brus, and Tony F. Heinz. The Optical Resonances in Carbon Nanotubes Arise from Excitons. *Science*, 308(5723):838–841, 2005. [10](#)
- [15] Eduardo B. Barros, Ado Jorio, Georgii G. Samsonidze, Rodrigo B. Capaz, Antnio G. Souza Filho, Josu Mendes Filho, Gene Dresselhaus, and Mildred S. Dresselhaus. Review on the symmetry-related properties of carbon nanotubes. *Physics Reports*, 431(6):261 – 302, 2006. [10](#), [11](#)
- [16] Mildred S. Dresselhaus, Gene Dresselhaus, Riichiro Saito, and Ado Jorio. Exciton photophysics of carbon nanotubes. *Annual Review of Physical Chemistry*, 58(1):719–747, 2007. [10](#)
- [17] Ajit Srivastava, Han Htoon, Victor I. Klimov, and Junichiro Kono. Direct observation of dark excitons in individual carbon nanotubes: Inhomogeneity in the exchange splitting. *Phys. Rev. Lett.*, 101(8):087402, Aug 2008. [12](#), [128](#)
- [18] J. Shaver and J. Kono. Temperature-dependent magneto-photoluminescence spectroscopy of carbon nanotubes: evidence for dark excitons. *Laser & Photonics Review*, 1(3):260–274, 2007. [12](#)
- [19] S. Zaric, G. N. Ostojic, J. Shaver, J. Kono, O. Portugall, P. H. Frings, G. L. J. A. Rikken, M. Furis, S. A. Crooker, X. Wei, V. C. Moore, R. H. Hauge, and R. E. Smalley. Excitons in carbon nanotubes with broken time-reversal symmetry. *Phys. Rev. Lett.*, 96(1):016406, Jan 2006. [12](#)
- [20] J. Lefebvre, Y. Homma, and P. Finnie. Bright band gap photoluminescence from unprocessed single-walled carbon nanotubes. *Phys. Rev. Lett.*, 90(21):217401, May 2003. [13](#)
- [21] Yoshikazu Homma, Shohei Chiashi, and Yoshihiro Kobayashi. Suspended single-wall carbon nanotubes: synthesis and optical properties. *Reports on Progress in Physics*, 72(6):066502 (22pp), 2009. [13](#)
- [22] W. Wenseleers, I.I. Vlasov, E. Goovaerts, E.D. Obraztsova, A.S. Lobach, and A. Bouwen. Efficient isolation and solubilization of pristine single-walled nanotubes in bile salt micelles. *Advanced Functional Materials*, 14(11):1105–1112, 2004. [15](#), [16](#)

-
- [23] R. Bruce Weisman and Sergei M. Bachilo. Dependence of optical transition energies on structure for single-walled carbon nanotubes in aqueous suspension: An empirical kataura plot. *Nano Letters*, 3(9):1235–1238, 2003. [16](#), [89](#), [90](#)
- [24] Zhengtang Luo, Fotios Papadimitrakopoulos, and Stephen K. Doorn. Intermediate-frequency raman modes for the lower optical transitions of semi-conducting single-walled carbon nanotubes. *Phys. Rev. B*, 75(20):205438, May 2007. [17](#), [18](#)
- [25] Laurent Cognet, Dmitri A. Tsyboulski, John-David R. Rocha, Condell D. Doyle, James M. Tour, and R. Bruce Weisman. Stepwise Quenching of Exciton Fluorescence in Carbon Nanotubes by Single-Molecule Reactions. *Science*, 316(5830):1465–1468, 2007. [17](#), [20](#), [35](#)
- [26] Carsten Georgi, Nicolai Hartmann, Tobias Gokus, Alexander A. Green, Mark C. Hersam, and Achim Hartschuh. Photoinduced luminescence blinking and bleaching in individual single-walled carbon nanotubes. *ChemPhysChem*, 9(10):1460–1464, 2008. [20](#)
- [27] Oliver Kiowski, Sergei Lebedkin, Frank Hennrich, and Manfred M. Kappes. Single-walled carbon nanotubes show stable emission and simple photoluminescence spectra with weak excitation sidebands at cryogenic temperatures. *Phys. Rev. B*, 76(7):075422, Aug 2007. [20](#), [21](#)
- [28] R. Q. Twiss R. Hanbury Brown. Correlation between photons in two coherent beams of light. *Nature*, 177:27–29, Aug 1956. [31](#)
- [29] Brahim Lounis and Michel Orrit. Single-photon sources. *Reports on Progress in Physics*, 68(5):1129–1179, 2005. [33](#)
- [30] Larry Luer, Sajjad Hoseinkhani, Dario Polli, Jared Crochet, Tobias Hertel, and Guglielmo Lanzani. Size and mobility of excitons in (6, 5) carbon nanotubes. *Nat Phys*, 5(1):54–58, January 2009. [34](#)
- [31] C.-X. Sheng, Z. V. Vardeny, A. B. Dalton, and R. H. Baughman. Exciton dynamics in single-walled nanotubes: Transient photoinduced dichroism and polarized emission. *Phys. Rev. B*, 71(12):125427, Mar 2005. [35](#)
- [32] Yoichi Murakami and Junichiro Kono. Existence of an upper limit on the density of excitons in carbon nanotubes by diffusion-limited exciton-exciton annihilation: Experiment and theory. *Phys. Rev. B*, 80(3):035432, Jul 2009. [35](#), [38](#)
- [33] Kazuhiko Seki and M. Tachiya. Theory of antibunching of photon emission i. *The Journal of Chemical Physics*, 130(2):024706, 2009. [36](#), [37](#)
- [34] Kazuhiko Seki and M. Tachiya. Theory of antibunching of photon emission ii. *The Journal of Chemical Physics*, 130(19):194507, 2009. [37](#)

- [35] T. A. Nguyen, S. Mackowski, H. E. Jackson, L. M. Smith, J. Wrobel, K. Fronc, G. Karczewski, J. Kossut, M. Dobrowolska, J. K. Furdyna, and W. Heiss. Resonant spectroscopy of ii-vi self-assembled quantum dots: Excited states and exciton-longitudinal optical phonon coupling. *Phys. Rev. B*, 70(12):125306, Sep 2004. [41](#), [83](#)
- [36] A. Lemaître, A. D. Ashmore, J. J. Finley, D. J. Mowbray, M. S. Skolnick, M. Hopkinson, and T. F. Krauss. Enhanced phonon-assisted absorption in single inas/gaas quantum dots. *Phys. Rev. B*, 63(16):161309, Apr 2001. [41](#), [83](#)
- [37] H. Htoon, M. J. O’Connell, P. J. Cox, S. K. Doorn, and V. I. Klimov. Low temperature emission spectra of individual single-walled carbon nanotubes: Multiplicity of subspecies within single-species nanotube ensembles. *Phys. Rev. Lett.*, 93(2):027401, Jul 2004. [43](#)
- [38] Hyung-Joon Shin, Sylvain Clair, Yousoo Kim, and Maki Kawai. Substrate-induced array of quantum dots in a single-walled carbon nanotube. *Nat Nano*, 4(9):567–570, September 2009. [43](#)
- [39] J. Maultzsch *et al.* Exciton binding energies in carbon nanotubes from two-photon photoluminescence. *Phys. Rev. B*, 72:241402, 2005. [44](#)
- [40] Rodrigo B. Capaz, Catalin D. Spataru, Sohrab Ismail-Beigi, and Steven G. Louie. Diameter and chirality dependence of exciton properties in carbon nanotubes. *Phys. Rev. B*, 74(12):121401, Sep 2006. [44](#), [66](#)
- [41] Thomas G. Pedersen. Exciton effects in carbon nanotubes. *Carbon*, 42(5-6):1007 – 1010, 2004. European Materials Research Society 2003, Symposium B: Advanced Multifunctional Nanocarbon Materials and Nanosystems. [44](#), [53](#)
- [42] Hidekatsu Suzuura and Tsuneya Ando. Phonons and electron-phonon scattering in carbon nanotubes. *Phys. Rev. B*, 65(23):235412, May 2002. [45](#), [46](#), [53](#), [67](#)
- [43] G. Pennington and N. Goldsman. Low-field semiclassical carrier transport in semiconducting carbon nanotubes. *Phys. Rev. B*, 71(20):205318, May 2005. [45](#), [53](#)
- [44] G. Pennington, N. Goldsman, A. Akturk, and A. E. Wickenden. Deformation potential carrier-phonon scattering in semiconducting carbon nanotube transistors. *Applied Physics Letters*, 90(6):062110, 2007. [46](#), [53](#)
- [45] A. J. Leggett, S. Chakravarty, A. T. Dorsey, Matthew P. A. Fisher, Anupam Garg, and W. Zwerger. Dynamics of the dissipative two-state system. *Rev. Mod. Phys.*, 59(1):1–85, Jan 1987. [48](#), [50](#)
- [46] B. Krummheuer, V. M. Axt, and T. Kuhn. Theory of pure dephasing and the resulting absorption line shape in semiconductor quantum dots. *Phys. Rev. B*, 65(19):195313, May 2002. [48](#), [49](#)

-
- [47] A. Vagov, V. M. Axt, and T. Kuhn. Electron-phonon dynamics in optically excited quantum dots: Exact solution for multiple ultrashort laser pulses. *Phys. Rev. B*, 66(16):165312, Oct 2002. [48](#)
- [48] Gerald D. Mahan. *Many Particle Physics*. Springer; 3rd edition, Berlin, 2000. [49](#)
- [49] P. Borri, W. Langbein, S. Schneider, U. Woggon, R. L. Sellin, D. Ouyang, and D. Bimberg. Ultralong dephasing time in ingaas quantum dots. *Phys. Rev. Lett.*, 87(15):157401, Sep 2001. [50](#)
- [50] M. Abbarchi, M. Gurioli, A. Vinattieri, S. Sanguinetti, M. Bonfanti, T. Mano, K. Watanabe, T. Kuroda, and N. Koguchi. Phonon sideband recombination kinetics in single quantum dots. *Journal of Applied Physics*, 104(2):023504, 2008. [50](#)
- [51] I. Favero, G. Cassabois, R. Ferreira, D. Darson, C. Voisin, J. Tignon, C. Delalande, G. Bastard, Ph. Roussignol, and J. M. Gérard. Acoustic phonon sidebands in the emission line of single inas/gaas quantum dots. *Phys. Rev. B*, 68(23):233301, Dec 2003. [50](#)
- [52] J. Jiang, R. Saito, Ge. G. Samsonidze, S. G. Chou, A. Jorio, G. Dresselhaus, and M. S. Dresselhaus. Electron-phonon matrix elements in single-wall carbon nanotubes. *Phys. Rev. B*, 72(23):235408, Dec 2005. [56](#)
- [53] A. Vagov, V. M. Axt, T. Kuhn, W. Langbein, P. Borri, and U. Woggon. Non-monotonous temperature dependence of the initial decoherence in quantum dots. *Phys. Rev. B*, 70(20):201305, Nov 2004. [57](#)
- [54] R. Doll, P. Hnggi, S. Kohler, and M. Wubs. Fast initial qubit dephasing and the influence of substrate dimensions on error correction rates. *The European Physical Journal B - Condensed Matter and Complex Systems*, 68(4):523–527, April 2009. [59](#)
- [55] Svetlana Kilina, Sergei Tretiak, Stephen K. Doorn, Zhengtang Luo, Fotios Papadimitrakopoulos, Andrei Piryatinski, Avadh Saxena, and Alan R. Bishop. Cross-polarized excitons in carbon nanotubes. *Proceedings of the National Academy of Sciences*, 105(19):6797–6802, 2008. [67](#)
- [56] Seiji Uryu and Tsuneya Ando. Exciton absorption of perpendicularly polarized light in carbon nanotubes. *Phys. Rev. B*, 74(15):155411, Oct 2006.
- [57] Paulo T. Araujo, Stephen K. Doorn, Svetlana Kilina, Sergei Tretiak, Erik Einarsson, Shigeo Maruyama, Helio Chacham, Marcos A. Pimenta, and Ado Jorio. Third and fourth optical transitions in semiconducting carbon nanotubes. *Phys. Rev. Lett.*, 98(6):067401, Feb 2007. [67](#)
- [58] J. A. Fagan, J. R. Simpson, B. J. Landi, L. J. Richter, I. Mandelbaum, V. Bajpai, D. L. Ho, R. Raffaele, A. R. Hight Walker, B. J. Bauer, and E. K. Hobbie. Dielectric response of aligned semiconducting single-wall nanotubes. *Phys. Rev. Lett.*, 98(14):147402, Apr 2007. [67](#)

-
- [59] Eros Mariani and Felix von Oppen. Electron-vibron coupling in suspended carbon nanotube quantum dots. *Phys. Rev. B*, 80(15):155411, Oct 2009. [67](#)
- [60] I. Wilson-Rae. Intrinsic dissipation in nanomechanical resonators due to phonon tunneling. *Phys. Rev. B*, 77(24):245418, Jun 2008. [68](#), [128](#), [130](#)
- [61] B. I. Yakobson, C. J. Brabec, and J. Bernholc. Nanomechanics of carbon tubes: Instabilities beyond linear response. *Phys. Rev. Lett.*, 76(14):2511–2514, Apr 1996. [68](#), [129](#)
- [62] Daniel Sanchez-Portal, Emilio Artacho, Jose M. Soler, Angel Rubio, and Pablo Ordejon. Ab initio structural, elastic, and vibrational properties of carbon nanotubes. *Phys. Rev. B*, 59(19):12678–12688, May 1999. [68](#), [129](#)
- [63] Indhira O. Maciel, Neil Anderson, Marcos A. Pimenta, Achim Hartschuh, Huihong Qian, Mauricio Terrones, Humberto Terrones, Jessica Campos-Delgado, Apparao M. Rao, Lukas Novotny, and Ado Jorio. Electron and phonon renormalization near charged defects in carbon nanotubes. *Nat Mater*, 7(11):878–883, November 2008. [72](#)
- [64] Y. F. Li, T. Kaneko, and R. Hatakeyama. Formation of quantum dots in single stranded dna-wrapped single-walled carbon nanotubes. *Applied Physics Letters*, 96(2):023104, 2010. [72](#)
- [65] Marcus Freitag, James C. Tsang, Ageeth Bol, Phaeton Avouris, Dongning Yuan, and Jie Liu. Scanning photovoltage microscopy of potential modulations in carbon nanotubes. *Applied Physics Letters*, 91(3):031101, 2007. [73](#)
- [66] Rodrigo B. Capaz, Catalin D. Spataru, Paul Tangney, Marvin L. Cohen, and Steven G. Louie. Temperature dependence of the band gap of semiconducting carbon nanotubes. *Phys. Rev. Lett.*, 94(3):036801, Jan 2005. [77](#)
- [67] J. Lefebvre, P. Finnie, and Y. Homma. Temperature-dependent photoluminescence from single-walled carbon nanotubes. *Phys. Rev. B*, 70(4):045419, Jul 2004. [77](#)
- [68] S. B. Cronin, Y. Yin, A. Walsh, Rodrigo B. Capaz, A. Stolyarov, P. Tangney, Marvin L. Cohen, Steven G. Louie, A. K. Swan, M. S. Ünlü, B. B. Goldberg, and M. Tinkham. Temperature dependence of the optical transition energies of carbon nanotubes: The role of electron-phonon coupling and thermal expansion. *Phys. Rev. Lett.*, 96(12):127403, Mar 2006. [77](#)
- [69] Richard Hildner, Laura Winterling, Ulrich Lemmer, Ullrich Scherf, and Jürgen Khler. Single-molecule spectroscopy on a ladder-type conjugated polymer: Electron-phonon coupling and spectral diffusion. *ChemPhysChem*, 10(14):2524–2534, 2009. [79](#)
- [70] F. Kuemmeth, S. Ilani, D. C. Ralph, and P. L. McEuen. Coupling of spin and orbital motion of electrons in carbon nanotubes. *Nature*, 452(7186):448–452, March 2008. [95](#), [103](#), [104](#), [105](#), [107](#), [112](#), [113](#), [118](#), [119](#)

-
- [71] Tsuneya Ando. Spin-orbit interaction in carbon nanotubes. *Journal of the Physical Society of Japan*, 69(6):1757–1763, 2000. [97](#), [98](#), [100](#)
- [72] Daniel Huertas-Hernando, F. Guinea, and Arne Brataas. Spin-orbit coupling in curved graphene, fullerenes, nanotubes, and nanotube caps. *Phys. Rev. B*, 74(15):155426, Oct 2006. [97](#)
- [73] Denis V. Bulaev, Björn Trauzettel, and Daniel Loss. Spin-orbit interaction and anomalous spin relaxation in carbon nanotube quantum dots. *Phys. Rev. B*, 77(23):235301, Jun 2008. [97](#), [113](#)
- [74] Phaeton Avouris, Zhihong Chen, and Vasili Perebeinos. Carbon-based electronics. *Nat Nano*, 2(10):605–615, October 2007. [99](#), [100](#)
- [75] E. D. Minot, Yuval Yaish, Vera Sazonova, and Paul L. McEuen. Determination of electron orbital magnetic moments in carbon nanotubes. *Nature*, 428(6982):536–539, April 2004. [112](#)
- [76] Antonio Badolato, Kevin Hennessy, Mete Atature, Jan Dreiser, Evelyn Hu, Pierre M. Petroff, and Atac Imamoglu. Deterministic Coupling of Single Quantum Dots to Single Nanocavity Modes. *Science*, 308(5725):1158–1161, 2005. [119](#)
- [77] Vasili Perebeinos and Phaeton Avouris. Phonon and electronic nonradiative decay mechanisms of excitons in carbon nanotubes. *Phys. Rev. Lett.*, 101(5):057401, Jul 2008. [119](#)
- [78] A. Imamoglu, D. D. Awschalom, G. Burkard, D. P. DiVincenzo, D. Loss, M. Sherwin, and A. Small. Quantum information processing using quantum dot spins and cavity qed. *Phys. Rev. Lett.*, 83(20):4204–4207, Nov 1999. [121](#)
- [79] J. Brendel, N. Gisin, W. Tittel, and H. Zbinden. Pulsed energy-time entangled twin-photon source for quantum communication. *Phys. Rev. Lett.*, 82(12):2594–2597, Mar 1999. [121](#)
- [80] I. Marcikic, H. de Riedmatten, W. Tittel, H. Zbinden, M. Legré, and N. Gisin. Distribution of time-bin entangled qubits over 50 km of optical fiber. *Phys. Rev. Lett.*, 93(18):180502, Oct 2004. [122](#)
- [81] C. W. Lai, P. Maletinsky, A. Badolato, and A. Imamoglu. Knight-field-enabled nuclear spin polarization in single quantum dots. *Phys. Rev. Lett.*, 96(16):167403, Apr 2006. [122](#)
- [82] L. Childress, M. V. Gurudev Dutt, J. M. Taylor, A. S. Zibrov, F. Jelezko, J. Wrachtrup, P. R. Hemmer, and M. D. Lukin. Coherent Dynamics of Coupled Electron and Nuclear Spin Qubits in Diamond. *Science*, 314(5797):281–285, 2006. [122](#)
- [83] Andreas K. Hüttel, Gary A. Steele, Benoit Witkamp, Menno Poot, Leo P. Kouwenhoven, and Herre S. J. van der Zant. Carbon nanotubes as ultrahigh quality factor mechanical resonators. *Nano Letters*, 9(7):2547–2552, July 2009. [125](#), [130](#)

-
- [84] I. Wilson-Rae, P. Zoller, and A. Imamoglu. Laser cooling of a nanomechanical resonator mode to its quantum ground state. *Phys. Rev. Lett.*, 92(7):075507, Feb 2004. [128](#), [129](#), [130](#)
 - [85] I. Wilson-Rae, N. Nooshi, W. Zwerger, and T. J. Kippenberg. Theory of ground state cooling of a mechanical oscillator using dynamical backaction. *Phys. Rev. Lett.*, 99(9):093901, Aug 2007. [128](#), [131](#)
 - [86] Alexander Högele, Christophe Galland, Martin Winger, and Atac Imamoglu. Photon antibunching in the photoluminescence spectra of a single carbon nanotube. *Phys. Rev. Lett.*, 100(21):217401, May 2008. [130](#)
 - [87] Florian Marquardt, Joe P. Chen, A. A. Clerk, and S. M. Girvin. Quantum theory of cavity-assisted sideband cooling of mechanical motion. *Phys. Rev. Lett.*, 99(9):093902, Aug 2007. [131](#)

List of Publications

1. J. Dreiser, M. Atatüre, C. Galland, T. Müller, A. Badolato, and A. Imamoglu. *Optical investigations of quantum dot spin dynamics as a function of external electric and magnetic fields*. Physical Review B **77**, 075317 (2008)
2. A. Högele, C. Galland, M. Winger, and A. Imamoglu. *Photon Antibunching in the Photoluminescence Spectra of a Single Carbon Nanotube*. Physical Review Letters **100**, 217401 (2008)
3. C. Galland, A. Högele, H. Türeci, and A. Imamoglu. *Non-Markovian Decoherence of Localized Nanotube Excitons by Acoustic Phonons* Physical Review Letters **101**, 067402 (2008)
4. C. Galland and A. Imamoglu. *All-Optical Manipulation of Electron Spins in Carbon-Nanotube Quantum Dots* Physical Review Letters **101**, 157404 (2008)

Acknowledgement

- ★ My first thoughts obviously go here to ATAÇ IMAMOĞLU who welcomed me in his group four years ago for what was meant to be a 4-month Master's thesis and finally extended to an exciting 4-year PhD thesis... I never regretted my choice to accept his generous offer although I had other plans at the time. This is due in part to the outstanding conditions for research provided for by the ETH and its staff. But Ataç's support was determining in my enjoying working in the group and in the success of my thesis. Professional discussions have been invaluable in guiding my research, improving my understanding, and reviving my sometime declining motivation. Besides, personal contact with him has always been of the most friendly and pleasant nature.
- ★ The other person who played a major role in my professional and personal development is ALEXANDER HÖGELE. He gave me the most valuable advice in our daily work and was the best mentor I can think of. His rigor and method remain to me as an ideal I endeavor to pursue. In addition it was a real pleasure to work at his sides.
- ★ Jan Dreiser and Mete Atatüre also deserve special mention. They introduced me to the physics and experimental techniques of quantum dots and optical spectroscopy. I had a wonderful time with them in my first months in the group, which certainly contributed to my decision to stay for my PhD.
- ★ Of course, nothing would have come out of my time here without the help and support of the whole Quantum Photonics Group's staff. Still I would like here to name a few people who were particularly helpful or whom I had the chance to make better acquaintance of: our secretaries, Monika and later Steffi; Martin (all of them!), Hakan, Lucio, Patrick, Christian... and all the others, who will surely recognize themselves!
- ★ Finally, I really want to thank my parents for their love and the outstanding education they offered to me. No success in my studies would have been possible without the optimal conditions prevailing at home and the constant support of my family. I would conclude by congratulating Olga and Sylvain for their recent marriage and wishing them a long and happy life together.

Curriculum Vitae

Personal Details

Name	Galland Christophe
Date of Birth	28. January, 1983
Place of Birth	Valence, France
email	galland@phys.ethz.ch

Education

1994 - 2001	<i>Baccalauréat scientifique.</i> Lycée C. Vernet, Valence.
2001 - 2003	<i>Classe Préparatoire aux Grandes Ecoles.</i> Lycée Champollion, Grenoble.
2003 - 2006	<i>Bachelor and Master degree.</i> Ecole Polytechnique, Paris.
Apr.-Aug. 2006	Master's Thesis: <i>Optical spin pumping in a single quantum dot.</i> Quantum Photonics Group, ETHZ.
March 2008	Awarded the title: <i>Diplômé de l'Ecole Polytechnique.</i>
2006 - 2010	PhD Student in the Quantum Photonics Group, ETH Zürich.

Experience

Languages	German, English, French.
Techniques	Confocal microscopy, cryogenics, fibre-optics, steady-state and time-resolved photoluminescence spectroscopy, time-correlated single photon counting, AFM, SEM, wet bench chemistry.
Computer Skills	Matlab (Numerical simulations), Mathematica, ComSol (FEM), LabView (Experiment control), Origin (Data treatment).

April 28, 2010

List of Figures

1.1	First observation of carbon nanotubes	1
1.2	Graphene real space and reciprocal space lattices	3
1.3	Band structure and energy dispersion of graphene	5
1.4	Forming a nanotube from the graphene lattice	6
1.5	Cutting Lines and nanotubes' subbands obtained from zone-folding	6
1.6	Subbands of semiconducting tubes and main optical transitions	7
1.7	The ratio problem	8
1.8	Many-body effects on the optical spectrum	9
1.9	Two-photon PL excitation	10
1.10	Symmetries of single-particle states and excitons	11
1.11	Brightening of the dark exciton under magnetic field	12
1.12	Photoluminescence from suspended nanotubes	13
1.13	Photoluminescence from surfactant-embedded nanotubes	14
1.14	Efficiency of different surfactants	15
1.15	Empirical Kataura plot	16
1.16	Schematic of the phonon-assisted excitation	17
1.17	Phonon-assisted PL excitation	18
1.18	PL bleaching and blinking: room-temperature vs. liquid nitrogen	19
1.19	PL spectral jumps and blinking at 4 Kelvin	20
1.20	PL stability: surfactant-embedded vs. suspended nanotubes	21
2.1	Simplified steps of sample preparation	24
2.2	AFM pictures and length statistics	25
2.3	Schematic of the setup for cryogenic confocal microscopy	26
2.4	PL spatial map and polarization selectivity	28
2.5	Functioning principle of a streak camera	29
2.6	Example of time-resolved PL measurement at 4 K	30
2.7	Schematic of the HBT setup	31
2.8	Photon statistics of typical emitters	33
2.9	Second-order correlation functions for typical emitters	33
2.10	Photon antibunching from a SWNT at different temperatures	34
2.11	Auger recombination: physical process	35
2.12	Number of emitted photon from an extended system	36
2.13	Photon pair correlation with Auger annihilation	37
2.14	Evidence for Auger recombination in PL saturation	38
2.15	PLE	40
3.1	Schematic view of a SWNT-QD	44
3.2	Low-energy acoustic phonons and their dispersion relations	45
3.3	Relevant acoustic phonons and their energy dispersions	46

3.4	SWNT-QD coupled to the phonon bath	47
3.5	Polarization and absorption calculated by Krummheuer <i>et al.</i>	49
3.6	Effect of the phonon bath dimensionality on the PL line shapes . . .	51
3.7	Deconvolution of the PL line shape	52
3.8	Calculated Fits to the PL line-shape of two SWNTs	54
3.9	An intuitive picture of phonon-induced broadening	55
3.10	RBM phonon replica in the PL of a bright nanotube	56
3.11	Non-Markovian decoherence of the SWNT-QD exciton	58
3.12	Temperature dependence of the quantum error correction rate	60
4.1	Schematic of exciton confinement by a field gradient	65
4.2	Perpendicular field coupling the exciton to the bending mode	67
4.3	Schematic of the nanotube resonator double-tip device	69
4.4	View of the mesh used in the FEM simulations	70
4.5	Results of the FEM simulations	72
4.6	Localized PL from a charged defect	72
4.7	Sketch of a charged impurity close to a SWNT	73
4.8	Parallel field and effective potential caused by a charged impurity . .	75
4.9	Confinement length and potential depth	76
4.10	Potential depth dependence on ϵ_S	77
4.11	Energy shift and spectral diffusion	78
4.12	QD ground state energy and its variation	78
4.13	PL line splitting and cross-correlation	80
4.14	Energy splitting due to tunnel coupling	82
4.15	Perpendicular electric field created by the charged impurity	85
4.16	Ohmic vs. sub-ohmic fits	87
4.17	Assessing the uncertainty in the fits	88
5.1	Spin-Orbit interaction in a hydrogenic atom	95
5.2	Aharonov-Bohm flux lifting the K-K' degeneracy	99
5.3	Spin-Orbit coupling as a topological flux	101
5.4	Orbital and Spin magnetic moments couple to the field	102
5.5	Experimental device used by Kuemmeth <i>et al.</i>	104
5.6	Experimental results from Kuemmeth <i>et al.</i>	105
5.7	First electron and hole levels in a magnetic field	106
5.8	Energy diagrams relevant for optical spin pumping	108
5.9	Level diagram of all relevant states and relaxations	111
5.10	Spin preparation fidelity color map as a function of magnetic field . .	114
5.11	Simplified picture of the spin pumping mechanism	115
5.12	Differential-transmission and spin preparation during laser scans . . .	116
5.13	Effect of K - K' mixing on the spin-pumping scheme	118
5.14	Color map: spin-flip v.s. valley-flip rates	119
5.15	Spin-pumping for asymmetric absorption lines in small SWNT-QDs .	120
5.16	Spin information transfer to a time-bin qubit	121
1	Effects of phonon coupling: short vs. long nanotubes	126
2	Level diagram and transitions in the cooling scheme	127
3	Numerical results of the achievable final phonon occupancy	131